Forschungszentrum Karlsruhe
Technik und Umwelt

Wissenschaftliche Berichte
FZKA 6030

Large Bundle PWR Test CORA-7: Test Results

S. Hagen, P. Hofmann, V. Noack, L. Sepold, G. Schanz, G. Schumacher

Hauptabteilung Ingenieurtechnik
Institut für Materialforschung
Institut für Neutronenphysik und Reaktortechnik
Projekt Nukleare Sicherheitsforschung

April 1998

Forschungszentrum Karlsruhe
Technik und Umwelt
Wissenschaftliche Berichte

FZKA 6030

Large Bundle PWR Test CORA-7: Test Results

S. Hagen, P. Hofmann, V. Noack, L. Sepold,
G. Schanz, G. Schumacher

Hauptabteilung Ingenieurtechnik
Institut für Materialforschung
Institut für Neutronenphysik und Reaktortechnik
Projekt Nukleare Sicherheitsforschung

Forschungszentrum Karlsruhe GmbH, Karlsruhe
1998

Forschungszentrum Karlsruhe GmbH
Postfach 3640, 76021 Karlsruhe

Mitglied der Hermann von Helmholtz-Gemeinschaft
Deutscher Forschungszentren (HGF)

ISSN 0947-8620

Abstract

Large Bundle PWR Test CORA-7; Test Results

The CORA out-of-pile experiments are part of the international Severe Fuel Damage (SFD) Program. They were performed to provide information on the damage progression of Light Water Reactor (LWR) fuel elements in loss-of-coolant accidents in the temperature range 1200°C to 2400°C.

Test CORA-7 should investigate if there is an influence of the bundle size on the fuel damage behaviour. Therefore the 25 rod PWR-type standard CORA bundle was replaced by a 57 rod bundle with five instead of two absorber rods. Power input and steam flow were increased proportional to the number of fuel rod simulators to give the same initial heat-up rate of 1 K/s as in the normal bundle. Furtheron the priority of the test was placed on the initial phase of the damage progression. More information on the chemical composition of initial and intermediate interaction products and their relocation behaviour should be obtained. Therefore power and steam input were terminated after the onset of the temperature escalation.

In general, test CORA-7 showed no difference in the damage behaviour, compared to the smaller bundle. The influence of the temperature escalation was confirmed. The escalation started at 750 mm at about 1200°C and continued over the upper half of the bundle, even after shutdown of the electric power input, as long as metallic Zircaloy and steam was available. At the upper end the maximum temperature was reached 400 s after shutdown of the electric power.

Due to the axial temperature profile melt formation and damage progression occurred only in the upper half of the bundle. The damage was initiated by the failure of the absorber rods at about 1250°C. The absorber melt liquefied the Zry of the fuel rod cladding. The posttest SEM investigations showed, that the absorber material was distributed over the whole bundle. It was not only found in the "refrozen" melt of the blockage within the bundle, but also in dishings between the pellets and inside the oxidised outer shell of the cladding. The absorber materials initiated the liquefaction of the Zircloy. The posttest investigation showed that the Zircaloy penetrated into the pellets and started the dissolution of the UO_2 far below its melting point.

The blockage formation of the solidified melt was mainly determined by the axial temperature profile. Obstacles like the spacers have only a minor influence. The hot melt penetrated locally the spacer. Then the melt solidified between the rods step by step according to the axial temperature profile. Melt relocation and axial temperature distribution are always strongly connected, i.e. the melt relocation is determined by the axial temperature distribution, but the axial temperature distribution on the other side is influenced by the melt relocation and the exothermal steam/Zircaloy reaction triggered by the heat transported with the melt.

Test CORA-7 supports the assumption that the bundle size with 25 rods, used in the other standard experiments, gives representative results on the damage progression for the larger PWR fuel element bundle.

Zusammenfassung

DWR Versuch CORA-7 mit größerem Bündelquerschnitt: Versuchsergebnisse.

Die CORA-Out-of-pile-Experimente wurden im Rahmen des internationalen „Severe Fuel Damage" Programms durchgeführt. Sie sollten Informationen über die Schadensmechanismen bei Leichtwasser-Reaktor-Brennelementen im Temperaturbereich von 1200°C bis 2400°C liefern.

Der Versuch CORA-7 sollte überprüfen, ob das normale CORA-Bündel mit 25 Stäben repräsentativ für die Schadensentwicklung im Brennelement ist. Das 25-Stab-Bündel wurde daher in Test CORA-7 durch ein 57-Stab-Bündel ersetzt, das fünf anstelle von zwei Absorberstäben enthielt. Leistungseinspeisung und Dampffluß wurden proportional zur Stabzahl erhöht, um den gleichen anfänglichen Temperaturanstieg von 1 K/s wie beim Normalbündel zu erreichen.

Beim Versuch CORA-7 sollten insbesondere Informationen über die Zusammensetzung der frühen und späteren Reaktionsprodukte und des Verlagerungsverhaltens der Schmelze gewonnen werden. Daher wurde die Leistungseinspeisung und die Dampfzufuhr beendet, sobald der Beginn der Temperatureskalation erreicht war.

Der Versuch CORA-7 zeigte keine signifikanten Unterschiede in der Schadensentwicklung und -progression im Vergleich zum Bündel mit 25 Stäben. Es bestätigte sich die Bedeutung der Temperatureskalation für das Aufheizverhalten des Bündels. Die Eskalation begann in der Höhe von 750 mm bei ca. 1200°C und setzte sich in der oberen Hälfte des Bündels auch nach Abschalten der elektrischen Leistungseinspeisung fort, solange wie metallisches Zirkaloy und Dampf vorhanden war. Am oberen Ende des Bündels wurde das Maximum der Temperatur erst 400 s nach Abschalten der elektrischen Leistung erreicht.

Entsprechend der axialen Temperaturverteilung war die Schadensausbreitung und Schmelzentwicklung nur in der oberen Hälfte des Bündels anzutreffen. Die Schadensentwicklung wird durch das Versagen der Absorberstäbe bei ca. 1250°C ausgelöst. Die Absorberschmelze verflüssigte das Zirkaloy der Brennstabhülle. Die SEM-Nachuntersuchungen haben gezeigt, daß sich das Absorbermaterial über das

gesamte Bündel ausgebreitet hatte. Absorbermaterial war nicht nur zwischen den Stäben in erstarrter Schmelze anzutreffen, sondern auch in dem Bereich zwischen Pellets und der äußeren Oxidschicht der Hüllrohre. Die Nachuntersuchungen zeigten, daß das verflüssigte Zirkaloy in die UO_2-Pellets eingedrungen war und die Auflösung des Pellets weit unter seiner Schmelztemperatur begonnen hat.

Das Erstarrungsverhalten der entstandenen Schmelzen ist im wesentlichen durch die axiale Temperaturverteilung bestimmt. Abstandshalter stellen nur geringe Hindernisse für die Schmelze dar. Die heiße Schmelze durchdringt den Abstandshalter durch Aufschmelzen und erstarrt darunter schrittweise zwischen den Stäben entsprechend der axialen Temperaturverteilung. Andererseits wird die axiale Temperaturverteilung durch den Wärmetransport durch Schmelzverlagerung und die dadurch wiederum geförderte exotherme Zirkon/Dampf-Reaktion beeinflußt.

Der Versuch CORA-7 unterstützt die Annahme, daß die in den anderen Versuchen gewählte Bündelgröße von 25 Stäben repräsentative Ergebnisse für die Schadensprogression von DWR-Brennelementen liefert.

Contents

1. Introduction

The TMI-2 accident has demonstrated that a severe fuel damage transient will not necessarily escalate to an uncontrolled core melt down accident if the design basis accident limits are exceeded. Therefore, comprehensive research programs have been initiated in various countries to investigate the relevant fuel rod bundle damage mechanisms that occur in an uncovered core, after an increase of temperature.

In the Federal Republic of Germany at the Forschungszentrum Karlsruhe (FZK) the Severe Fuel Damage (SFD) Program is now co-ordinated by the project Nuclear Safety Research (PSF) as successor of Project Nuclear Safety (PNS) and LWR Safety Project Group (PRS). As part of this program, out-of-pile experiments (the CORA-Program) were conducted at the Hauptabteilung Ingenieurtechnik (HIT), These experiments have been designed to provide information on the behaviour of Light water Reactor (LWR) fuel elements under severe fuel damage (SFD) conditions up to meltdown. The results of the out-of-pile experiments can be used for the assessment of the SFD computer codes.

Within the frame work of international co-operation the out-of-pile experiments are contributing confirmatory and complementary information to the results obtained from the limited number of inpile tests. The investigation of the basic phenomena of the damage process is supported by separate-effect tests.

The most important aspects concerning fuel rod failure and subsequent core degradation are the chemical interactions amongst the fuel element components in competition with the oxidation of the cladding by steam, which causes also the temperature escalation. Melt formation starts around 1200 °C by chemical interactions of the Inconel spacer grids and absorber materials (Ag, In, Cd) for PWRs and B_4C/stainless steel for BWRs with Zircaloy cladding. The dissolution of the UO_2 pellets by liquid Zircaloy starts far below the UO_2 melting point.

Melt formation, relocation, blockage formation and finally fragmentation of fuel elements during reflooding characterise the degraded core and the potential of long term coolability. Furthermore the influence of internal pressure of the fuel rods (ballooning and bursting) and external pressure of the system (solid contact between pellets and cladding) on the bundle meltdown behaviour was investigated.

Further on, the investigation of the influence of pre-oxidation, initial heat-up rate, steam availability, water level in the bundle and bundle size was included in the program. The damage behaviour of WER fuel elements was the subject of the last two CORA-tests.

The tests performed in the CORA-facility are listed in the test matrix (Table 1). The original test matrix was directed towards the behaviour of PWR fuel elements only. In 1988 discussion showed that in most countries using nuclear energy, information on the behaviour of BWRs in severe accident conditions was needed. In consequence, five planned PWR experiments were replaced by BWR tests in the revised test matrix. Also the original sequence of tests was changed, as one can see from the test numbers.

In this report the large bundle test CORA-7 is discussed. This test should investigate, if there is an influence of the bundle size on the damage progression. Furtheron more information on the chemical compositions of the initial and intermediate interaction products and their relocation behaviour should be gained. Therefore the test was terminated at lower temperatures than in the normal experiments.

In all other PWR tests, bundles with 25 rods were used. CORA-7 was built by 57 rods. According to the ratio in the PWR fuel element five of the 57 rods were replaced by absorber rods. With this arrangement the bundle of test CORA-7 contains 32 heated rods, 20 unheated rods and 5 absorber rods. To make the starting conditions comparable to the normal tests, power, steam and argon input were scaled to the size of bundle. To concentrate on the initial damage mechanisms, power and steam input were stopped after reaching the start of the temperature escalation.

2. Description of the CORA test facility

The CORA out-of-pile facility was designed to investigate the behaviour of LWR fuel elements under severe fuel damage accident conditions. In the experiments the decay heat was simulated by electrical heating. Great emphasis was placed on the fact that the test bundles contain the original materials used in light-water reactor fuel elements to investigate the different material interactions.

As in the other test, also in CORA-7 pellets, cladding, grid spacers, absorber rods and channel box walls were typical of the investigated PWR reactor with respect to their compositions and radial dimensions. Original UO_2 pellets, Zry-4 cladding, Zry-4 and Inconel-718 spacer, and (80 Ag, 15 In, 5 Cd) absorber rods in stainless steel cladding and Zry-4 guide tubes were used.

Figure 1 gives a simplified flow diagram of the facility. The geometrical arrangement of the different CORA components is given in Figure 2. The central part of the facility was the fuel rod bundle. The bundle was enclosed in a Zry shroud with ZrO_2 fibre insulation. A high temperature radiation shield surrounded the bundle and shroud assembly, leaving an annular space for introduction of the quench cylinder. The bundle was connected to the power supply system at the upper and lower ends.

Below the bundle there was the quench unit with a water filled quench cylinder, which can be raised around the bundle at a controlled speed. The cylinder was guided by three rods, which also connect the electric power to the bundle lower end.

The bundle upper end was fixed in the bundle head plate. The plate was connected by a funnel shaped tube to the surge condenser. The surge condenser was double-walled, leaving access to the bundle end fittings above the bundle head funnel.

The steam was produced in the steam generator, superheated and guided to the lower end of the bundle. The steam not consumed within the bundle condensed in two parallel condensers and the hydrogen produced was fed into the off-gas system after dilution by air to a low H_2 concentration.

Bundle design:

The bundle and its surroundings are shown in Figure 3 and 4. The bundle horizontal arrangement is given in Figure 5 and the bundle components in Figure 6. The same components as in the normal tests were used . In CORA-7 only the number of rods was increased. Characteristic data of the bundle are presented in Table 2. The bundle consisted of 32 heated rods, 20 unheated rods and 5 absorber rods inside the Zry guide tube.

The heated fuel rod simulator was sheathed with standard Zry-4 cladding tube, containing UO_2 annular pellets with a central heater. The heater consisted of a 1024 mm long tungsten rod (6 mm diameter), the upper electrode (300 mm

molybdenum; 689-770 mm copper) and the lower electrodes (300 mm molybdenum; 183-219 mm copper). The electrodes have a diameter of 9 mm. The electrodes are flame-sprayed with 0.2 mm thick layer of ZrO_2. Large flexible copper cables provided the connection to the electrical system. The resistance of the flexible cables for the voltage measurement and determination of the power was less than 1 mΩ per rod (recommended value: 0.5 mΩ).

The resistivities R of tungsten, molybdenum and copper respectively are given in the following three equations:

$$R_w = 2.61 \bullet 10^{-2} + 2.63 \bullet 10^{-4} T_w + 2.20 \bullet 10^{-8} T^2_w$$

$$R_{Mo} = 2.29 \bullet 10^{-2} + 5.36 \bullet 10^{-5} T_{mo} + 1.38 \bullet 10^{-7} T^2_{Mo} - 2.22 \bullet 10^{-11} T^3_{Mo}$$

$$R_{cu} = 7.89 \bullet 10^{-3} + 9.90 \bullet 10^{-5} T_{cu} - 5.49 \bullet 10^{-8} T^2_{Cu} + 3.16 \bullet^{-11} T^3_{Cu}$$

with T in [Kelvin] and R in [$\Omega mm^2/m$].

The unheated fuel rod simulators consisted of solid UO_2 pellets and Zry cladding. The unheated rods extended to about -200 mm elevation, i.e. to about 20 mm above the initial water level of the quench cylinder (-220 mm). Zry-4 spacers were used at 880 mm and -5mm elevation and an Inconel 718 spacer at 496 mm (Figure 3).

The absorber rods (Figure 6) were built from original components: (80 Ag, 15 In, 5 Cd; wt%) absorber alloy in 10,2/11,2 mm stainless steel cladding. The rod was surrounded by the 12,2/13,8 mm Zry-4 guide tube.

The fuel rod simulators and the absorber rods were screwed into the bundle head plate, sealing it hermetically. The bundle head plate thus gave the fixed elevation for the axial thermal movement of the rods.

For upper end bundle cooling the heated rods (the copper electrode inside the Zry-4 cladding) and the connectors for the pressure capillaries and the thermocouples of the unheated rods were surrounded by water. The water was cooled by a heat exchanger.

At the lower end the heated fuel rod simulators were cooled by the water of the quench cylinder. The initial water level was at the -220 mm elevation. The unheated rods were in contact with the water of the quench cylinder only through the

thermocouple connections. The gross volume of water inside the quench cylinder (230 mm ID) was about 70 l.

The bundle was surrounded by a Zry-4 shroud of 1.2 mm thickness. The shroud conducted the steam through the bundle. The steam entered at an orientation of 180° into the lower end (0 mm elevation). To minimise the heat losses through the shroud, it was surrounded by a 19 mm (0.75 inch) thick insulating layer of ZrO_2 fibre. On account of the low heat conductivity and heat capacity of the ZrO_2 fibre the shroud temperature could follow the bundle temperature closely. The shroud participated in the interaction with steam. The resulting oxidation energy contributed substantially to bundle heat-up.

The connection between the steam inlet at 0 mm elevation and shroud was made by a stainless steel tube. This tube extended down into the water of the quench cylinder thus forming a lower closure. The time history of the water level in the quench cylinder showed that there was no net condensation of steam in the quench cylinder.

The steam distribution tube joined into the shroud at an elevation of 36 mm. From this elevation the shroud extended in vertical direction to 1216 mm and the insulation to 1036 mm. At 6 elevations (390 mm to 890 mm) windows of 60 mm x 25 mm in the shroud and shroud insulation allowed the bundle inspection by the video systems.

The annuli between the shroud and the high-temperature shield and between high temperature shield and pressure containment were closed at the upper end by fibre ceramic layers of 38 mm thickness.

High temperature shield:

To keep the heat losses as low as possible, the bundle was surrounded by an additional high temperature shield (HTS). The vertical and the horizontal cross-sections of the high temperature shield are given in Figures 3 and 4. The high temperature shield consisted mainly of ceramic fibre plates. The inner layer of plates consisted of ZrO_2, and the outer layer of Al_2O_3. The fibre ceramics were excellent insulators and had a low density which resulted in a low heat capacity. The thermal shock behaviour of the fibre ceramics was also excellent.

The mechanical stability of the high temperature shield was improved by external walls of stainless steel (0.9 mm). The fibre ceramic plates were fixed at the stainless

steel cover by ceramic nails. The inner ZrO_2 layer was 38 mm thick, and the outer Al_2O_3 layer was 76 mm. They were separated by a gap of 23 mm. The distance from the inner insulation wall surface to the centre of the bundle was 153 mm.

The high temperature shield was located inside the pressure tube. A large number of flanges in the pressure tube allowed access to the bundle. Through these holes and their extensions in the temperature shield, the bundle could be inspected during the test with the help of the videoscope systems.

Heating system:

In test CORA-7 it was necessary to heat 32 rods instead of the normal 16 rods. As the facility was designed for the use of 24 heated rods only, for 16 simulator positions the copper rods of the electrodes of two adjacent rods were connected by a copper bridge to the connecting cable. Through this lines the current flow was twice as large, as through the single rod cables. The combination of rods can be recognised from the tables on the right side of Figure 17.

The CORA facility allows the rods to be individually connected to three power systems which could be operated at different voltage to produce a different power input per rod. In this test the intended power input was the same for all rods. After the voltages and the currents of the individual rods or "double rod groups" were measured, the power input for each rod could be determined. The power input was controlled by a computer. The time dependent power history was programmed before the test. The power was controlled by measurement of the currents of the groups, and by setting the voltage to obtain the desired power. The coordination of the 32 heated rods to the three power systems can be seen from Figure 17. The double rods can be recognized by the slash between the two rod numbers in the tables on the right side of Figure 12.

3. Test Conduct

To get comparable results (same starting temperature, same initial temperature increase) we used per rod nearly the same conditions as for the small PWR bundles. The values were chosen according to precalculations at INEL, Idaho Falls and the

Technology Centre at Winfrith. The flow of preheated argon (16 g/s), and the steam input (12 g/s) and the integral power were twice as large, as in the small bundles.

In the CORA experiments the following phases for the test sequence were generally distinguished (Figure 9):

1. 0-3000 s: pre-heating

2. 3000-4150 s: transient

3. > 4150: cooldown.

The pressure in the system was controlled as in all tests to 0.22 MPa. The argon input is devided in two parts. The first part of 16 g/s Argon is preheated and enters at the lower end into the bundle (0 mm elevation). The second part of 1,4 g/s does not flow through the bundle, but is used for keeping the windows of the videoscopes clean. The second part is marked with the label "videoscopes". Both parts contribute to the dilution of the hydrogen that leaves the facility. In test CORA-7 there was not yet an argon flow used for the protection of bundle head plates, as in tests performed later.

The flow of 16 g/s preheated argon through the bundle and a low constant electric power input of about 0.88 kW increase the temperature to a level high enough to avoid condensation of steam (16 g/s) added after 3300 sec.

During the transient phase the initial temperature increase of about 1 K/s was realised by raising the electric power input from 12 to 39 kW (Figure 9). The test was terminated by turning off the electric power at 4150 s (slow cooldown by heat losses). The steam input was stopped at 4100 s.

The boundary conditions during the test are given in detail in (Figure 10 to 24). Figure 10 shows the argon flow within the facility. Figure 11 presents the overpressure of 1,2 bar (2,2 bar absolute) in the system. Figure 12 gives the total electric power input, which was produced by the voltage inputs to the three groups of rods (Figure 13) and the resulting total current (Figure 15). The electric power input is controlled by measurement of the voltages of the rod groups and the currents of the individual rods (Figure 17). Then the computer sets the voltages to have the power that is required. The total electric energy input corresponds to the time integral of the power input (Figure 14).

In Figure 16 the time dependence of the electrical resistance of the bundle is given. After 4000 s the resistance of the bundle is increasing faster. This corresponds to the fact that for getting a linear power increase (Figure 12) the voltage (Figure 13) has to be increased faster to compensate the current decrease (Figure 15) after 4000 s. This resistance increase is correlated to the temperature increase caused by the starting of the temperature escalation and reflects the strong temperature dependency of the resistance of the tungsten heater.

In Figure 17 course of the currents of the single rods for the three groups are given. The irregularities after 4100 s are caused by the melt formation due to the temperature escalation peak.

The resistance of the rod groups and the single rods are given in Figure 18 and Figures 19-21. In all graphs the influence of temperature can be seen. The sharp spikes during power shutdown are artificial due to measurement of voltage and current at not exact by the same time.

In Figure 22 the water temperatures in the quench cylinder for tests CORA-18 and CORA-29 are given because for CORA-7 no measurement could be performed. CORA-18 was the large test with a BWR typical bundle and CORA-29 a PWR test with a normal bundle. The data should give a hint for the possible temperature course in test CORA-7.

At -50 mm elevation (Figure 23) the temperature was measured at the outside of the steam tube (15° and 195°) and 15 mm inside the steam tube (165° and 345°). For the same side 165°/195° or 345°/15° the temperature measured 15 mm inside the tube is higher than the temperature of the steam tube, which has contact to the water of the quench cylinder. But comparing the same type of measurements, the thermocouples at the side of the steam entrance (165°, 195°) give the higher reading.

The temperature of the incoming argon at the steam inlet is measured with two thermocouples (Figure 24). The resulting measurements give practically the same value. The increase of the steam inlet temperature is caused by the heatup of the walls of the connecting tube from the superheater to the entrance of the bundle due to the additional heat capacity of the steam.

4. Temperature measurements

The temperatures in the bundle were measured by high-temperature thermocouples of WRe5/WRe26 wires and HfO_2 insulating material. The sheath was made of tantalum and Zircaloy. Four thermocouples (Figure 33) were shielded additionally with a ZrO_2 sheath. The measurements in the high temperature shield were performed with NiCrNi-thermocouples sheathed with stainless steel. Also the compensation cables were sheathed with stainless steel. The positions of the thermocouples in the bundle are given in Table 3 and Figures 25 and 37 and those in the high temperature shield in Figures 50 and 51.

The temperature measurements of the bundle are presented as function of time in the following way: on one hand, the temperatures of the components (heated rods, unheated rods, channel box walls, absorber blade, etc.) are given in Figures 26 - 39. On the other hand - for comparison reasons - the temperature measurements for different components are grouped by axial elevations (Figures 40 - 49). The temperature of the high temperature shield are given in Figures 52 - 66.

4.1 Temperature in the bundle

Due to the bundle arrangement with a Zircaloy shroud, participating in the exothermic reaction with steam and the low heat conductivity and heat capacity of the fibre insulation, a flat radial temperature profile was obtained. The temperature of the shroud is not lower than that of the components of the bundle. The temperature graphs, measured on identical components at the same elevation are close to each other with a similar shape. The differences in some regions up to about 100 K, may be caused by local differences in the bundle arrangement, relocated material or steam flow. We have therefore defined in Figure 48 best-estimate temperatures of the bundle by using mainly the temperature of the unheated rods (Figure 32). The temperature at 750 mm elevation is combined with the temperature of the ceramic protected TC (Figure 33) and the missing temperature at 850 mm elevation is determined by interpolation between the temperatures at 750 mm and 950 mm. In Figure 49a these temperature values are re-arranged as axial temperature

distribution for different times in the test sequence. In Figure 49b the isothermal distribution as function of time and elevation is given.

Up to 3200 s the temperature in the bundle was mainly determined by the heating effect of the incoming gas of about 500°C. The result was an axial temperature profile with the maximum at the lower end and decreasing temperatures with increasing elevations. After increased power input and temperature level the incoming gas and steam was cooler than the bundle and acted as coolant. The maximum of the temperature moved to the upper end of the bundle. Beginning at 750 mm elevation the temperature escalation begun first in the interval 750 mm to 950 mm elevation. After the start of the temperature escalation the steam input was stopped at 4080 s. But due to the remaining steam in the facility the Zry/steam reaction still produced enough energy to keep the temperature escalation going. At 950 mm elevation the temperature maximum appears between 4200 and 4300 s. At 1050 mm elevation the maximum was reached at 4300 s. Towards the lower end of the bundle at 550 mm and 450 mm elevation, the maximum was reached at 4450 s. At the upper end at 1150 and 1250 mm the temperatures did not reach their maxima before 4600 s, that was about 400 s after the shutdown of the electric power. No escalation was found at 350 mm elevation and below. The small peak at 150 mm was caused by droplets of relocated melt in the neighbourhood of that thermocouple.

In the upper diagram of Figure 67 the hydrogen production in test CORA-7 is given. The beginning of the acceleration of the hydrogen production at about 3900 s is correlated to the acceleration of the temperature increase in the upper part of the bundle. The maximum of the hydrogen production corresponds to the fast acceleration of the temperature. The exothermic Zry/steam reaction, which produces the hydrogen parallel to the chemical heat production was the reason for the temperature escalation in the bundle.

The temperatures of the absorber rods are given in Figure 35. The thermocouples were positioned inside the stainless steel absorber cladding at 350 mm and 750 mm elevation. All thermocouple readings show at both elevations a delay in the temperature increase at about 800°C, the melting temperature of the (Ag,In,Cd)-alloy. The start of the delay is found for both elevations at the same time (about

+3650 s), but the delay lasts much longer for the lower elevations. This is due to the much faster general increase at 750 mm.

The small peaks in the temperature at the lower end of the bundle (Figures 23, 34, 36) between about 4000 and 4250 s are assumed to be caused by melt, which was produced in the upper part of the bundle and then has moved down into the neighbourhood of the respective thermocouple.

4.2 Temperatures of the High Temperature Shield

The time dependant temperatures at different elevations are given in Figures 52 to 55 for the inside surface of the HTS (153 mm radius), inside the insulation (192 mm and 255 mm radius) and for the outer surface (293 mm radius).

At 153 mm radius (Figure 52) the maximum temperature is reached at about 4600 s in the upper half of the bundle and some hundred seconds later in the lower half. From 90 mm to 950 mm elevation the maximum increases from 150°C to 850°C.

At the outside of the bundle insulation (Figure 39), - the surface opposite to the inner surface of the HTS – the maximum temperature increased from 250 °C at 150 mm to 1000°C at 950 mm. A comparison yields in a temperature difference of 100-150 K between outside of the bundle and the HTS inner surface.

The maximum bundle temperature increased between 150 mm and 850 mm from about 700 °C to 1800 °C. Comparison with the maximum of the outside of the bundle shows that the temperature gradient through the 20 mm ZrO_2-fibre insulation increased form 450 to 800 K from the lower to the upper end of the bundle.

Inside the HTS the temperature increase from the lower to the upper end was much slower. At 192 mm radius the maximum temperature varied between 190°C and 260°C. At 255 and 293 mm the maximum temperature increased from about 70°C to 100°C between 150 mm to 950 mm elevation. Thus temperature gradient inside the HTS yields 80 K to 850 K in the region from the lower to the upper part of the HTS.

In Figures 56 to 60 temperatures are compared at equivalent positions on opposite sides in the High Temperature Shield. The radial temperature profile is given in Figure 61 to 66 for different elevations. Figures 61 to 63 show the temperature for

the usually shown test time 3000-6000 s. The time span from 0 to 10 000 s is given in Figures 64 to 66. The slightly higher values for 293 mm radius, compared to 255 mm hint to an additional small heat conduction effect due to the outer stainless steel surface, which reaches to the hotter upper end of the HTS.

5. Hydrogen generation

The main measurement for the hydrogen produced by the zirconium/steam reaction was performed with a mass spectrometer system. As the hydrogen produced in the bundle had to pass through the condenser, the mixing chamber and the capillary to the mass spectrometer, a delay and peak broadening between production and measurement took place.

To correct for this change we have performed in connection with CORA-7 a calibration of the response of the system. This calibration was performed by running the system with the normal gas flow and introducing at 750 mm elevation through a small tube a constant flow of hydrogen during 100 seconds as shown in Figure 67a. The measured response is given in the same figure. With a Fast Fourier Transformation the transfer function K(t) was determined. Figure 67b shows the determination of a second hydrogen input from the measured response with the help of the transfer function determined in the first test. A combination of both tests is used for the transfer function used in the actual experiment.

A schematic diagram of the probes, gas lines, and gas analysis systems is provided in Figure 8. The off-gas mixture which contained hydrogen among other gases is transported to the spectrometer via capillary tubes. It was analysed by quadrupole mass spectrometers of the type Leybold PQ 100. The ion currents representing the concentration of the respective gases were determined. The production rate of a gas component was calculated with the ratio of the partial pressure of the particular gas to that of argon (carrier gas) and multiplied by the argon flow rate through the test bundle. The hydrogen generation rate was evaluated as follows:

$R_m = 2 \bullet p_H F_{Ar} / (22.4 \bullet p_{Ar})$ [g/s]

with

R_m = mass production rate of hydrogen [g/s]

p_H = partial pressure of hydrogen

p_{AR} = partial pressure of argon

F_{ar} = volumetric argon flow through mixing chamber [l/s]

The transfer function was applied to the measured data. The results is a corrected curve that represents the H_2 production rate in the test section.

For test CORA-7 the measured as well as the corrected hydrogen production rates are given in Figure 67. The measured data are obtained from the gas probes of the mixing chamber. The hydrogen production corresponds to the change of the temperature increase in the bundle as seen in Figure 48. Integral values of the hydrogen production are given in the lower diagram of Figure 67. The total produced hydrogen amounts to about 114 g.

Figure 68 shows the chemical energy produced in the exothermal reaction which is calculated from the corrected measured hydrogen in comparison to the electric power input.

In the maximum of hydrogen production the chemical input is about 25% higher than the electrical input. In the determination of this ratio it is neglected, that the electric power is produced over the whole length of the rod, while the escalation takes place only in the hot part of the upper end of the rod.

6. Failure of the absorber rods and fuel rod simulators

For the absorber rods and the central fuel rod simulator the internal pressure was registered to determine the time of rod failure. The results are shown in Figures 70 and 71. From Figure 71 it can be seen, that the absorber rods fail within 80 s from about 4020 s to 4100 s. The failure times are given in Figure 72. The failure times and the temperatures of the absorber rods at 750 mm can be used to determine the failure temperatures: (6.6: 1250°C; 4.8: 1260°C; 2.4: 1300°C; 8.2: 1220°C; 4.0: 1300°C). In the cross section of Figure 72 the sequence of absorber rod failure is marked. Also shown is the sequence of the temperatures at 1250 mm elevation (730 - 670°C) as the first digit in the double number of the relevant fuel rod position. The second digit represents the sequence of temperatures at 50 mm (660 – 600°C).

In Figure 73 the movement of melt as seen by the video system, is shown. Movement of melt is first visualised at the 800 mm window at about 4030 seconds. As it results from the pressure loss measurements the first absorber rod failed at 4020 s. 10 s were needed for the absorber melt to penetrate the guide tube and after that to distribute through the bundle.

7. Post-test appearance of the bundle

The post-test appearance of the bundle is given in Figures 82 to 101. Figure 82 shows the bundle with insulation at three different orientations. These pictures demonstrate the state of the bundle in its original position after the test without any changes. Only the surrounding high temperature shield was moved down, to give access to the bundle. Generally the insulation has kept its smooth appearance of the original arrangement. Only in the region from about 700 to 900 mm the insulation has developed cracks and was slightly deformed.

In Figure 83 the bundle can be seen after the insulation has been removed. In accordance with the axial temperature distribution the Zry shroud is oxidised and deformed between about 550 and 1000 mm. This region can be seen in more detail in Figures 84 and 85.

Six windows were cut into the shroud and shroud insulation to allow the inspection of the bundle by the video system. The appearance of these areas are given in Figure 86 and 87. In most of the windows relocated, refrozen melt can be recognised. At 900 mm elevation (Figure 86) the oxidised outer surface of the guide tube 4.0 can be recognised. The black lower part of the visible region shows the influence of the absorber melt. Also the cladding of the rod L5 on the right side is strongly influenced by the absorber melt while the rod on the left side L3 has developed an undisturbed oxidised cladding. On the outer most rod L1 one can recognise the fragmentation of the oxidised cladding. At 700 mm elevation the absorber rod was positioned on the left side behind rods B1 and B3. The region between these rods is filled preferentially with relocated absorber melt. At 500 mm elevation the Inconel spacer can be

recognised. The spacer is still intact on this side of the bundle. Only a small amount of melt was relocated and has attacked the spacer on the right side of the window.

In Figure 87 at 120° orientation two windows at 800 mm and 600 mm are shown. At the positions of the absorber rod 4.8 it can be recognised, that at 600 mm and 800 mm the absorber melt has relocated on the outside of the absorber rod position. At 600 mm elevation in front of the neighbouring rod 2.8 absorber melt has relocated.

The post-test appearance of the bundle after removal of the shroud is shown in Figure 88. A distinct behaviour change can be recognised at about 500 mm elevation, the approximate elevation of the Inconel spacer. Below the spacer the cladding of the rods has its original appearance, while above the spacer, a strong oxidation with flowering has developed. At 120°, 210° and 300° direction absorber rods are positioned in the second row of the bundle edge. In the neighbourhood of this absorber rods a much stronger melt relocation can be recognised. This axial dependence of the damage behaviour corresponds to the axial temperature profile. At 450 mm elevation in the bundle a temperature of only about 1250°C is reached, while at 550 mm the temperature has increased to about 1750°C.

Details of the bundle appearance are given in Figures 89 to 101. In Figure 89 the failure of the Zry guide tube can be recognised up to 1200 mm elevation. Figure 90 demonstrates the survival of the Zry spacer and a strong flowering of the cladding of the two neighbouring rods to the absorber rod. In Figure 91 the strong flowering of the cladding can be recognised for all outer fuel rods. Most of the melt has relocated in front of the absorber rod (marked with "a" in the picture). In Figure 92 changes of the surface of the Zircaloy guide tube can be seen down to about 400 mm. A similar behaviour as on the 120° side can be seen in Figures 93 to 101 for the 165° and 210° sides.

The damage in the bundle can best be seen from the horizontal and vertical cross sections. To enable the cutting of the cross sections, a Lucite box was set around the bundle for encapsulation with epoxy resin. The lower end of this box was closed by a paraffin layer which was produced by refreezing paraffin floating on the water of the quench cylinder. Rutapox 0273 with the hardener LC (Bakelite GmbH, Iserlohn) was used as epoxy. This epoxy was chosen as its reaction time was slow enough, so that the shrinkage effect is negligible. The hardening time was one week. The bundle

was filled starting from the bottom through the steam inlet. A saw with 2.3 mm thick diamond blade of 500 mm OD (mean diamond grain size 138 μm) was used to cut the bundle at 3200 rpm. The horizontal and vertical cross sections are given in Figures 104 to 111 and in appendix C. In Figures 113 to 147 the damage development is demonstrated in detail with the help of additional enlarged presentations of cross sections and the results of SEM investigations.

The horizontal cross sections in Figures 104 and 105 complement the information gained from the outer appearance of the bundle. The damage has developed in the upper part of the bundle above 480 mm elevation. The absorber disappeared and one can recognise the strong damage to the cladding in the interior of the bundle. From the later discussed SEM/EDX investigations it can be seen, that this damage is strongly influenced by the interaction of absorber material with the Zry of the cladding.

The neighbourhood of the absorber rods 4.0 and 6.6 is shown in Figures 108 and 109. The areas of all five absorber rods are shown in Figure 108 for the different axial elevations. Above about 500 mm elevation the absorber rods have disappeared. Only remnants of the oxidised Zry guide tube have survived at some locations. Remnants of the stainless steel cladding can firstly be seen at about 1150 mm. At 1230 mm elevation for most of the absorber rods stainless steel cladding and Zry-guide have survived. The cross sections below 480 mm elevation show that the absorber material, liquefied at about 800°C, has relocated inside the gap between absorber and guide tube down to about 100 mm. The gap is filled completely by relocated melt down to about 270 mm elevation.

As the liquid Ag is not stable in contact with the Zry of the guide tube, it has dissolved the metallic guide tube in the upper half of the bundle. The liquid containing Ag, In, Cd from the absorber and the stainless steel components from the absorber cladding, was spread into the bundle and has attacked the Zry cladding. The eutectic interaction of the absorber melt with the Zircaloy has liquefied the cladding much below the melting temperature of Zry. The cross sections show the flowering of the oxidised cladding preferentially at outer rods of the bundle.

The melt formed in the upper part of the bundle penetrated the Inconel spacer and relocated into the region below. The distribution can clearly be recognised from the

axial cross sections in Figure 109. The spacer cannot stop the melt. The blockage is influenced by the spacer, but the main influence is given by the axial temperature profile. On the other hand the resulting axial profile is influenced by the relocated melt, due to the heat transported by the melt and the chemical heat at the resulting higher temperature.

Figures 109 and 111 show that the lower crust is formed by stepwise relocated material. Melt refrozen between the rods formed an even oxide-layer at the surface and then is covered by the next fraction of downcoming melt. To understand the material interactions special regions of the vertical and horizontal cross sections are investigated by a Scanning Electron Microscope (SEM/EDX). The results of these investigation demonstrate the strong influence of the interaction of the absorber materials with the Zircaloy of the cladding and of the liquefied Zircaloy with the UO_2 of the pellet.

The following figures illustrate expressively the spreading of the materials from the absorber rods. Ag, In Cd and Fe, Cr, Ni were found not only in the refrozen melt but also in the dishings between the pellets and inside the oxide layers of the fuel rod cladding. The pictures and the determination of the element distribution show in many examples the penetration of the Zry into the UO_2.

Parallel to the interaction with the absorber material the oxidation of Zry takes place. These two types of processes are in competition as both are enhanced with increasing temperature . The typical Zry oxide formation and the oxidation of the solidified melt can be recognised in the following figures.

Figure 113 shows the investigated regions from the vertical cross section of the upper edge of the blockage (482 to 512 mm). An enlarged presentation of area 1 is given in Figure 115, with the positions of the investigations. But this picture also shows clearly the smooth protective oxide formation in regions with no melt contact, compared to regions covered by melt.

Figure 115a gives an overview of the different processes which can be seen in area 1. Short explanations are given in each picture. The numbers for positions in Figure 115a do not agree with those used in Figure 115 to identify the regions invetigated in Figures 116-120. Figure 116 should illustrate the smooth uniform oxidation of the Zry. In region 4 the oxide layer is about 3 times larger than that at

region 3. This reflects the strong temperature gradient in this area. In addition in the UO_2, seen on the left side of region 4 and on the right side of region 3, one can recognise the beginning of the penetration of Zry into the UO_2 pellet.

In Figure 117 the results of point analysis from SEM investigations are given for different positions of region 7 in contact of liquefied cladding to the UO_2 pellet. In the region of former Zry cladding absorber material and U was found (1, 2, 5, 9, 10). Inside the pellet Zr is found (3, 6, 8) and at position 7 even the absorber materials. The upper optical picture shows the typical "layer-like" penetration of the Zry into the UO_2. In Figure 118 the region around the dishing between the pellets is investigated. At the corners one can again recognise the "layer-like" penetration of the Zry. The point analysis confirms the absorber materials in the gap between the pellet (1, 2, 8) and the Zr inside the pellets (3, 4, 6).

In Figure 119 at position 6 the composition of the materials more inside the same dishing is investigated. Absorber materials are found in all phases. In Figure 120 analysis values are given from the dishing after one pellet lower. Again the absorber materials are found.

Area 13 of the axial cross section of Figure 113 is given in enlarged presentation in Figure 121. In this area the axial cross section has passed a fuel rod simulator close to the surface and in this way represents well the interaction between Zry and pellet. In Figure 121a again an overview of regions from area 13 is given with explaining remarks. Figure 122 demonstrates the "layer-like" penetration of Zr into the pellet. The pictures also show the change in the fragmentation inside the pellet.

In Figure 124 the composition of the phases at a pellet melt contact area is given. As usual all phases in the solidified melt contain absorber materials. As one can see from analysis at Point 4, the globules at the surface of the pellet are formed by a ceramic (U,Zr,O)) alloy. The structure of the refrozen material is given in Figure 125.

Area 24 of the axial cross section of Figure 113 is shown in Figure 128 in enlarged form. Positions 25, 27 and 29 mark areas for further examination inside oxidised cladding. The double arrow in the right upper part of the Figure 128 marks the change of thickness of the oxide layer at transition from cladding covered with relocated melt to cladding in steam.

In Figure 129 a region in the neighbourhood of oxidised cladding is selected, in which also relocated, refrozen melt was oxidised and than covered again with melt. So an oxide layer of the cladding and of refrozen melt can be seen. This two types of oxide layers can be compared also in Figures 130 and 131.

Position 1 in Figure 129 shows that the melt relocated on the oxidised refrozen melt consists of absorber melt. The composition at positions 2 and 5 show that also the oxidised refrozen melt contains U and absorber materials, as it is found in the relocated refrozen melt below this oxidised layer (points 5 and 6).

Figure 131 shows that the oxide layer formed in steam on the outside of the cladding is reduced by the metallic melt when it covers the oxide layer. At position 27 of Figure 133 again the composition of phases inside oxidised cladding are given. At this region of former cladding most phases contain also U and the absorber materials. This results show, that absorber melt, which has attacked the cladding at a different elevation must have moved inside the outer oxidised cladding layer to this position. The presence of U in the melt formed shows, that the liquefied Zry has started the dissolution of the UO_2 pellet.

In Figure 135 a horizontal cross section at 480 mm is given. The general temperature of this elevation allowed the Inconel spacer to survive. In the region, with relocation of melt from above, the melt has penetrated the spacer and relocated into the region below the spacer.

The pictures of Figure 136 from the cross section at 480 mm show that also at this elevation the blockages have formed stepwise. This can be concluded from the oxide layers inside the refrozen melt. Melt which only partly covered the area between the rods is oxidised on the surface exposed to the steam. One can recognise the even layers of oxide formed. Then melt moving down later has again covered this oxidised surface. Area 13 shows that the oxidation of the relocated refrozen melt is very similar to that of the cladding.

In Figure 138 at different positions of the horizontal cross section at 480 mm the oxide layers are shown. The smooth protective oxide layer is found at all positions. The different thickness is caused by the different temperature due to the different distance from the relocated melt.

In Figure 140 from the axial cross section between 428 mm to 465 mm the area 7a is chosen for further investigation. Region 11 at the dishing between two pellets is enlarged in Figure 141. Due to the lower temperature at this elevation (462 mm) the penetration of Zr into the UO_2 is just starting. In Figure 142 this dishing is compared to the dishing at 512 mm with higher temperature. One clearly can see the progress of the penetration of Zr.

From the axial cross section between 422 mm and 465 mm of Figure 143 (see also Figure 109) the area 17 is chosen for investigation of oxidation of the relocated melt at the regions 18 and 20. Region 18 starts in Figure 143 on the left side at the oxide layer of the fuel rod simulator. The same orientation can be found in the orientation picture in the upper left corner of Figure 144. The enlarged picture of region 18 is shown side-inverted. The oxidised part of the cladding has survived. The horizontal oxide layer shows in general a similar structure like the cladding. One can recognise that melt relocating on the oxide layer is again oxidised in an even layer at the surface. This structured layer formation can be seen especially in the region 20.

In Figure 145 the horizontal cross section at 863 mm is shown. This elevation belongs to the region of highest temperature within the bundle. The result of the dissolution of UO_2 by Zry can be clearly seen in subregion 4 of region 1. Subregion 4 is enlarged in Figure 146. In pictures 5, 6, 7 parts of subregion 4 are again highly enlarged that one can recognise the detailed structure. We have to remember, that we see the state of the material after cooling of the bundle. In pictures 5 and 6 we see the penetration of the Zr into the UO_2. At the position of picture 7 the homogenous (U, Zr, O) melt precipitated the (U, Zr)O_2 crystals at cooldown in the typical rectangular shaped form.

In Figure 146a it is shown that we have received in test CORA-3 the same form for the precipitated (U, Zr)O_2 crystals in the melt relocated between the UO_2 columns. On the left side of Figure 146a the TMI-2 specimen K9-P2/F is shown for comparison with a similar structure of relocated melt between the UO_2 pellet columns. An enlargement of the cross section by the same factor reveals the same structure of the precipitated crystals. This good agreement of the resulting microstructure confirms that our out-of-pile experimentation is a satisfactory method to simulate reactor conditions.

8. Summary and discussion

Test CORA-7 should investigate if the normal bundle size is representative for the damage development of the reactor bundle. Furthermore more information of the chemical compositions of the initial and intermediate interaction products and their relocation behaviour should be gained. Therefore CORA-7 used a bundle of 57 rods. According to the ratio in the fuel element 5 rods were replaced by absorber rods. To make the starting conditions comparable to the normal tests, power, steam and argon input were scaled to the size of the bundle. To concentrate on the initial damage mechanisms, power and steam input were stopped after reaching the start of the temperature escalation.

In general the large PWR-type bundle showed the same damage behaviour as found in the smaller bundles. The temperature escalation started in the upper part of the bundle at 750 mm elevation after surpassing 1200°C and progressed downwards to 450 mm and upwards to 1250 mm elevation. Of interest was the fact that the temperature was still increasing several hundred seconds after the power input to the bundle had stopped. Limiting processes for the exothermic reaction are the decrease of metallic Zry and steam and the increase of the protective oxide layer.

The posttest bundle appearance and the cross sections showed that the melt formation and the damage progression developed in the upper part of the bundle according to the axial temperature profile.

Oxidation and interaction with the absorber materials are competitive reactions for the Zircaloy of the cladding. Preferentially, in the outer region smooth oxide layers are formed influenced by the "flowering" process. The damage process in the bundle was initiated by the failure of the absorber rods at about 1250°C. The AgInCd-melt, liquefied at about 800°C, is stable against the stainless steel of the absorber rod cladding. But the stainless steel of the cladding in contact to the Zry of the guide tube starts an eutectic reaction, which can lead to a failure of the cladding at about 1250°C. The absorber melt filled the gap to the guide tube down to at least 270 mm elevations. Refreezing absorber melt has formed a closure of the gap according to axial temperature profile. First absorber melt moving though the bundle is already seen by the video system about 10 s after the absorber rod failure. At the end of the

test the absorber melt dissolved the guide tubes above 480 mm and spread through the bundle.

The dominant influence of absorber materials on the initial damage development is proved by the detailed post-test investigations with optical and scanning electron microscopy. Absorber material was found throughout the whole bundle: Not only in the refrozen melt of the blockage between the fuel rod simulators, but also in dishings between the pellets and in the gap between the oxidised outer skin of the cladding and the pellet. This means that the absorber material, spreading around into the bundle is not only attacking the cladding from the outside. If the absorber material has dissolved the cladding at a certain elevation, the interaction proceeds into the metallic Zry layer between oxide skin and pellet. The melt containing the absorber material can penetrate into the dishings. The vertical and horizontal cross sections have shown that the Zry penetrated into the UO_2 pellets, to start the dissolution process of UO_2. This behaviour is clearly proved by all SEM/EDX analysis measurements. Though we have reached in CORA-7 only maximal temperatures of about 1800°C, U was found at many locations inside the refrozen melt.

Concerning the relocation behaviour CORA-7 has proved the results gained in the smaller bundle tests. The spreading of the melt formed by interaction in the upper half of the bundle, is influenced but not stopped by the Inconel spacer. The hot melt penetrated the spacer by melting and then formed a blockage between the fuel rods simulators according to the axial temperature profile. The axial cross sections show that the blockage was formed stepwise. Material was oxidised and then new melt relocated onto the top of the oxide layer.

Melt relocation and axial temperature distribution are always strongly connected, i.e. the melt relocation is determined by the axial temperature distribution, but the axial temperature distribution on the opposite is influenced by the heat transported with the relocated melt and the possible influence on the exothermal Zircaloy/steam reaction triggered by the temperature changes.

9. References

1. J.M. Broughton; P. Kuan, D.A. Petti; "A Scenario of the Three Mile Island Unit 2 Accident", *Nuclear Technology*, Vol. 87, 34-53 (1989).
2. S. Hagen, K. Hain: "Out-of-pile Bundle Experiments on Severe Fuel Damage (CORA-Program)", *KfK* 3677 (1986).
3. S. Hagen, P. Hofmann, G. Schanz, L. Sepold; "Interactions in Zircaloy/UO_2 Fuel Rod Bundles with Inconel Spacers at Temperatures above 1200°C (CORA-2 and CORA-3)", *KfK* 4378 (1990).
4. S. Hagen, P. Hofmann, V. Noack, G. Schanz, G. Schumacher, L. Sepold; "Results of SFD Experiment CORA-13 (OECD International Standard Problem 31)" *KfK* 5054 (1993).
5. M. Firnhaber, K. Trambauer, S. Hagen, P. Hofmann, G. Schanz, L. Sepold:ISP-31, "CORA-13 Experiment on Severe Fuel Damage GRS-106", *KfK* 5287, NEA/CSNI/R (93) 17 (1993).
6. S. Hagen, P. Hofmann, V. Noack, G. Schanz, G. Schumacher, L. Sepold; "BWR Slow Heat-up Test CORA-31: Test Results", *KfK* 5383 (1994)
7. S. Hagen, P. Hofmann, V. Noack, G. Schanz, G. Schumacher, L. Sepold; "Dry Core BWR Test CORA-33: Test Results", *KfK* 5261 (1994).
8. S. Hagen, P. Hofmann, V. Noack, G. Schanz, G. Schumacher, L. Sepold; "Behaviour of a VVER Fuel Element Tested under Severe Accident Conditions in the CORA Facility (Test Results of Experiment CORA-W1)" *KfK* 5212 (1994).
9. S. Hagen, P. Hofmann, V. Noack, G. Schanz, G. Schumacher, L. Sepold; "Behaviour of a VVER-1000 Fuel Element with Boron Carbide/Steel Absorber Tested under Severe Fuel Damage Conditions in the CORA Facility (Results of Experiment CORA-W2)", *KfK* 5363 (1994).
10. J. Burbach; "Results of SEM/EDX Microrange Analyses of the PWR Fuel Element Meltdown Experiment CORA-13", *KfK* 5162 (1993).
11. J. Burbach; "Results of SEM/EDX Microrange Analyses of the BWR Fuel Element Meltdown Experiment CORA-16", *KfK* 5282 (1994).

12. S. Hagen, P. Hofmann, V. Noack, L. Sepold, G. Schanz, G. Schumacher;" Comparison of the Quench Experiments CORA-12, CORA-13, CORA-17", *FZKA* 5679, (1996).

13. S. Hagen, P. Hofmann, V. Noack, L. Sepold, G. Schanz, G. Schumacher; "Impact of Absorber Rod Material on Bundle Degradation Seen in CORA Experiments", *FZKA* 5680 (1996).

14. S. Hagen, P. Hofmann, V. Noack, L. Sepold, G. Schanz, G. Schumacher; "Pre-oxidised BWR Test CORA-28: Test Results"; FZKA 5571 (1997)

15. S. Hagen, P. Hofmann, V. Noack, L. Sepold, G. Schanz, G. Schumacher; "Pre-oxidised PWR Test CORA-29: Test Results"; FZKA 5928 (1997)

16. S. Hagen, P. Hofmann, V. Noack, L. Sepold, G. Schanz, G. Schumacher; "Cold Lower End Test CORA-10: Test Results" FZKA 5572 (1997)

17. S. Hagen, P. Hofmann, V. Noack, L. Sepold, G. Schanz, G. Schumacher; "Slow Heatup PWR Test CORA-30: Test Results" FZKA 5929 (1997)

18. S. Hagen, P. Hofmann, V. Noack, L. Sepold, G. Schanz, G. Schumacher; "Large Bundle BWR Test CORA-18: Test Results FZKA 6031 (1998)

10. Acknowledgements

At the Forschungszentrum Karlsruhe a variety of support needed for preparation, conduct, and evaluation of the experiment is hereby gratefully acknowledged. The facility was designed by K. Hain and his team. The special bundle set up was designed by Mr. H. Junker. The test rods were assembled by Mr. E. Mackert, the test bundles by Messrs. H. Gießmann and R. Röder. The authors would like to thank Messrs. H. Benz, C. Grehl and H.J. Röhling for test preparations and conduct. Mr. K. P. Wallenfels was responsible for arrangement of camera and video systems and for the preparation of temperature measurements. Messrs. R. Huber and H. Malauschek prepared and conducted the on-line measurements of the off-gas composition. The post-test investigations by the optical microscope were performed by Mr. Metzger and the SEM investigations by Mr. Burbach.

Finally we would like to express our gratitude to Mrs. U. Ivanitsch for the careful typing of this report.

List of tables

Tab. 1: CORA Test Matrix

Test No.	Max. Cladding Tempera-tures	Absorber Material	Other Test Conditions	Date of Test
2	≈ 2000°C	-	UO_2 refer., inconel spacer	Aug. 6, 1987
3	≈ 2400°C	-	UO_2 refer., high temperature	Dec. 3, 1987
5	≈ 2000°C	Ag, In, Cd	PWR-absorber	Febr. 26, 1988
12	≈ 2000°C	Ag, In, Cd	quenching	June 9, 1988
16	≈ 2000°C	B_4C	BWR-absorber	Nov. 24, 1988
15	≈ 2000°C	Ag, In, Cd	rods with internal pressure	March 2, 1989
17	≈ 2000°C	B_4C	quenching	June 29, 1989
9	≈ 2000°C	Ag, In, Cd	10 bar system pressure	Nov. 9, 1989
7	< 2000°C	Ag, In ,Cd	57-rod bundle, slow cooling	Febr. 22, 1990
18	< 2000°C	B_4C	59-rod bundle, slow cooling	June 21, 1990
13	≈ 2200°C	Ag, In, Cd	OECD/ISP; quench initiation at higher temperature	Nov. 15, 1990
29*	≈ 2000°C	Ag, In, Cd	pre-oxidized,	April 11, 1991
31*	≈ 2000°C	B_4C	slow initial heat-up (≈ 0.3 K/s)	July 25, 1991
30*	≈ 2000°C	Ag, In, Cd	slow initial heat-up (≈ 0.2 K/s)	Oct. 30, 1991
28*	≈ 2000°C	B_4C	pre-oxidized	Febr. 25, 1992
10	≈ 2000°C	Ag, In, Cd	cold lower end 2 g/s steam flow rate	July 16, 1992
33	≈ 2000°C	B_4C	dry core conditions, no extra steam input	Oct. 1, 1992
W1	≈ 2000°C	-	WWER-test	Febr. 18, 1993
W2	≈ 2000°C	B_4C	WWER test with absorber	April 21, 1993

Initial heat-up rate: ≈ 1,0 K/s; Steam flow rate, PWR: 6 g/s BWR: 2 g/s;
CORA 10: 2g/s; CORA W1 + W2: 4 g/s; quench rate (from the bottom) ≈1 cm/s

Tab. 2: Design characteristics of bundle CORA-7

Bundle type:			PWR
Bundle size:			57 rods
Number of heated rods:			32
Number of unheated rods:			20
Pitch:			14.3 mm
Rod outside diameter:			10.75 mm
Cladding material:			Zircaloy-4
Cladding thickness:			0.725 mm
Rod length	- heated rods:		1840 mm
	(elevation		-369 to 1471 mm)
	- unheated rods:		1672 mm
	(elevation		-201 to 1471 mm)
Heated length:			1000 mm
Heater material:			Tungsten (W)
Heater diameter:			6 mm
Fuel pellets	- heated rods:		UO_2 annular pellet s
	- unheated rods:		UO_2 full pellets
Pellet stack	- heated rods:		0 to 1000 mm
	- unheated rods:		-200 to 1300 mm
U-235 enrichment			0.2 %
Pellet outer diameter (nominal)			9.1 mm
Grid spacer	- material:		Zircaloy-4, Inconel 718
	- length:	Zry	42 mm
		Inc.	38 mm
	- location:	lower (Zry)	-5 mm
		center (Inc.	+496 mm
		top (Zry)	+880 mm
Shroud	- material		Zircaloy-4
	- wall thickness		1.2 mm
	- outside dimensions		143 x 143 mm
	- elevation		36 mm to 1216 mm
	- insulation material		ZrO_2 fiber
	- insulation thickness		20 mm
Absorber rod	- number of rods		5
	- material and composition		80Ag,15In,5Cd (wt.%)
	- cladding		Stainless steel
	- cladding OD		11.2 mm
	- cladding ID		10.2 mm
	- length		1489 mm
	- elevation		-189 mm to +1300 mm
Absorber rod guide tube			
	- material		Zircaloy-4
	- OD		13.8 mm
	- wall thickness of tube		0.8 mm

Note: Elevations are referred to the bottom of the heated zone (0 mm = EL 5121). The values for the grid spacers refer to the top end.

Tab. 3: Positions of thermocouples

Positions of thermocouples in unheated rods (CORA-7)			
Slot number	Elevation [mm]	Rod number	Type of TC
111	1250	8.6	NiCrNi
112	1250	**8.0**	NiCrNi
113	1250	**6.0**	NiCrNi
114	1250	4.2	NiCrNi
115	1250	2.8	NiCrNi
116	1250	2.6	NiCrNi
117	1250	0.8	NiCrNi
118	1250	0.2	NiCrNi
81	1150	4.6	WRe *
82	1050	2.2	WRe *
83	950	6.4	WRe*
84	950	**0.0**	WRe *
85	850	6.2	WRe *
86	750	8.8	WRe *
87	750	4.4	WRe *
161	550	8.8	WRe*
162	550	4.4	WRe *
163	550	**0.0**	WRe *
164	450	6.2	WRe *
165	350	2.2	WRe *
166	250	6.4	WRe *
167	150	4.6	WRe*
191	50	8.6	NiCrNi
192	50	**8.0**	NiCrNi
193	50	**6.0**	NiCrNi
194	50	4.2	NiCrNi
195	50	2.6	NiCrNi
196	50	0.8	NiCrNi
197	50	0.2	NiCrNi
198	50	2.8	NiCrNi

Positions of thermocouples in the absorber rods (CORA-7)			
Slot number	Elevation [mm]	Rod number	Type of TC
96	750	2.4	WRe**
97	750	**4.0**	WRe**
98	750	4.8	WRe**
99	750	6.6	WRe**
100	750	8.2	WRe**
176	350	2.4	WRe**
177	350	**4.0**	WRe**
178	350	4.8	WRe**
179	350	6.6	WRe**
180	350	8.2	WRe**

Positions of thermocouples at the heated rods (CORA- 7)			
Slot number	Elevation [mm]	Rod number	Type of TC
94	950	5.3	WRe *
93	750	5.5	WRe *

Positions of thermocouples at the guide tube (CORA-7)			
Slot number	Elevation [mm]	Rod number	Type of TC
168	150	2.4	WRe*
169	150	**4.0**	WRe*
170	150	4.8	WRe*
171	150	6.6	WRe*
172	150	8.2	WRe*

Positions of thermocouples at the grid spacer (CORA-7)			
Slot number	Elevation [mm]	Orientation of TE	Type of TC
205	475	120°	NiCrNi
206	475	210°	NiCrNi
207	475	300°	NiCrNi
208	475	30°	NiCrNi
209	-26	120°	NiCrNi
210	-26	210°	NiCrNi
211	-26	300°	NiCrNi
212	-26	30°	NiCrNi

Positions of thermocouples at the shroud outer surface (CORA-7)			
Slot number	Elevation [mm]	Orientation of TE	Type of TC
95	950	30°	WRe*
88	750	30°	WRe *
173	550	30°	WRe *
174	350	30°	WRe *
175	150	30°	WRe*

*) WRe wires,duplex sheath (Ta/Zr)

**) WRe wires,Ta sheath

Tab. 3: (Continuation)

Positions of thermocouples at the shroud insulation (CORA-7).			
Slot number	Elevation [mm]	Orientation of TE	Type of TC
199	950	210°	NiCrNi
201	750	210°	NiCrNi
202	550	210°	NiCrNi
203	350	210°	NiCrNi
204	150	210°	NiCrNi

Positions of thermocouples for gas temp. meas. betw. shroud + HTS (CORA-7)			
Slot number	Elevation [mm]	Orientation of TE	Type of TC
91	950	30°	WRe*
92	950	210°	WRe*
89	750	300°	WRe*
90	750	120°	WRe*

Positions of thermocouples btw.shroud + hts and at steam distribution tube (CORA-7)			
Slot number	Elevation [mm]	Orientation of TE	Type of TC
121	351	180°	NiCrNi
215	0	180°	NiCrNi
216	0	180°	NiCrNi
217	0	15°	NiCrNi
218	0	195°	NiCrNi
213	0	345°	NiCrNi
214	0	165°	NiCrNi

*) WRe wires,duplex sheath (Ta/Zr)

**) WRe wires,Ta sheath

Tab. 4: List of cross sections for test bundle CORA-7

Sample	Sample length	Elevation bottom	top	Comments
7-a	xxx mm	-xxx mm	-60 mm	Lower remnant
Cut	2 mm			
7-01a	13 mm	-58 mm	-45 mm	Horizontal cross section
Cut	2 mm			
7-01	13 mm	-43 mm	-30 mm	Horiz. cross sect., lower spacer
Cut	2 mm			
7-01b	13 mm	-28 mm	-15 mm	Horizontal cross section
Cut	2 mm			
7-b	125 mm	-13 mm	112 mm	
Cut	2 mm			
7-02	13 mm	114 mm	127 mm	Horizontal cross section
Cut	2 mm			
7-c	140 mm	129 mm	269 mm	
Cut	2 mm			
7-03	13 mm	271 mm	284 mm	Horizontal cross section
Cut	2 mm			
7-d	140 mm	286 mm	426 mm	With 2 add. vert. sections (7-d-L)
Cut	2 mm			
7-e	37 mm	428 mm	465 mm	With additional vertical section
Cut	2 mm			
7-04	13 mm	467 mm	480 mm	Horiz. cross sect., central spacer
Cut	2 mm			
7-f1	34 mm	482 mm	516 mm	With 2 add. vert. sect. (7-f1-R)
Cut	2 mm			
7-f2	104 mm	518 mm	622 mm	With additional vertical section
Cut	2 mm			

Tab. 4: (Continuation)

7-05	13 mm	624 mm	637 mm	Horizontal cross section
Cut	2 mm			
7-g	140 mm	639 mm	779 mm	
Cut	2 mm			
7-06	13 mm	781 mm	794 mm	Horizontal cross section
Cut	2 mm			
7-h	54 mm	796 mm	848 mm	
Cut	2 mm			
7-07	13 mm	850 mm	863 mm	Horiz. cross sect., upper spacer
Cut	2 mm			
7-i	140 mm	865 mm	1005 mm	
Cut	2 mm			Above heated zone
7-j	140 mm	1007 mm	1147 mm	
Cut	2 mm			
7-k	81 mm	1149 mm	1230 mm	
Cut	2 mm			
7-l	xx mm	1232 mm	xxxx mm	Upper remnant

Table 5: Distribution of void volumes in unheated and heated rods

Void volume of one unheated rod

	elevation [mm]	volume [cm^3]	relative volume [cm^3/cm]
dishing of uranium pelletts; gap between pellet stack and cladding	-201 to 1315	4.083	0.027
void volume above pellet stack	1315 to 1439	8.378	0.678
	1439 to 1456	0.711	0.419
	1456 to 1522	3.658	0.55
	1522 to 1531	0.387	0.43
	1531 to 1762	6.531	0.283
	1762 to 1764	0.084	0.419
system for pressure measurement		15.120	
total void volume		38.952	

Void volume of one heated rod

	elevation [mm]	volume [cm^3]	relative volume [cm^3/cm]
void volume below pellet stack	-369 to -334	0.826	0.236
	-334 to 0	1.391	0.0417
gap between pellet stack and cladding and between pellet stack and heater	0 to 1024	2.311	0.023
void above pellet stack	1024 to 1875	3.545	0.0417
	1875 to 1911	0.852	0.24
system of pressure measurement		10.860	
total void volume		19.785	

Table 6: Total specific mass data of bundle CORA-7

Specific mass [kg/m]	
Tungsten heater elements	17.48
UO_2	25.82
Zircaloy in rods	7.80
Zircaloy in absorber rods	1.08
Stainless steel in absorber rods	0.65
Ag/In/Cd absorber	3.98
Inconel grid spacer	0.25
Zircaloy grid spacer	0.32
Zircaloy of shroud	3.58
Total zircaloy	12.46

Table 7: Areas of bundle CORA-7

Cross section areas [m^2]	
Tungsten	$9.048\ 10^{-4}$
UO_2	$2.482\ 10^{-3}$
Zircaloy cladding	$1.187\ 10^{-3}$
Absorber, Ag/In/Cd	$4.085\ 10^{-4}$
Absorber, Stainless steel cladding	$8.40\ 10^{-5}$
Absorber, Zircaloy guide tube	$1.635\ 10^{-4}$
Zircaloy shroud	$5.46\ 10^{-4}$

List of figures

26 : Temperatures of heated rods

27 : Temperatures of unheated rods, 1250 mm elevation

28 : Temperatures of unheated rods, 950 mm elevation

29 : Temperatures of unheated rods, 750 mm elevation

30 : Temperatures of unheated rods, 550 mm elevation

31 : Temperatures of unheated rods, 50 mm elevation

32 : Temperatures of unheated rods (TCs in central position)

33 : Temperatures between bundle and shroud measured with ceramic protected TCs

34 : Temperatures of the spacers

35 : Temperatures of the absorber rods

36 : Temperatures of the guide tubes of absorber rods

37 : Location of the thermocouples at shroud and shroud insulation (CORA-7)

38 : Temperatures of outer side of shroud

39 : Temperatures of the shroud insulation

40 : Temperatures at elevations given (1250 mm)

41 : Temperatures at elevations given (1150-1050 mm)

42 : Temperatures at elevations given (950-850 mm)

43 : Temperatures at elevations given (750 mm)

44 : Temperatures at elevations given (550-450 mm)

45 : Temperatures at elevations given (350-250 mm)

46 : Temperatures at elevations given (150 - 50 mm)

47 : Temperatures at elevations given (0 - -300 mm)

48 : Best-estimate bundle temperatures at different elevations

49a : Axial temperature distribution during the transient of test CORA-7

49b : Isothermal distribution of the bundle temperature

50 : Locations of thermocouples in the high temperature shield (CORA-7)

51 : Position of thermocouples in the high temperature shield for test CORA-7

52 : Temperatures of HTS, Inner surface at 153 mm radius

53 : Temperatures of HTS, Temperatures in HT shield at 192 mm radius, 345°

54 : Temperatures of HTS, Temperatures in HT shield at 255 mm radius

55 : Temperatures of HTS, Temperatures in HT shield at 293 mm radius

56 : Temperatures of HTS, Comparison on inner surface at 153 mm radius

57 : Temperatures of HTS, Comparison on inner surface at 153 mm radius, 990 mm and 890 mm elevation

58 : Temperatures of HTS, Comparison on inner surface at 153 mm radius, 390 mm and 90 mm elevation

59 : Temperatures of HTS, Comparison in HT-shield at 192 mm radius, 950 mm and 750 mm elevation

60 : Temperatures of HTS, Comparison in HT-shield at 192 mm radius, 550 mm and 150 mm elevation

61 : Temperatures of HTS, Radial dependence at about 950 mm elevation

62 : Temperatures of HTS, Radial dependence at about 550 mm elevation

63 : Temperatures of HTS, Radial dependence at about 100 mm elevation

64 : Temperatures of HTS, Radial dependence at about 950 mm elevation, 0 - 10000 s

65 : Temperatures of HTS, Radial dependence at about 550 mm elevation, 0 - 10000 s

66 : Temperatures of HTS, Radial dependence at about 100 mm elevation, 0 - 10000 s

67a : Determination of the transfer function by measurement of the delta-function of the hydrogen input

67b : Comparison of corrected measured curve with the hydrogen input

67 : Measured hydrogen production in test CORA-7; production rate (top) and integral values (bottom)

68 : Comparison of chemical and electric power

69 : not used

70 : Internal pressure of fuel rod simulator 4.4 and absorber rods

71 : Determination of failure time by pressure loss measurement

72 : Sequence of absorber rod failure compared to sequence of temperature at 1250 mm and 50 mm elevation

73 : Melt movement as seen by the video system

74 - 81 : not used

82 : Posttest appearance of bundle, shroud and shroud insulation; 30°, 120°, 300° orientation

83 : Posttest view of bundle CORA-7 after removal of shroud insulation; 30°, 120°, 210°, 300° orientation

84 : Posttest view of bundle CORA-7 after removal of shroud insulation; partial view 30° and 120° orientation, 500 -1000 mm elevation

85 : Posttest view of bundle CORA-7 after removal of shroud insulation; partial view 210° and 300° orientation, 500 - 1000 mm elevation

86 : Posttest view; windows at 900 mm 300° orientation, 700 mm 210° orientation and 500 mm 30° orientation

87 : Posttest view; 120° orientation; windows at 800 mm and 600 mm elevation

88 : Posttest view of bundle CORA-7 after removal of shroud; 30°, 120°, 210°, 300° orientation

89 : Posttest view of bundle; 120° partial view, 1050 - 1350 mm

90 : Posttest view of bundle, 120° partial view, 800 - 1050 mm

91 : Post test view of bundle, 120° partial view, 550-800 mm

92 : Post test view of bundle, 120° partial view, 250-500 mm

93 : Post test view of bundle, 165° partial view, 1050-1350 mm

94 : Post test view of bundle, 165° partial view, 800-1050 mm

95 : Post test view of bundle, 165° partial view, 550-800 mm

96 : Post test view of bundle, 165° partial view, 250-500 mm

97 : Post test view of bundle, 165° partial view, 100-350 mm

98 : Post test view of bundle, 210° partial view, 1050-1350 mm

99 : Post test view of bundle, 210° partial view, 800-1050 mm

100 : Post test view of bundle, 210° partial view, 500-800 mm

101 : Post test view of bundle, 210° partial view, 250-500 mm

102 : not used

103 : Bundle sectioning

104 : Horizontal cross sections of bundle CORA-7, top view, 1147 to 480 mm elevation

105 : Horizontal cross sections of bundle CORA-7, top view, 465 to -45 mm elevation

106 Region of absorber rod 4.0

107 Region of absorber rod 6.6

108 : Failure of the 5 absorber rods

109 : Comparison of horizontal cross sections and vertical cross sections through absorber rods 4.0 and 4.8 (268 - 622 mm)

110 : Comparison of left and right sights of vertical cross sections through absorber rods 4.0 and 4.8

111 : Vertical cross sections through absorber rods 4.0 and 4.8 (286-426 mm)

112 : not used

113 : Vertical cross section used for further examinations

114 : not used

115a : Overview: Microstructures of area 1 of the vertical cross section 482 - 516 mm; CORA7-f (see Fig. 113)

115 : Positions of examination of region 1

116 : Oxidation at positions 4 and 3 (picture 1)

117 : Pellet / melt interaction (region1, position 7)

118 : Pellet / melt interaction (region1, position 2)

119 : Phase composition in gap between pellets (region 1, position 6)

120 : Pellet / melt interaction (region1, position 8)

121a : Overview: Microstructures of area 13 of the vertical cross section 482 - 516 mm; CORA7-f (see Fig. 113)

121 : Positions of examination of region 13

122 : Interaction Zry / UO_2

123 : not used

124 : Composition of phase at melt / pellet contact (region 13, position 22)

125 : Structure of refrozen melt

126 : not used

127 : not used

128a : Overview: Microstructures of area 24 of the vertical cross section 482 - 516 mm; CORA7-f (see Fig. 113)

128 : Positions of examination of region 14

129 : Composition around oxidised relocated melt (region 14, position 25)

130 : Oxidised cladding and oxidation of relocated melt

131 : Interaction of melt with oxidised cladding

132 : Oxidised cladding

133 : Composition of melt inside the oxidised cladding

134 : not used

135a : Overview: Material behavior at the Inconel grid spacer cross section CORA7-04 (480 mm)

135 : Cross section at 480 mm used for further examinations

136 : Oxidation of relocated material (480 mm)

137 : not used

138 : Oxidation of the cladding at different positions within the bundle (480 mm elevation)

139 : not used

140 : Vertical cross section 428 - 465 mm and region 7a

141 : Melt penetration into pellet gap (region 7a, position 11)

142 : Comparison of melt / pellet interaction at 512 and 462 mm

143 : Region 17 of vertical cross section (428 - 465 mm) used in further investigations

144 : Oxidation of relocated melt (region 17)

145a : Overview: Material behavior at the zircaloy grid spacer cross section CORA7-07 (863 mm)

145 : Cross section at 863 mm and region 1 used for further examinations

146 : UO_2 / Zry interaction (region 1, position 4)

146a : Comparison of microstructure of TMI-2 core bore specimen K9-P1/F and CORA-3 vertical cross section 3-b

Appendix

A1 : Power input during pre-heat phase

A2 : Resistance of bundle during pre-heat phase

A3 : Argon input prior to test

A4 : Temperatures at steam inlet; pre-heat phase

A5 : Temperatures of heated rods; pre-heat phase

A6 : Temperatures of unheated rods, 1250 mm elevation; pre-heat phase

A7 : Temperatures of unheated rods, 950 mm elevation; pre-heat phase

A8 : Temperatures of unheated rods, 750 mm elevation; pre-heat phase

A9 : Temperatures of unheated rods, 550 mm elevation; pre-heat phase

A10 : Temperatures of unheated rods, 50 mm elevation; pre-heat phase

A11 : Temperatures of unheated rods (Tcs in central position)1250 mm elevation; pre-heat phase

A12 : Temperatures between bundle and shroud measured with ceramic protected TCs; pre-heat phase

A13 : Temperatures of the spacers; pre-heat phase

A14 : Temperatures of the absorber rods; pre-heat phase

A15 : Temperatures of the guide tubes of absorber rods; pre-heat phase

A16 : Temperatures of outer side of shroud; pre-heat phase

A17 : Temperatures of the shroud insulation; pre-heat phase

B1 : System overpressure, argonflow, steamflow and power (Pretest CORA-7)

B2 : Pretest temperatures in unheated rods at elevations given (Pretest CORA-7)

B3 : Pretest temperatures in unheated rods at elevations given (Pretest CORA-7)

B4 : Pretest temperatures on the guide tube at 150 mm elevation (Pretest CORA-7)

B5 : Pretest temperatures in absorber rods at 350 mm elevation (Pretest CORA-7)

B6 : Pretest temperatures on the shroud at elevations given (Pretest CORA-7)

B7 : Comparison of temperatures in unheated fuel rod simulators at elevations given for pretest (P) and test CORA-7

C1 : Horizontal cross section; top view, 1230 mm

C2 : Horizontal cross section; top view, 1147 mm

C3 : Horizontal cross section; top view, 1005 mm

C4 : Horizontal cross section; top view, 863 mm

C5 : Horizontal cross section; top view, 848 mm

C6 : Horizontal cross section; top view, 794 mm

C7 : Horizontal cross section; top view, 779 mm

C8 : Horizontal cross section; top view, 637 mm

C9 : Horizontal cross section; top view, 622 mm

C10 : Horizontal cross section; top view, 480 mm

C11 : Horizontal cross section; top view, 465 mm

C12 : Horizontal cross section; top view, 426 mm

C13 : Horizontal cross section; top view, 284 mm

C14 : Horizontal cross section; top view, 269 mm

C15 : Horizontal cross section; top view, 127 mm

C16 : Horizontal cross section; top view, 112 mm

C17 : Horizontal cross section; top view, -30 mm

C18 : Horizontal cross section; top view, -45 mm

C19 : Horizontal cross section; bottom view, -58 mm

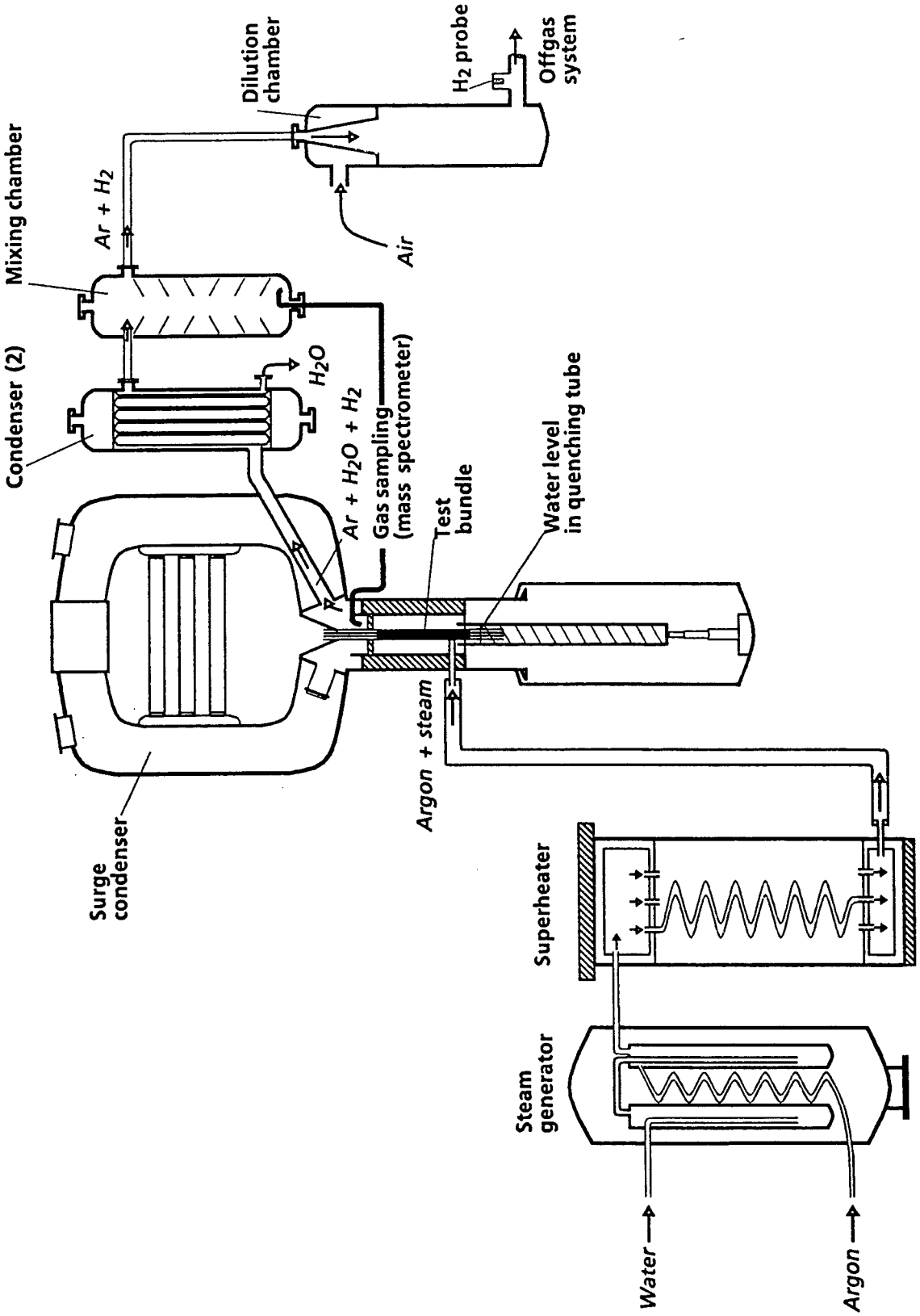

Fig. 1: SFD Test Facility (simplified flow diagram)

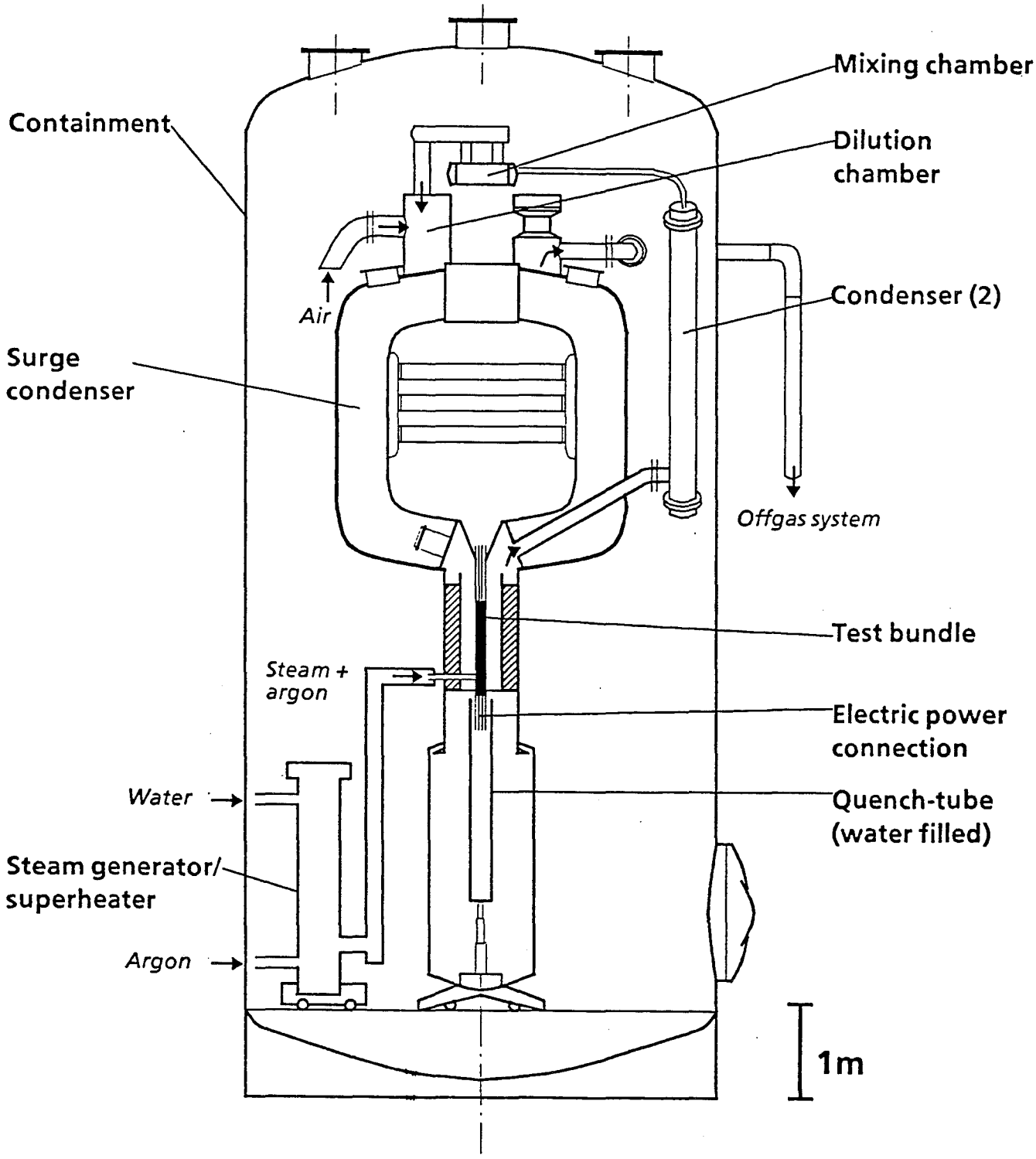

Fig. 2: SFD Test Facility CORA (Main Components)

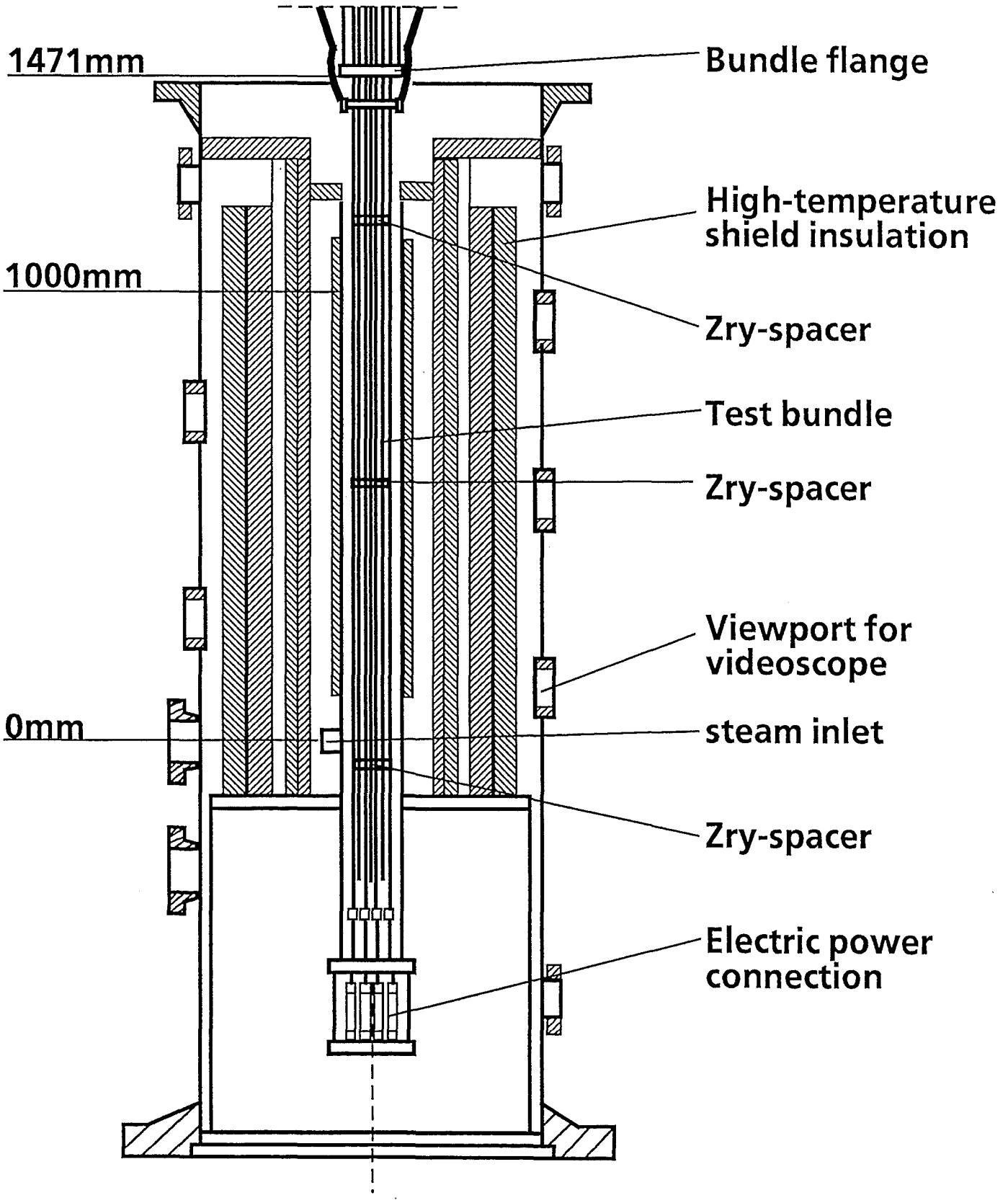

Fig. 3: CORA bundle arrangement

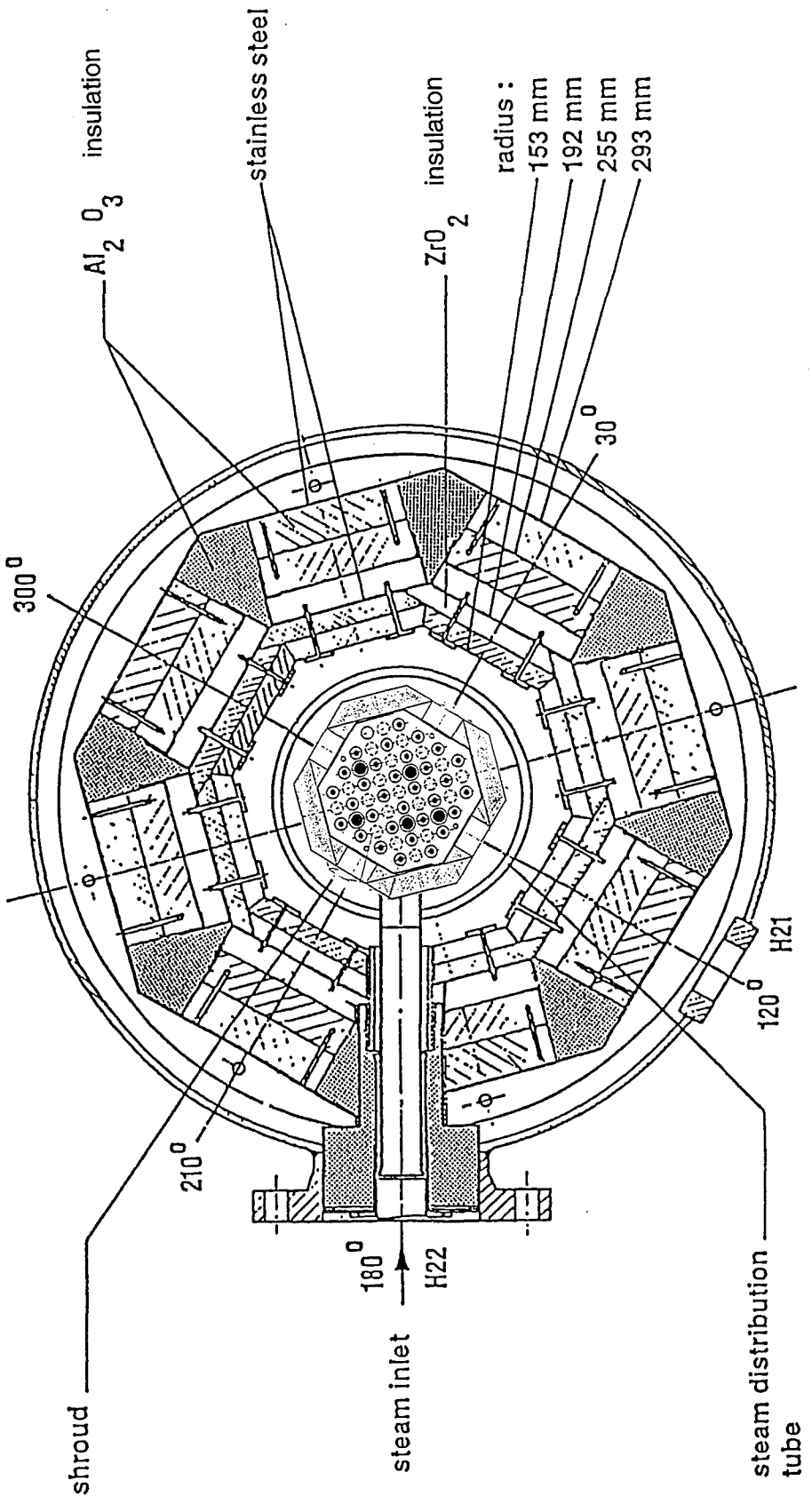

Fig. 4: Horizontal cross section of the high-temperature shield

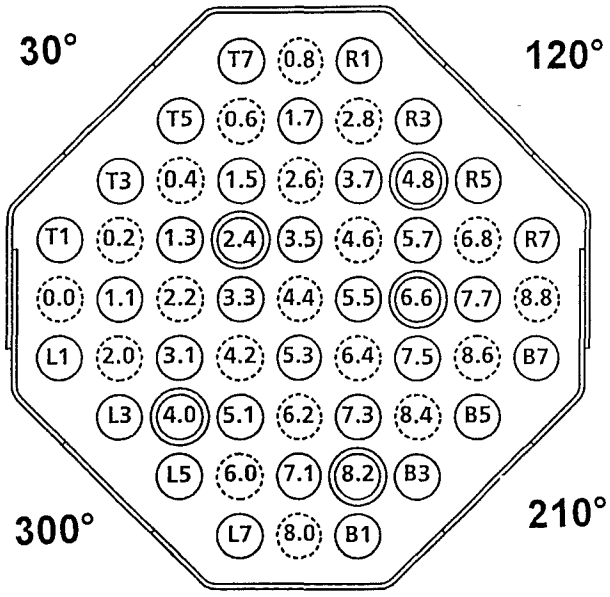

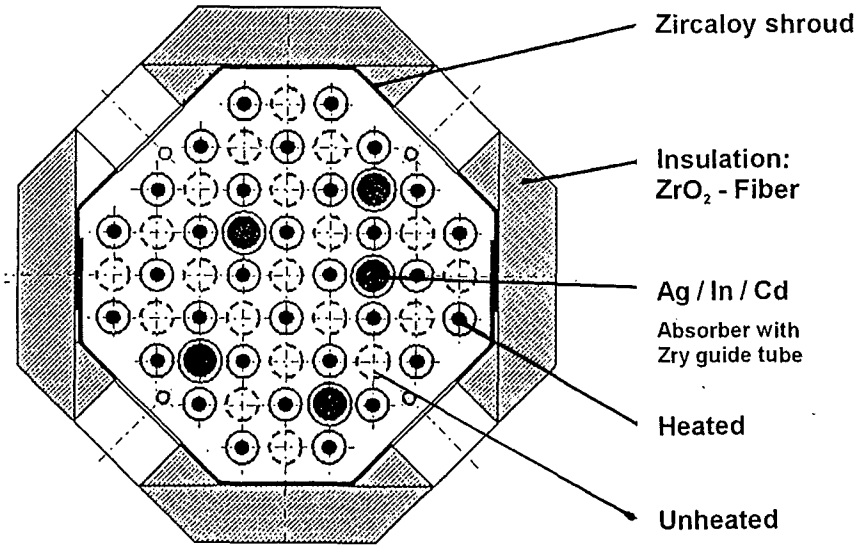

Fig. 5: Rod arrangement and test rod designation of bundle CORA-7

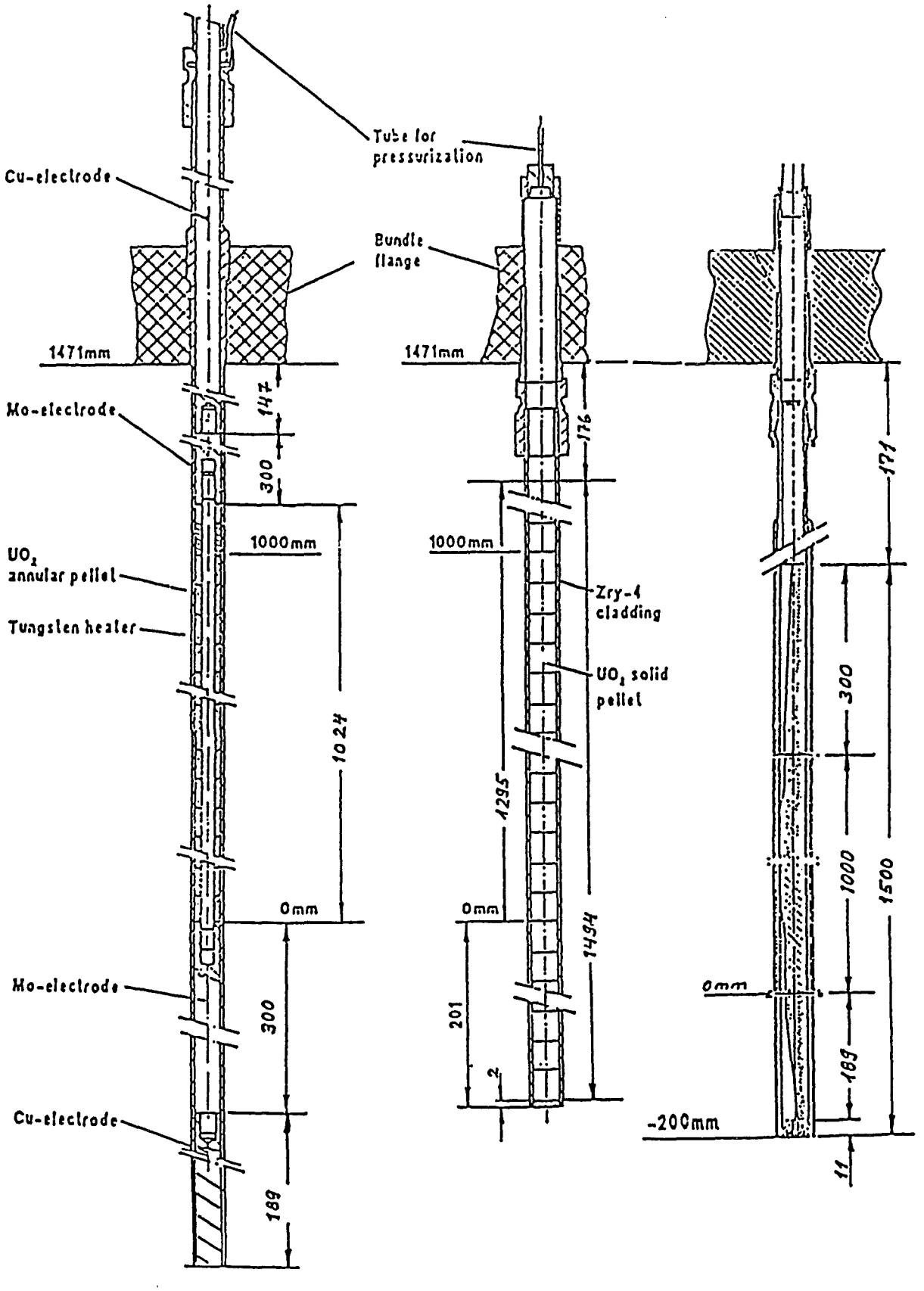

Fig. 6: Rod types used in the CORA experiments

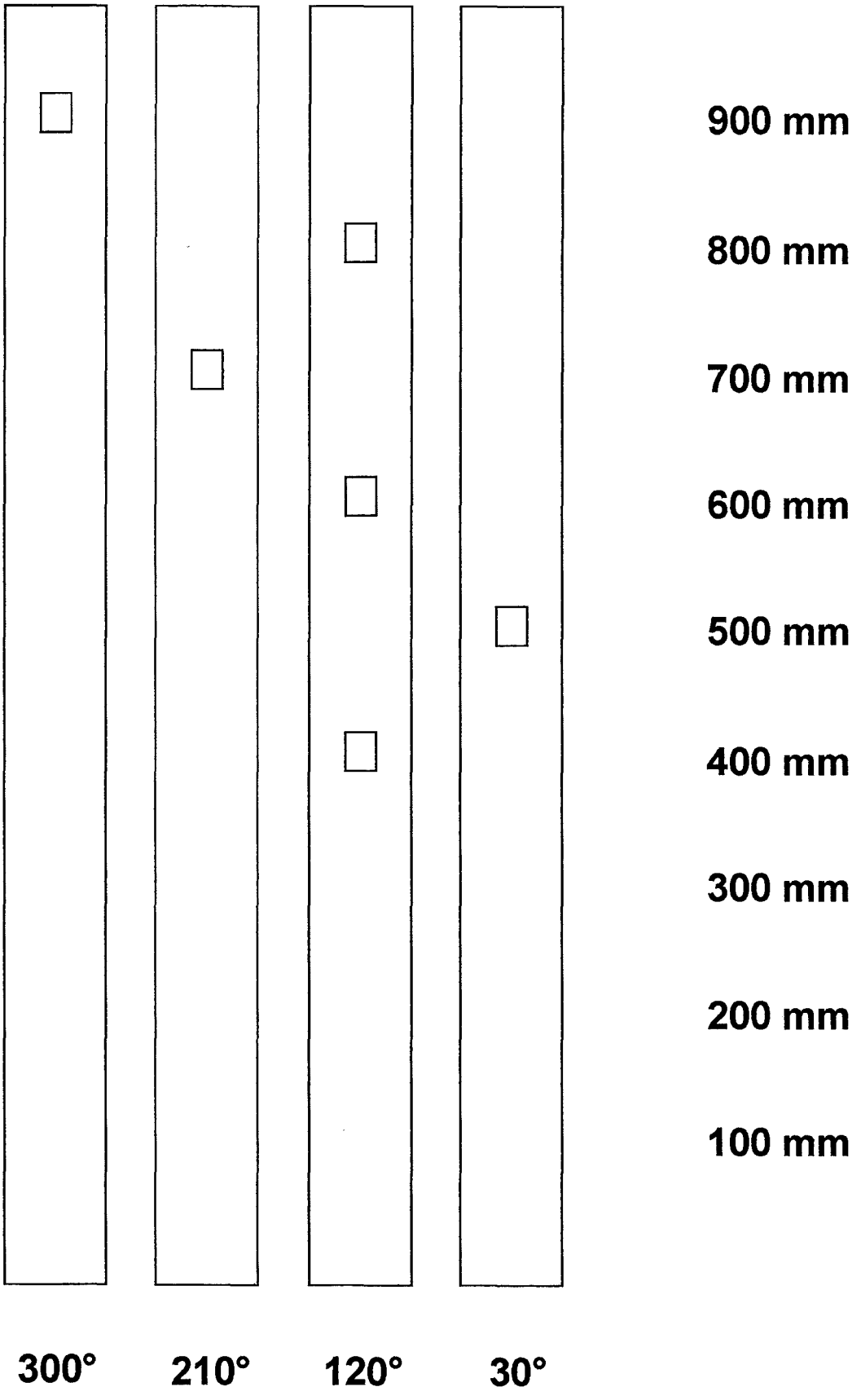

Fig. 7: CORA-7; Positions of windows in the shroud

(a)

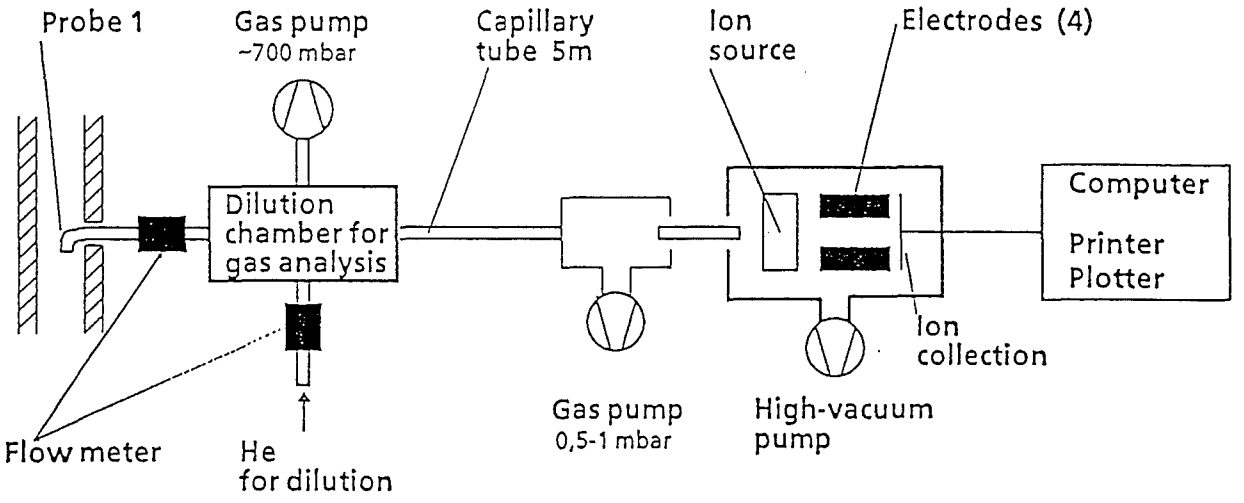

(b)

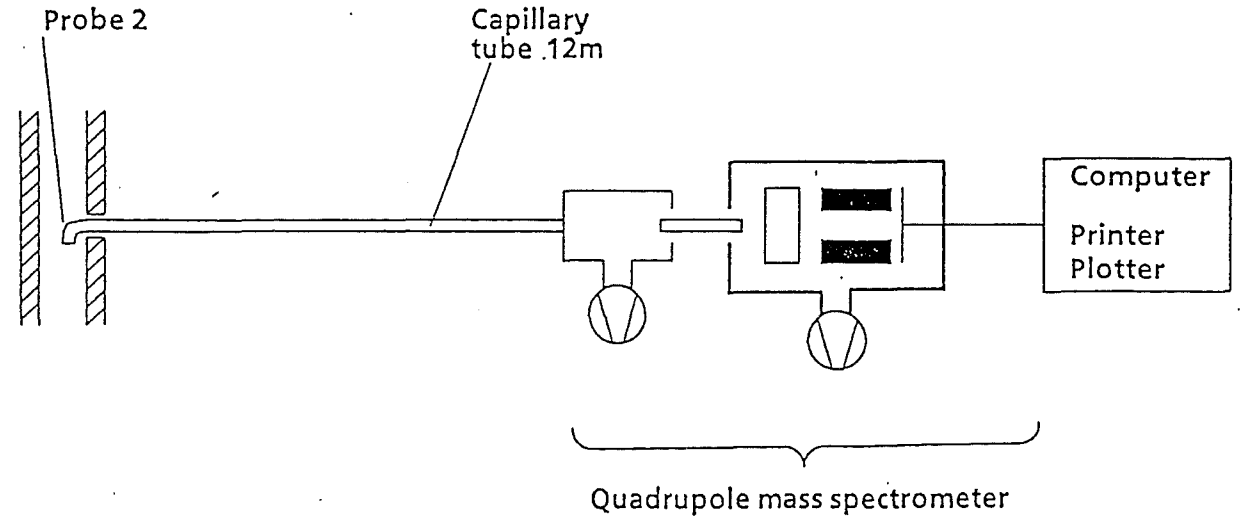

Location (a) : Outlet of test section

Location (b) : Mixing chamber

Fig. 8: Facility of hydrogen measurement

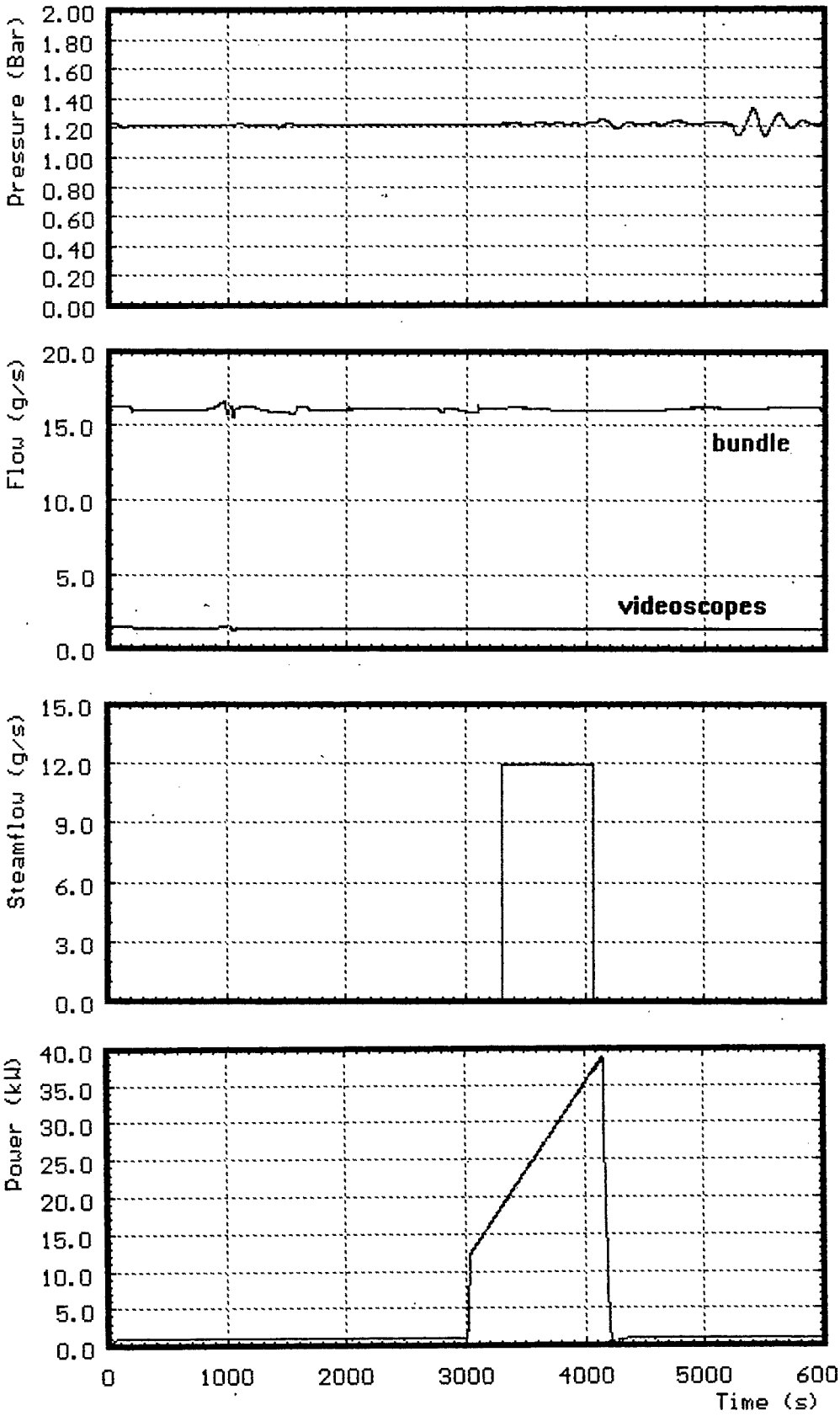

system overpressure

argon flow

water input for steam production

electric power input

Fig.9: CORA-7; System pressure, argon flow, steam input and power

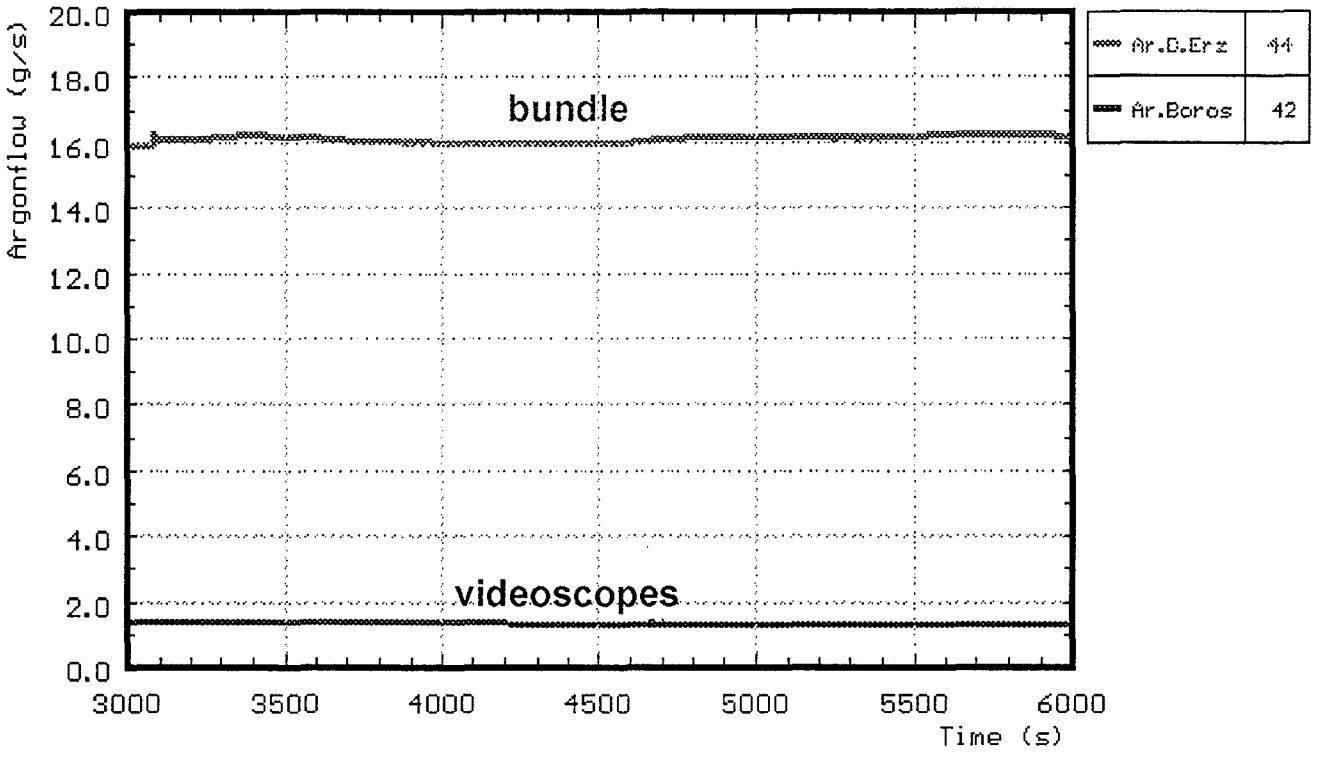

Fig. 10: CORA-7; Argon flow through bundle and videoscopes

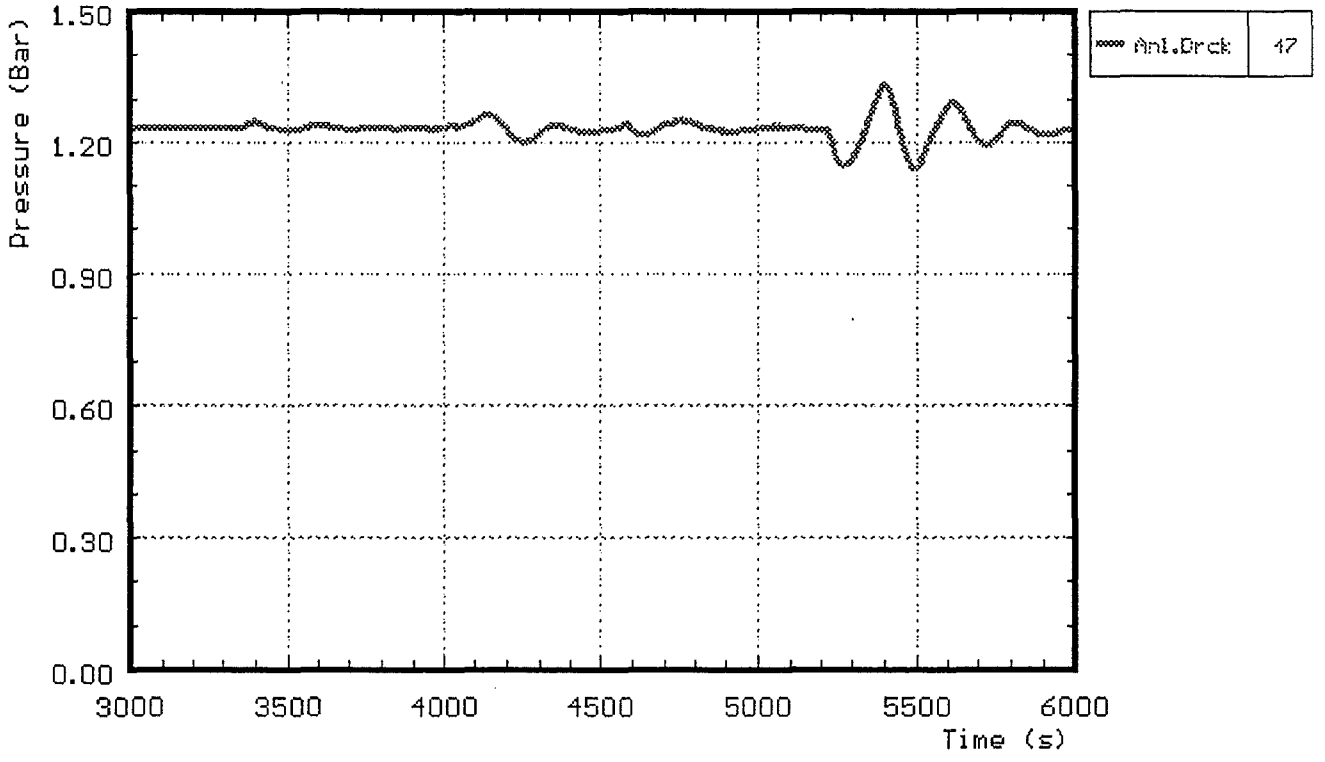

Fig. 11: CORA-7; System pressure (gauge)

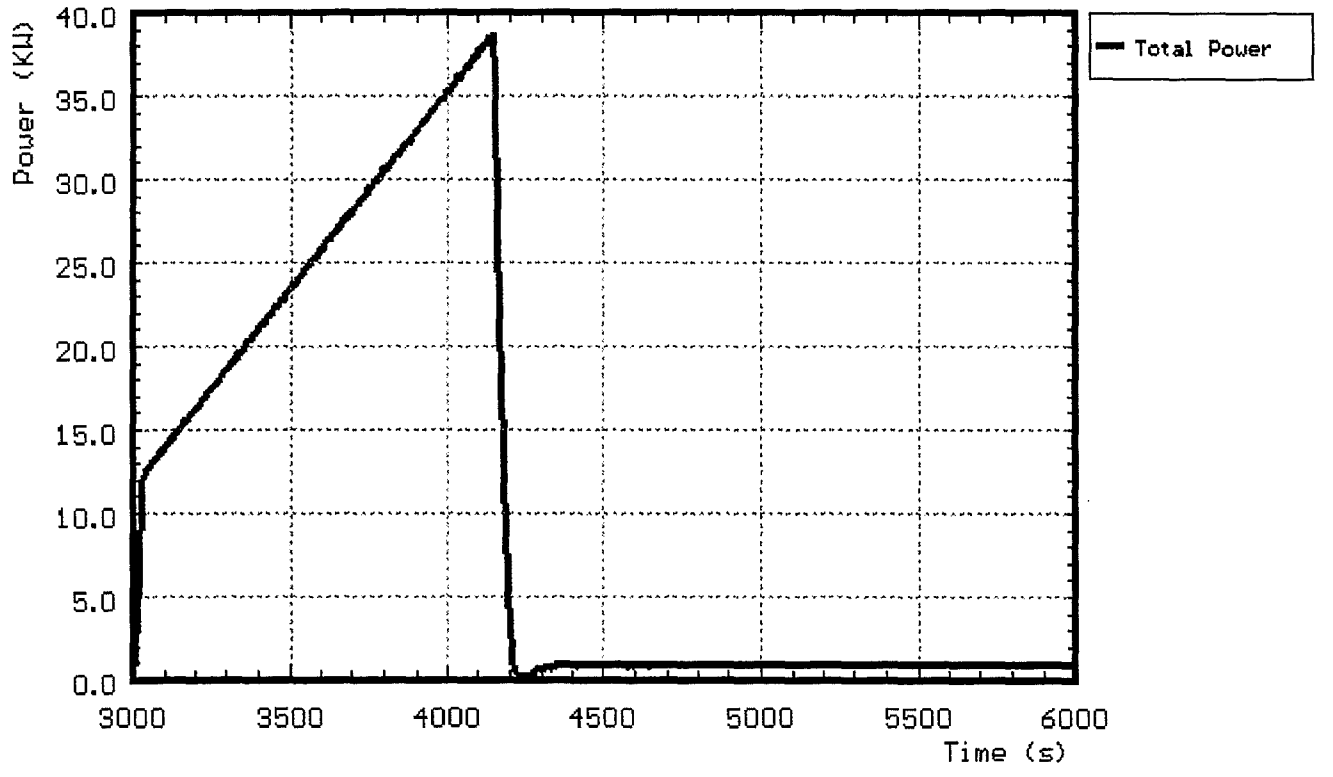

Fig.12: CORA-7; Total electric power input

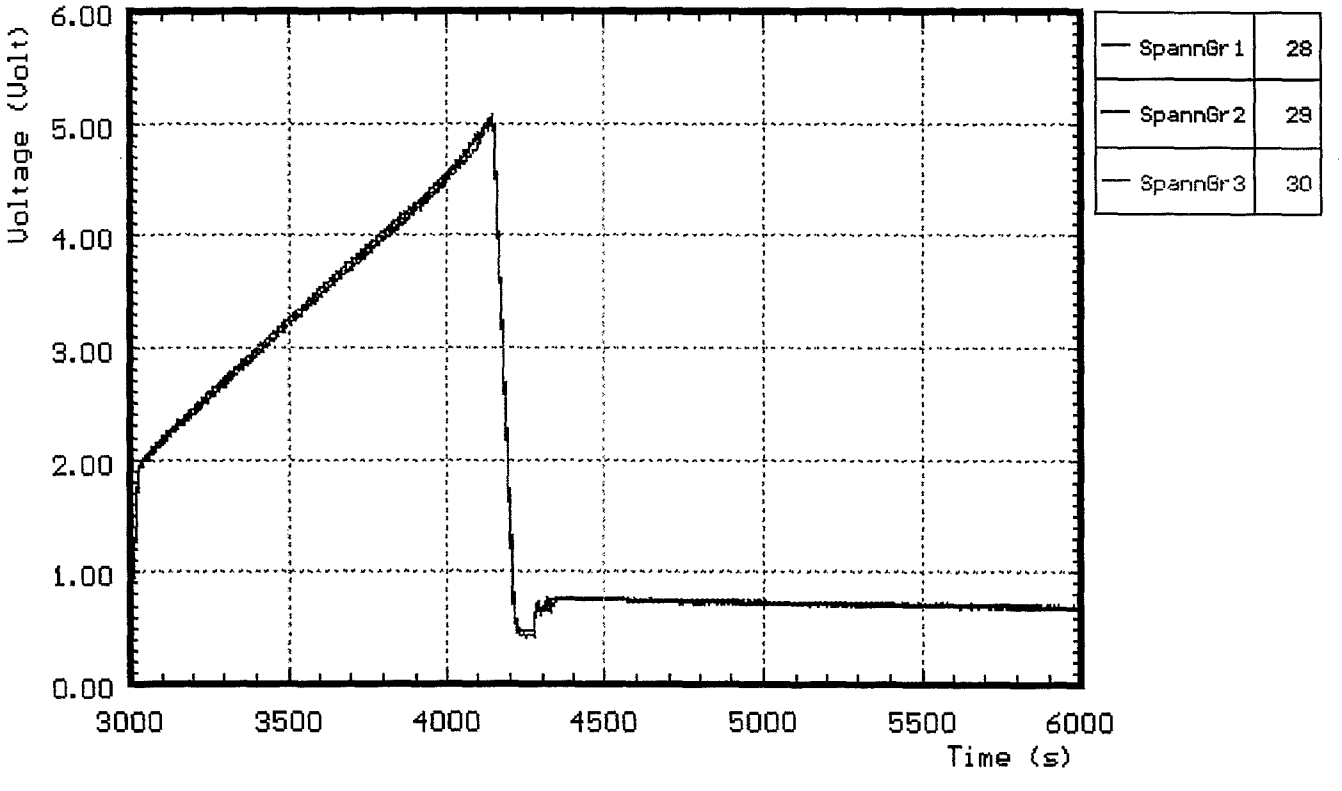

Fig. 13: CORA-7; Voltage input for the 3 rod groups

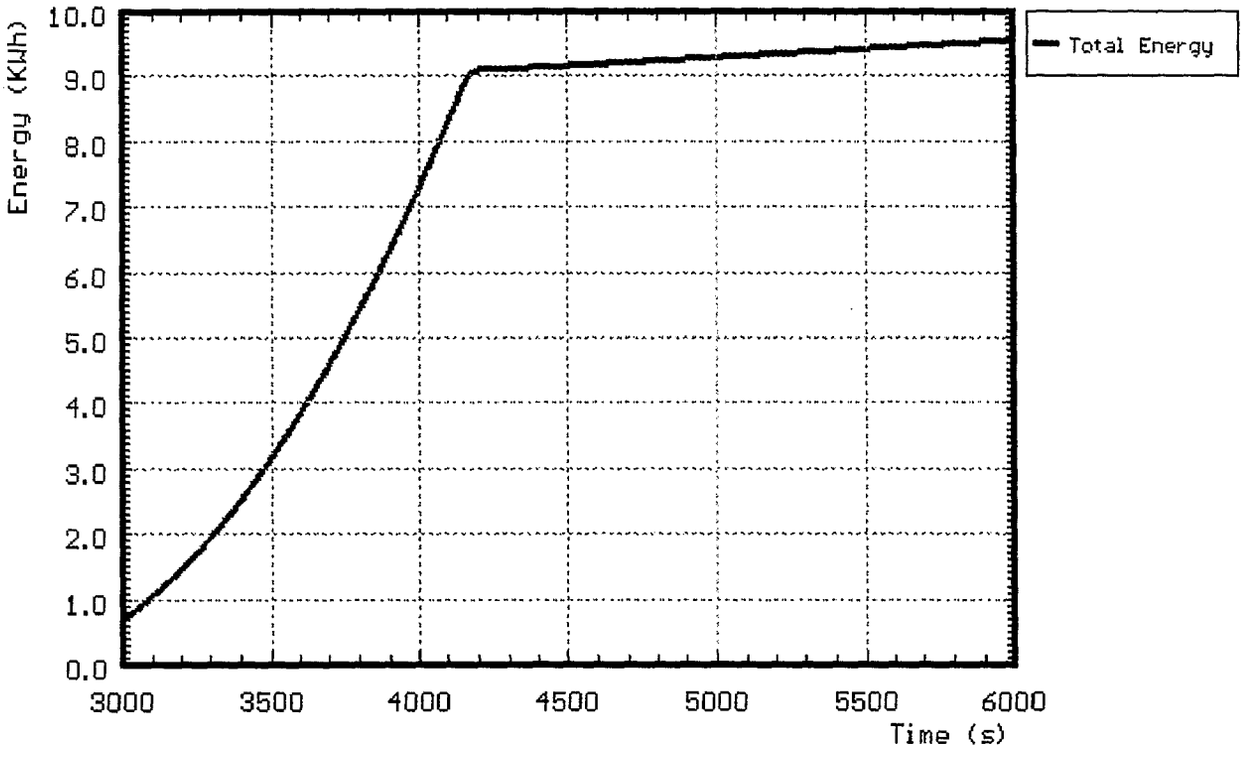

Fig. 14: CORA-7; Total electric energy input

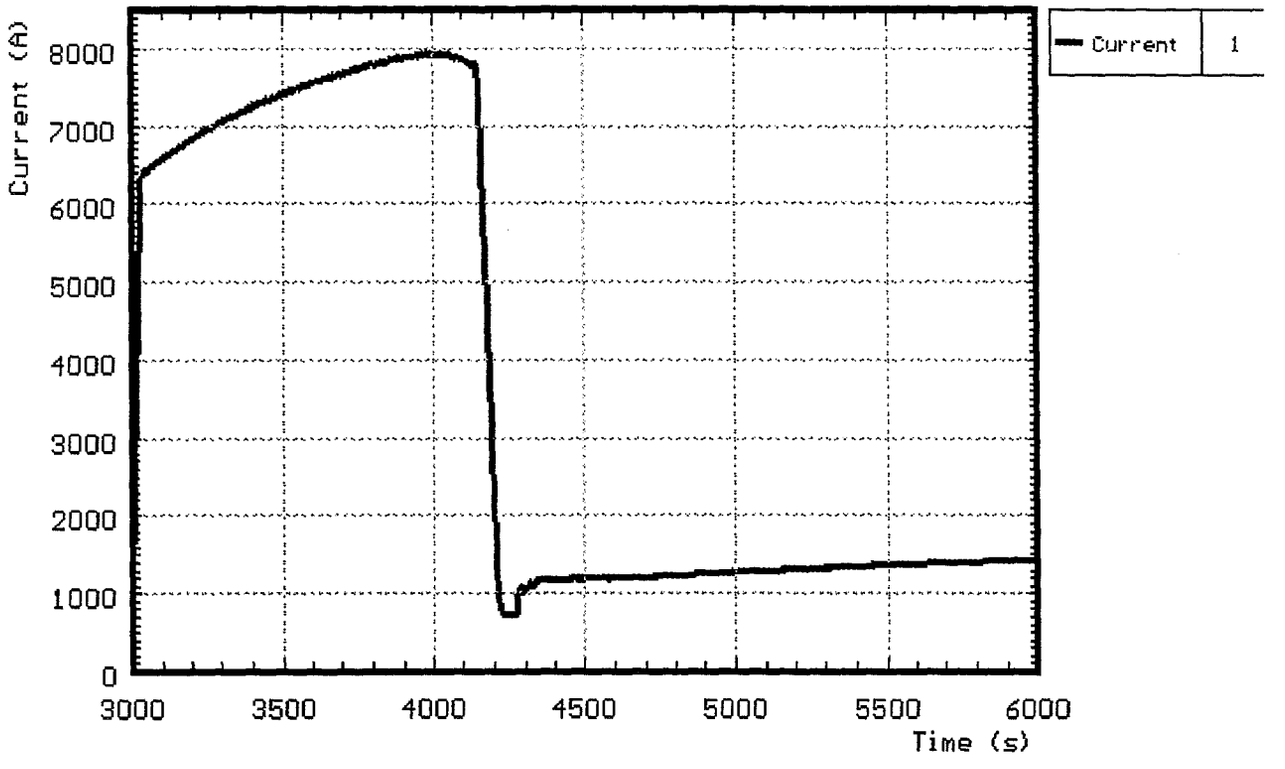

Fig. 15: CORA-7; Total current

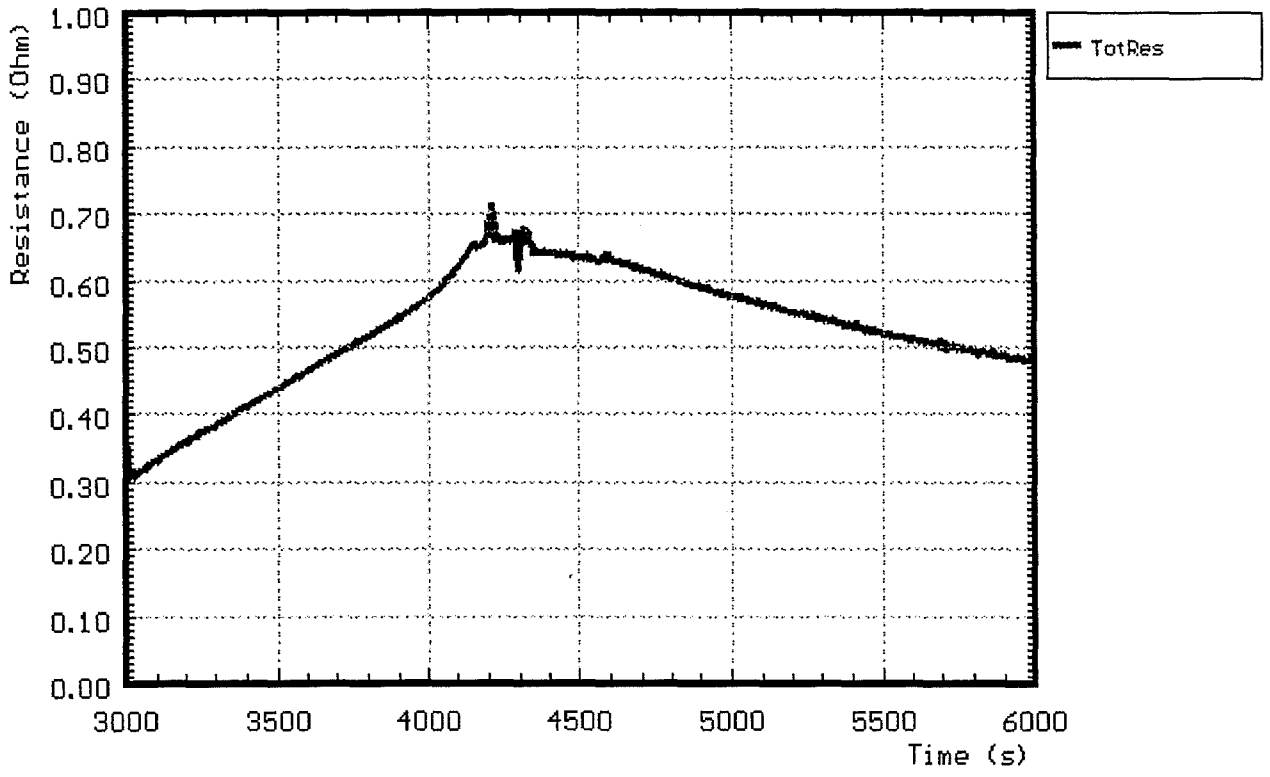

Fig. 16: CORA-7; Resistance of bundle (Voltage group 1/total current)

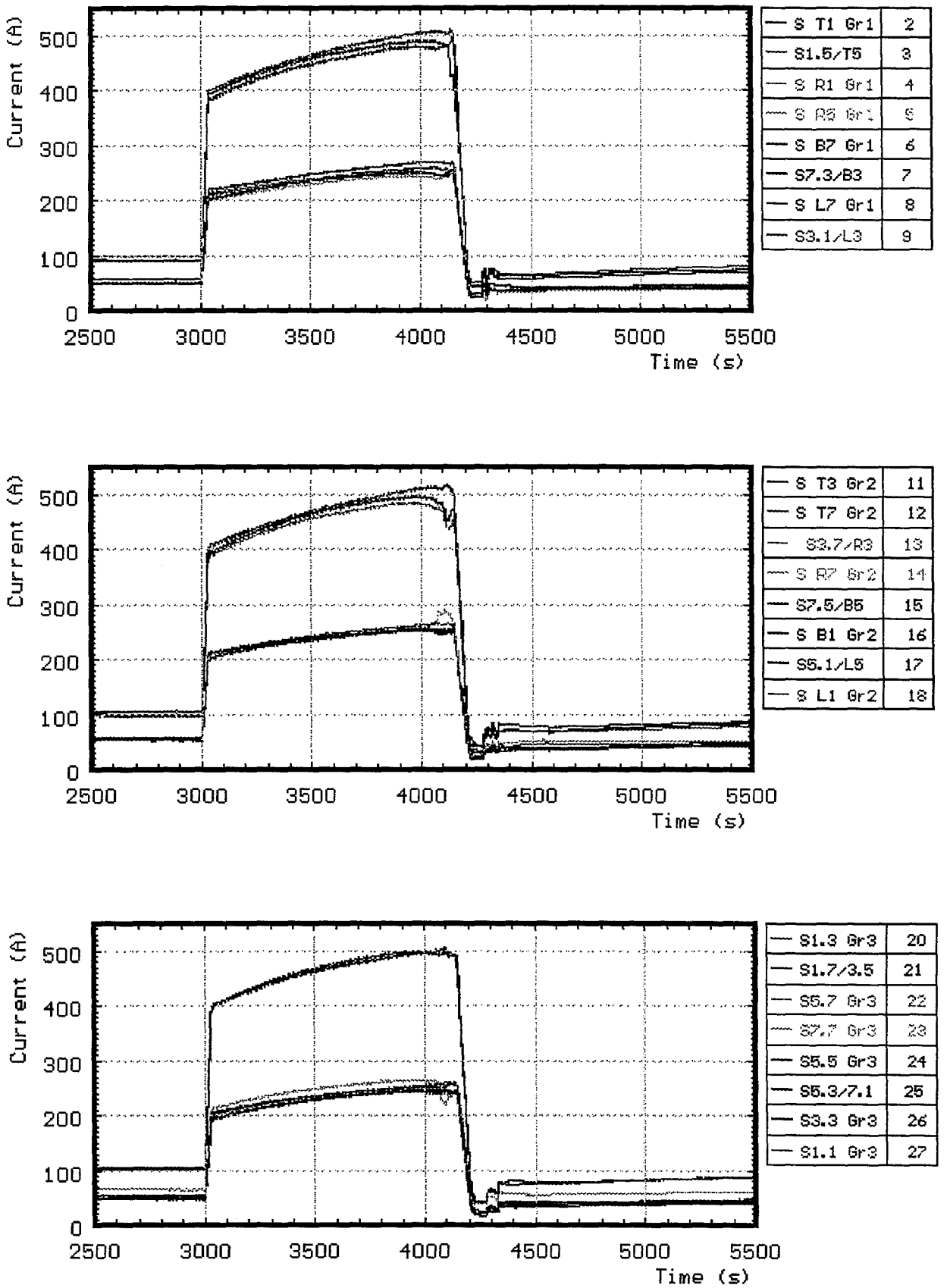

Fig. 17: CORA-7; Variations of currents within the rod groups

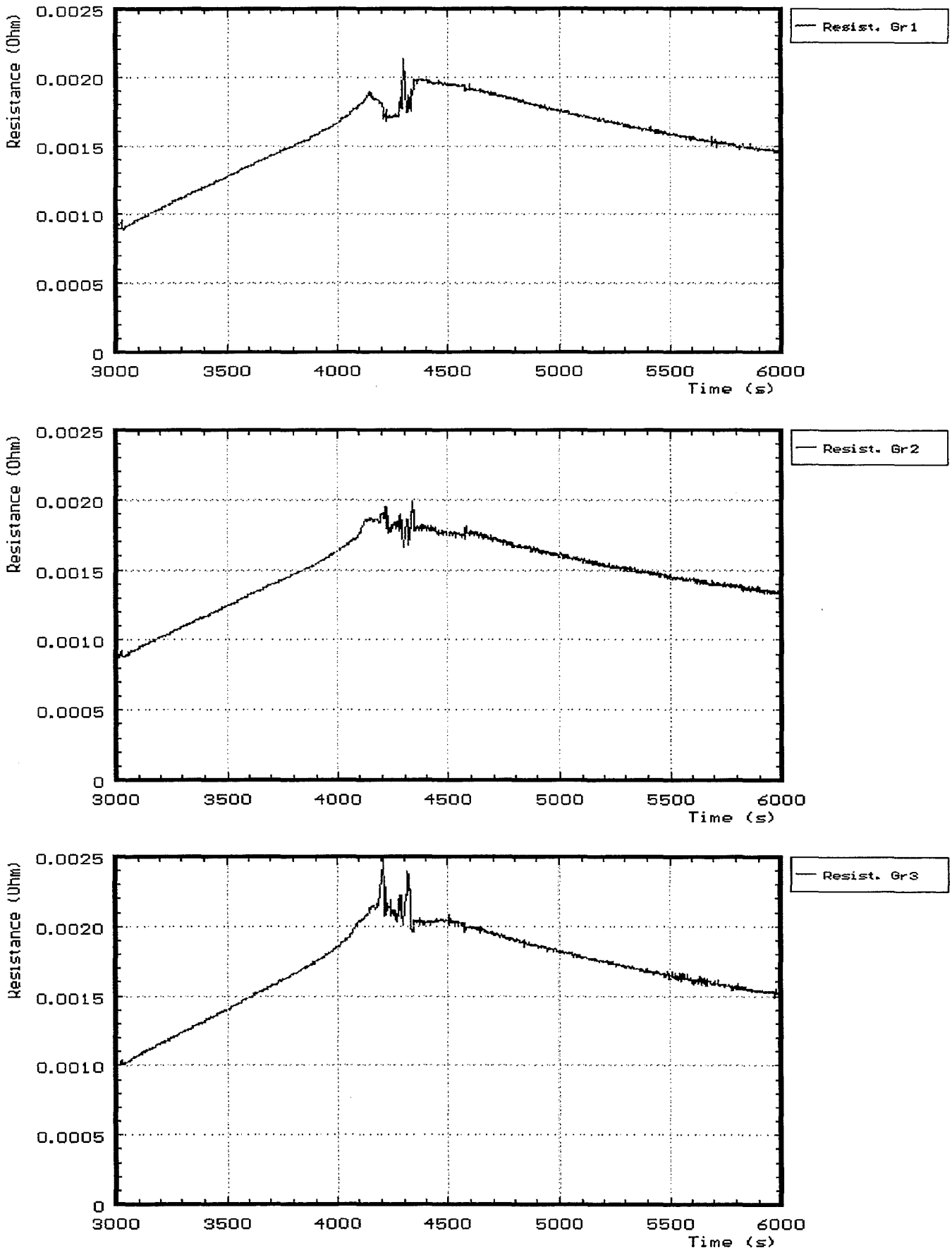

Fig. 18: CORA-7; Resistance of the rod groups

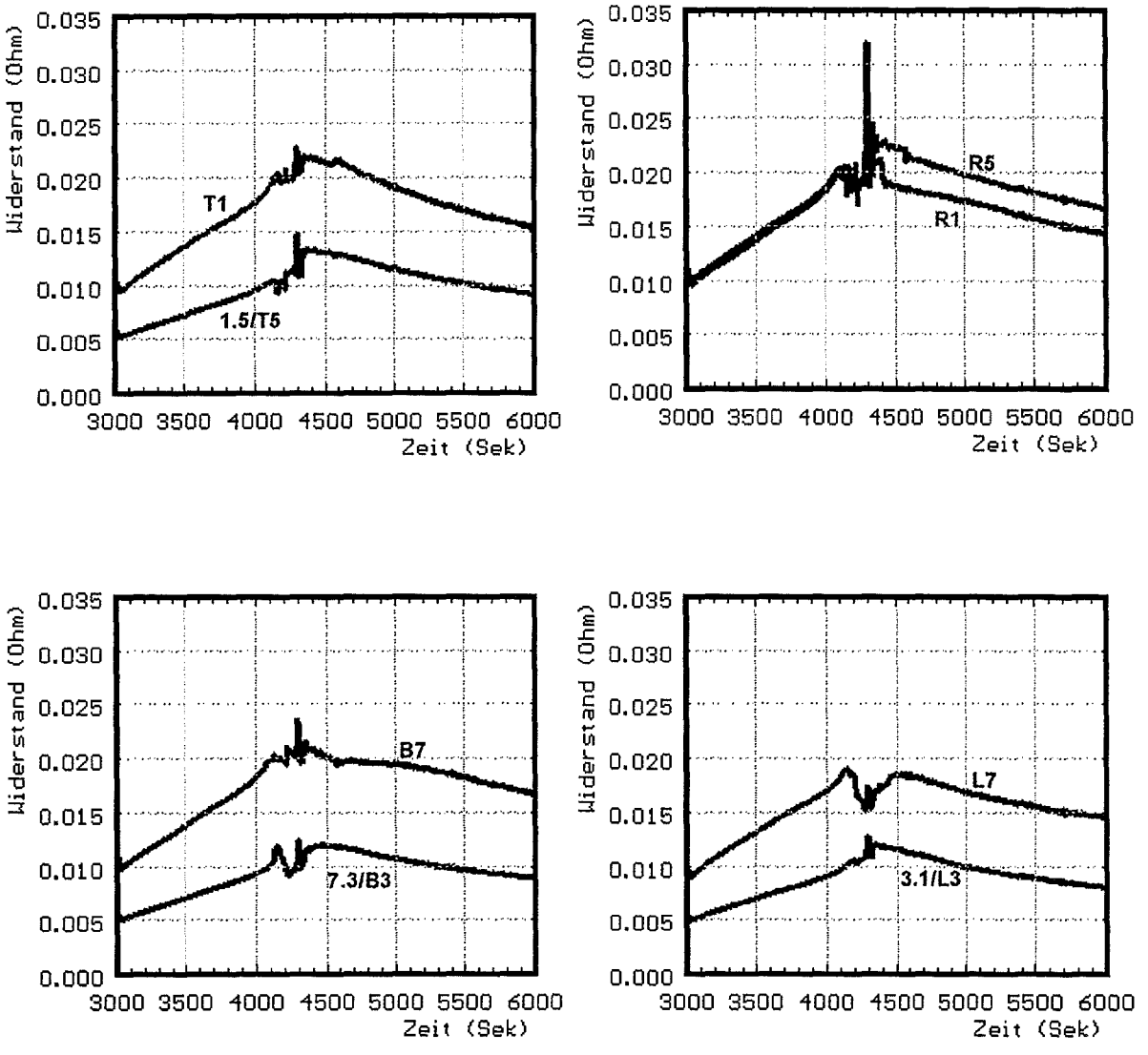

Fig. 19: CORA-7; Resistance of single rods group 1

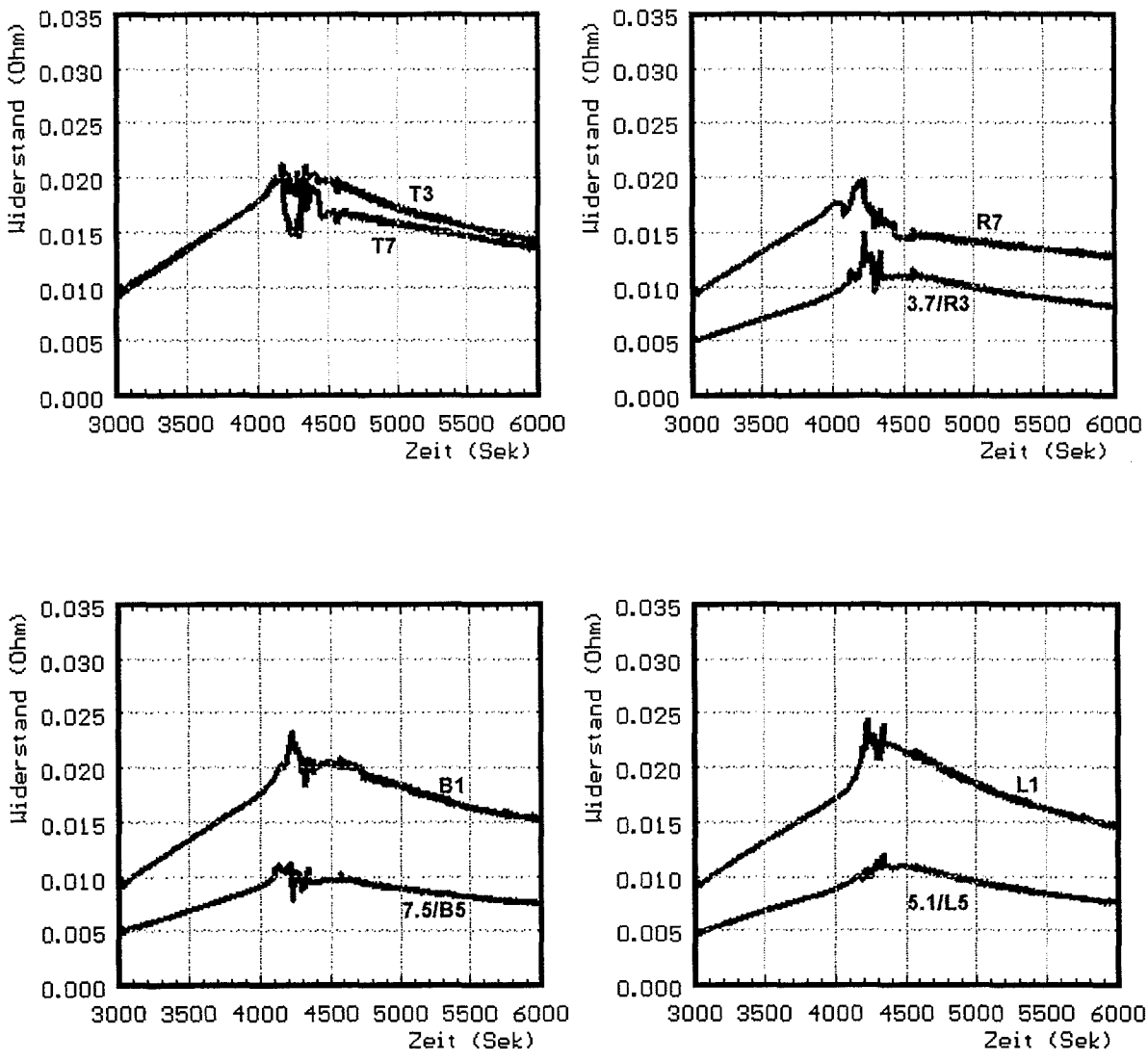

Fig. 20: CORA-7; Resistance of single rods group 2

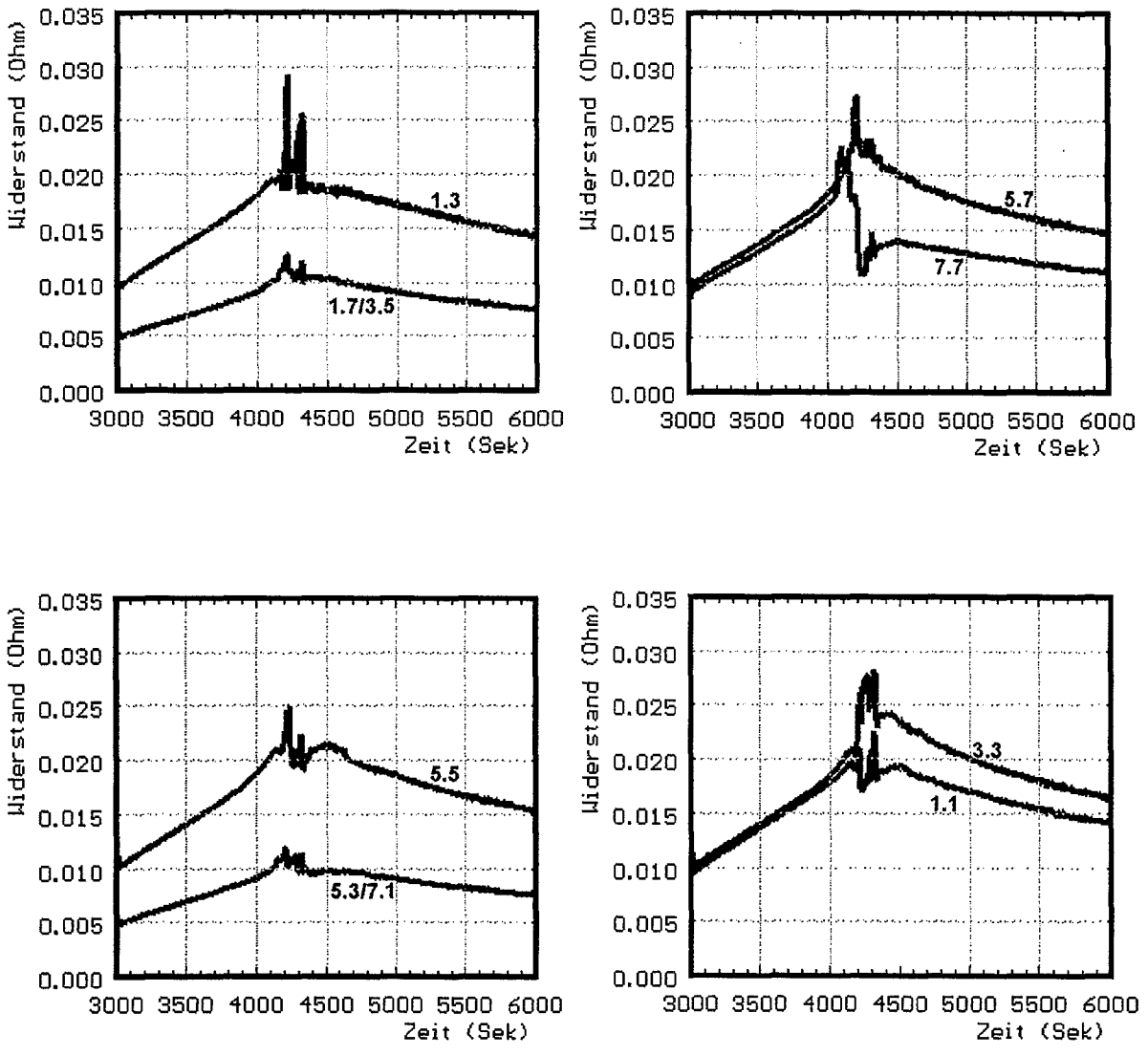

Fig. 21: CORA-7; Resistance of single rods group 3

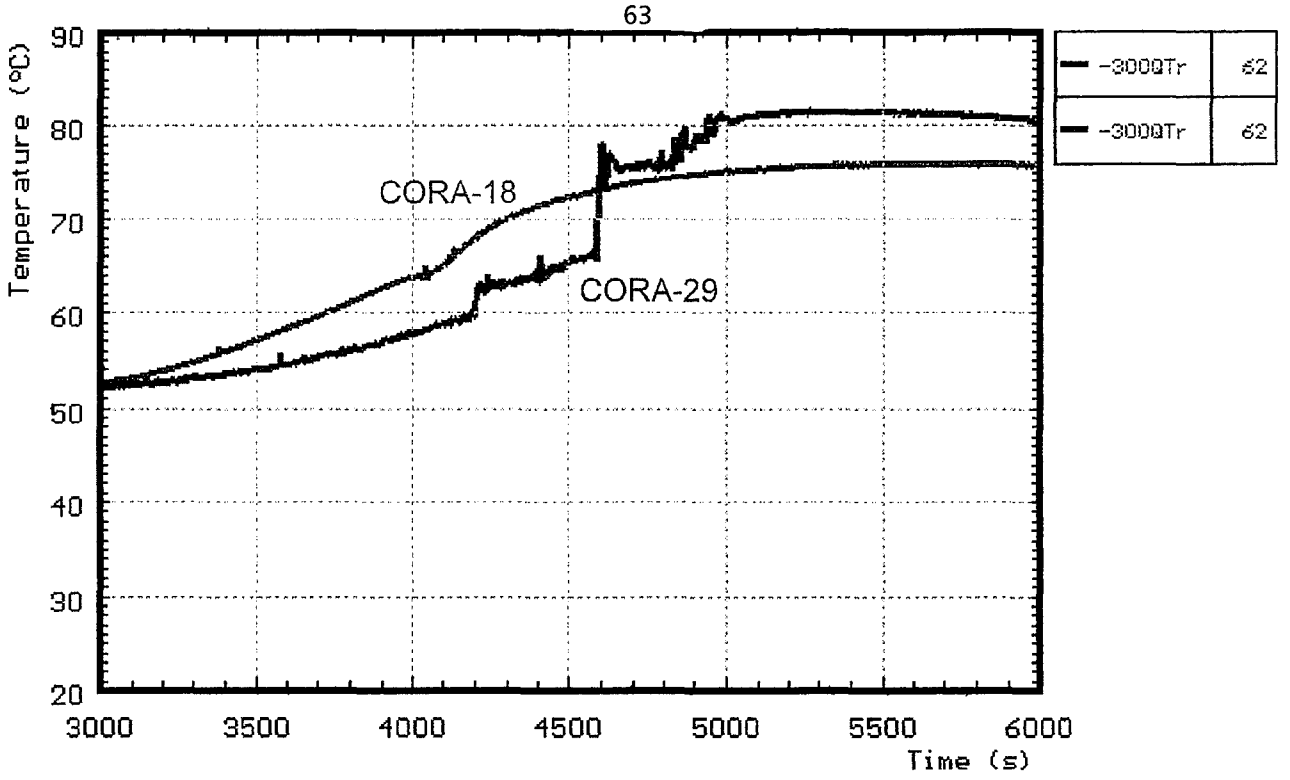

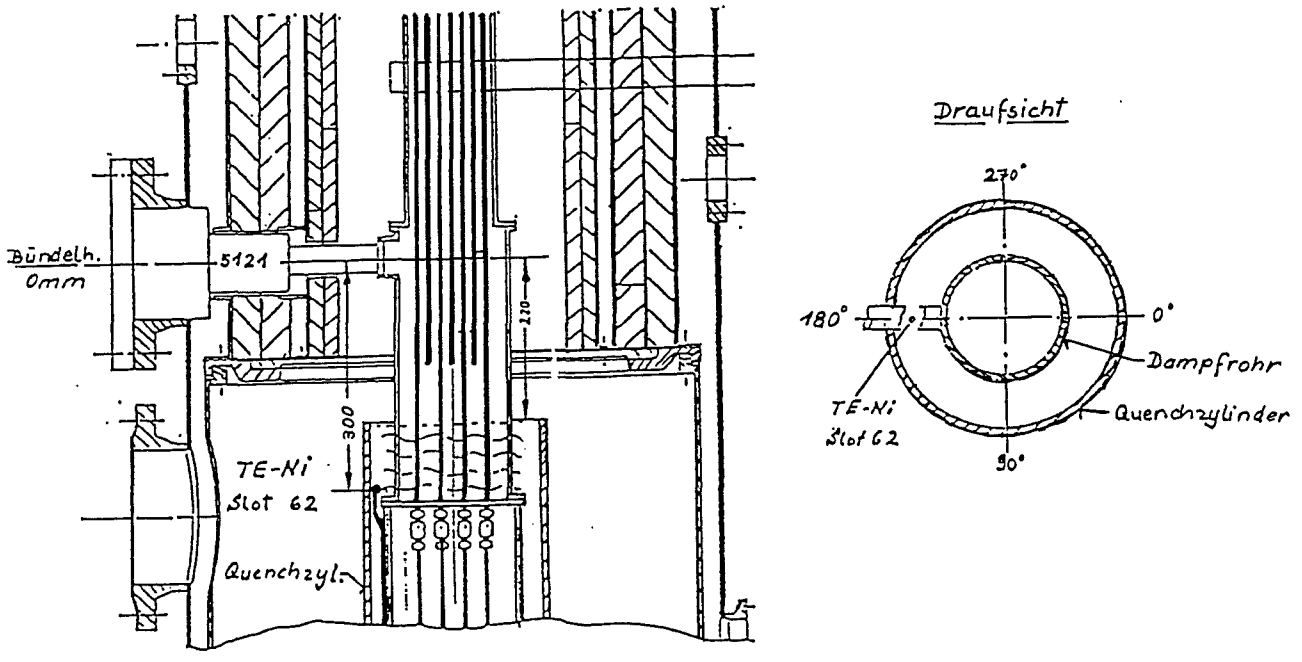

Fig. 22: Water temperature in the quench cylinder for tests CORA-18 (large BWR) and CORA-29 (normal PWR). (no measurement of water temperature in the quench cylinder for test CORA-7)

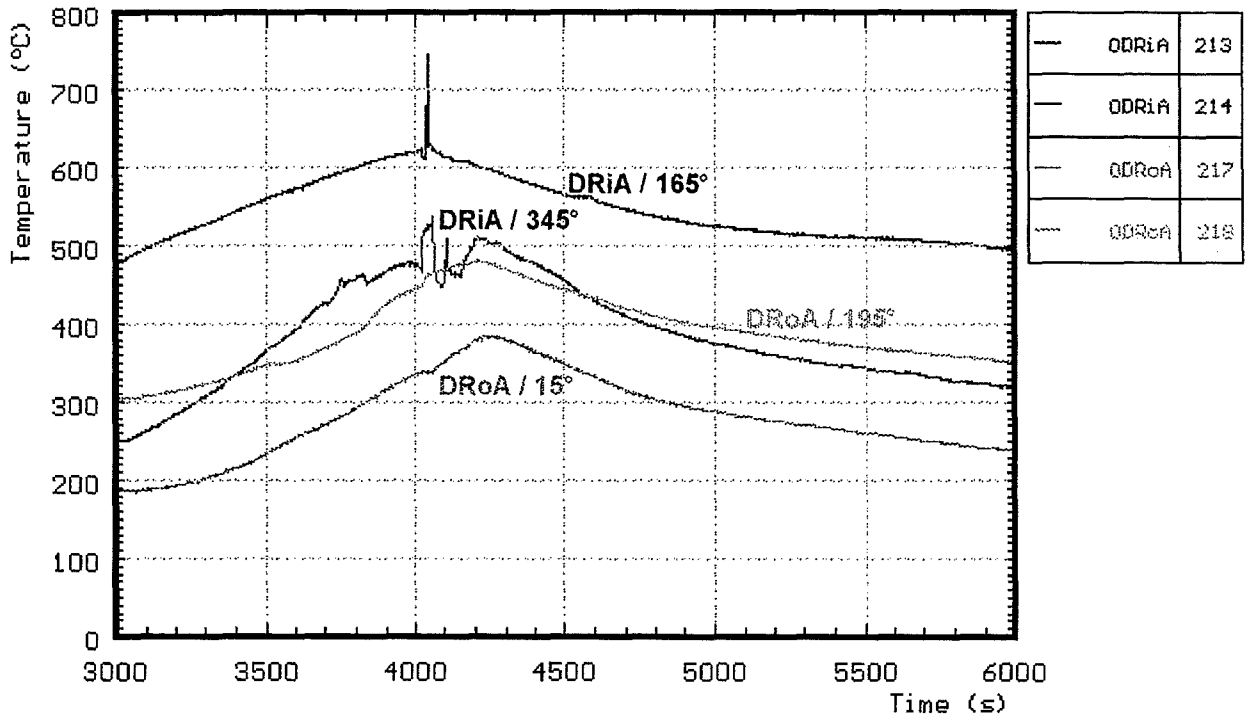

DRiA : steam tube, inner side
DRoA : steam tube, outer side

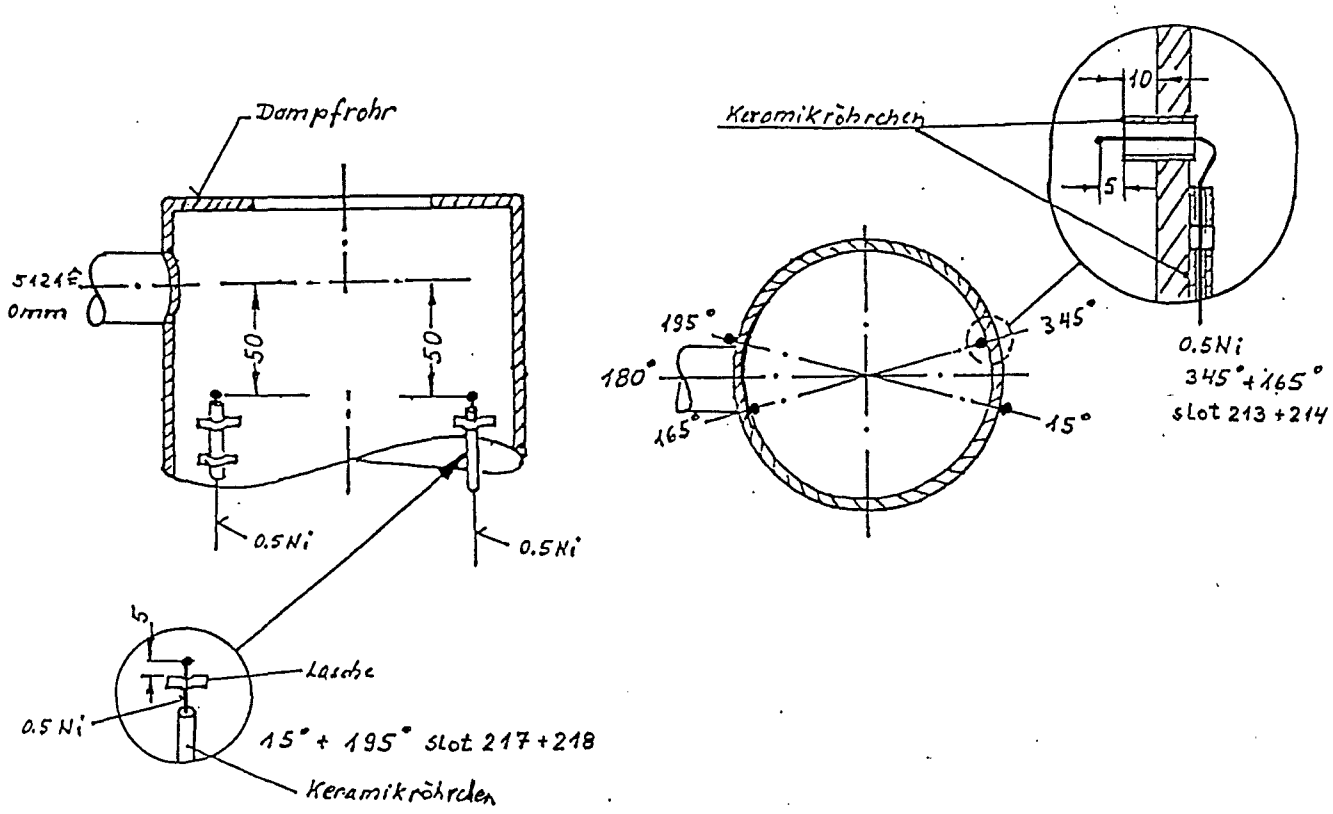

Fig. 23: CORA-7; Temperature in and on steam tube at 0mm elevation

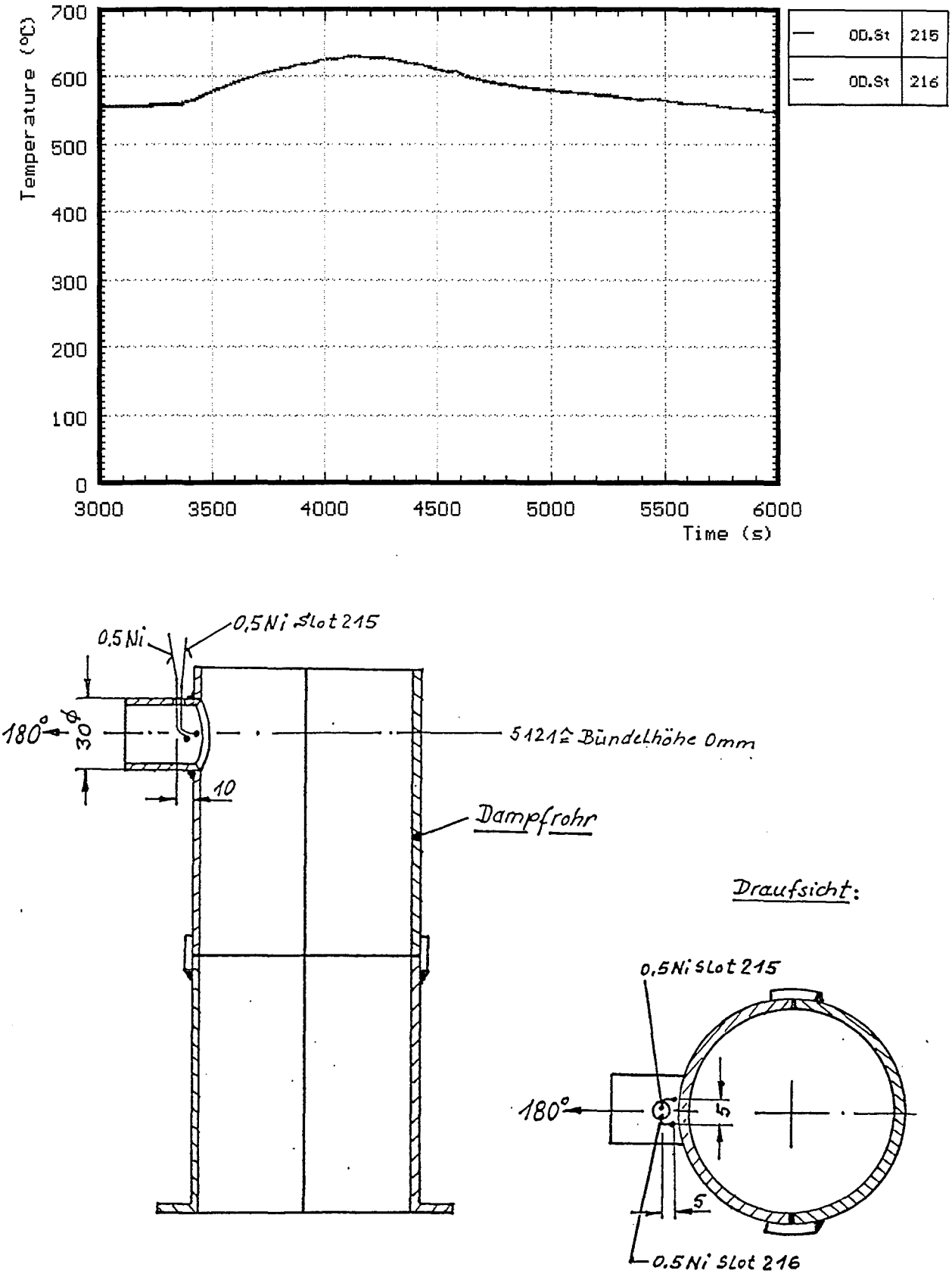

Fig. 24: CORA-7; Temperatures at steam inlet

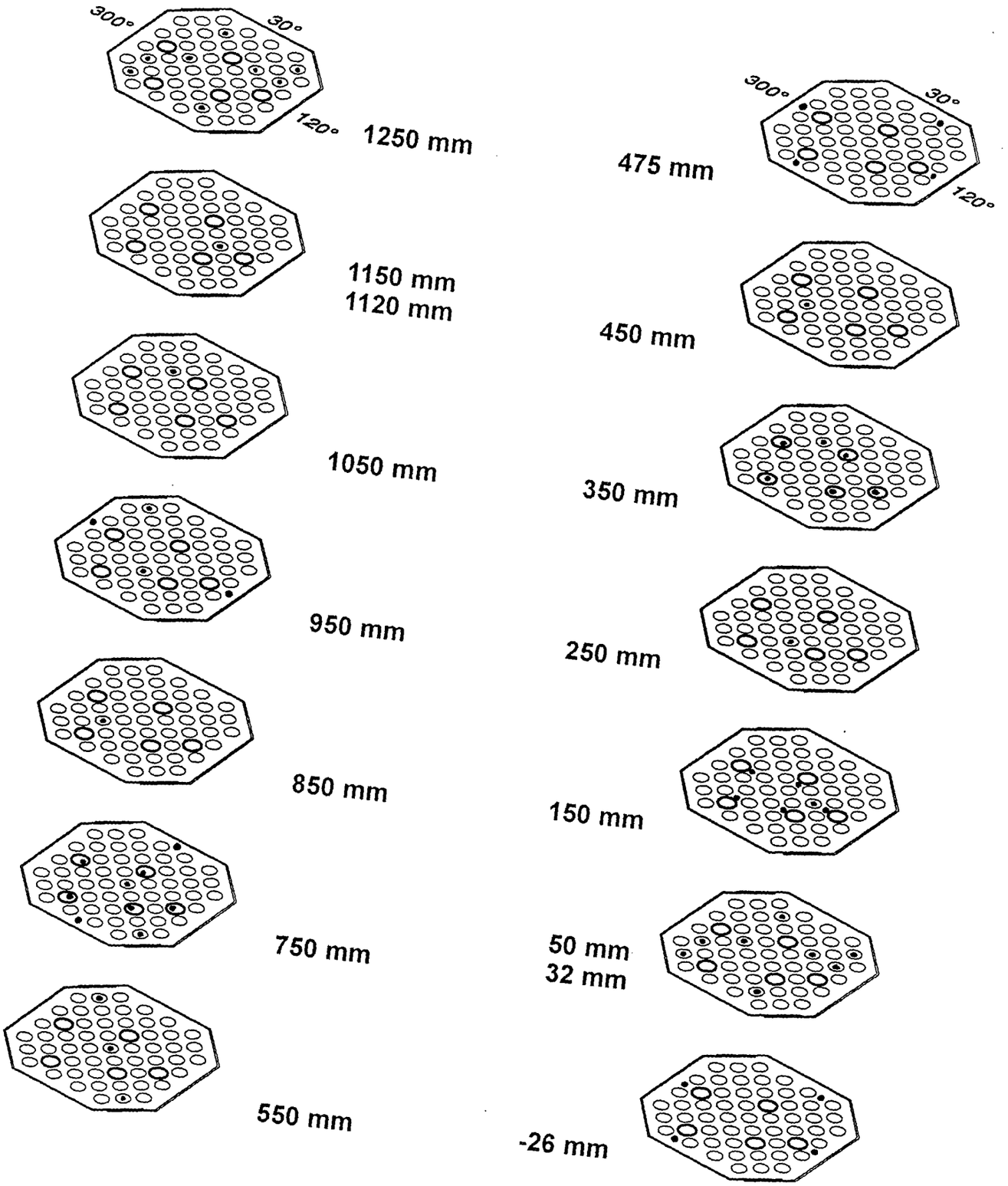

Fig.25: Thermocouple locations within the bundle (CORA-7)

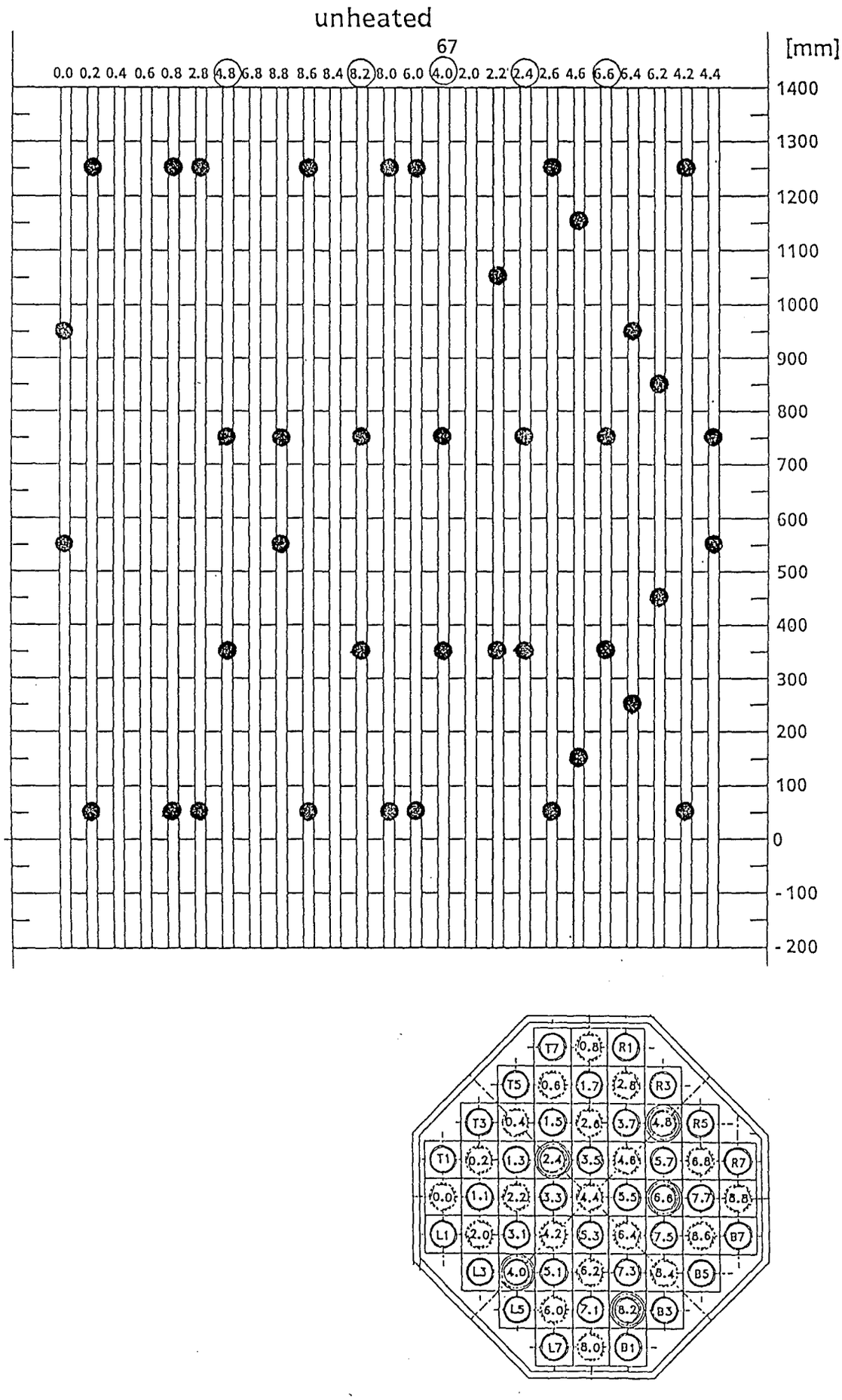

Fig. 25a: CORA-7; Positions of thermocouples in unheated rods

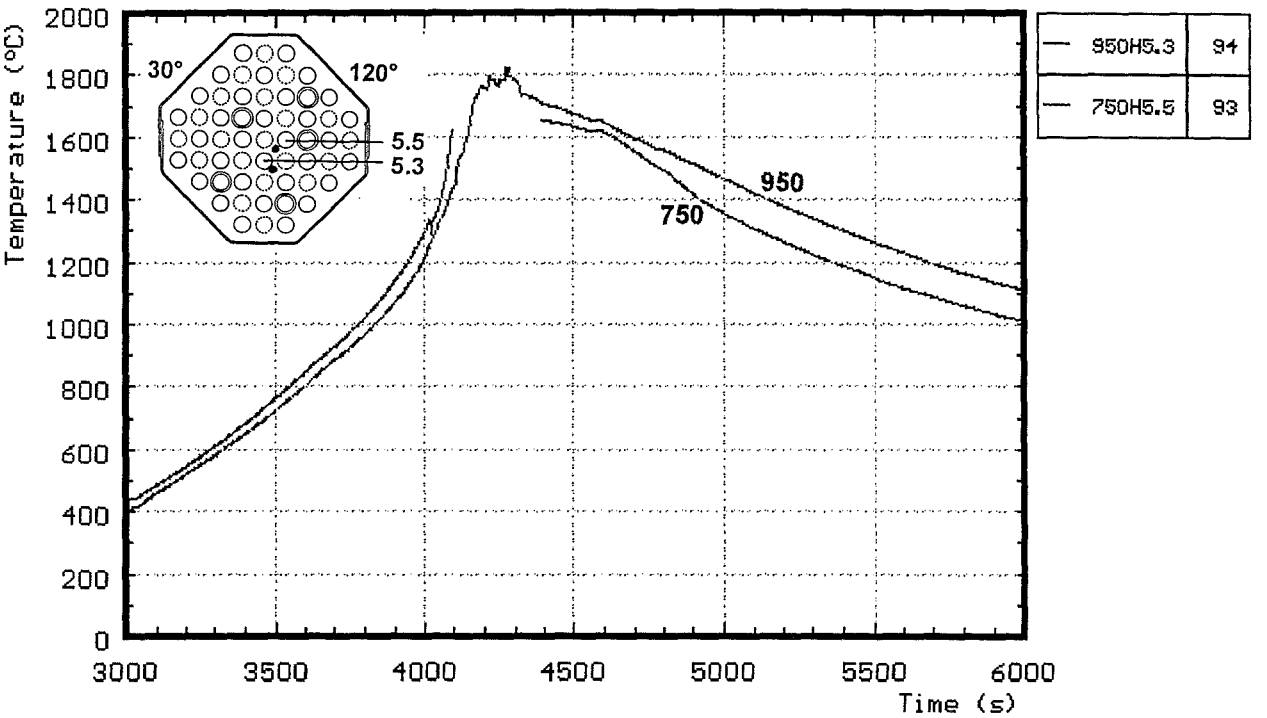

Fig. 26: CORA-7; Temperatures of heated rods

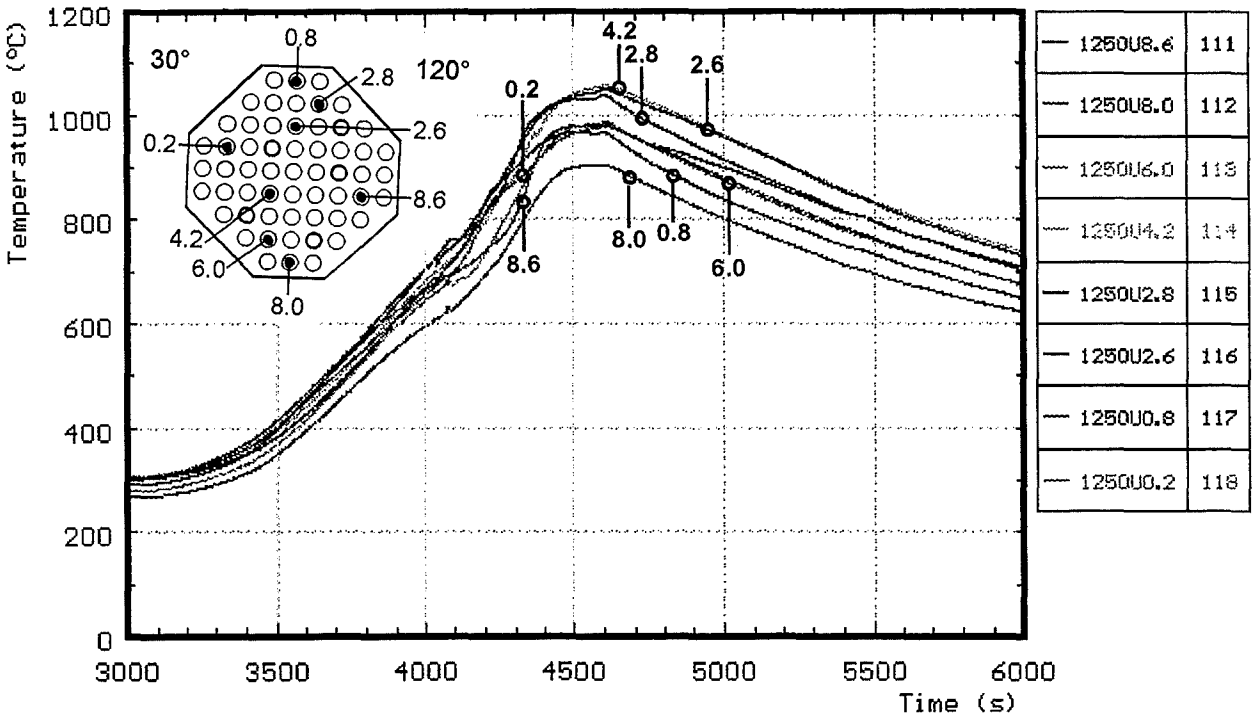

Fig. 27: CORA-7; Temperatures of unheated rods, 1250 mm elevation

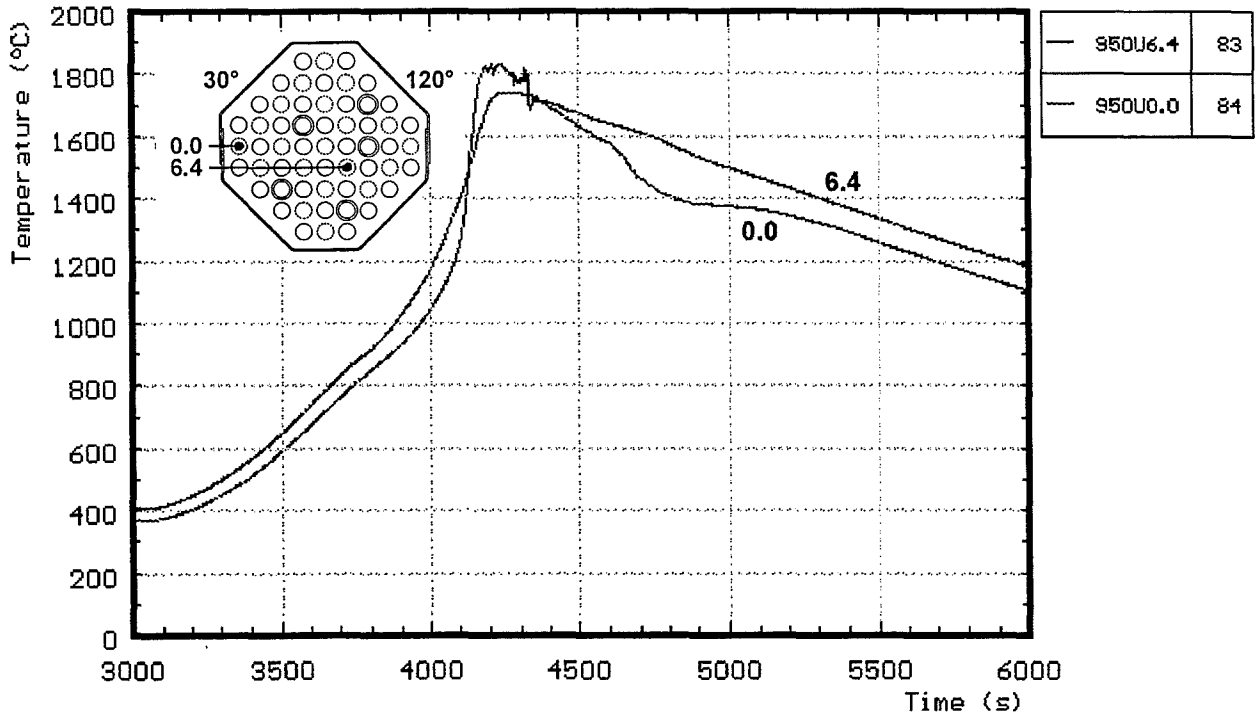

Fig. 28: CORA-7; Temperatures of unheated rods, 950 mm elevation

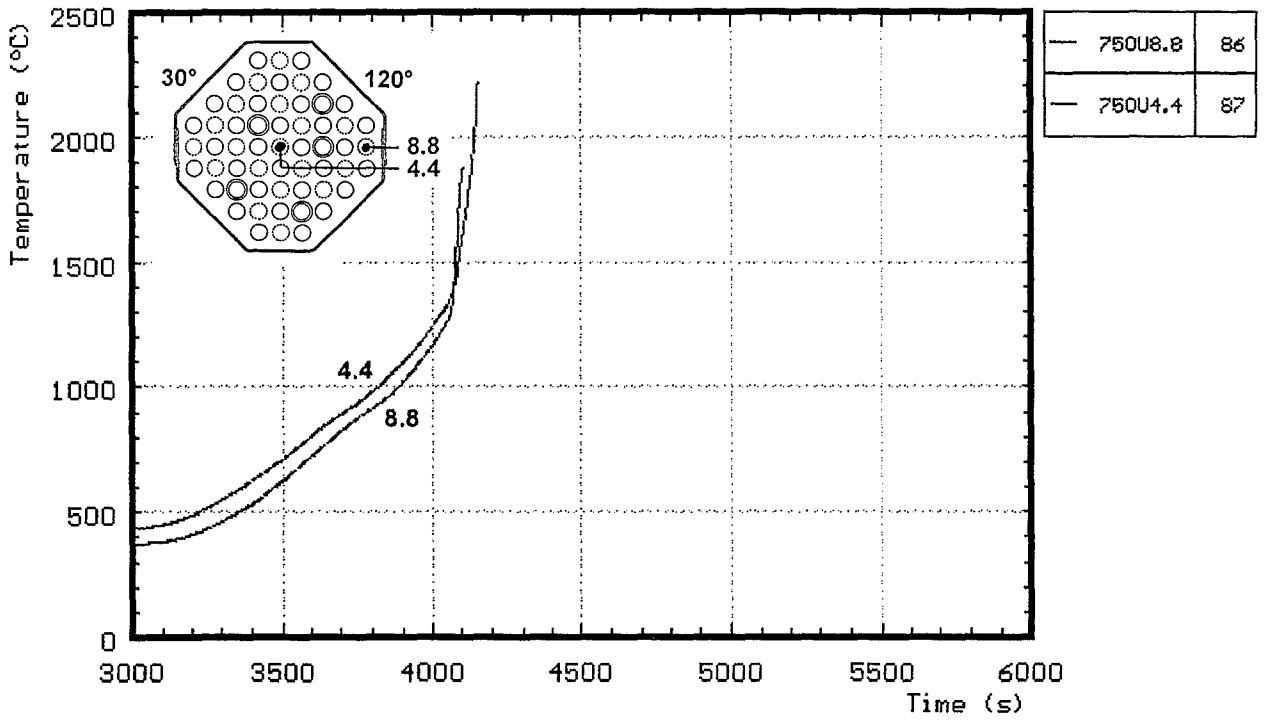

Fig. 29: CORA-7; Temperatures of unheated rods, 750 mm elevation

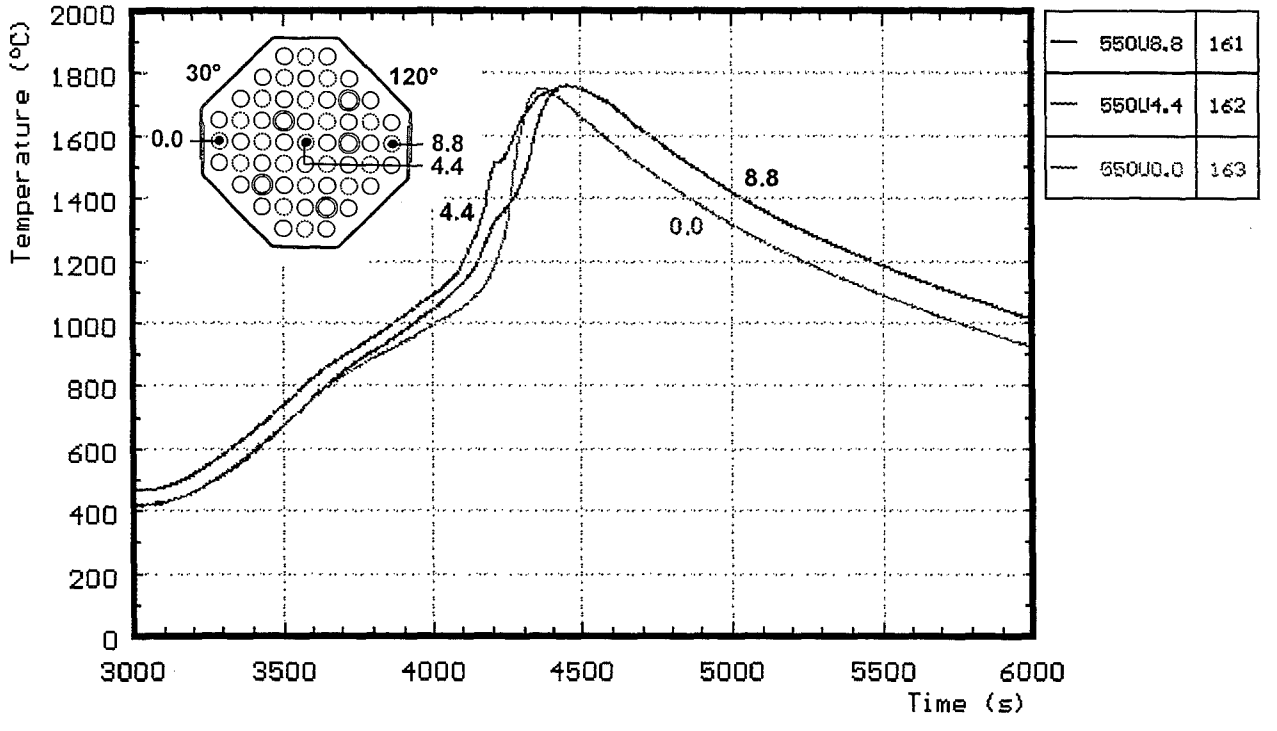

Fig. 30: CORA-7; Temperatures of unheated rods, 550 mm elevation

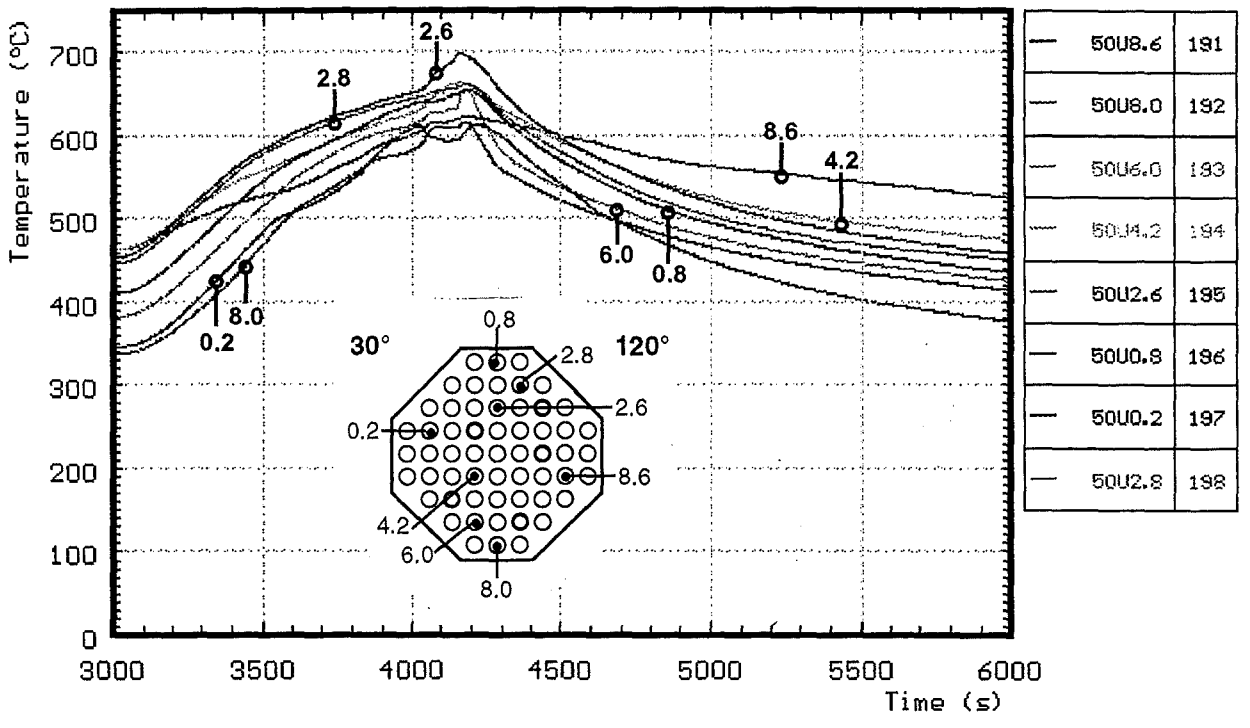

Fig. 31: CORA-7; Temperatures of unheated rods, 50 mm elevation

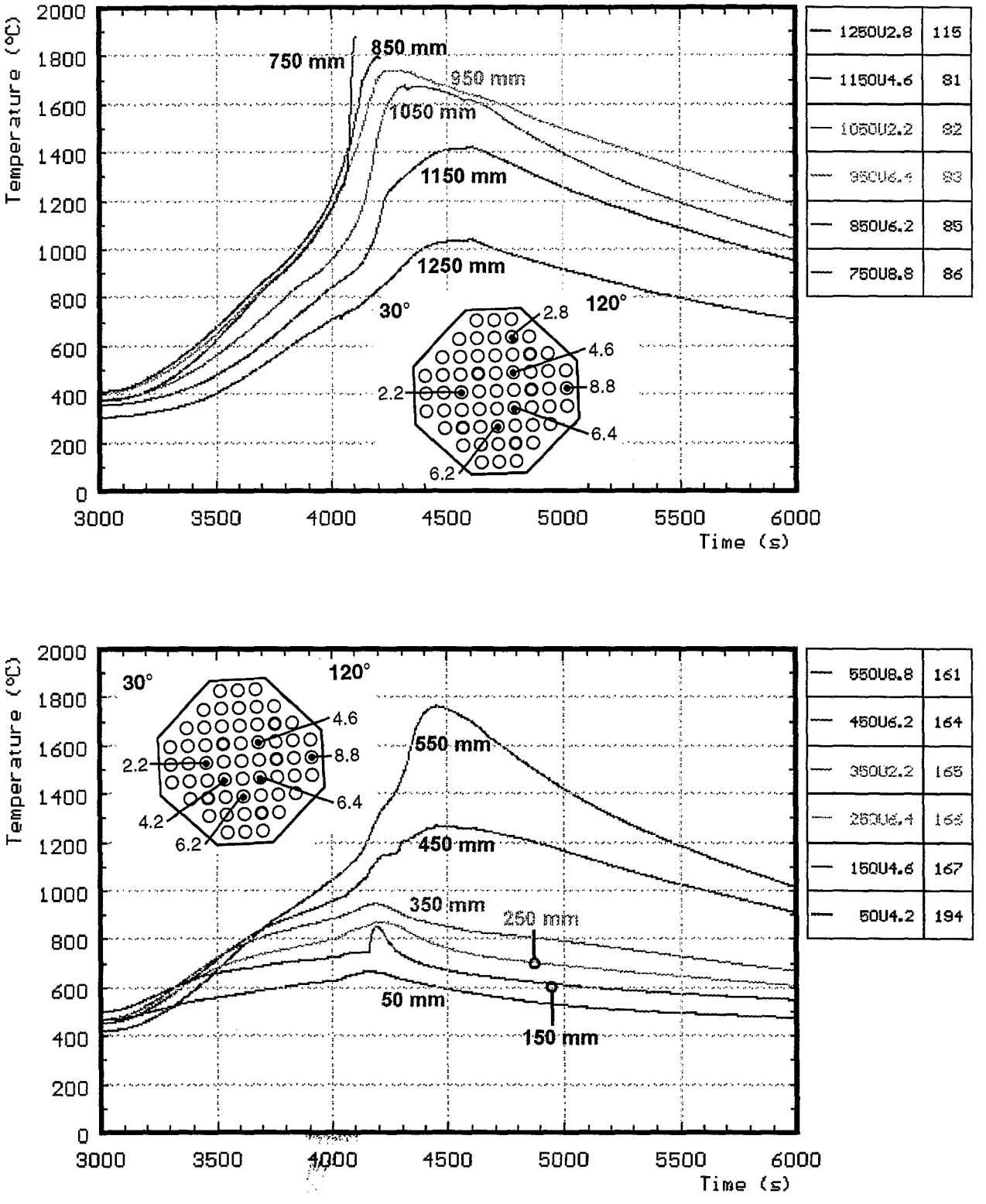

Fig. 32: CORA-7; Temperatures of unheated rods, (TCs in central position)

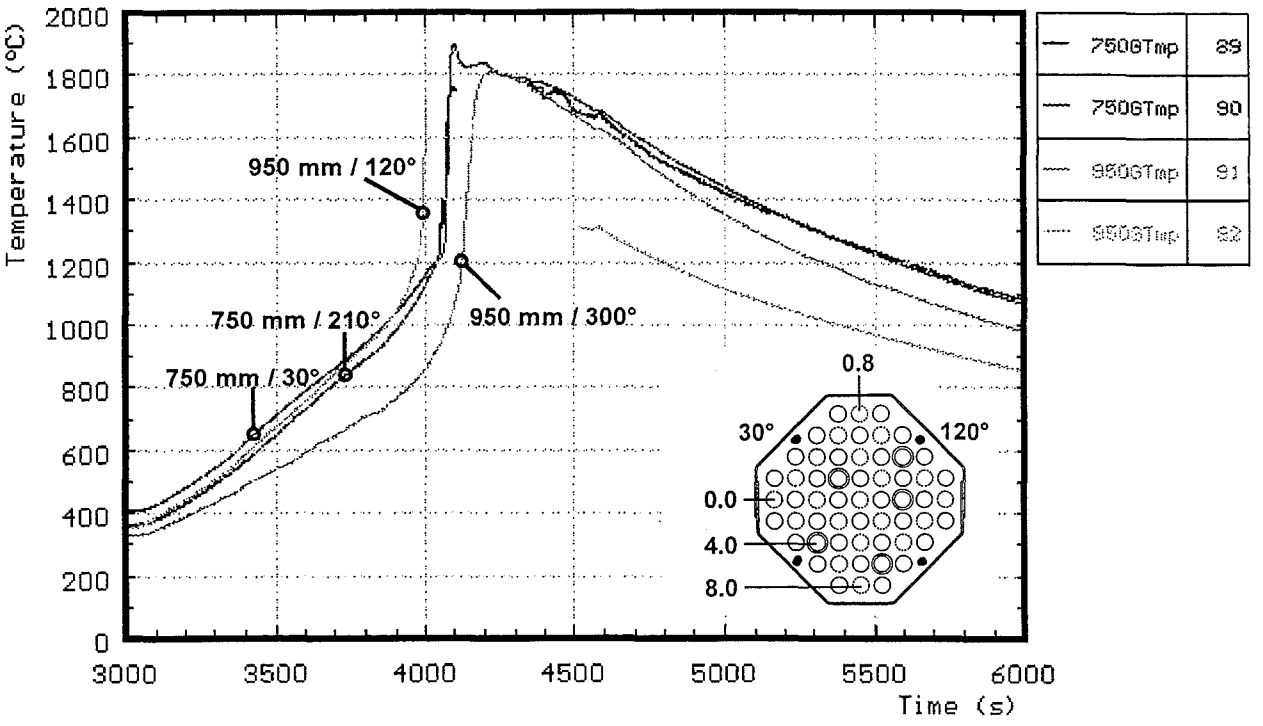

Fig. 33: CORA-7; Temperatures between bundle and shroud measured with ceramic protected TCs

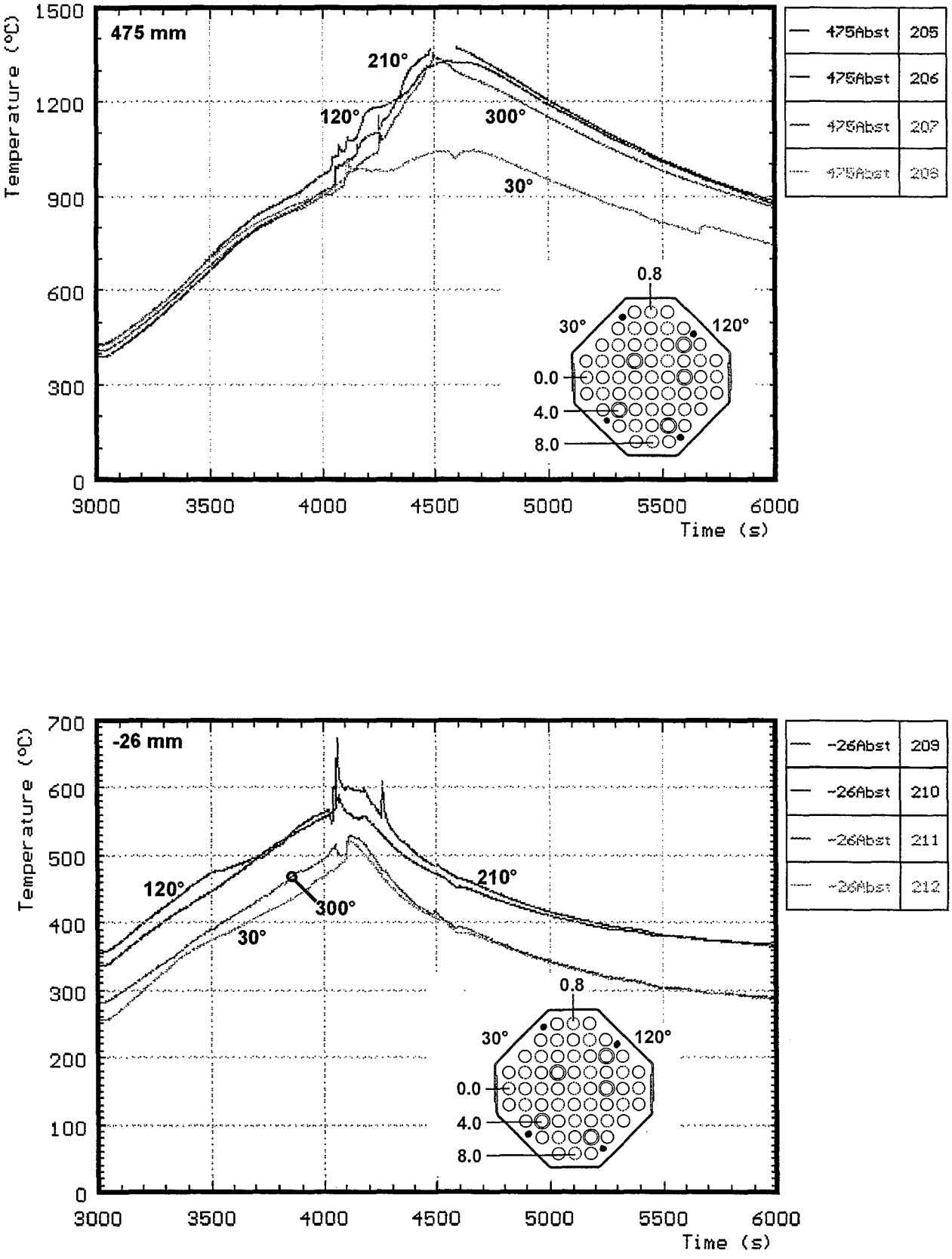

Fig. 34: CORA-7; Temperatures of the spacers

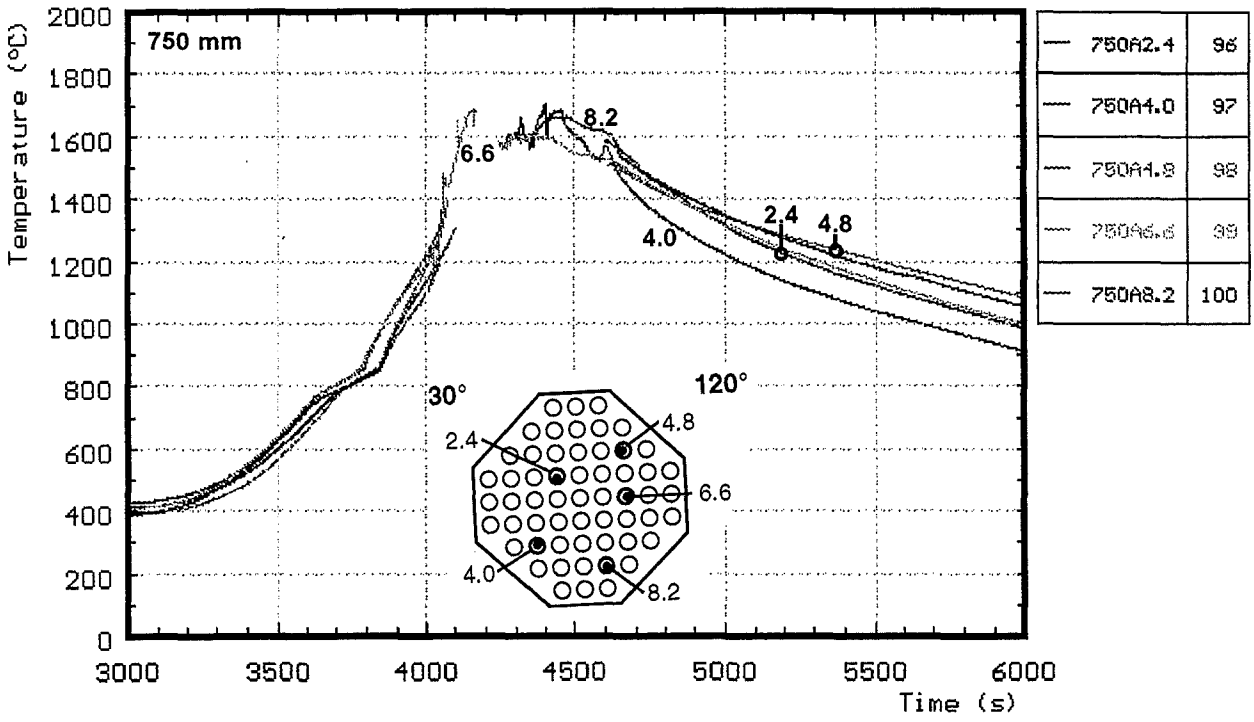

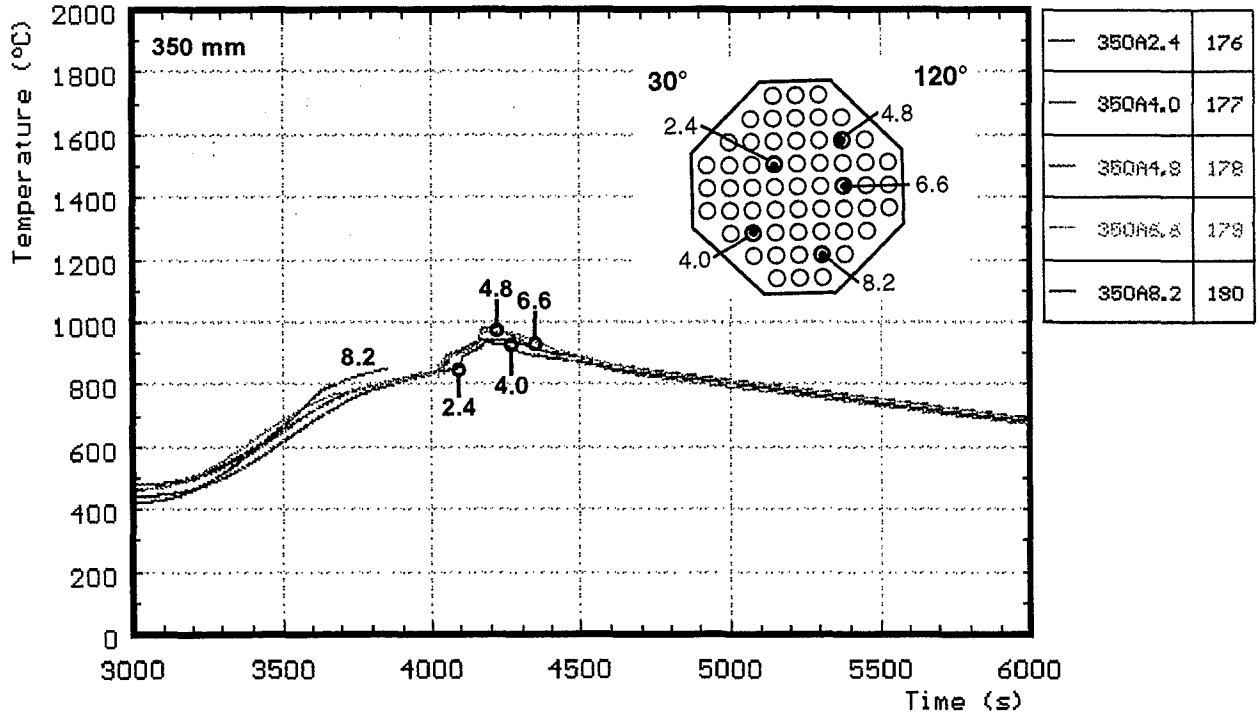

Fig. 35: CORA-7; Temperatures of the absorber rods

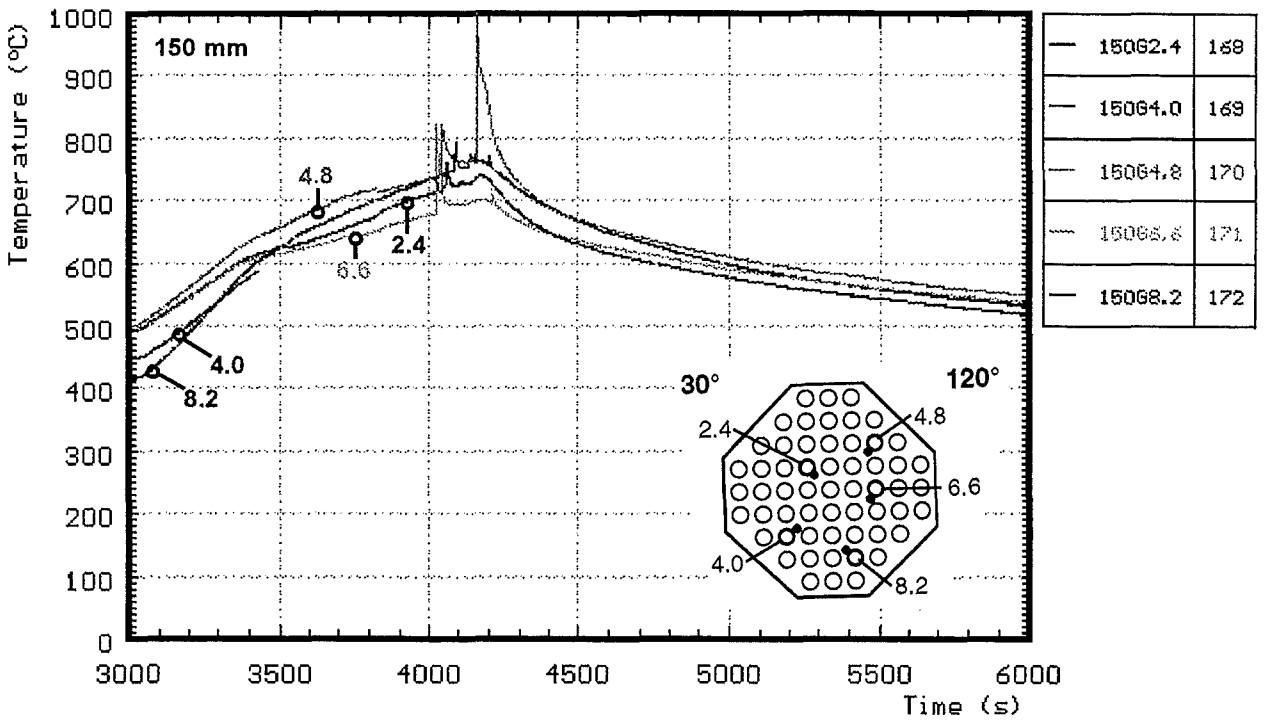

Fig. 36: CORA-7; Temperatures of the guide tubes of absorber rods

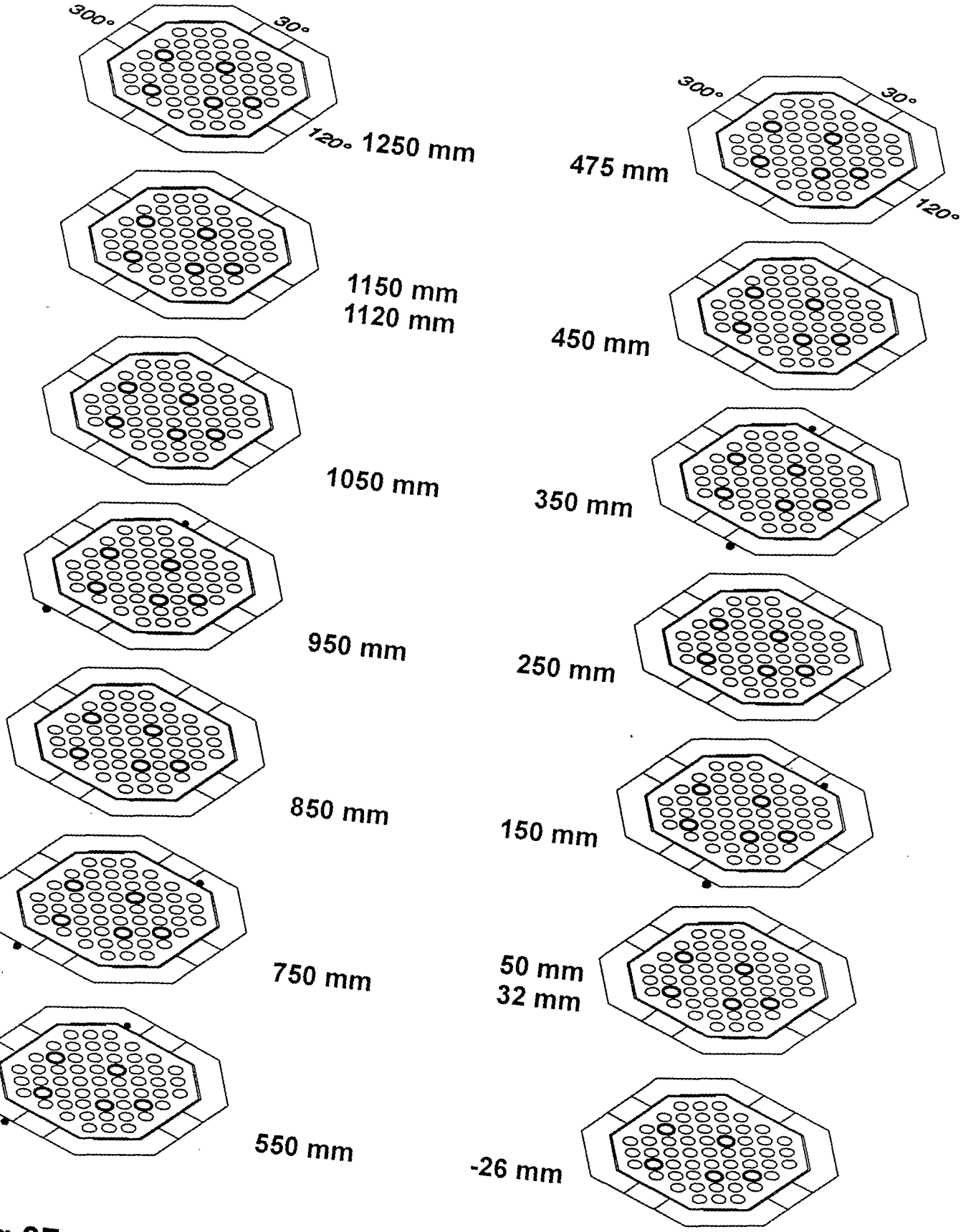

Fig.37: Location of the thermocouples at shroud and shroud insulation (CORA-7)

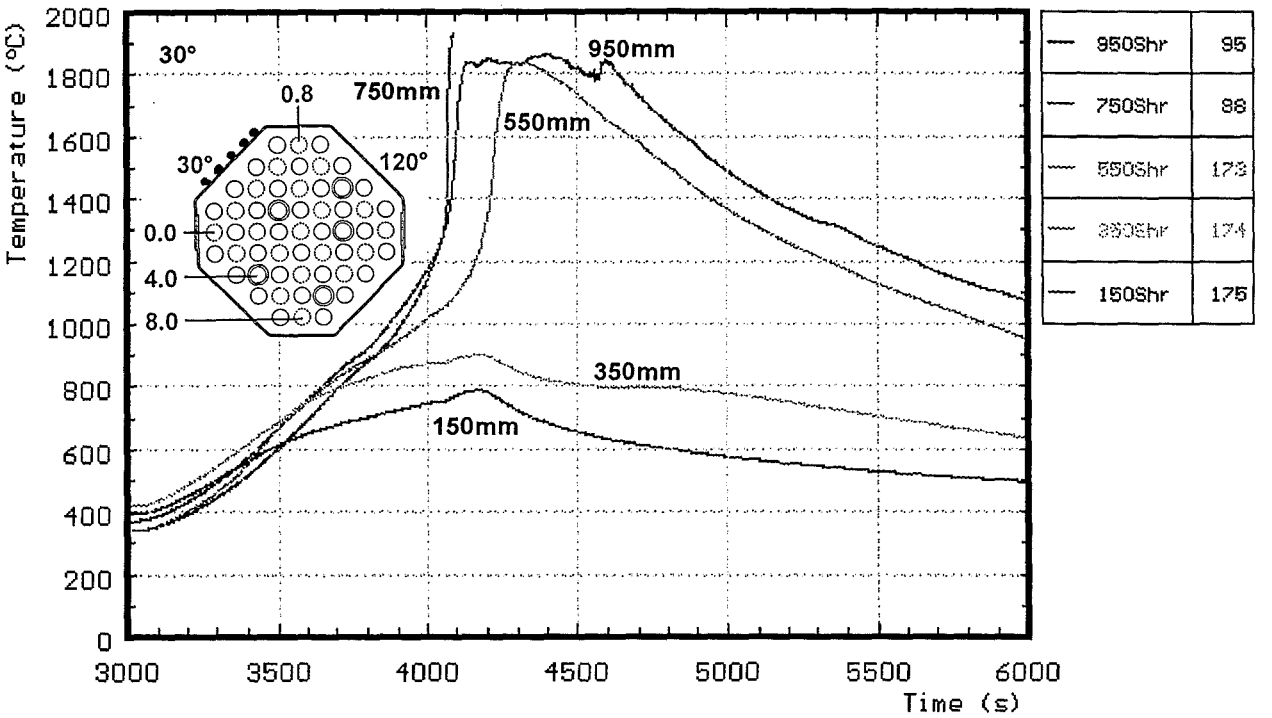

Fig. 38: CORA-7; Temperatures of outer side of shroud

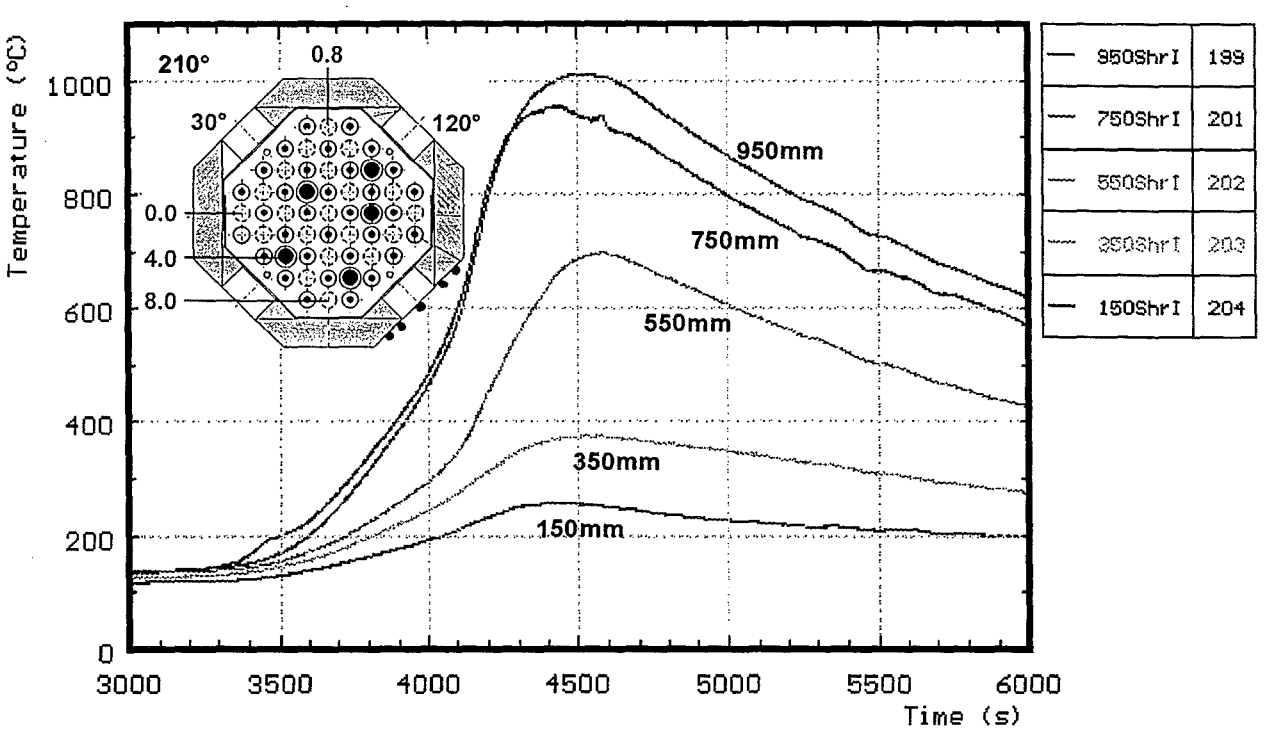

Fig. 39: CORA-7; Temperatures of the shroud insulation

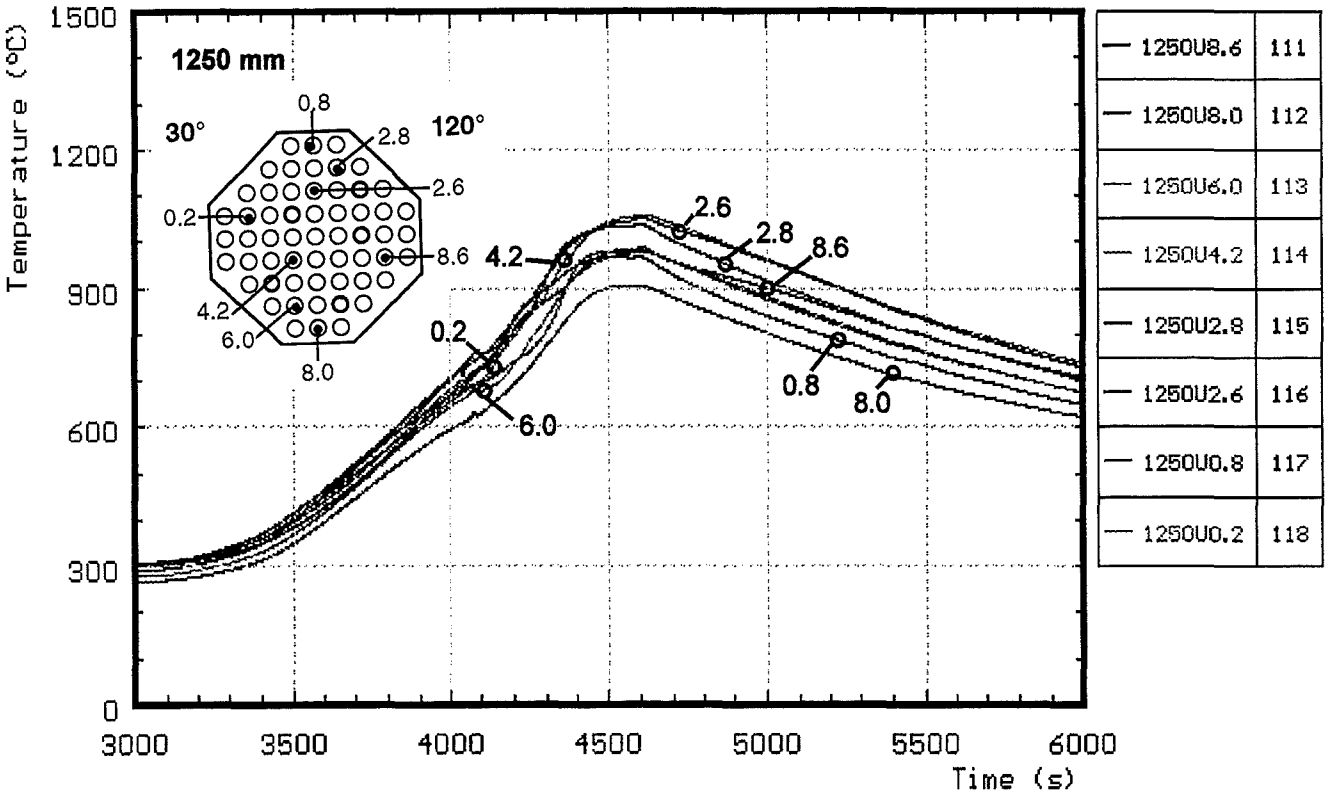

Fig. 40: CORA-7; Temperatures at elevations given (1250 mm)

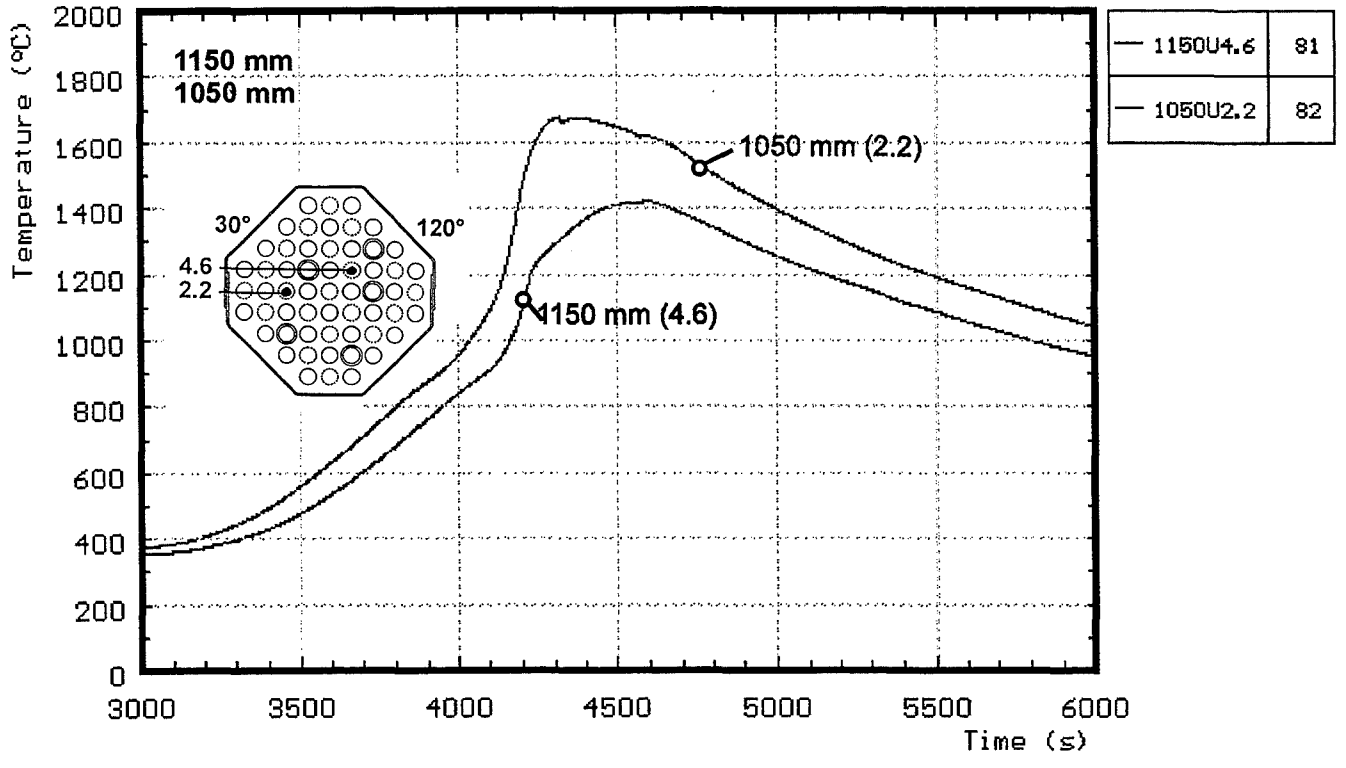

Fig. 41: CORA-7; Temperatures at elevations given (1150 - 1050 mm)

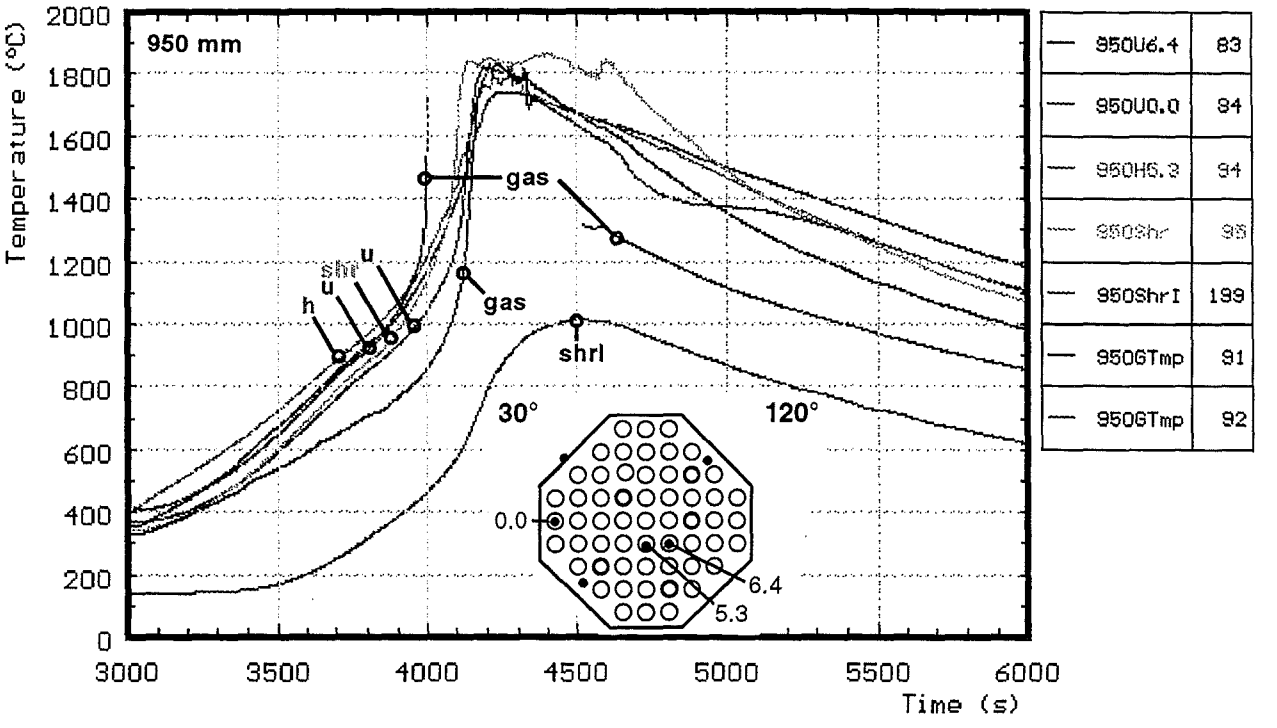

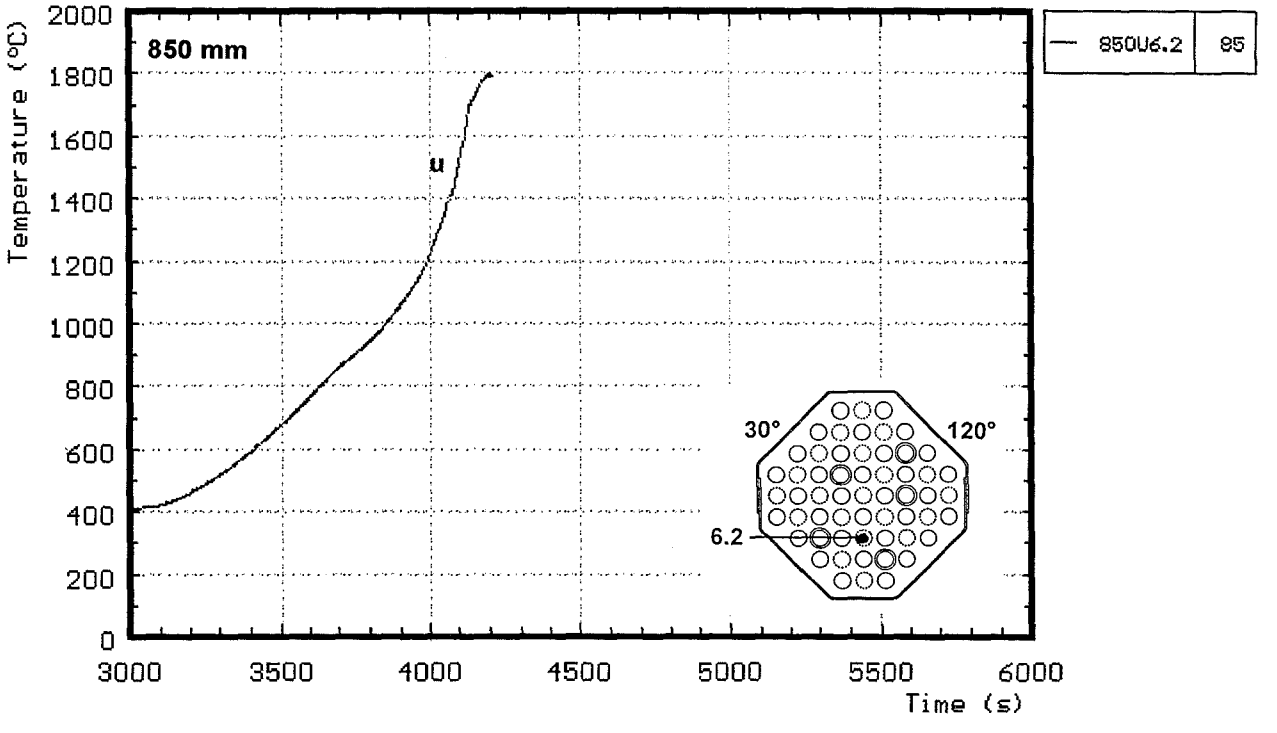

h : heated rods **shr : outer side of shroud**
u : unheated rods **shrl : on shroud insulation**
gas : gas temperature

Fig. 42: CORA-7; Temperatures at elevations given (950 - 850 mm)

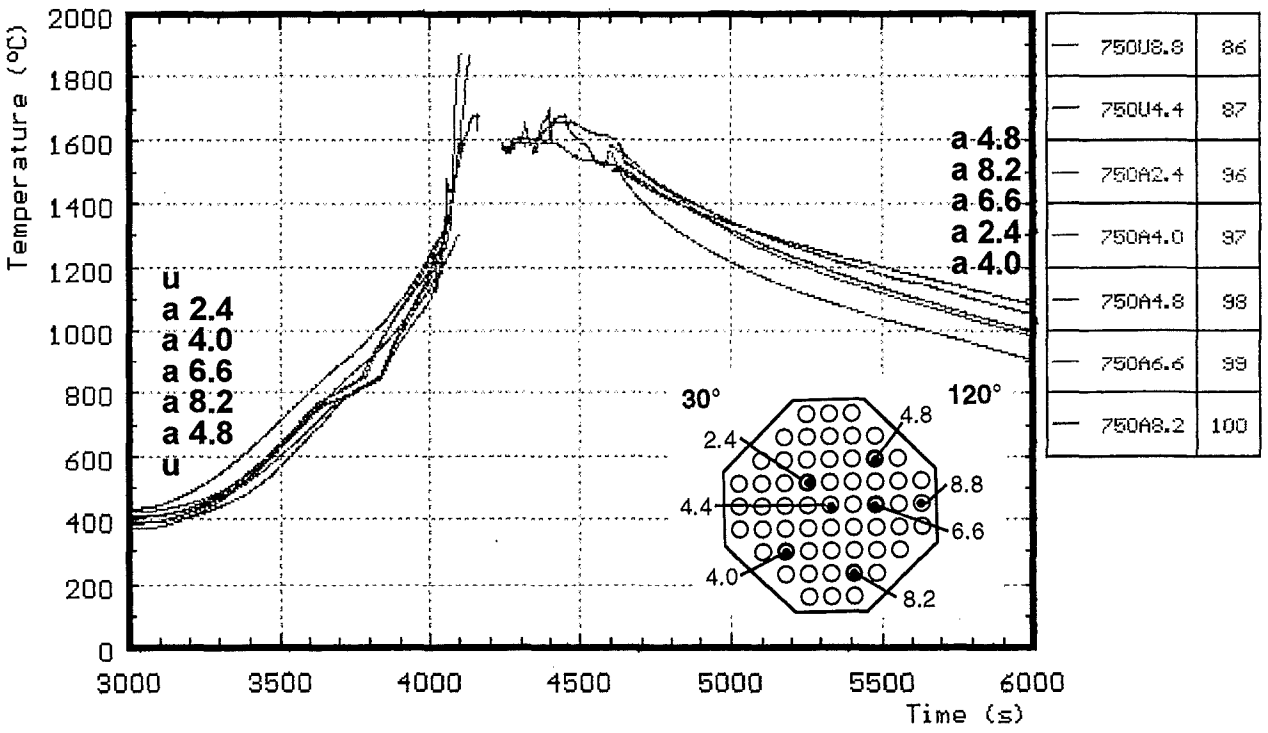

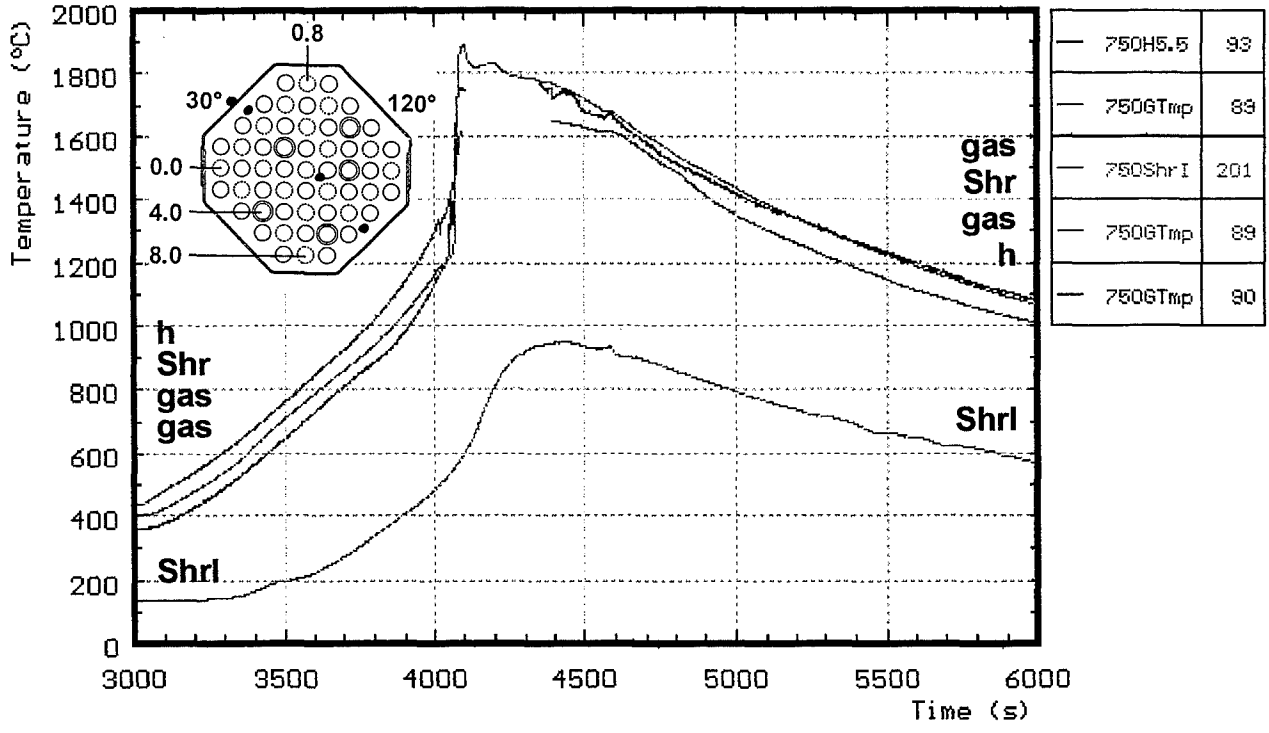

h : heated rods
u : unheated rods
a : in absorber

shr : outer side of shroud
shrl : on shroud insulation
gas : gas temperature

Fig. 43: CORA-7; Temperatures at elevations given (750 mm)

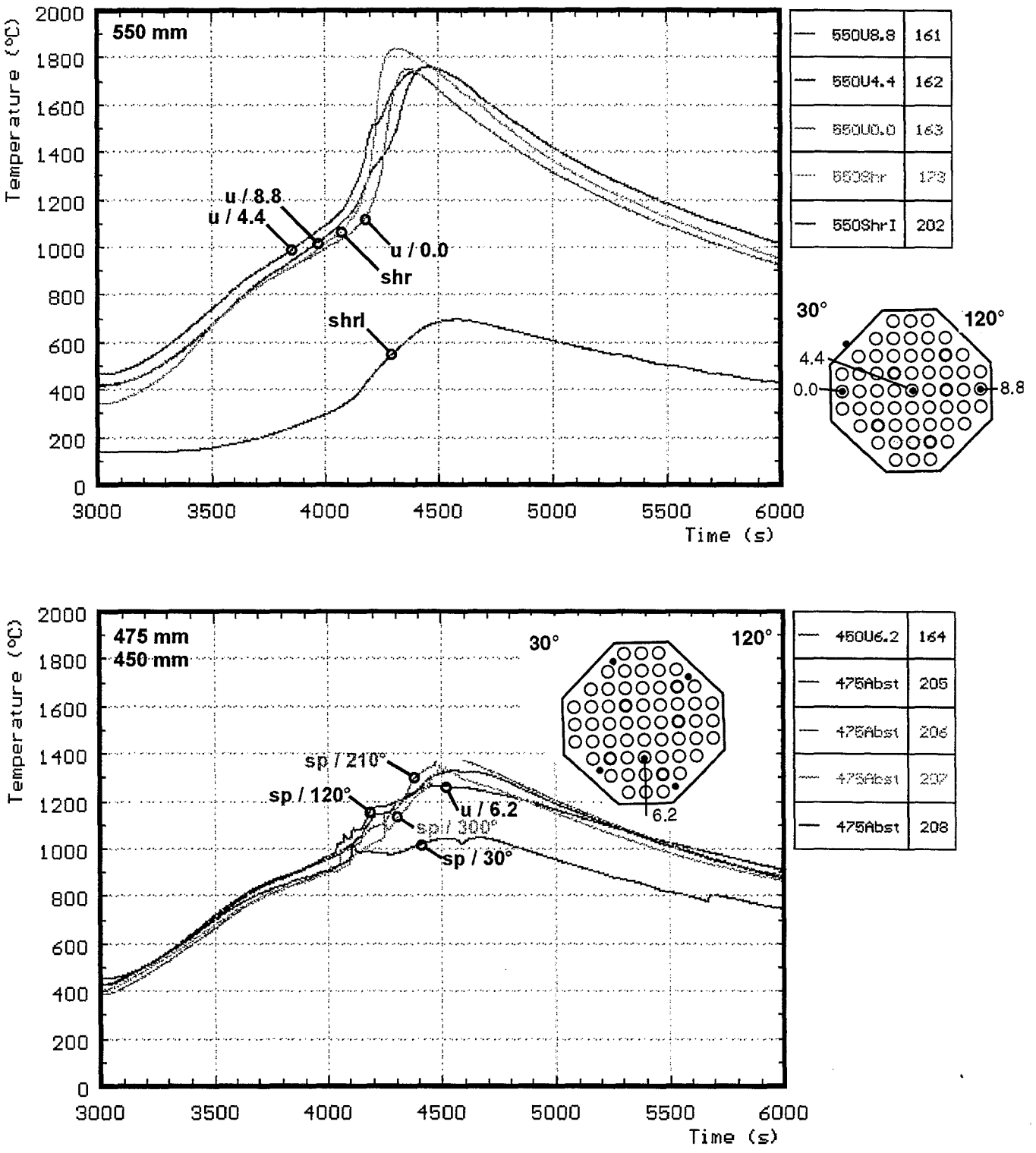

u : unheated rods
sp : spacer
shr : outer side of shroud
shrl : on shroud insulation

Fig. 44: CORA-7; Temperatures at elevations given (550 - 450 mm)

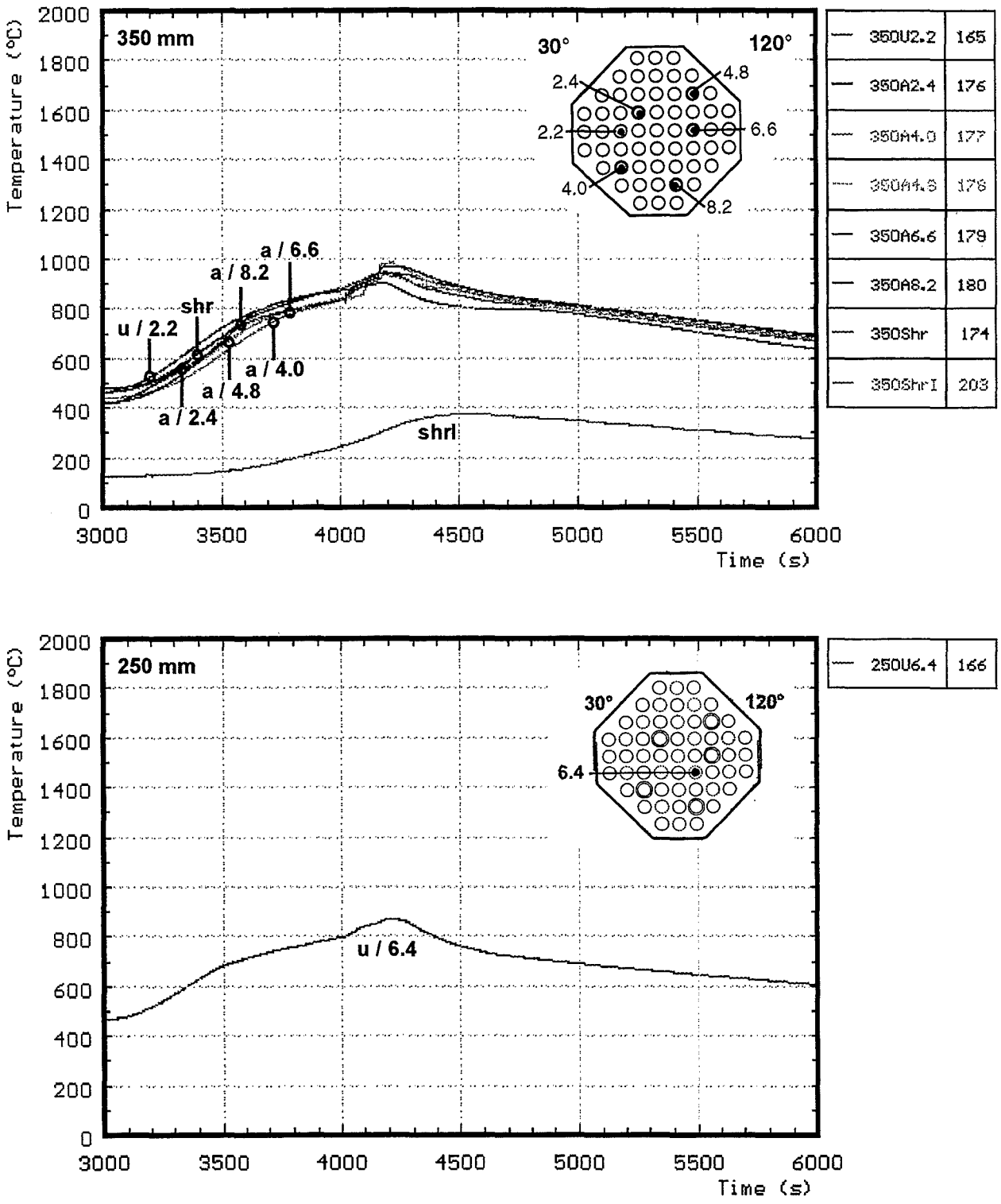

u : unheated rods
a : in absorber
shr : outer side of shroud
shrl : on shroud insulation

Fig. 45: CORA-7; Temperatures at elevations given (350 - 250 mm)

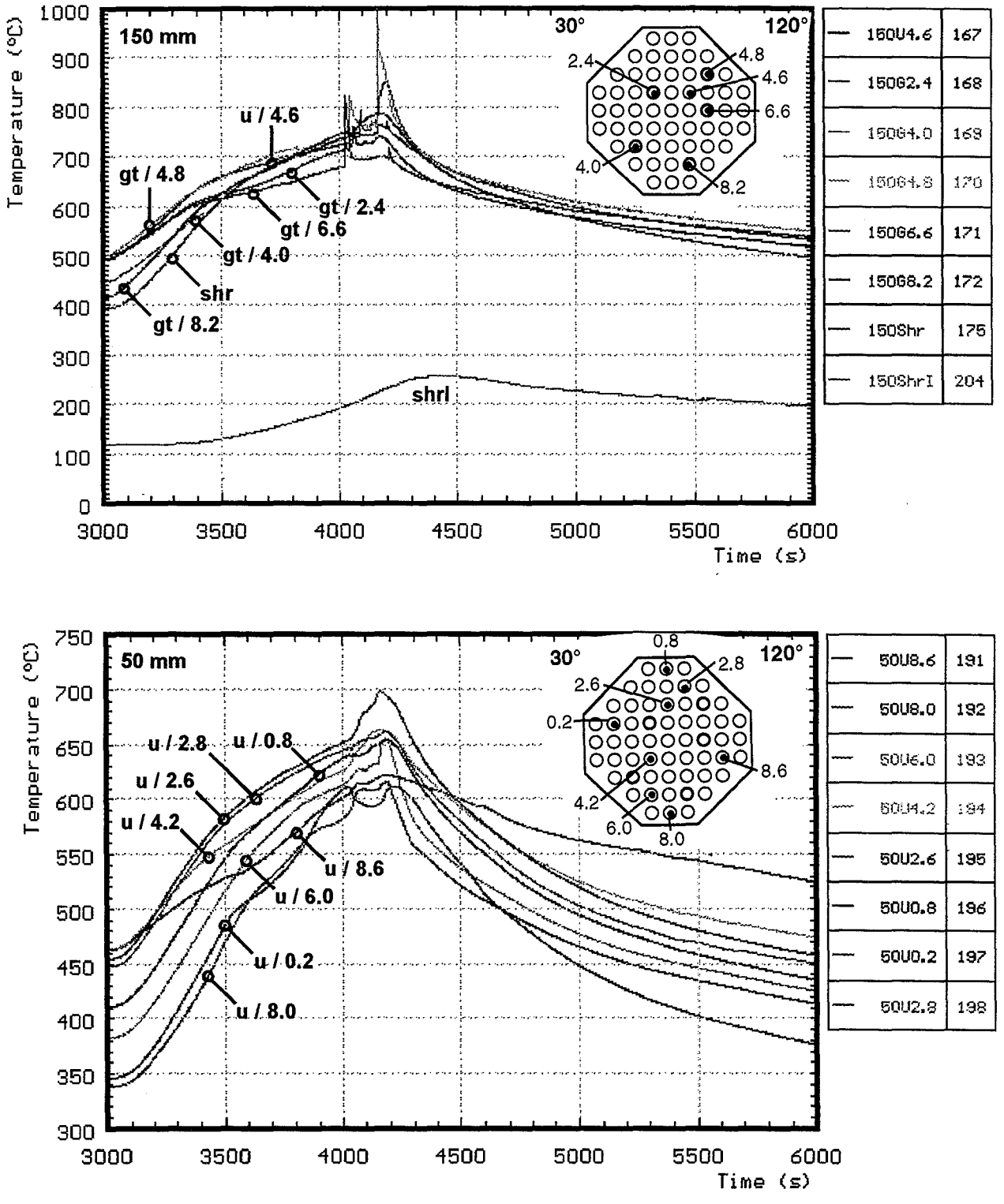

u : unheated rods
gt : guide tube
shr : outer side of shroud
shrl : on shroud insulation

Fig. 46: CORA-7; Temperatures at elevations given (150 - 50 mm)

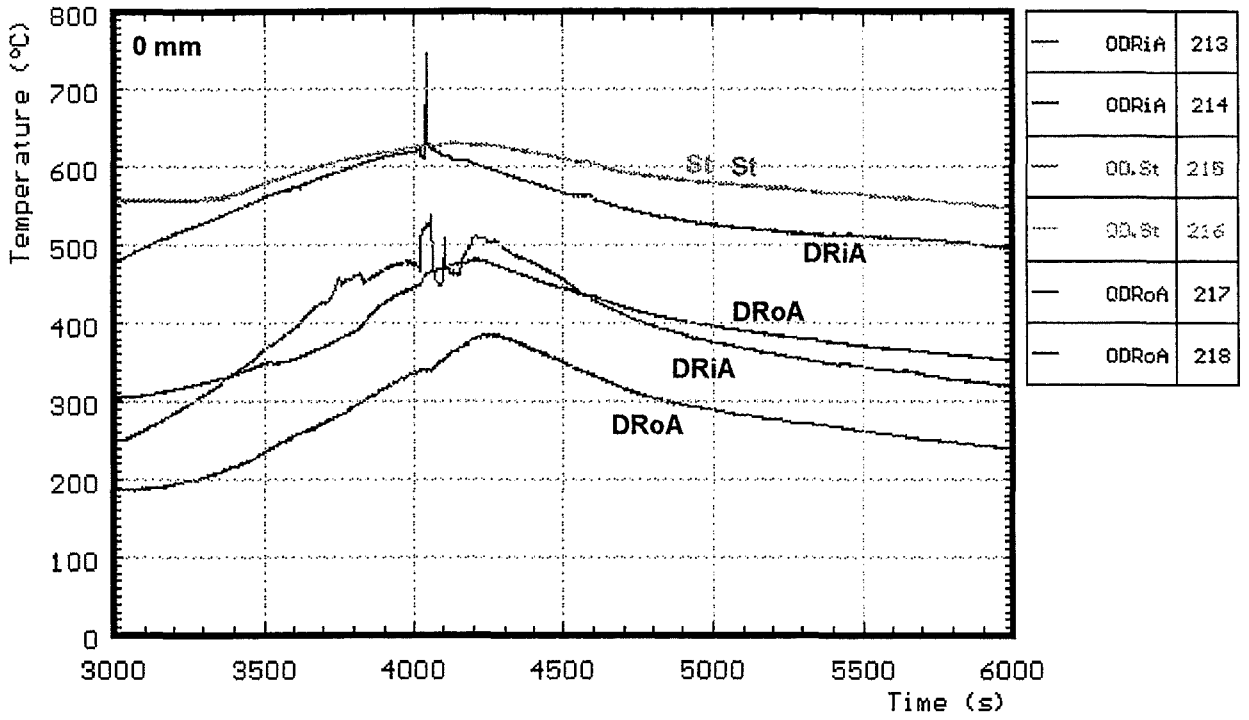

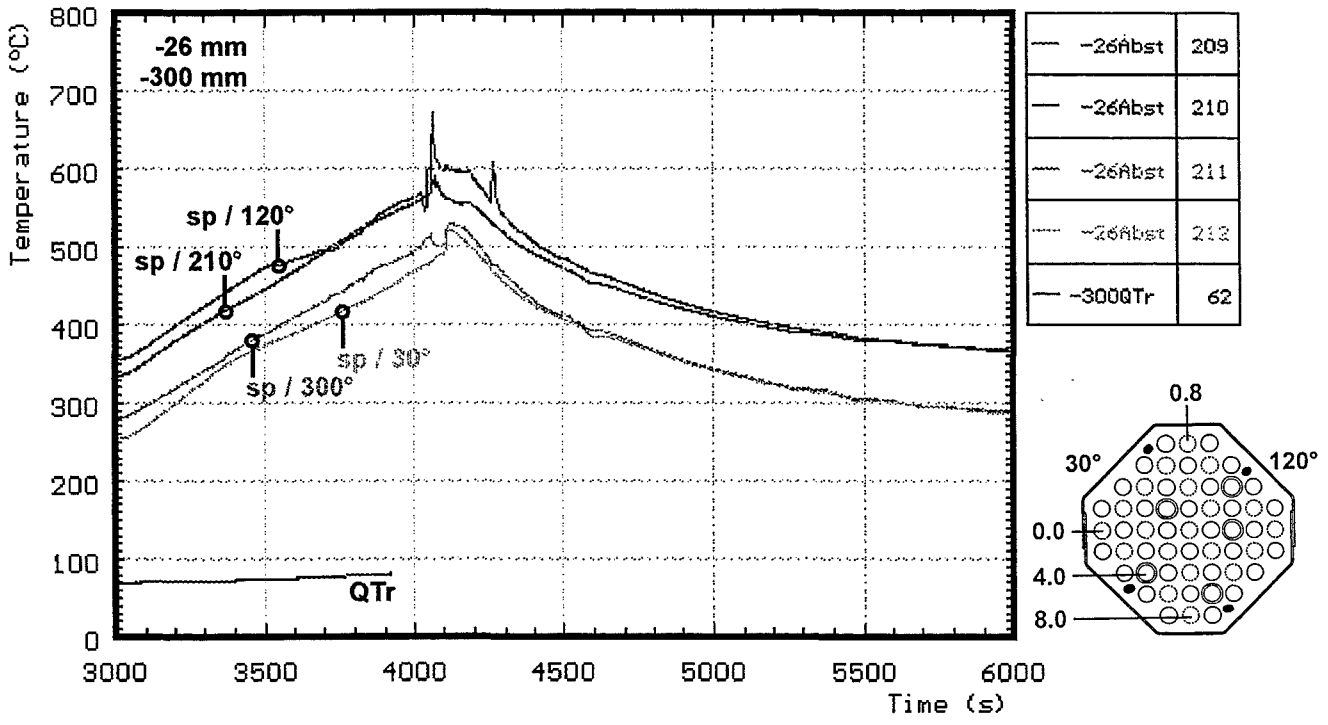

DRoA : steam tube, outer side **sp : spacer**
DRiA : steam tube, inner side **QTr : watertemperature in quenchcylinder**
St : steam inlet

Fig. 47: CORA-7; Temperatures at elevations given (0 - -300 mm)

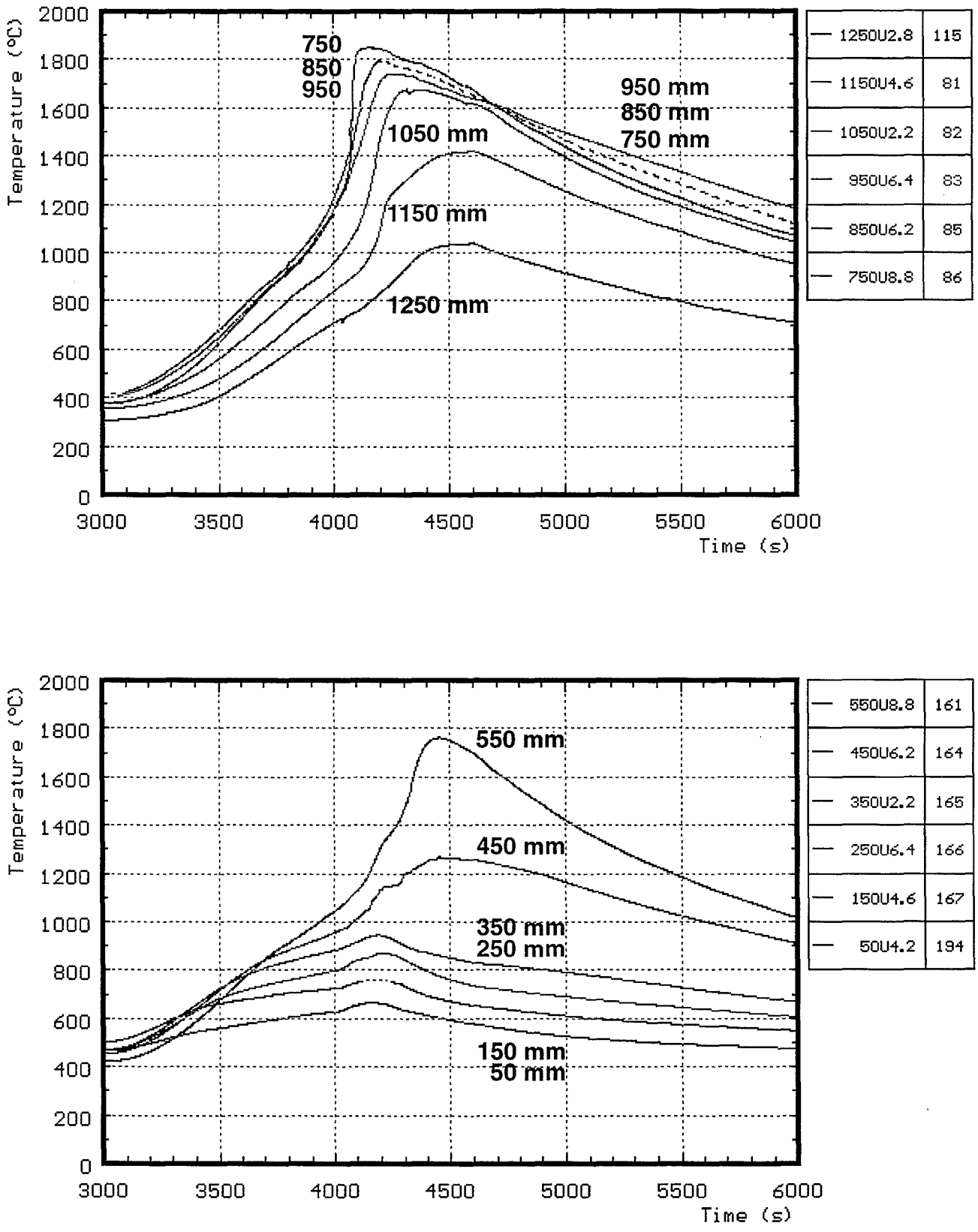

Fig. 48: CORA-7; Best-estimate bundle temperatures at different elevations

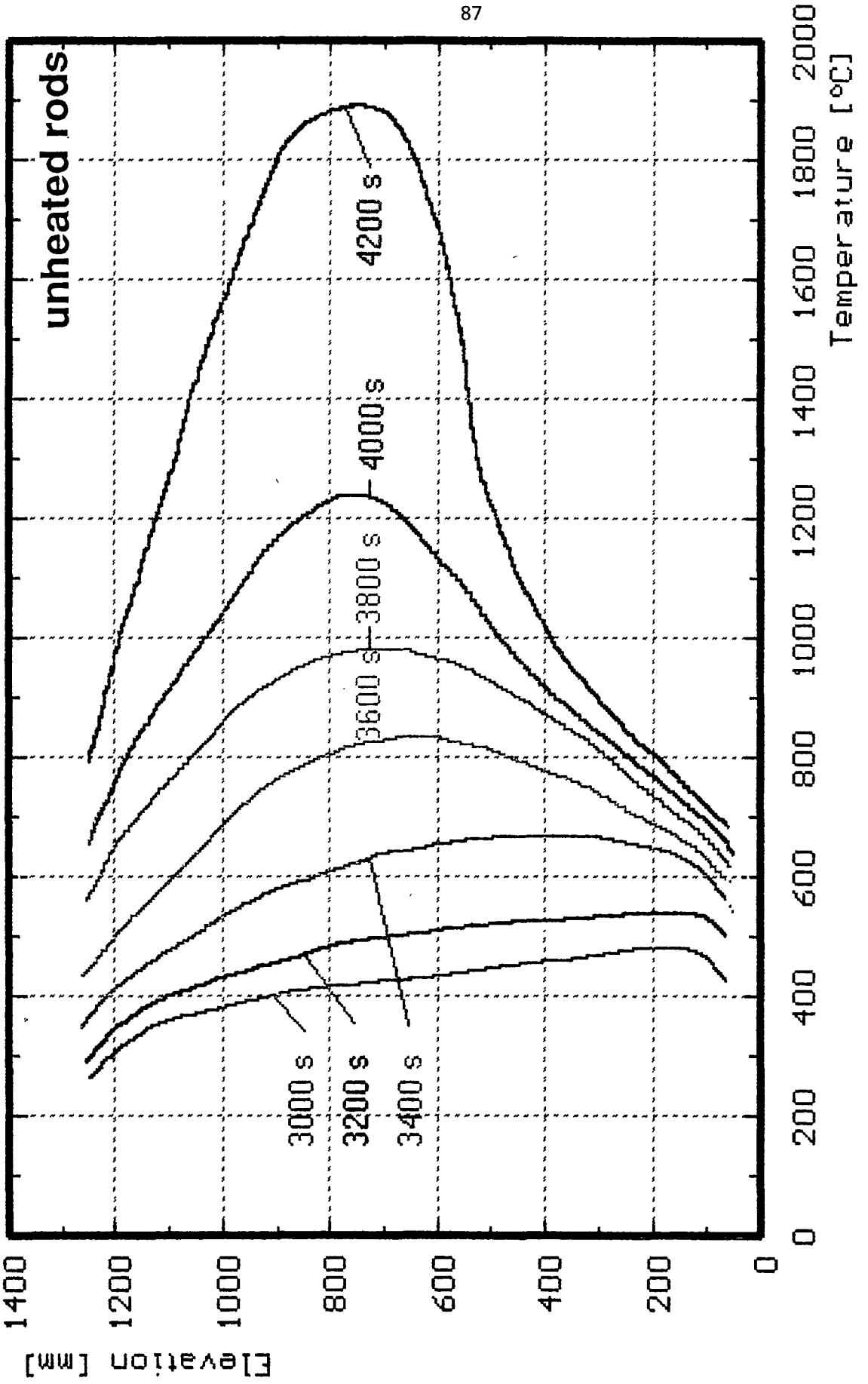

Fig. 49a: Axial temperature distribution during the transient of test CORA-7

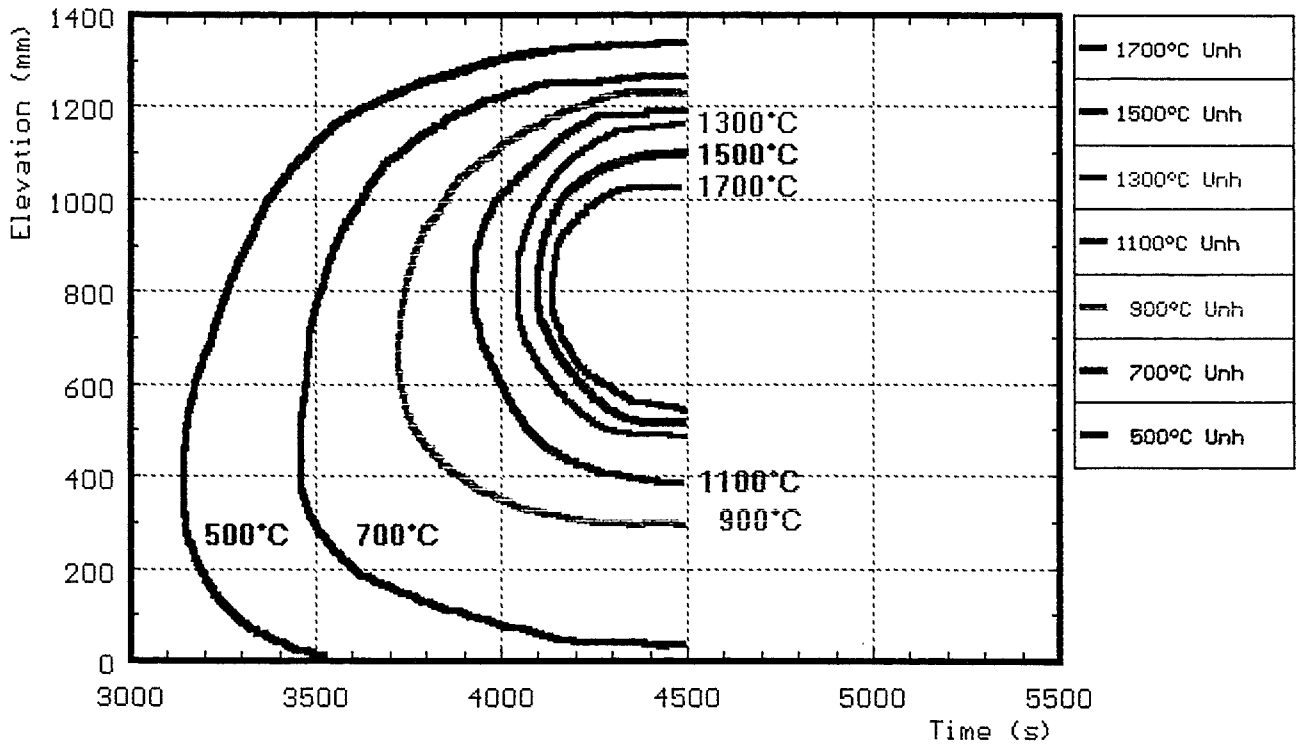

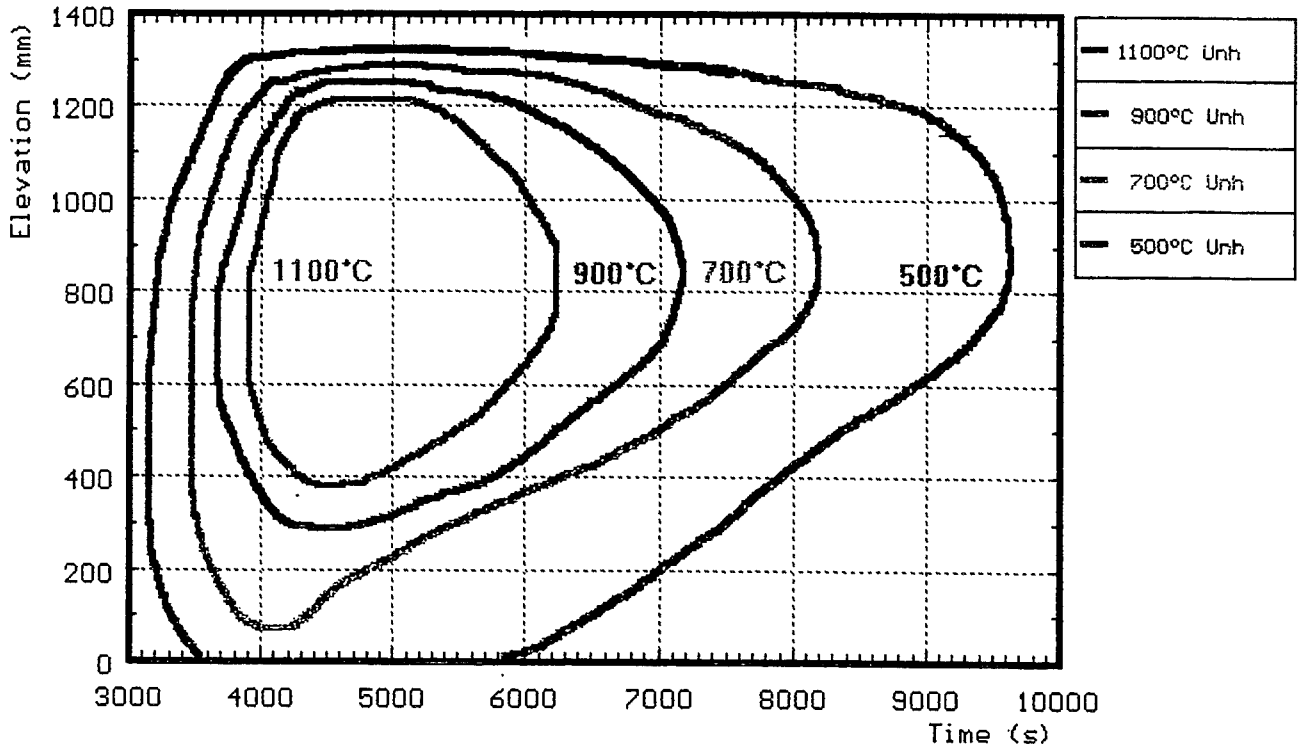

Fig. 49b: CORA-7; Isothermal distribution of the bundle temperature

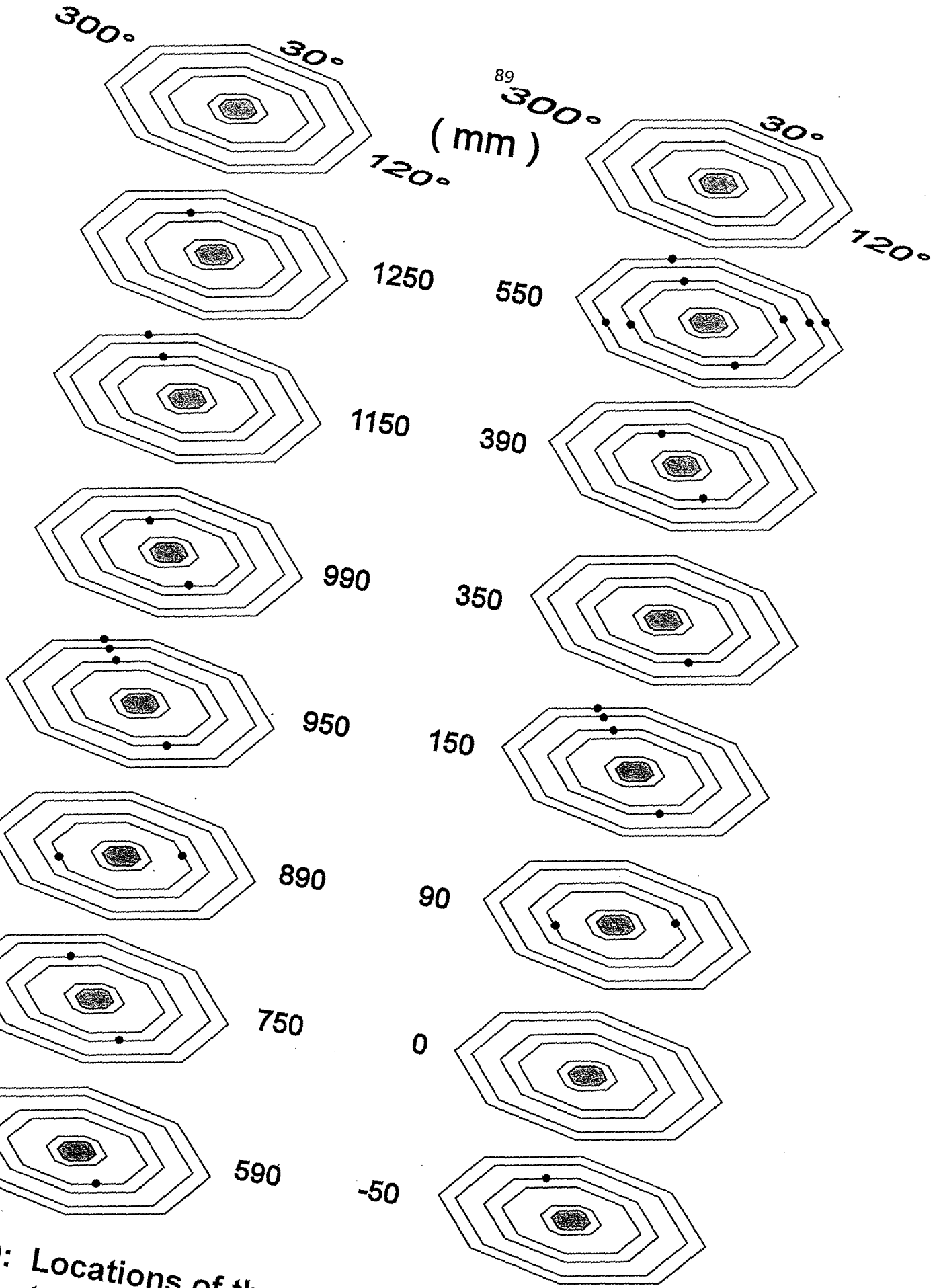

Fig.50: Locations of thermocouples in the high temperature shield (CORA-7)

angle		75°					165°			255°				345°				
radius (mm)	elevation in bundle (mm)	153	172	192	255	293	153	192	153	172	192	255	153	192	255	293
1250														128 234Ni		
1150														129 235Ni		137 245Ni
990							126 78Ni						142 1B			
950								150 229Ni						133 236Ni	154 242Ni	138 246Ni
890		148 20B							144 7B							
750								151 230Ni						130 237Ni		
590							146 21B									
550				132 126Ni	125 130Ni	136 244Ni		152 231Ni			124 127Ni	149 131Ni		131 238Ni		139 247Ni
390							145 22B						141 23B			
350								153 232Ni								
150								127 233Ni						135 240Ni	155 243Ni	140 248Ni
90		147 33B							143 26B							
-50														134 241Ni		

Fig. 51: Position of thermocouples in the high temperature shield for test CORA-7

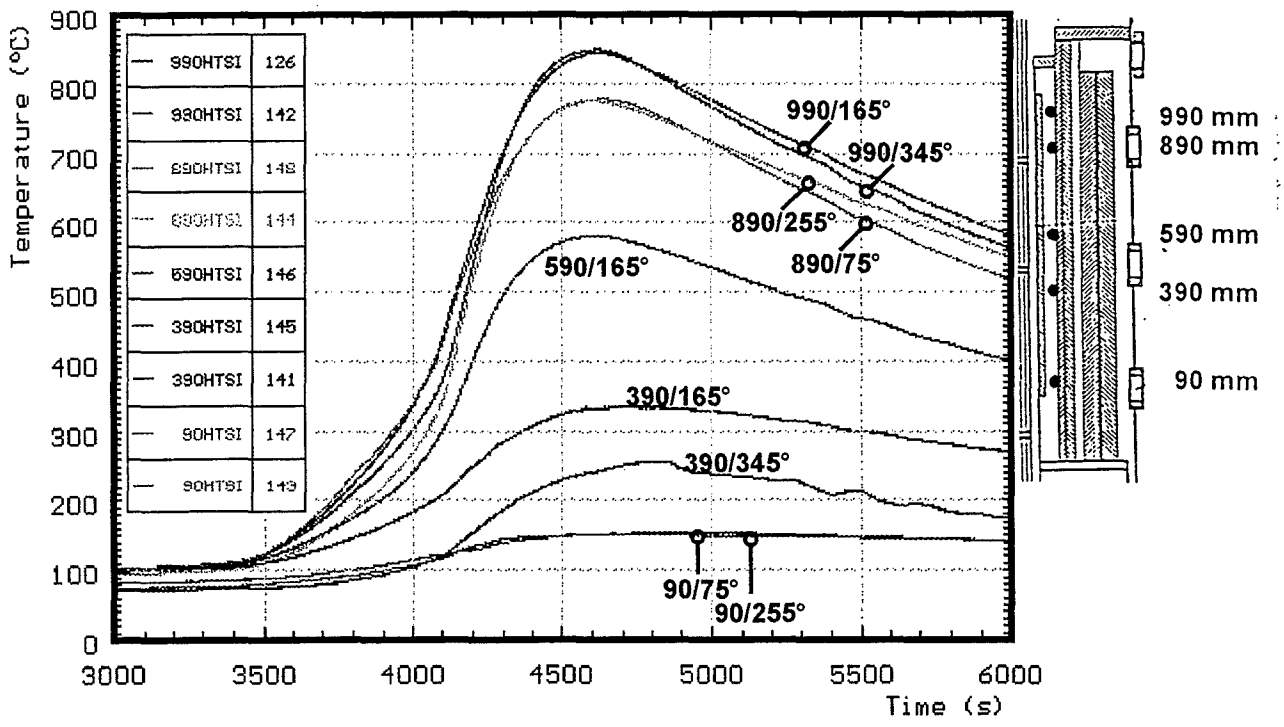

Fig. 52: CORA-7; Temperatures of HTS, Inner surface at 153 mm radius

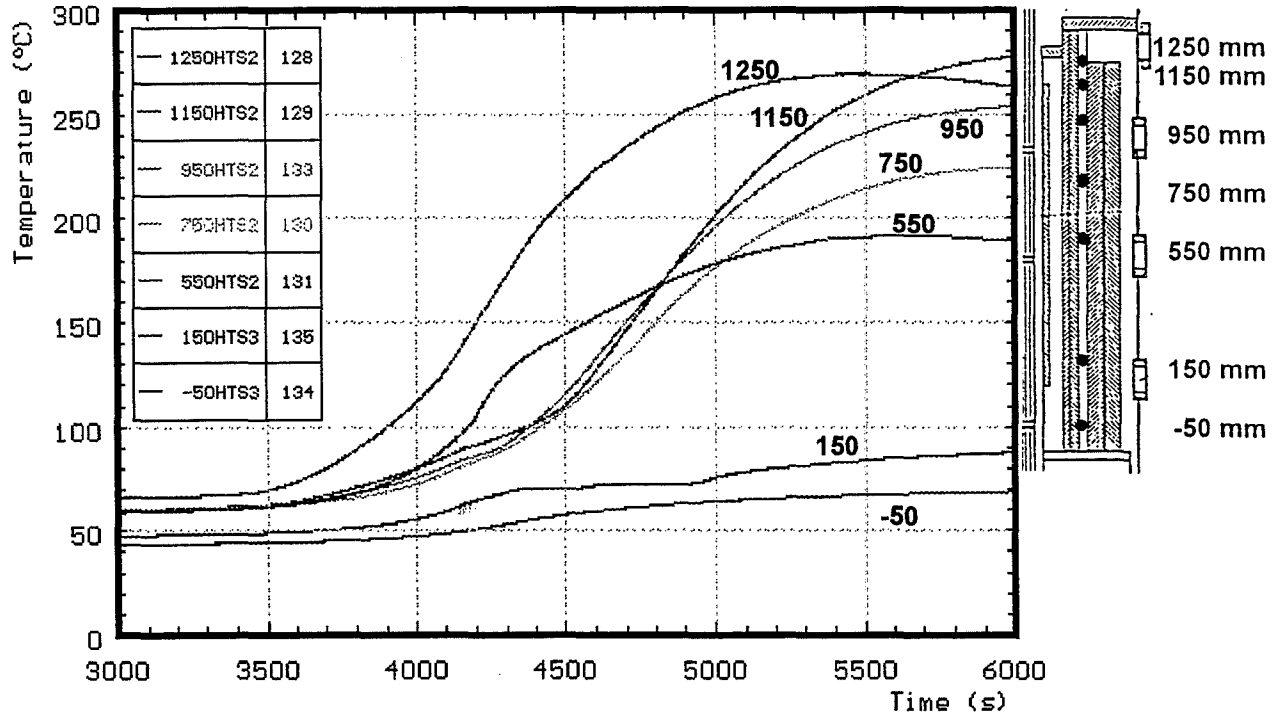

Fig. 53: CORA-7; Temperatures of HTS, Temperatures in HT shield at 192 mm radius, 345°

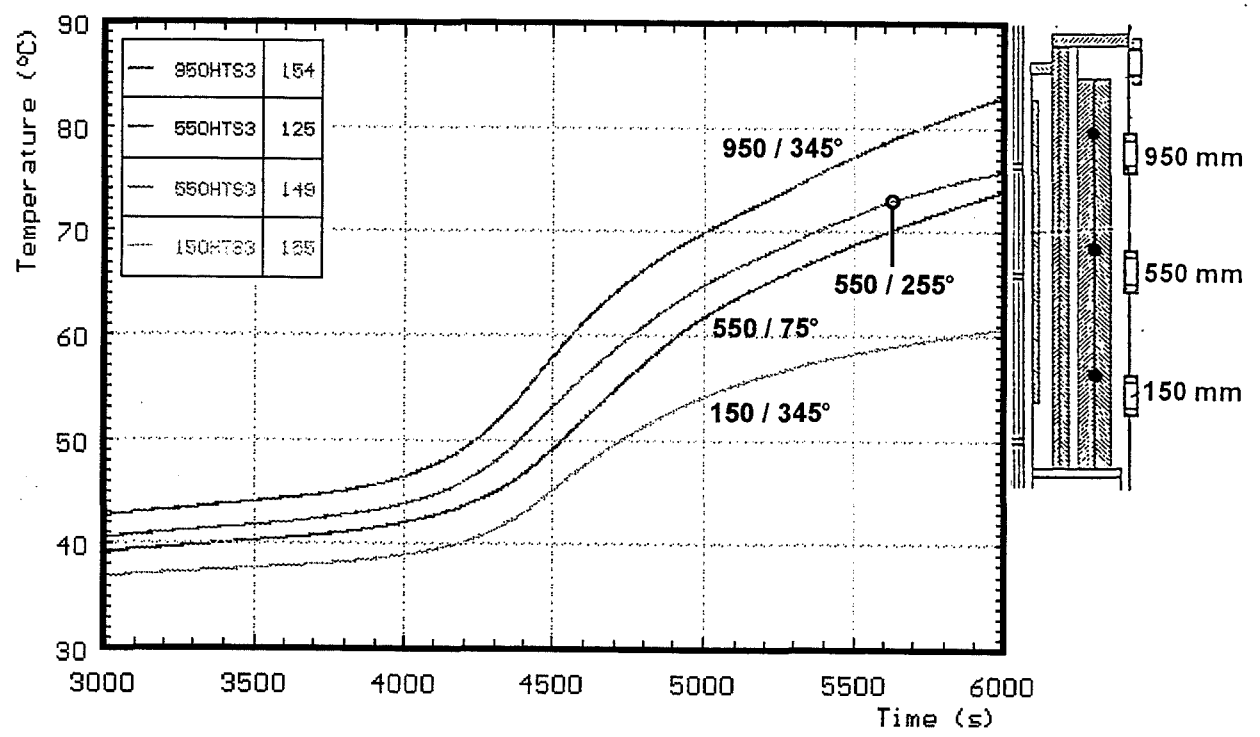

Fig. 54: CORA-7; Temperatures of HTS, Temperatures in HT shield at 255 mm radius

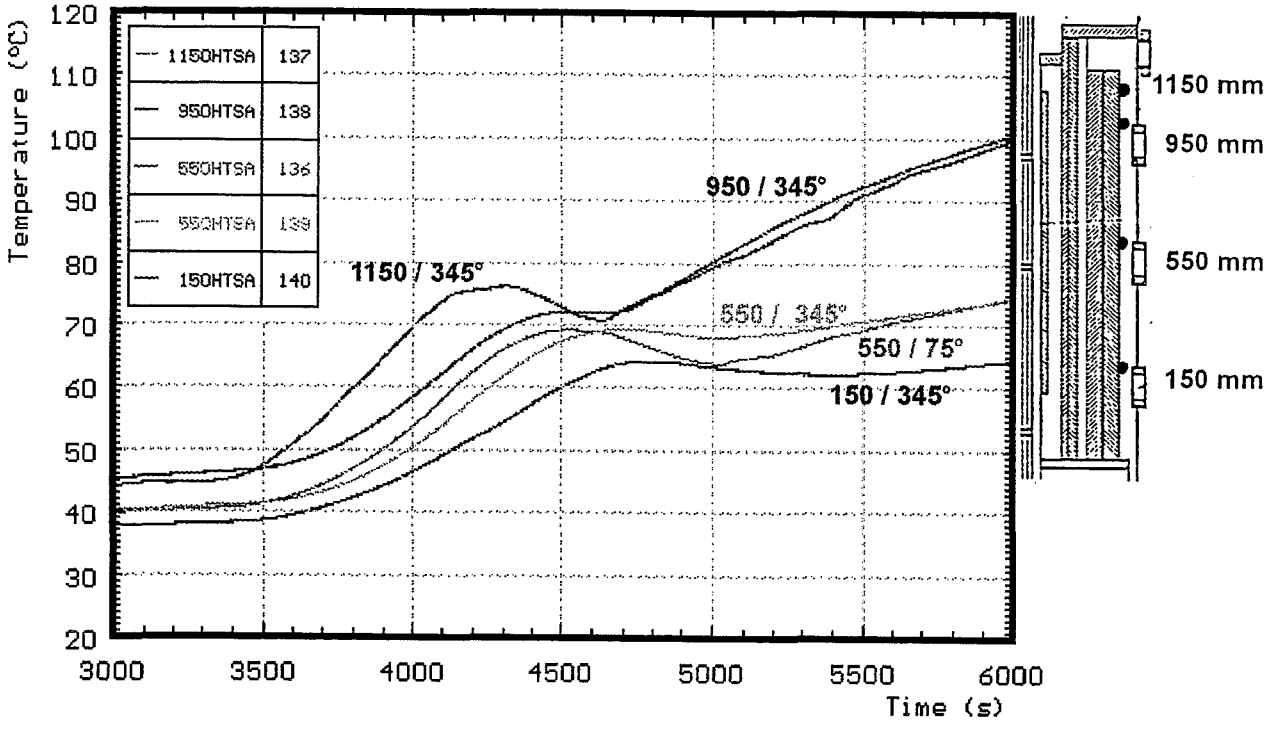

Fig. 55: CORA-7; Temperatures of HTS, Temperatures in HT shield at 293 mm radius

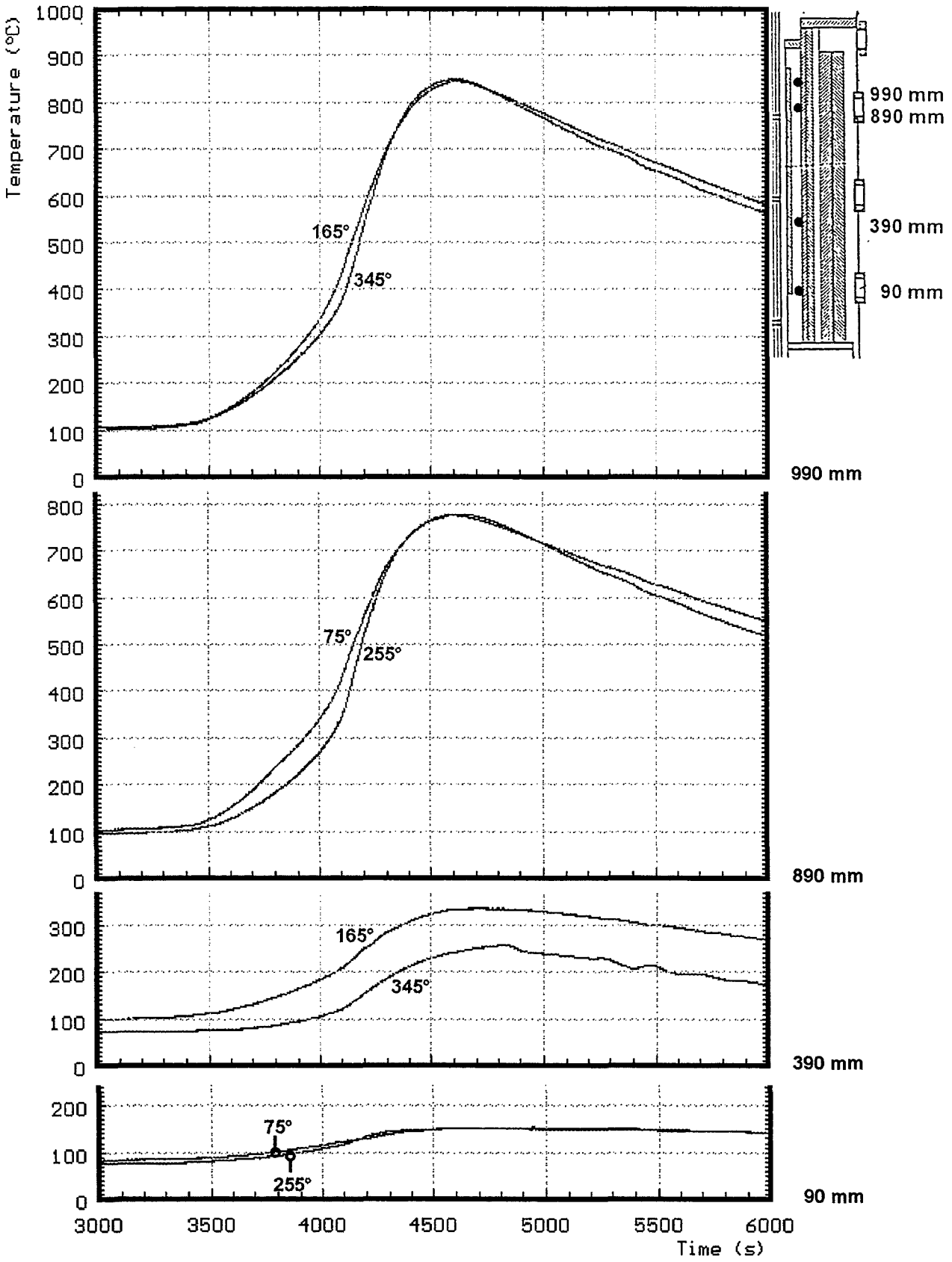

Fig. 56: CORA-7; Temperatures of HTS, Comparison on inner surface at 153 mm radius

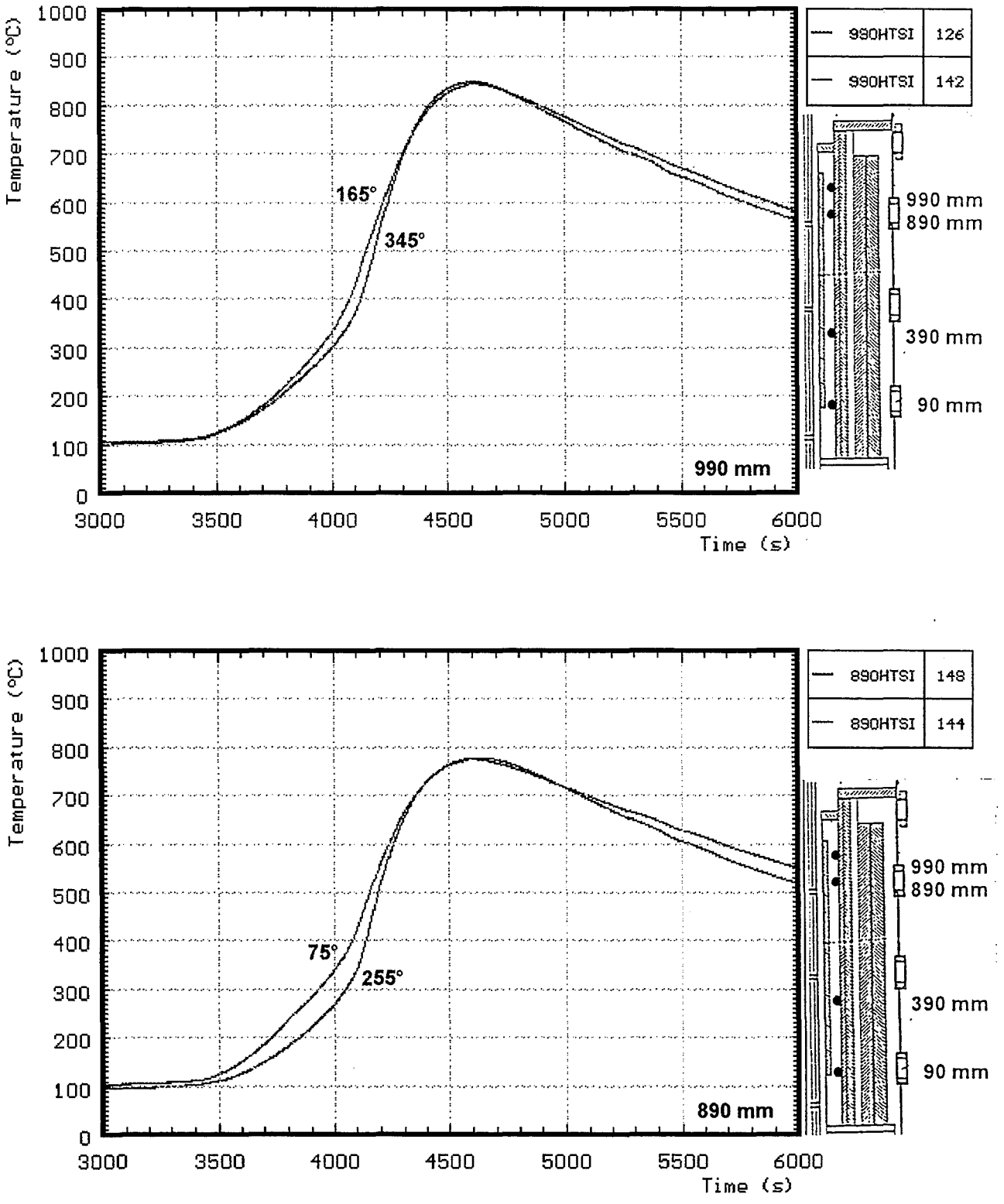

Fig. 57: CORA-7; Temperatures of HTS, Comparison on inner surface at 153 mm radius, 990 mm and 890 mm elevation

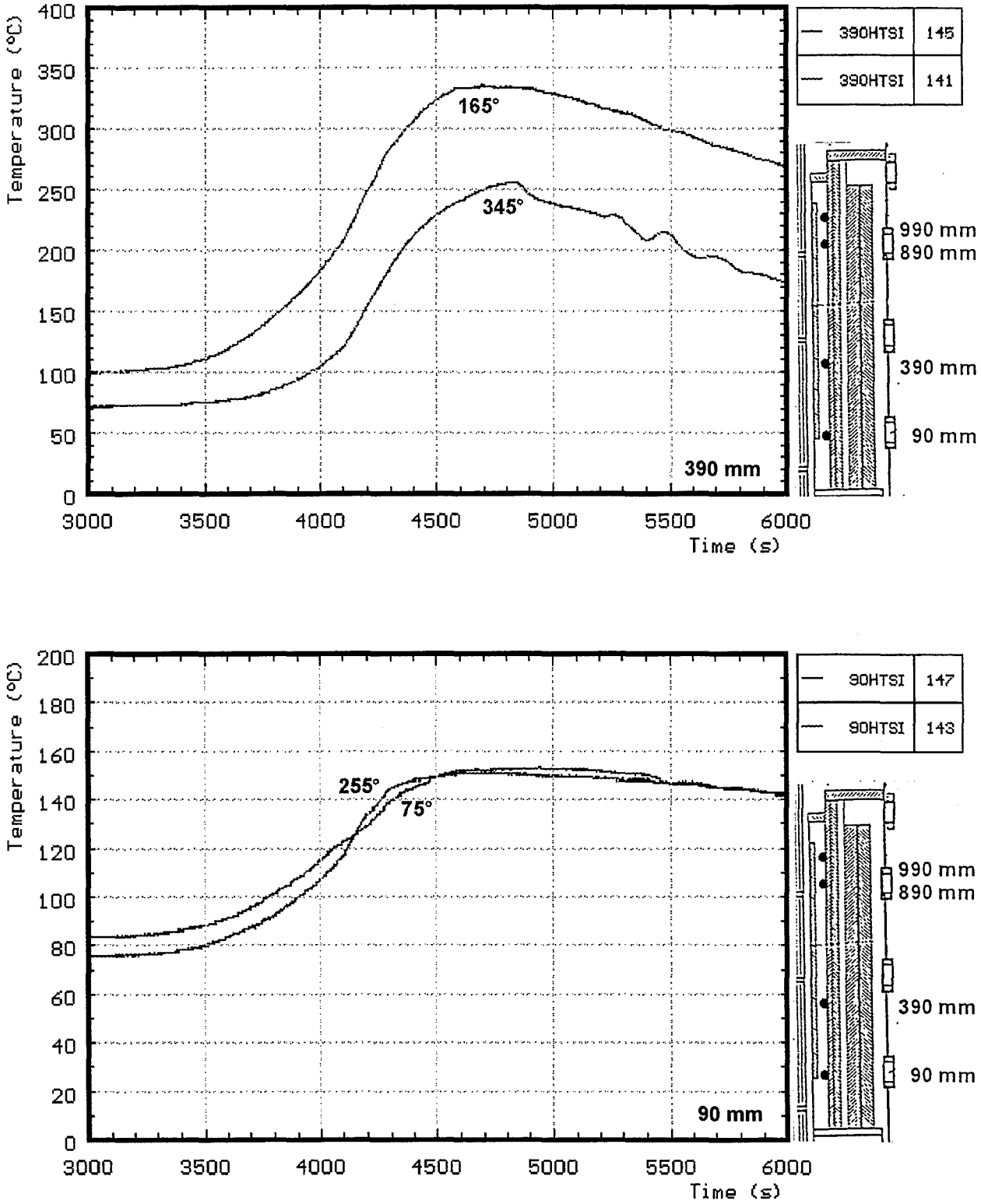

Fig. 58: CORA-7; Temperatures of HTS, Comparison on inner surface at 153 mm radius, 390 mm and 90 mm elevation

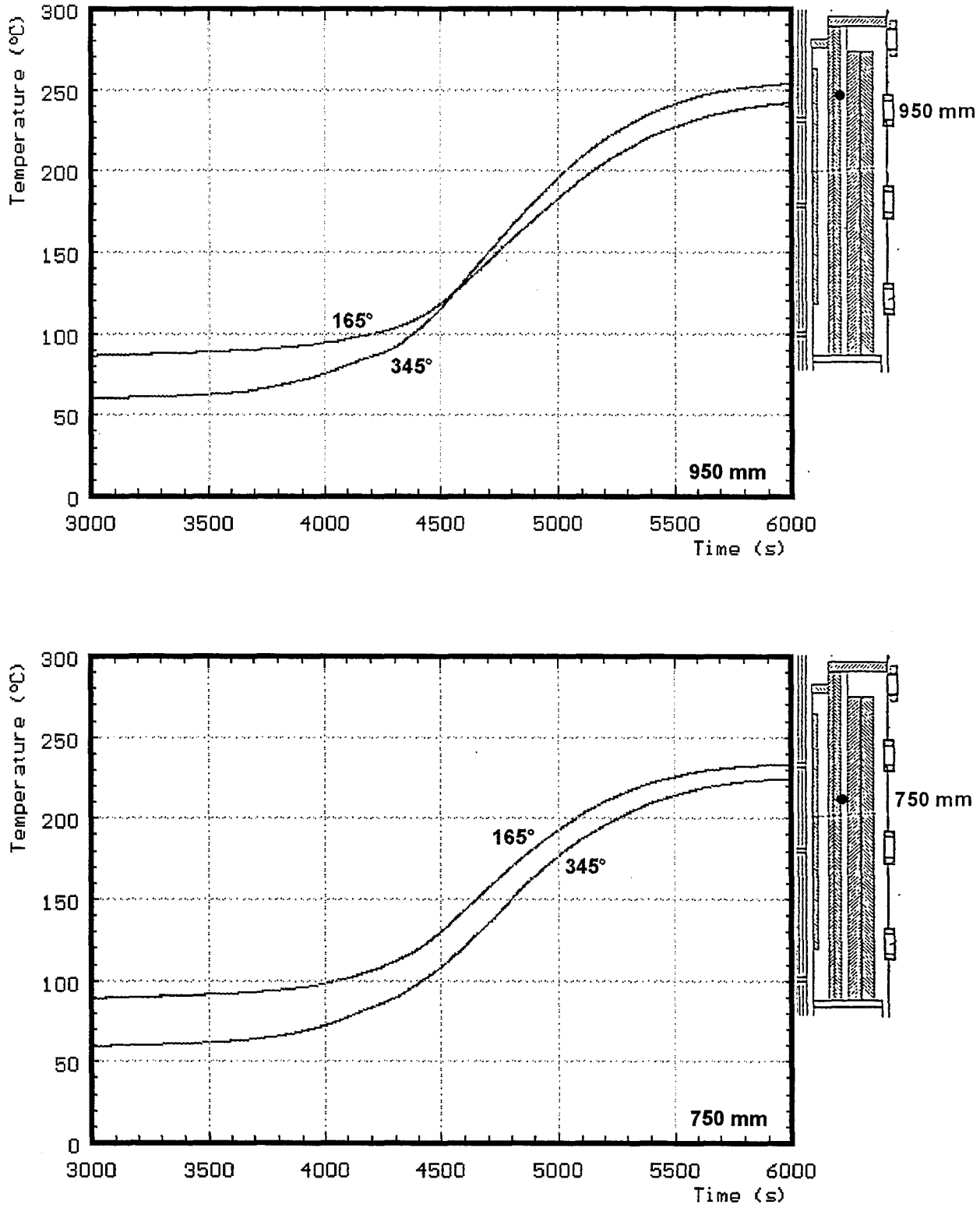

Fig. 59: CORA-7; Temperatures of HTS, Comparison in HT-shield at 192 mm radius, 950 mm and 750 mm elevation

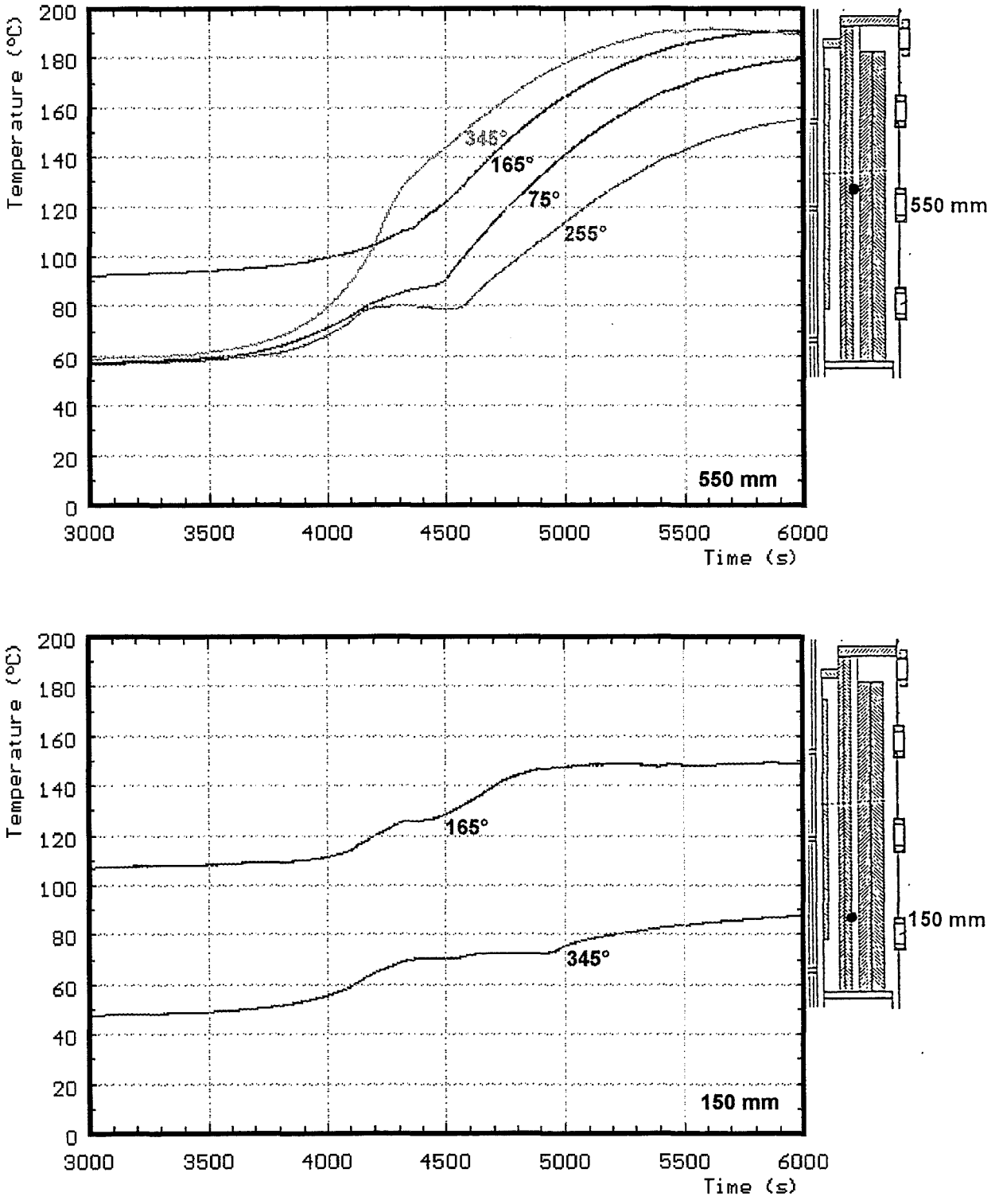

Fig. 60: CORA-7; Temperatures of HTS, Comparison in HT-shield at 192 mm radius, 550 mm and 150 mm elevation

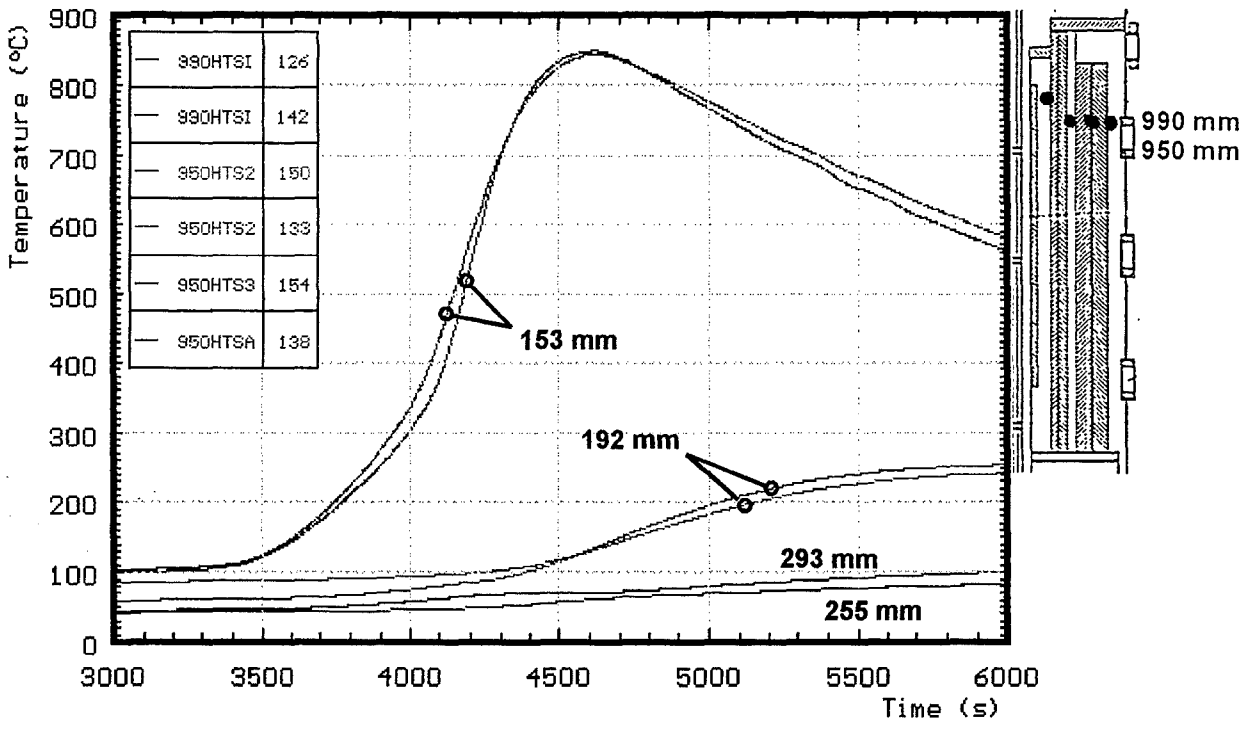

Fig. 61: CORA-7; Temperatures of HTS, Radial dependence at about 950 mm elevation

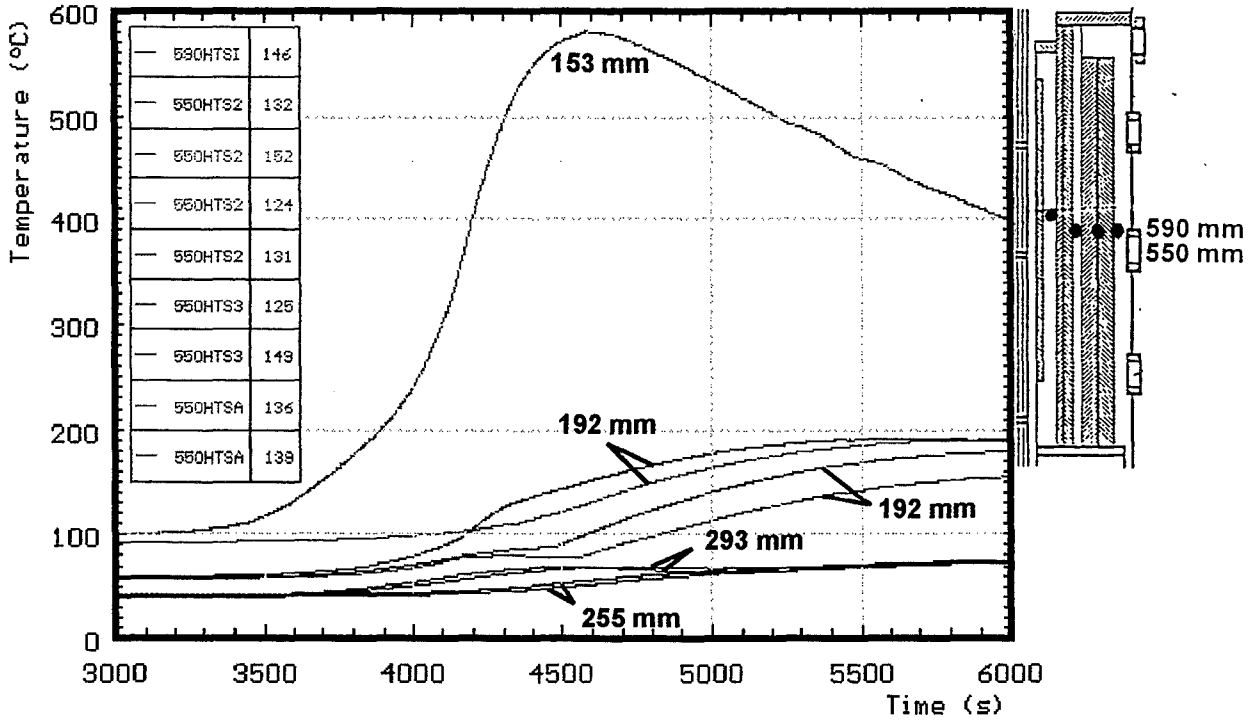

Fig. 62: CORA-7; Temperatures of HTS, Radial dependence at about 550 mm elevation

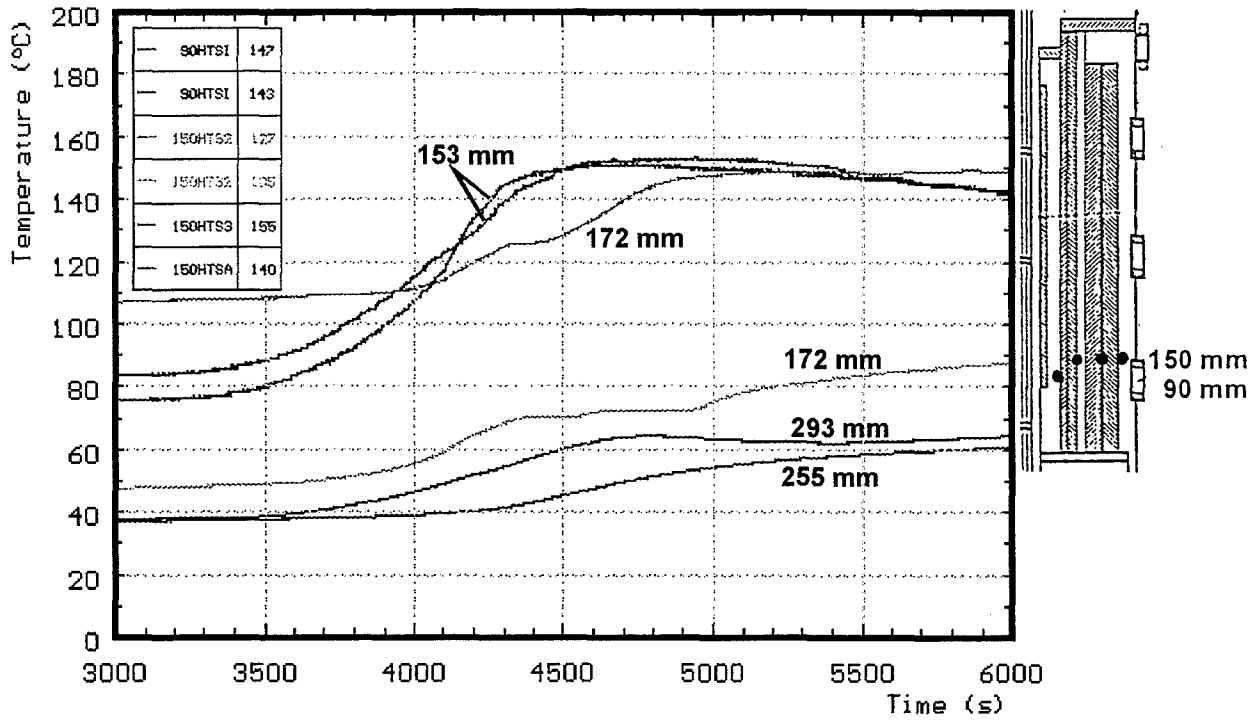

Fig. 63: CORA-7; Temperatures of HTS, Radial dependence at about 100 mm elevation

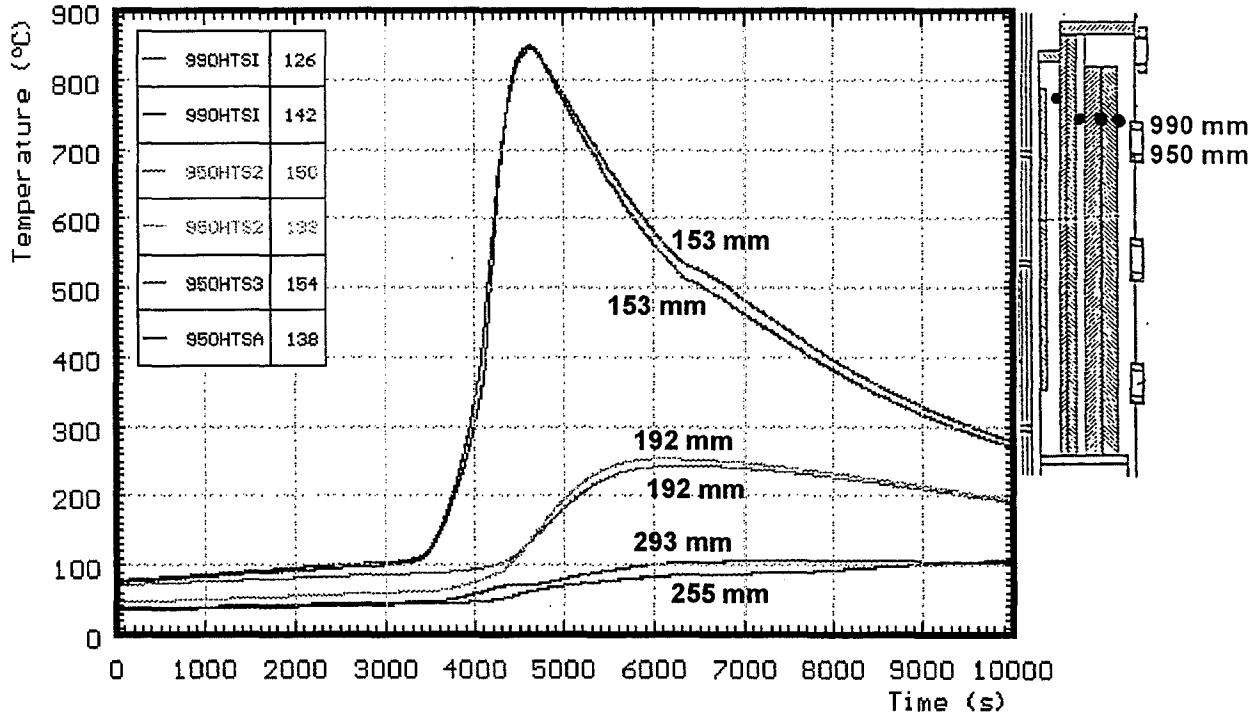

Fig. 64: CORA-7; Temperatures of HTS, Radial dependence at about 950 mm elevation, 0 - 10000s

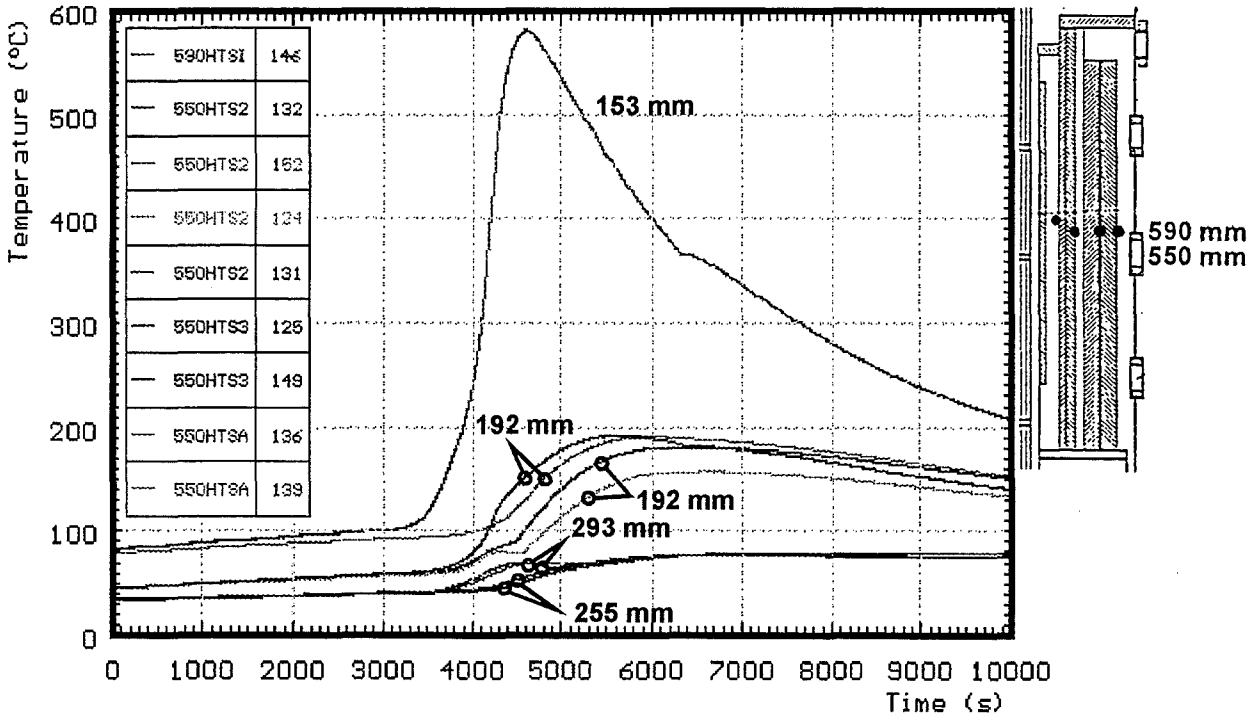

Fig. 65: CORA-7; Temperatures of HTS, Radial dependence at about 550 mm elevation, 0 - 10000 s

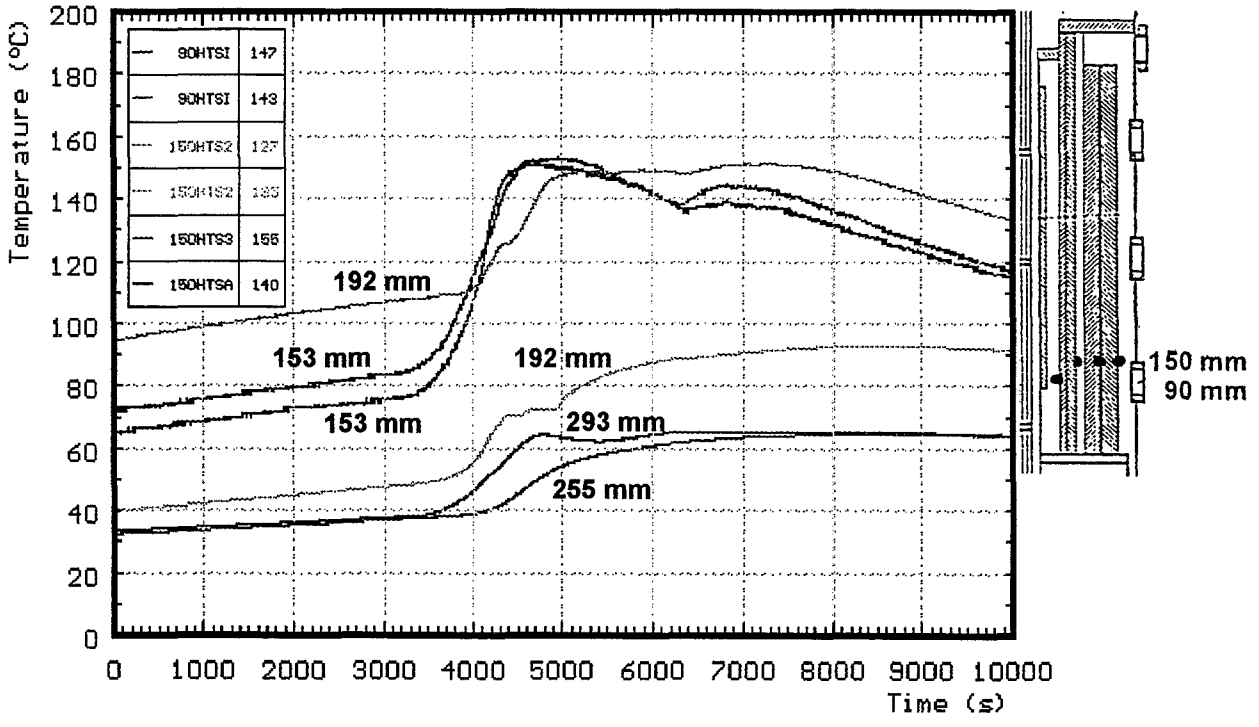

Fig. 66: CORA-7; Temperatures of HTS, Radial dependence at about 100 mm elevation, 0 - 10000s

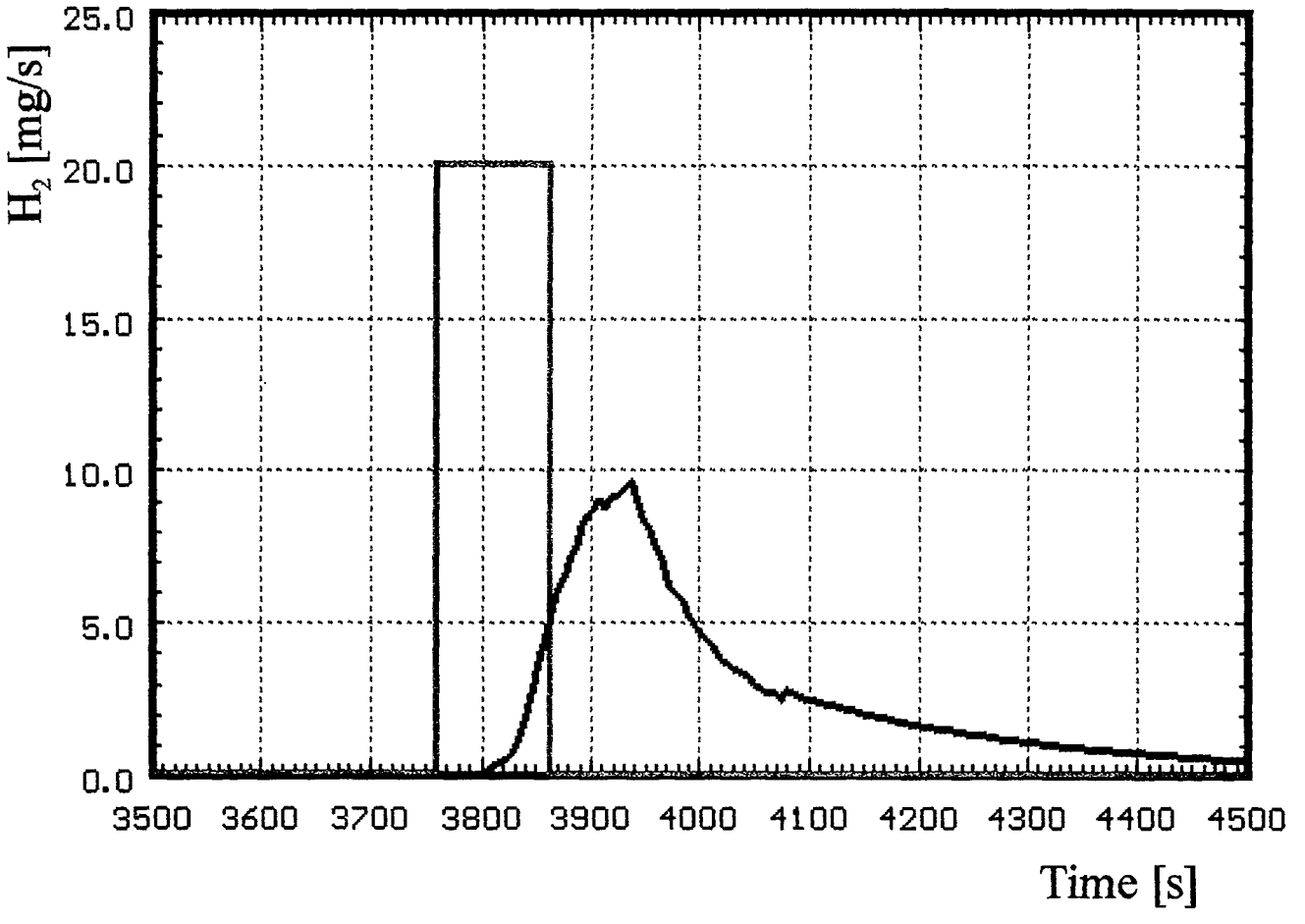

input X(t)

measured output Y(t)

K(t) transfer function

$$Y(t) = \int_{-\infty}^{+\infty} K(t-\tau)\, X(\tau)\, d\tau$$

Fig. 67a: Determination of the transfer function by measurement of the delta-function of the hydrogen input

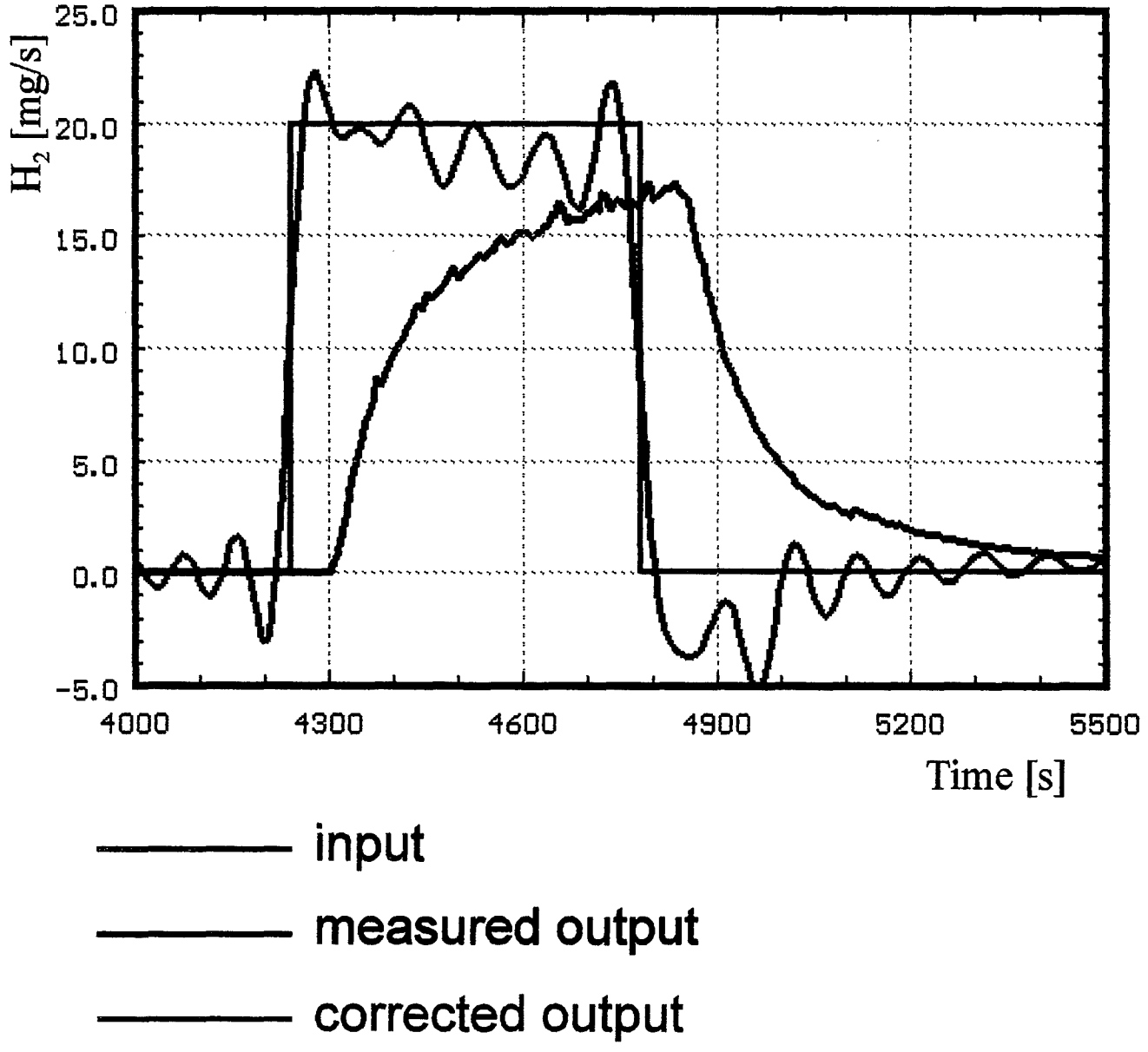

Fig. 67b: Comparison of corrected measured curve with the hydrogen input

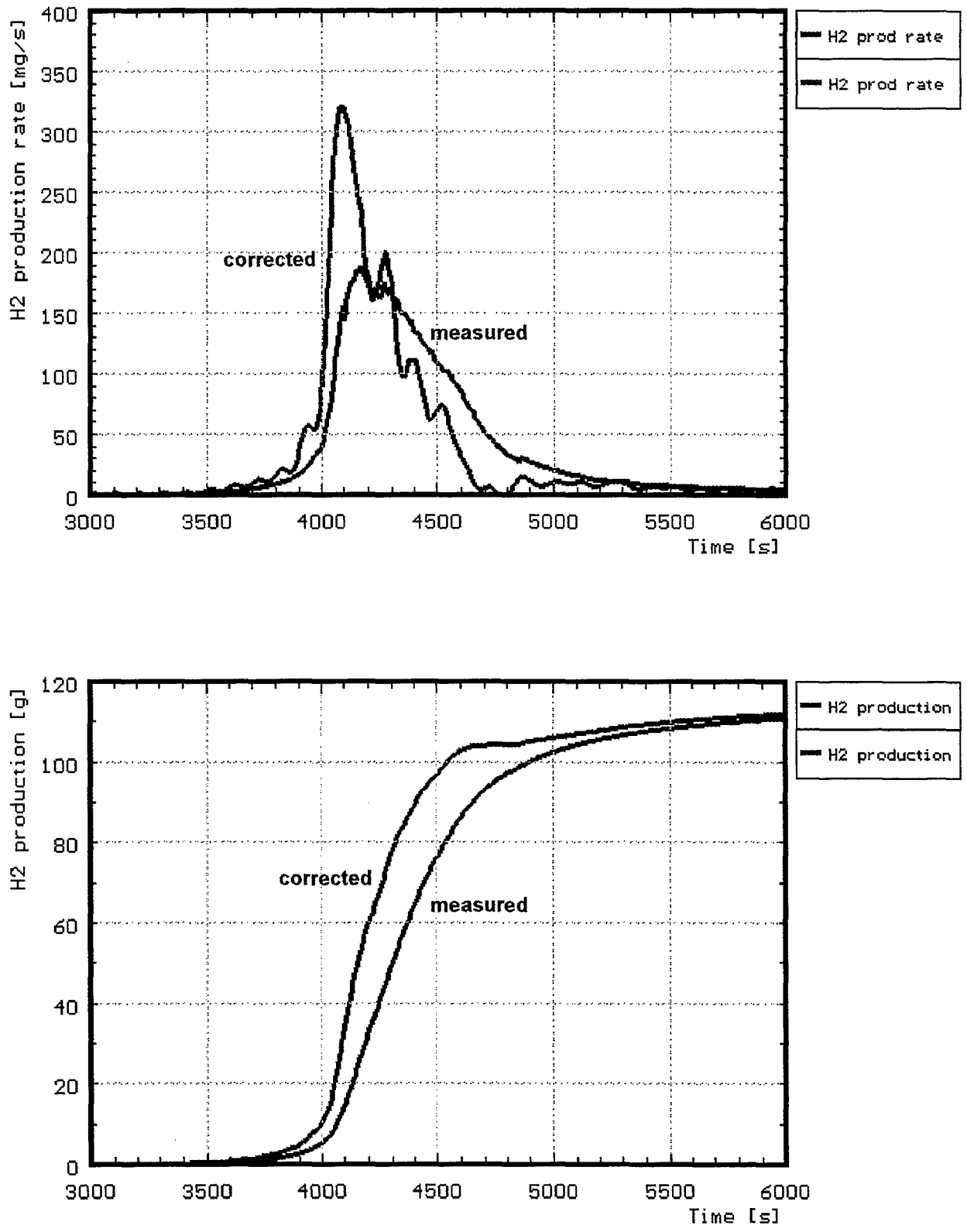

Fig. 67: Measured hydrogen production in test CORA-7; production rate (top) and integral values (bottom)

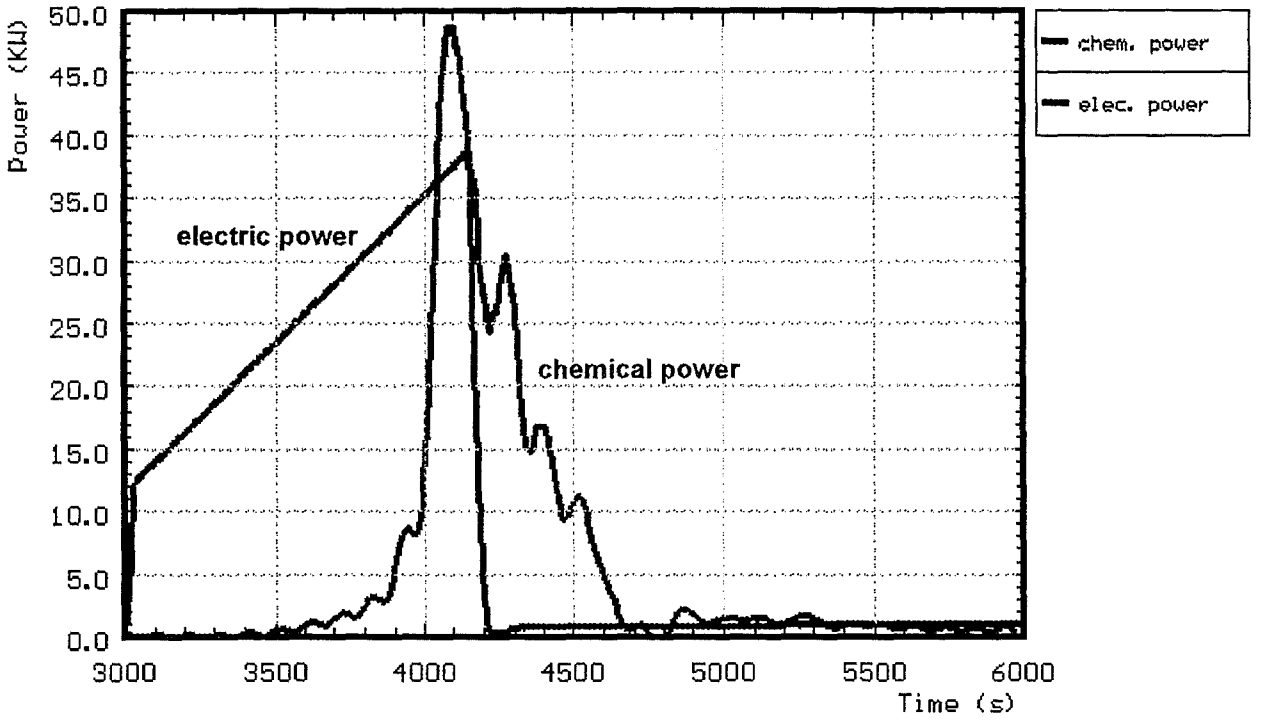

Fig. 68: CORA-7; Comparison of chemical and electric power

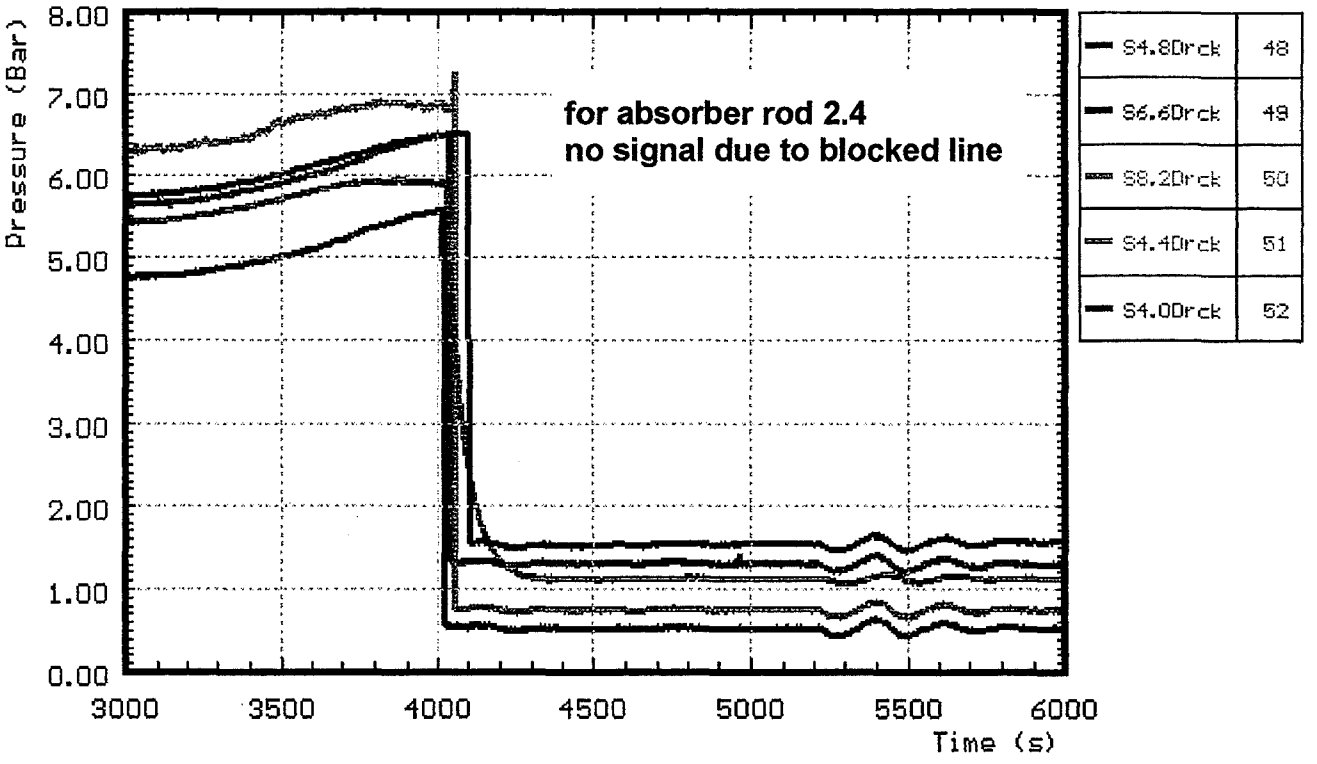

Fig. 70: CORA-7; Internal pressure of fuel rod simulator 4.4 and absorber rods

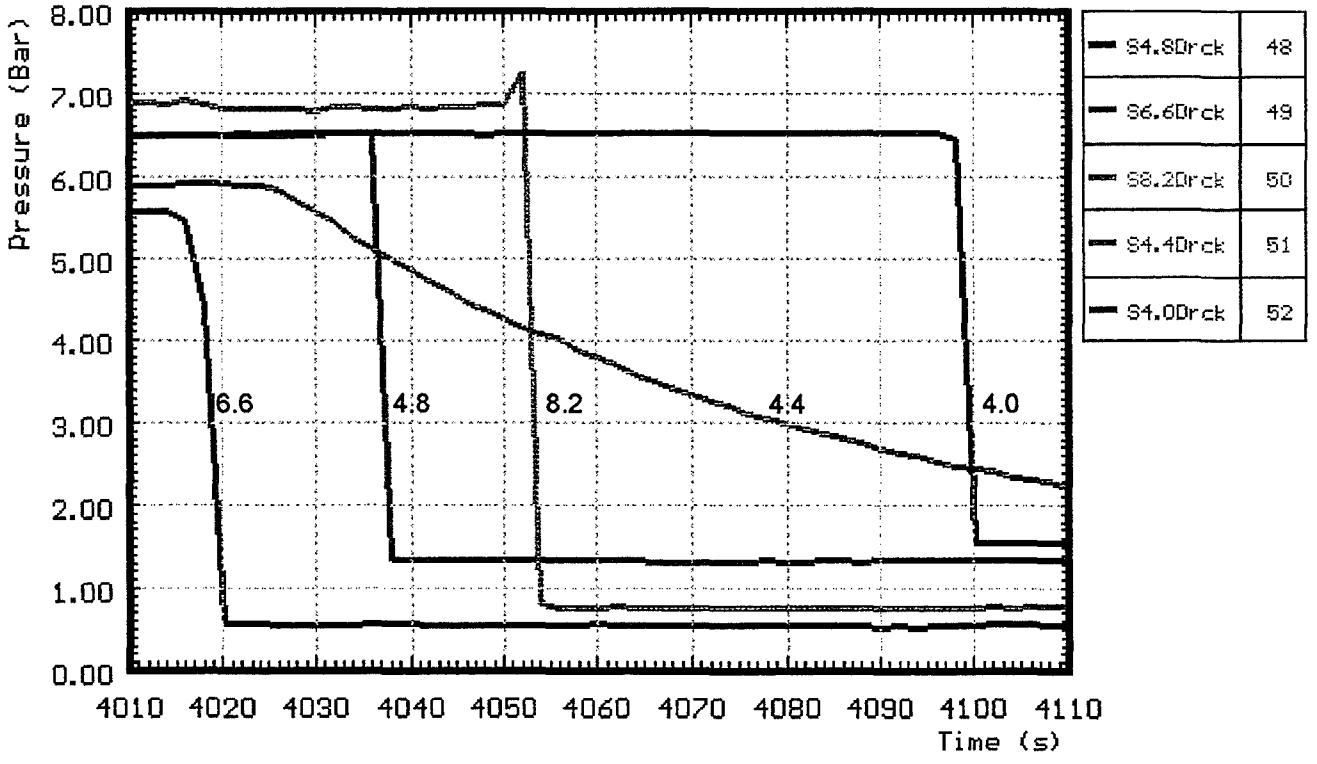

Fig. 71: CORA-7; Determination of failure time by pressure loss measurement

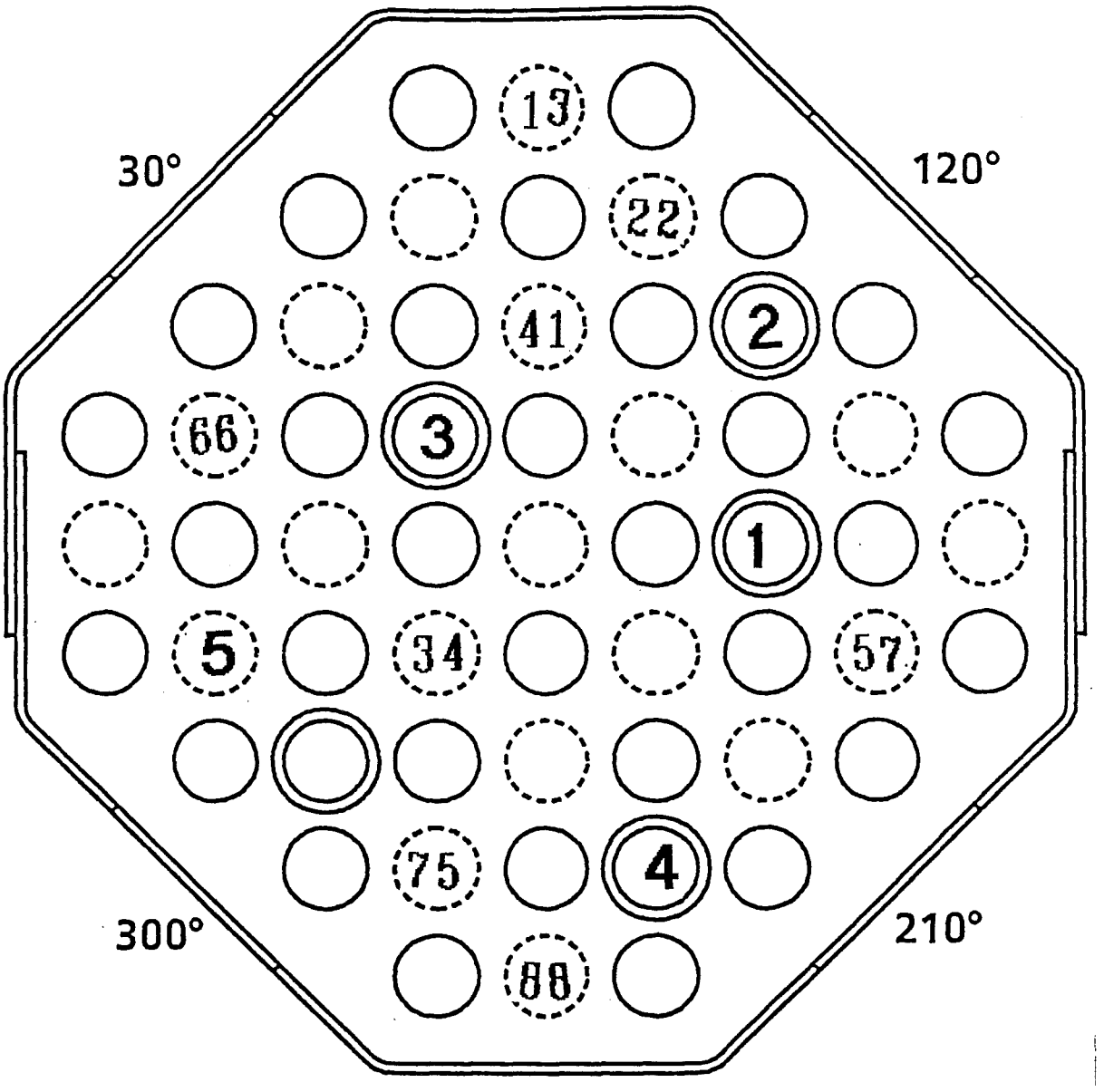

rod number	time of failure
6.6	4018
4.8	4036
2.4	4044
8.2	4053
4.0	4098

sequence of failure 1-2-3-4-5

sequence of temperatures at

1250 mm (first number; 730 - 670 °C)
50 mm (sec. number; 660 - 600 °C)

Fig. 72: CORA-7; Sequence of absorber rod failure compared to sequence of temperature at 1250 mm and 50 mm elevation.

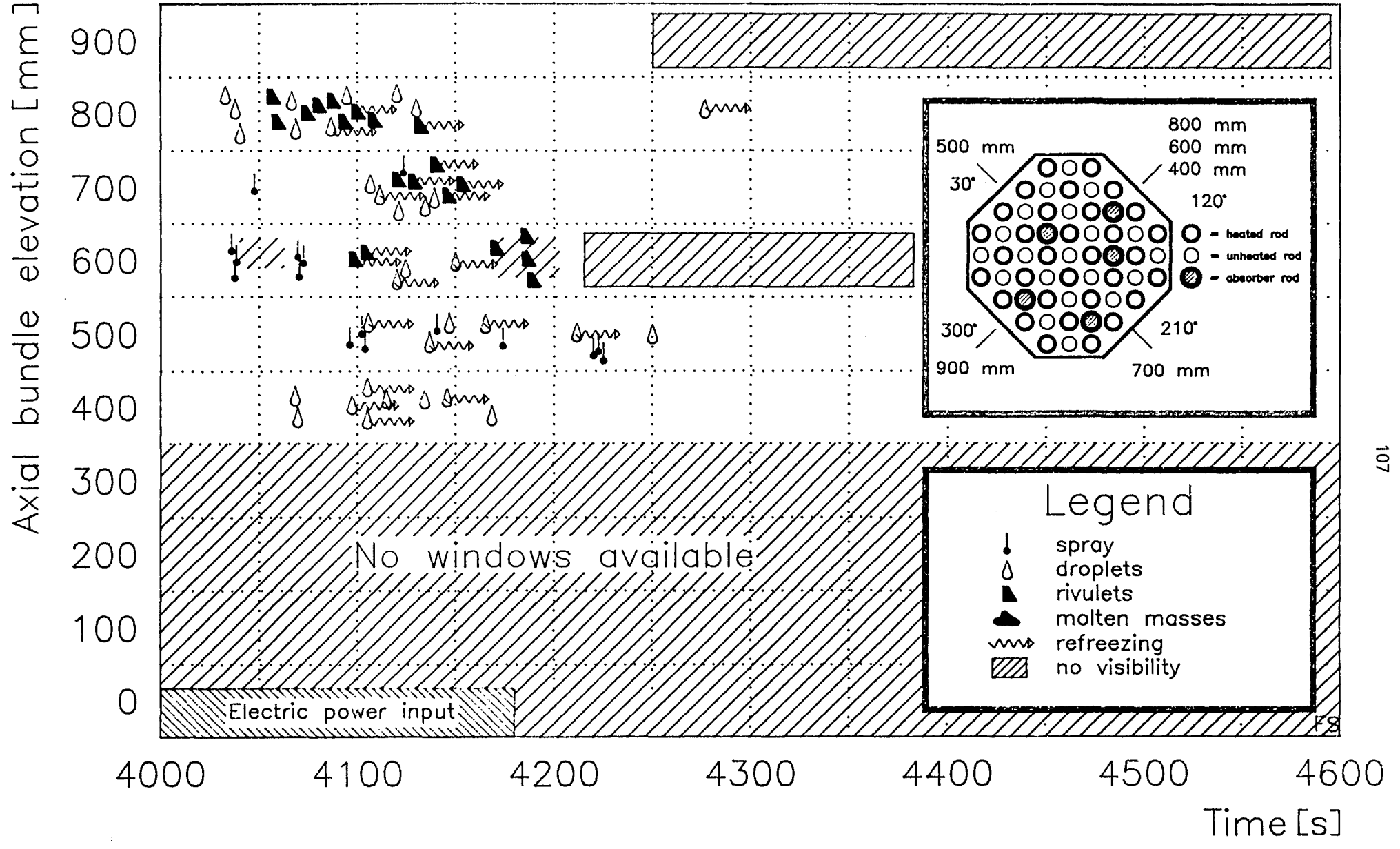

107

Fig. 73: Melt movement as seen by the video system

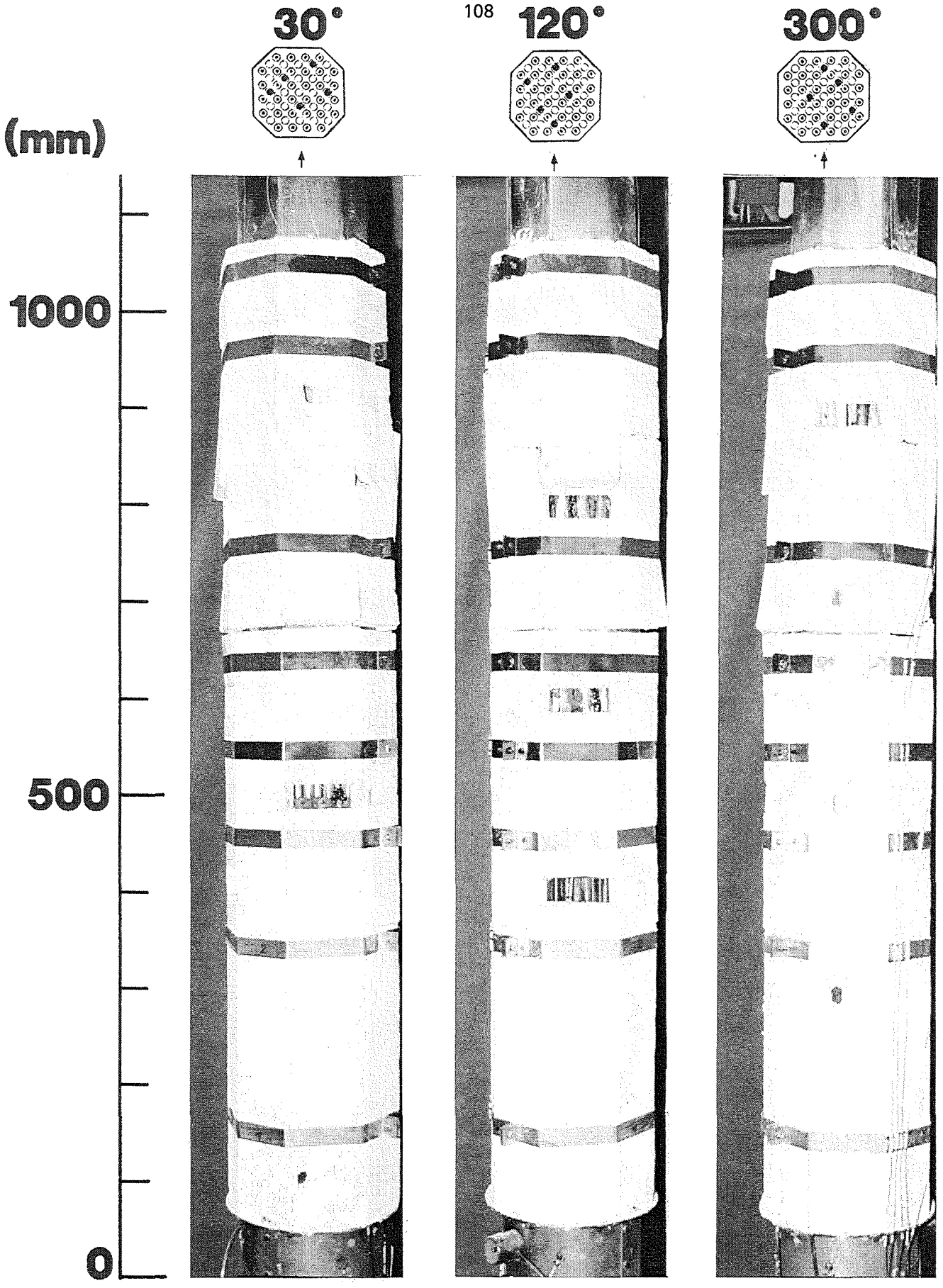

Fig. 82: CORA-7; Posttest appearance of bundle, shroud and shroud insulation; 30°, 120°, 300° orientation

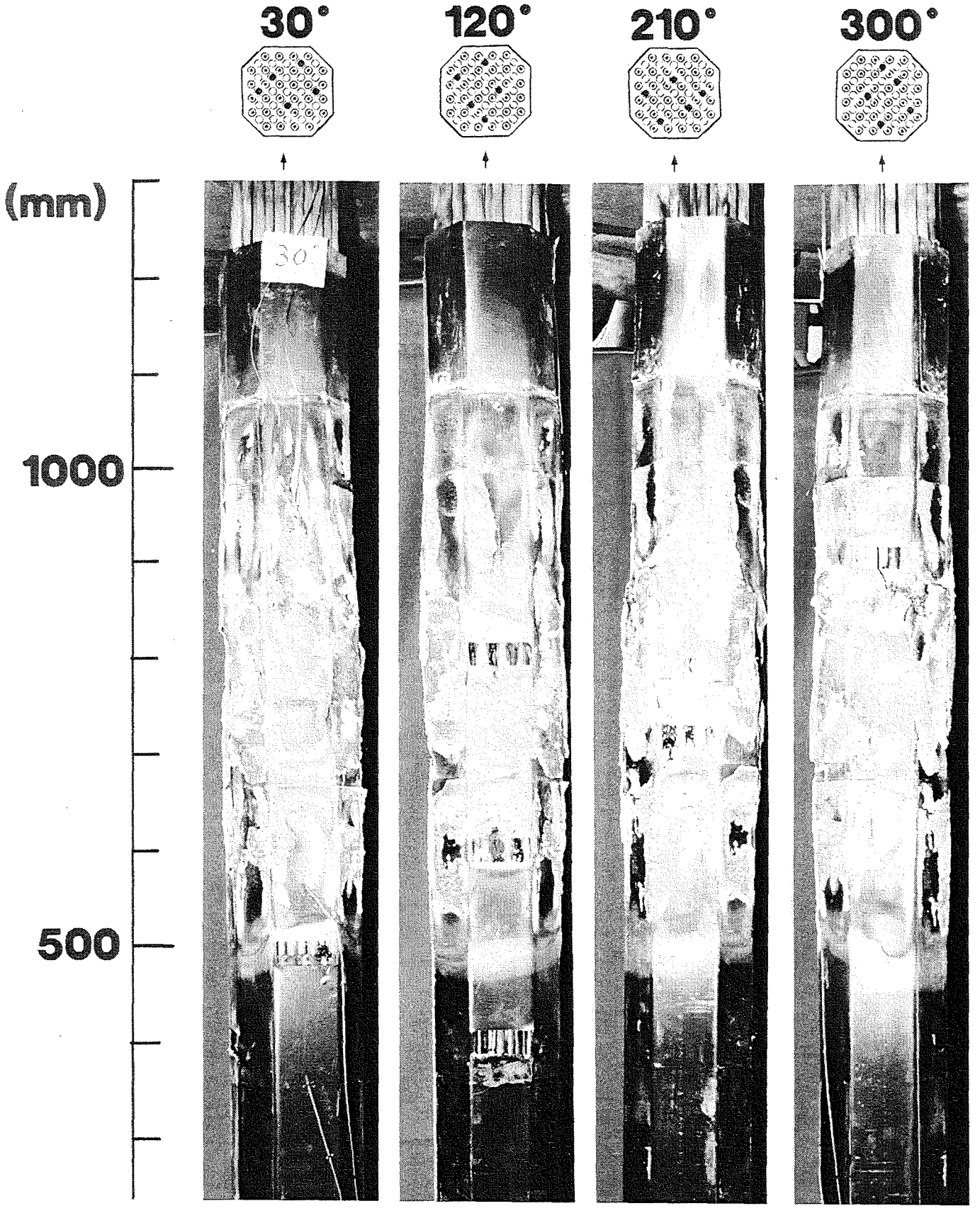

Fig. 83: Posttest view of bundle CORA-7 after removal of shroud insulation; 30°, 120°, 210°, 300° orientation

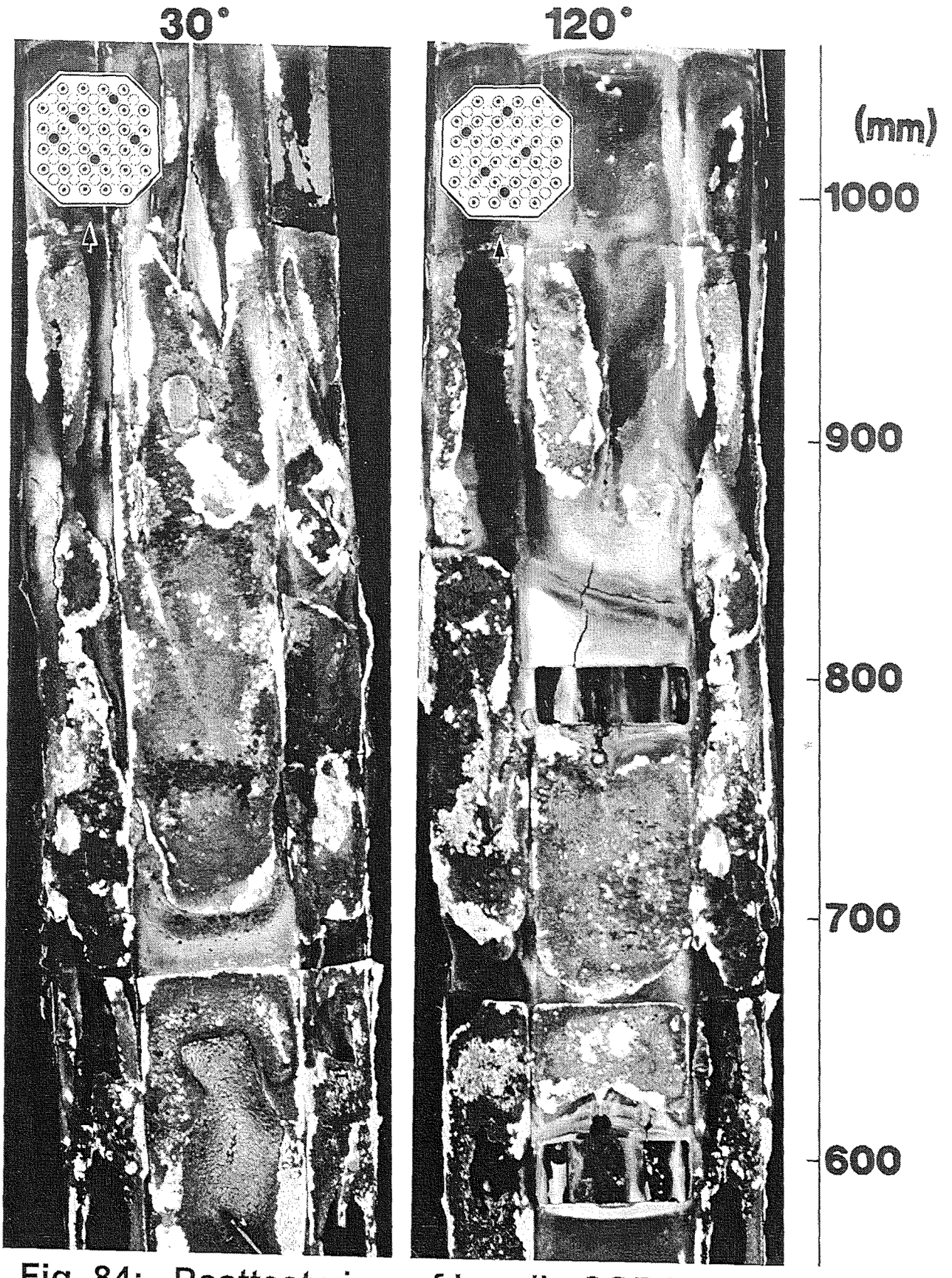

Fig. 84: Posttest view of bundle CORA-7 after removal of shroud insulation; partial view 30° and 120° orientation, 500 - 1000 mm elevation

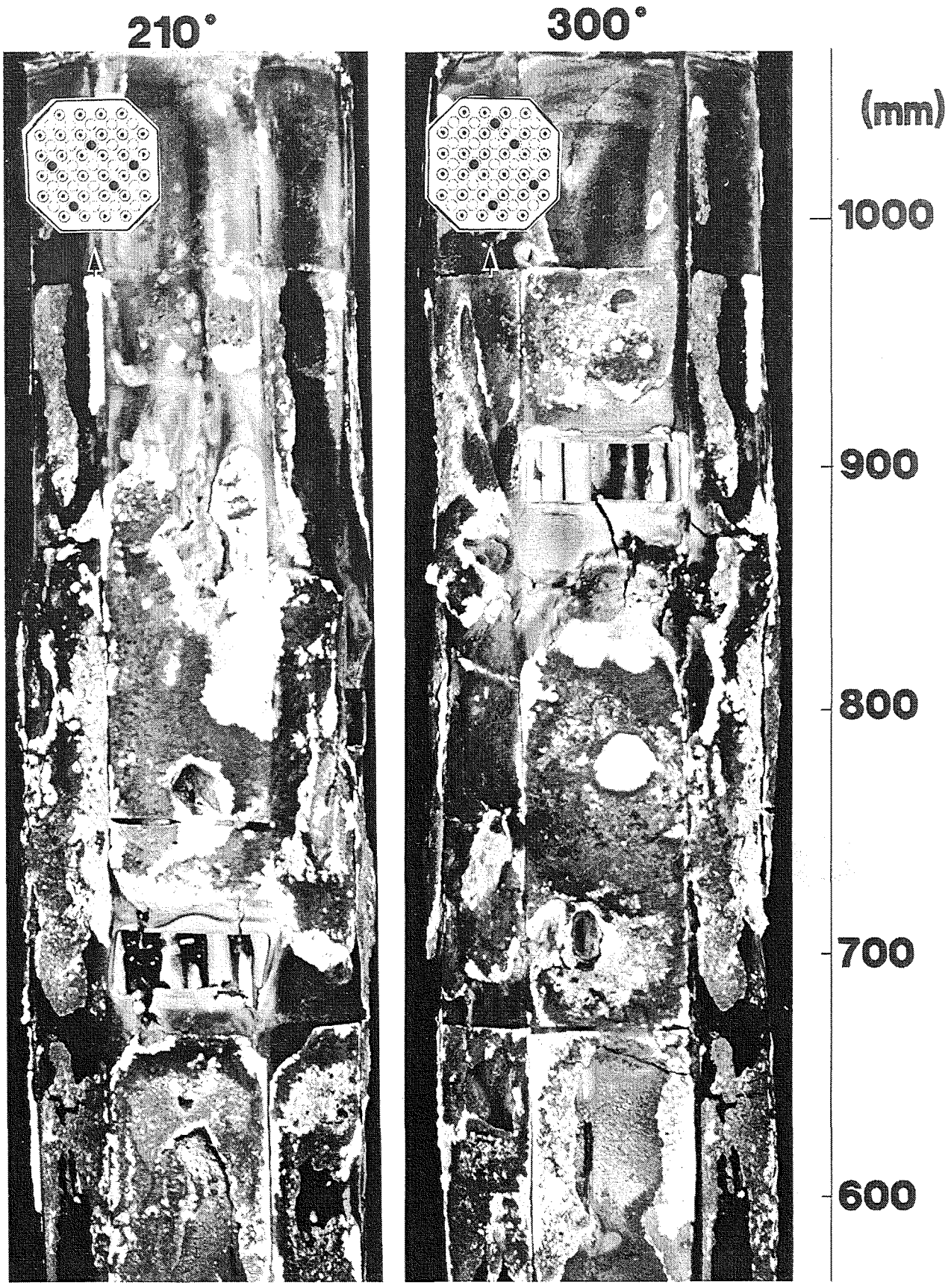

Fig. 85: Posttest view of bundle CORA-7 after removal of shroud insulation; partial view 210° and 300° orientation, 500 - 1000 mm elevation

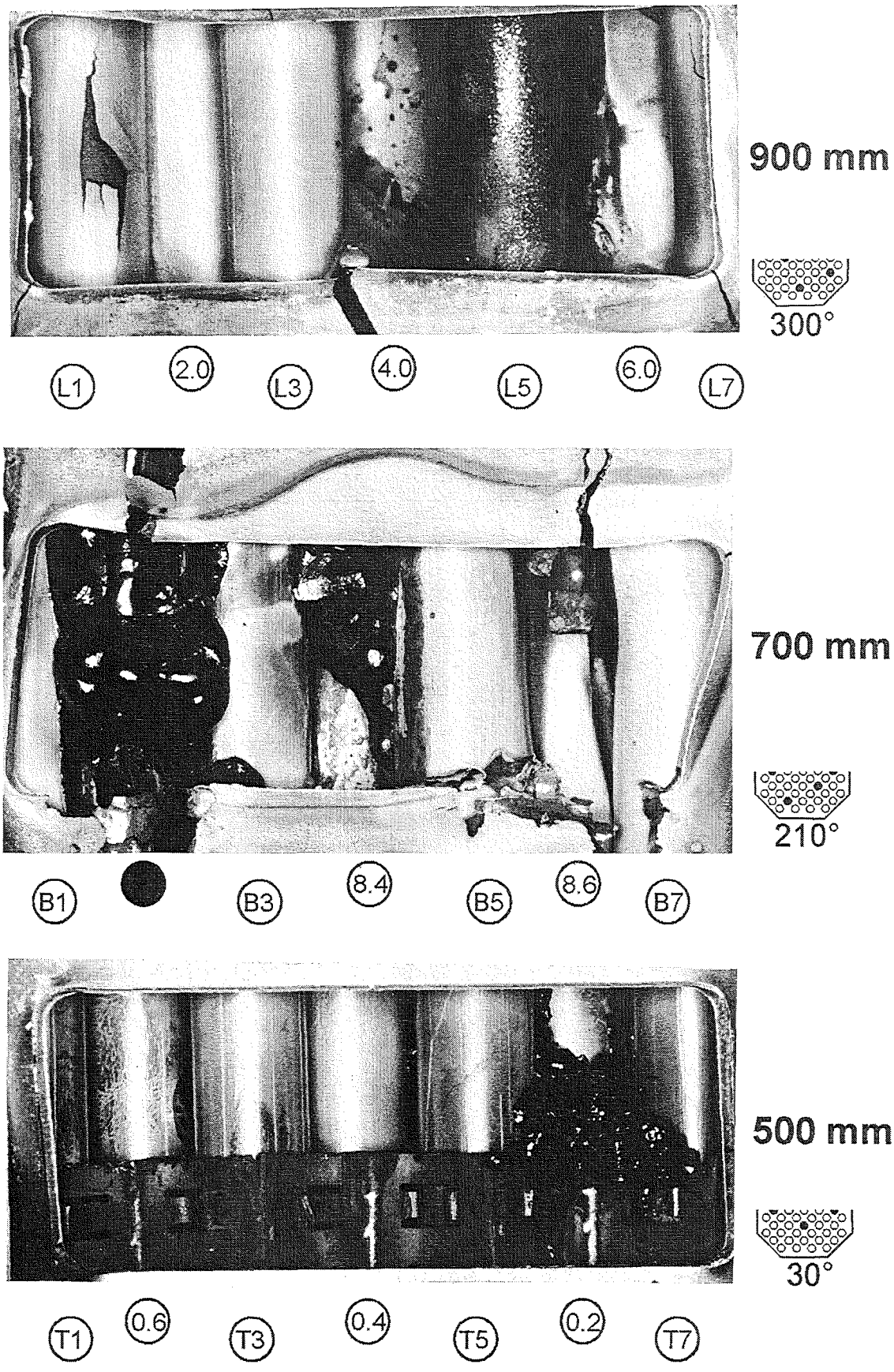

Fig. 86: CORA-7; Posttest view; windows at 900 mm 300° orientation, 700 mm 210° orientation and 500 mm 30° orientation

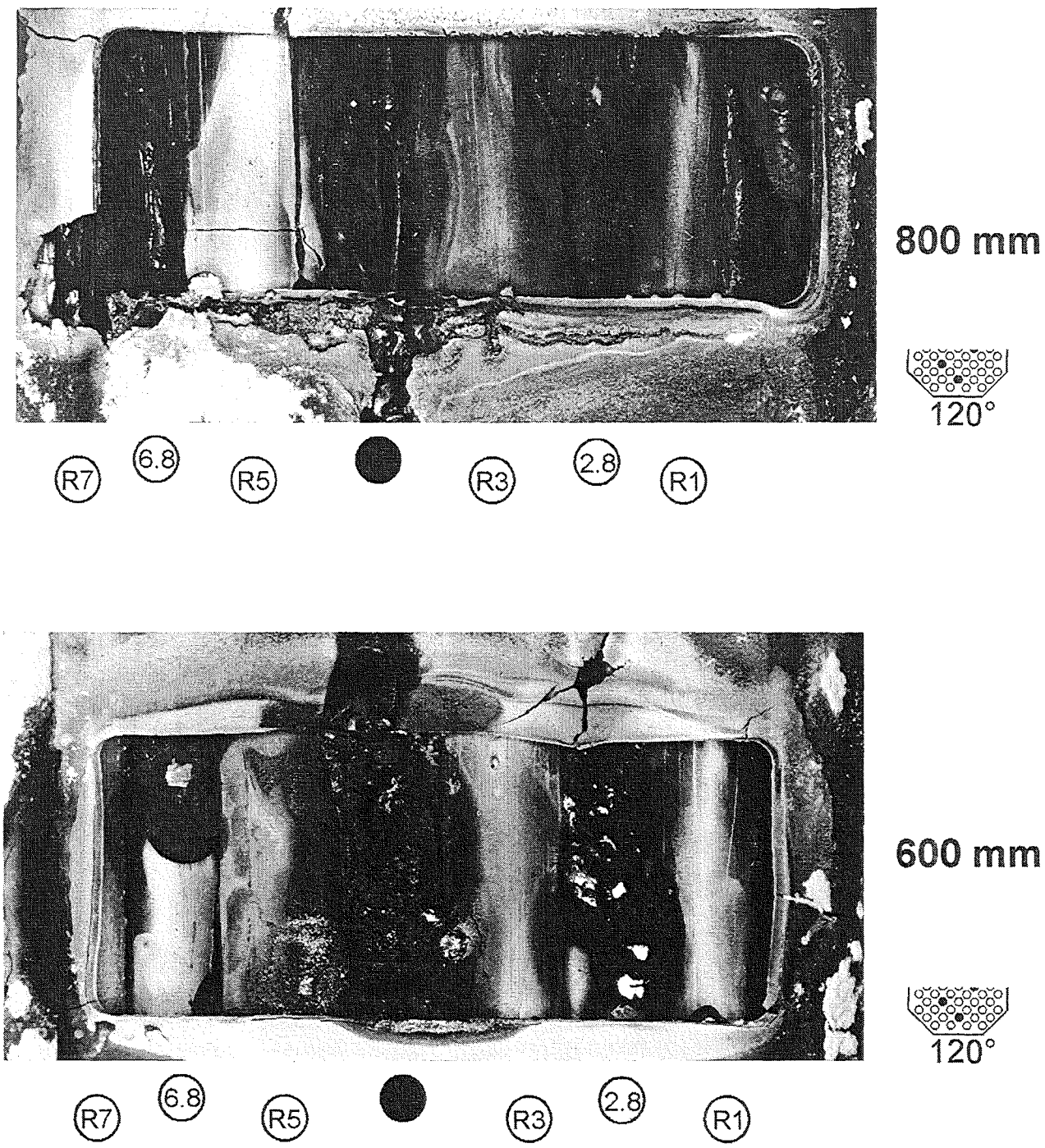

Fig. 87: CORA-7; Posttest view; 120° orientation; windows at 800 mm and 600 mm elevation

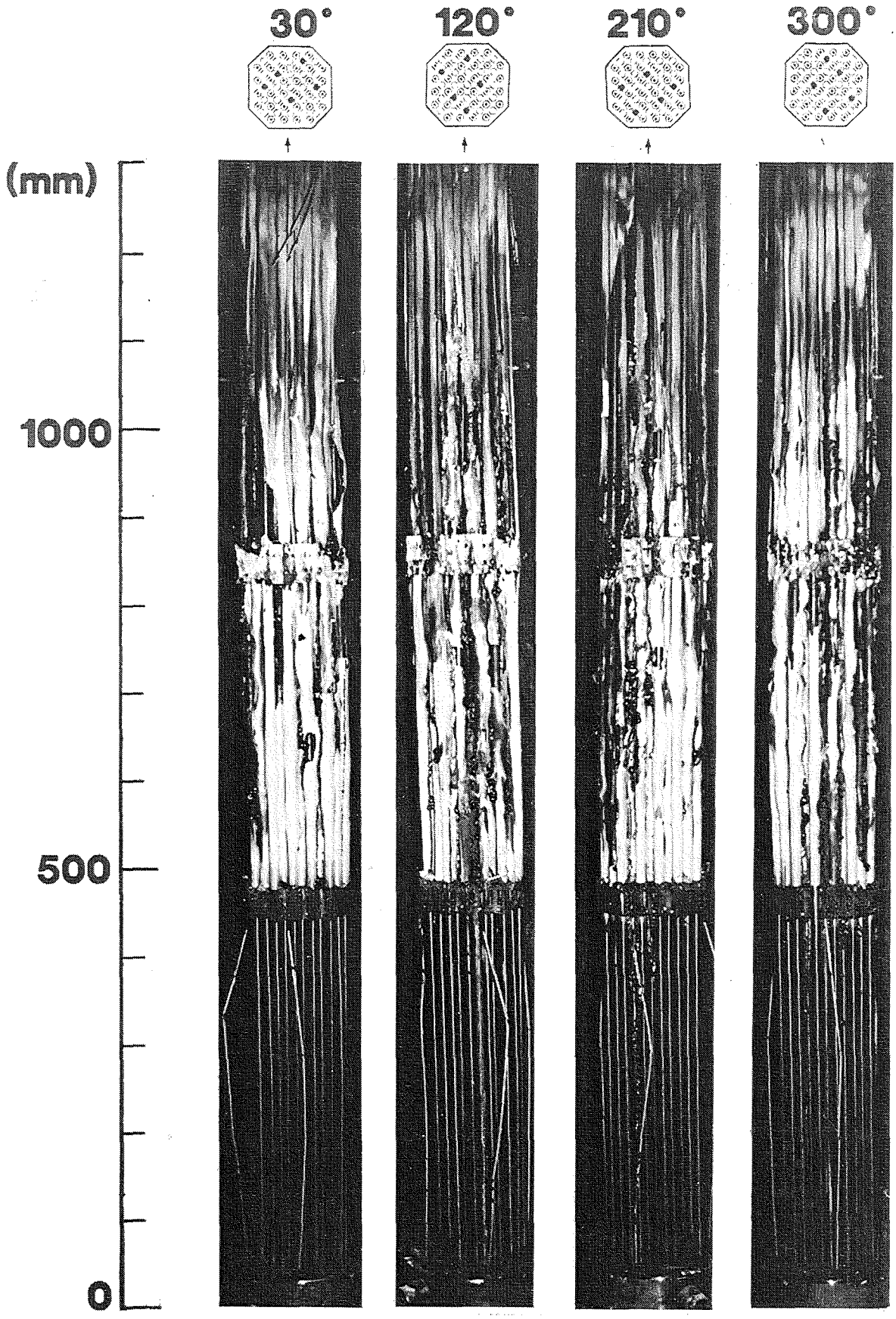

Fig. 88: Posttest view of bundle CORA-7 after removal of shroud;
30°, 120°, 210°, 300° orientation

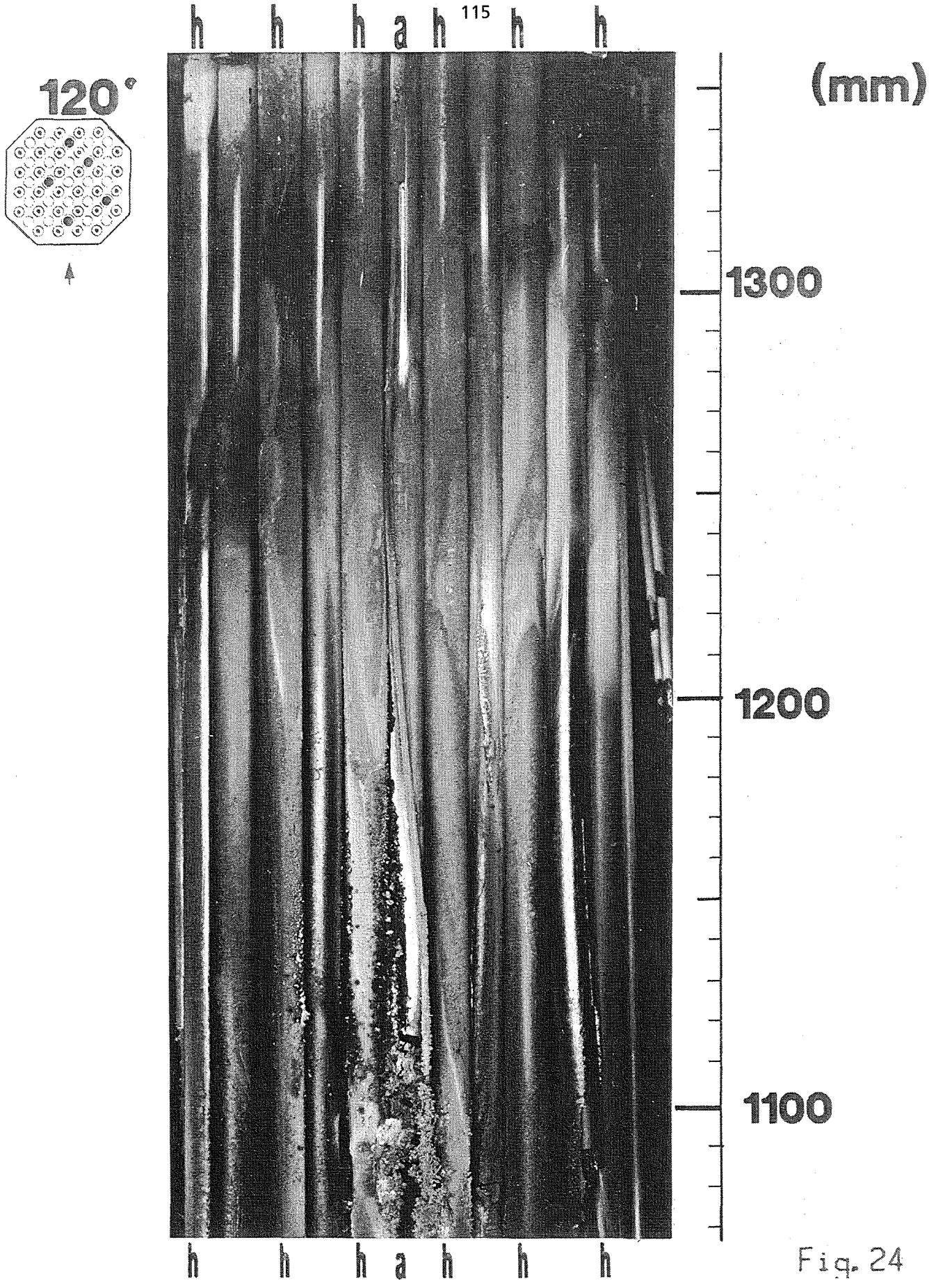

Fig. 89: Post test view of bundle, 120° partial view, 1050-1350 mm

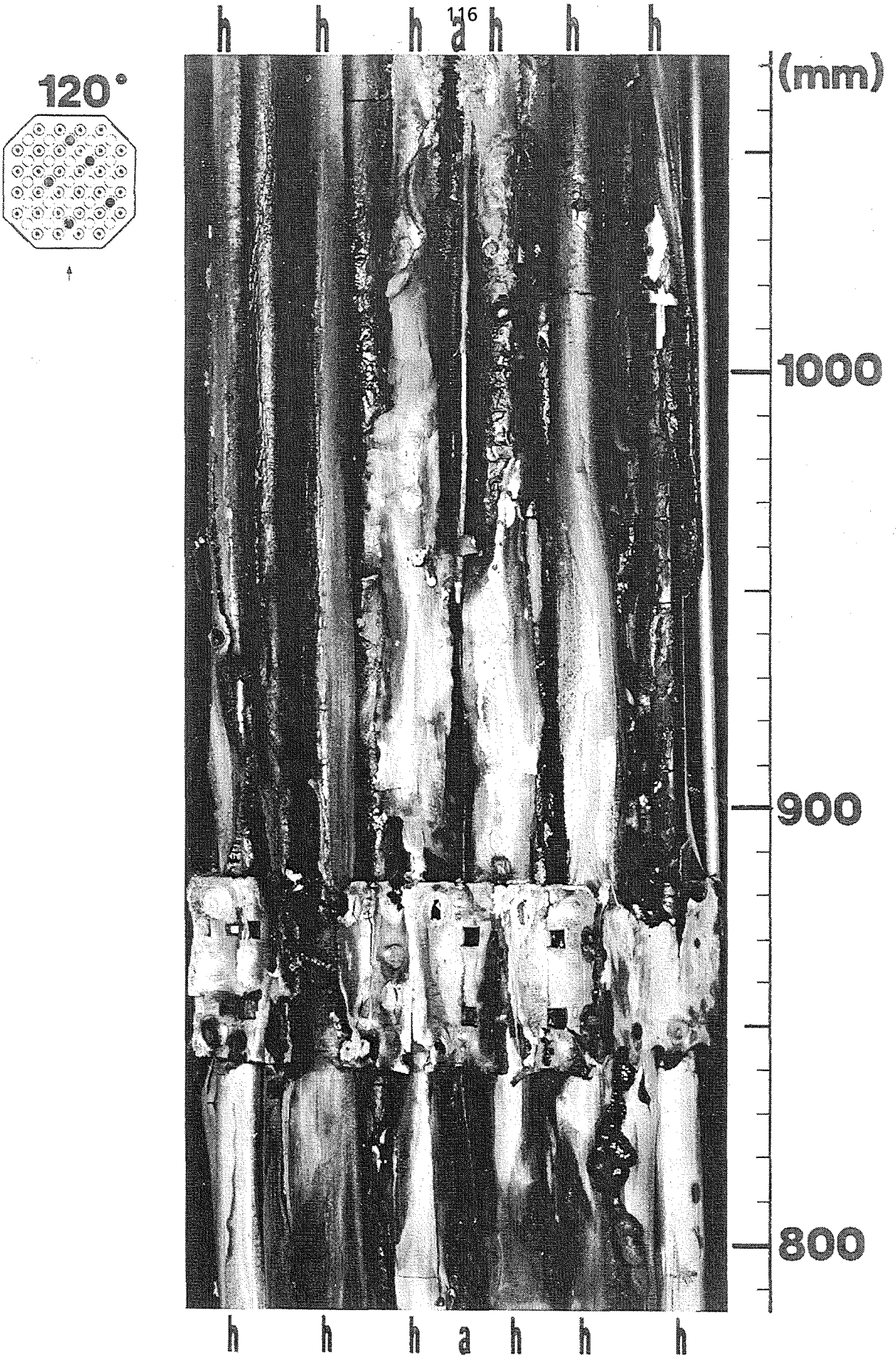

Fig. 90: Post test view of bundle, 120° partial view, 800-1050 mm

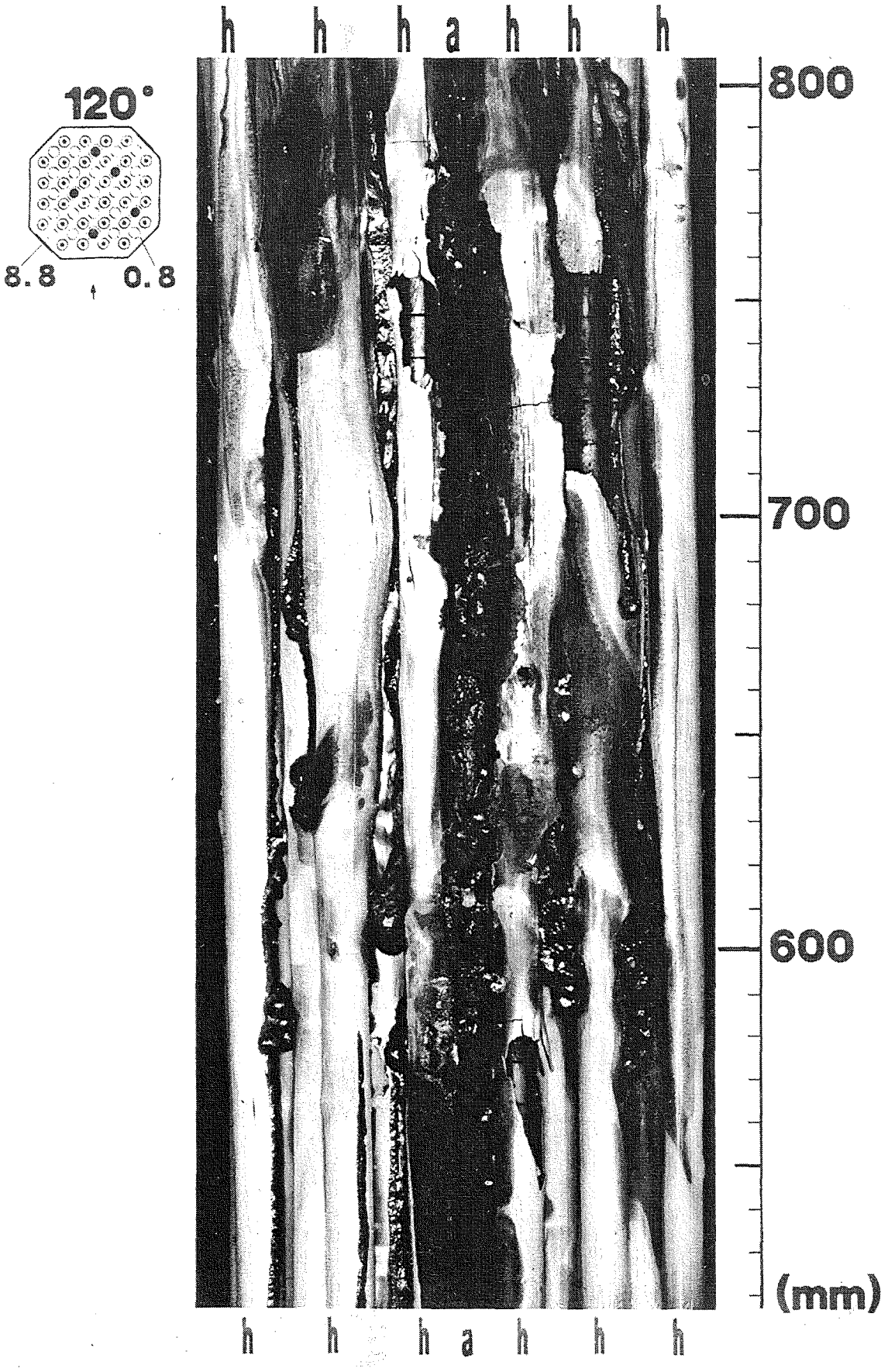

Fig. 91: Post test view of bundle, 120° partial view, 550 - 800 mm

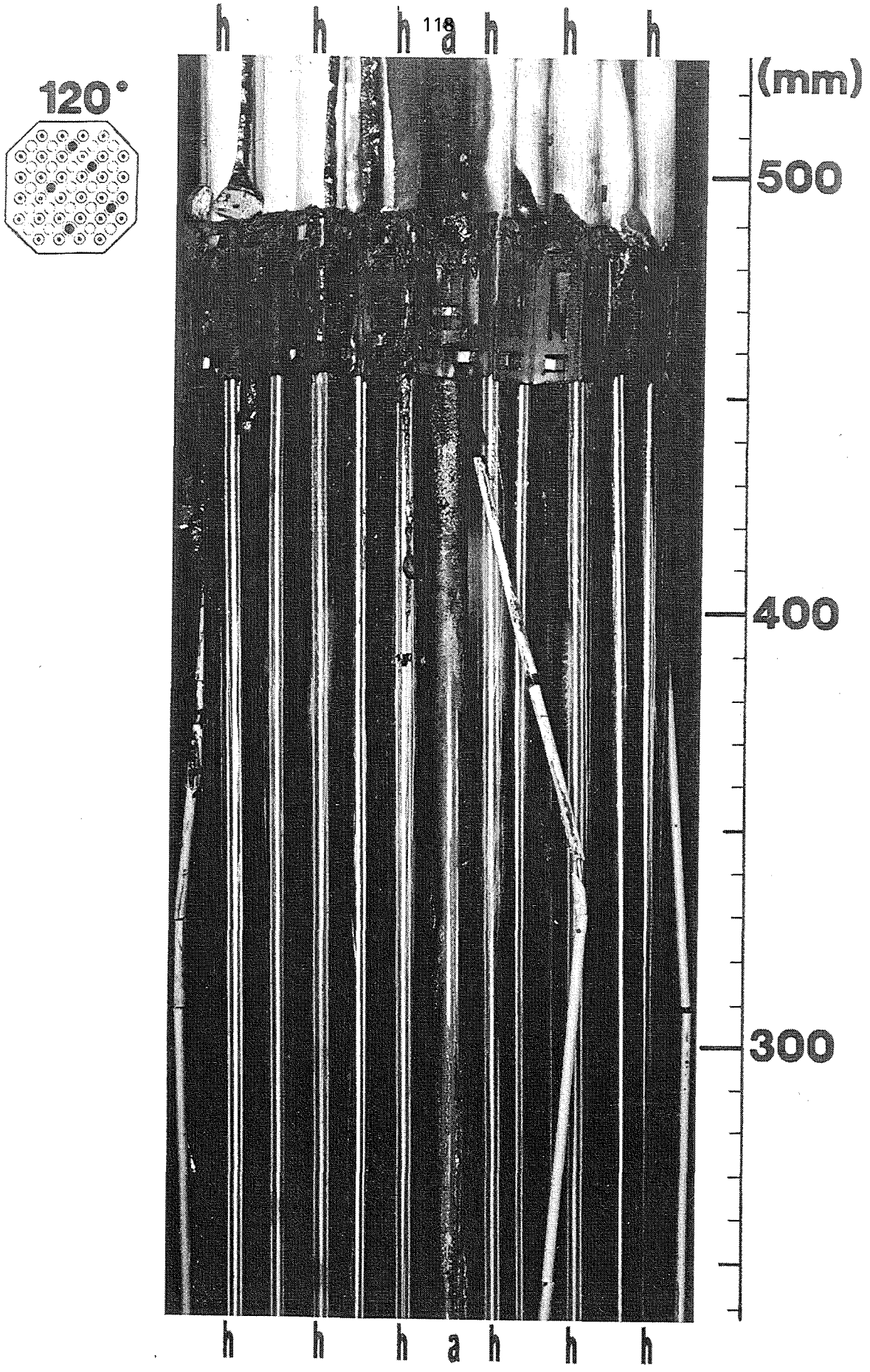

Fig. 92: Post test view of bundle, 120° partial view, 250-500 mm

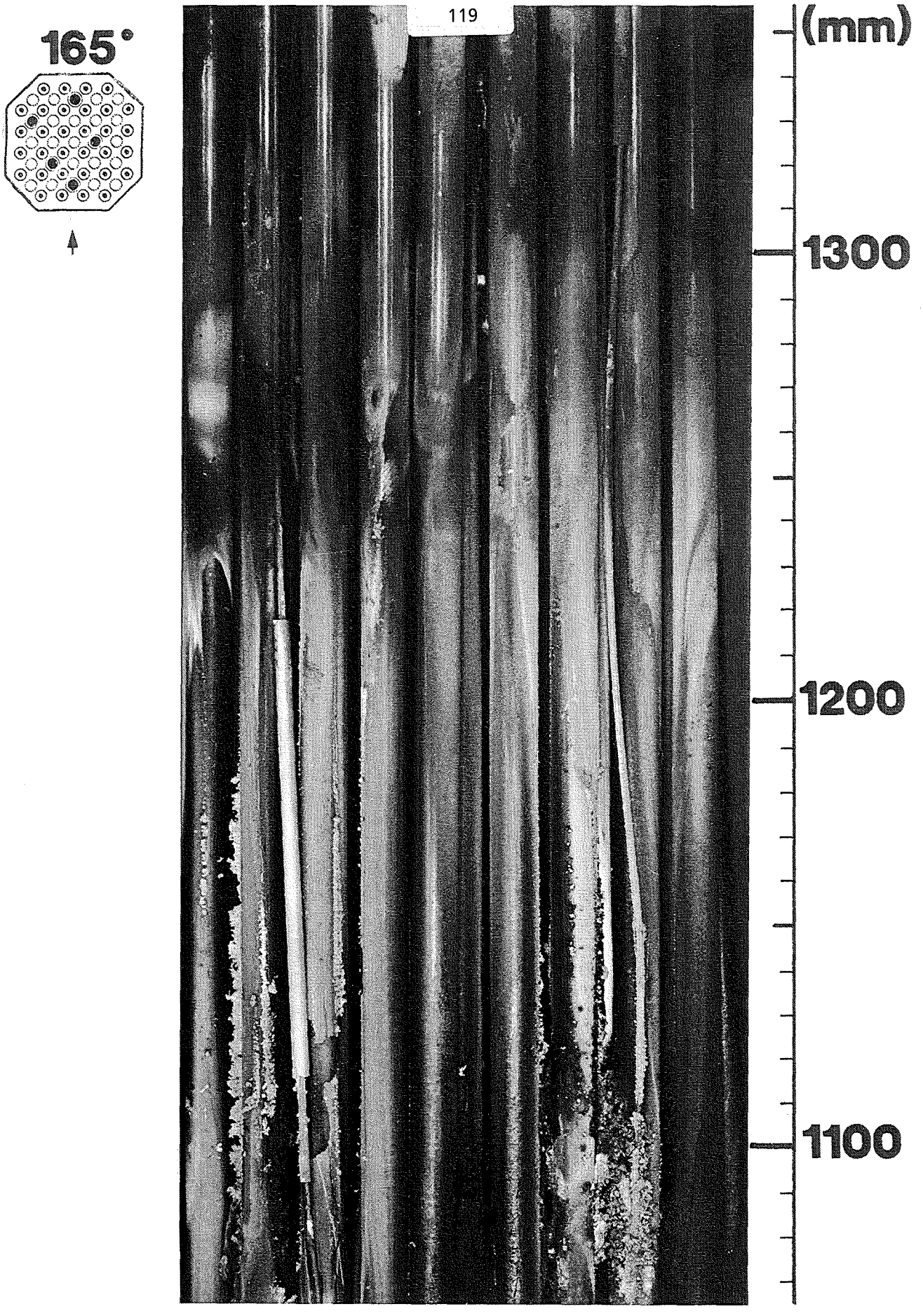

Fig. 93: Post test view of bundle, 165° partial view, 1050-1350 mm

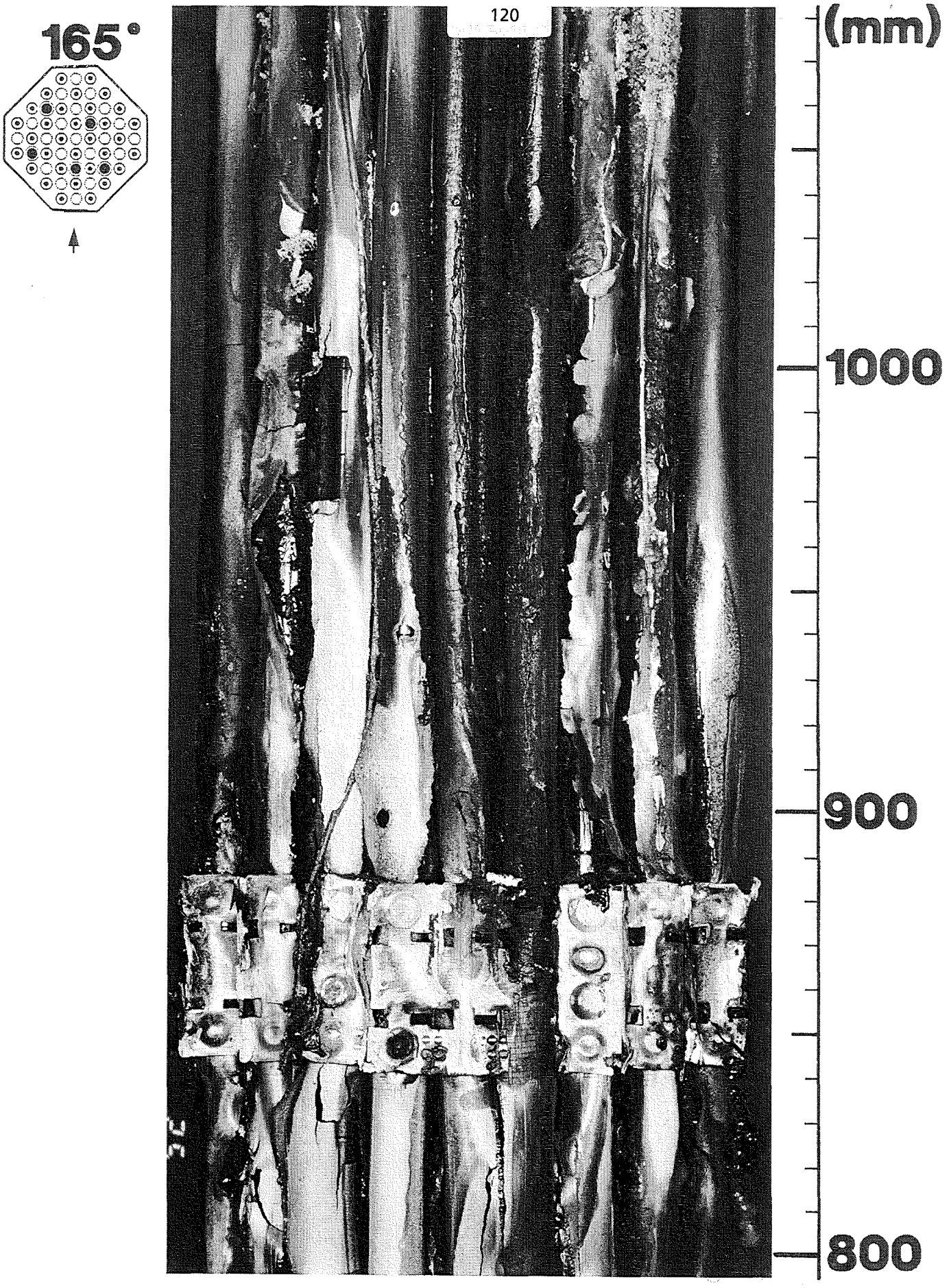

Fig. 94: Post test view of bundle, 165° partial view, 800-1050 mm

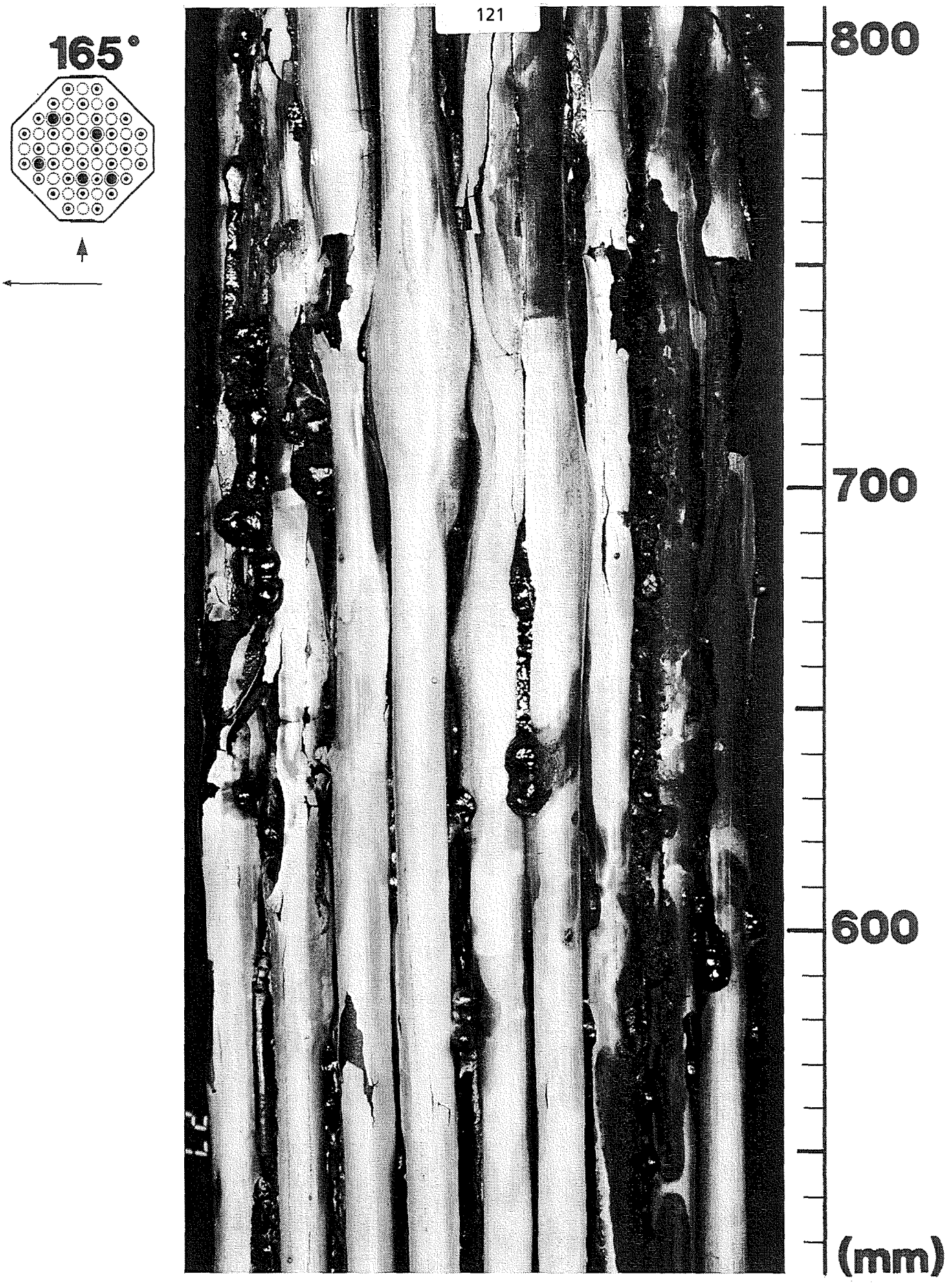

Fig. 95: Post test view of bundle, 165° partial view, 550-800 mm

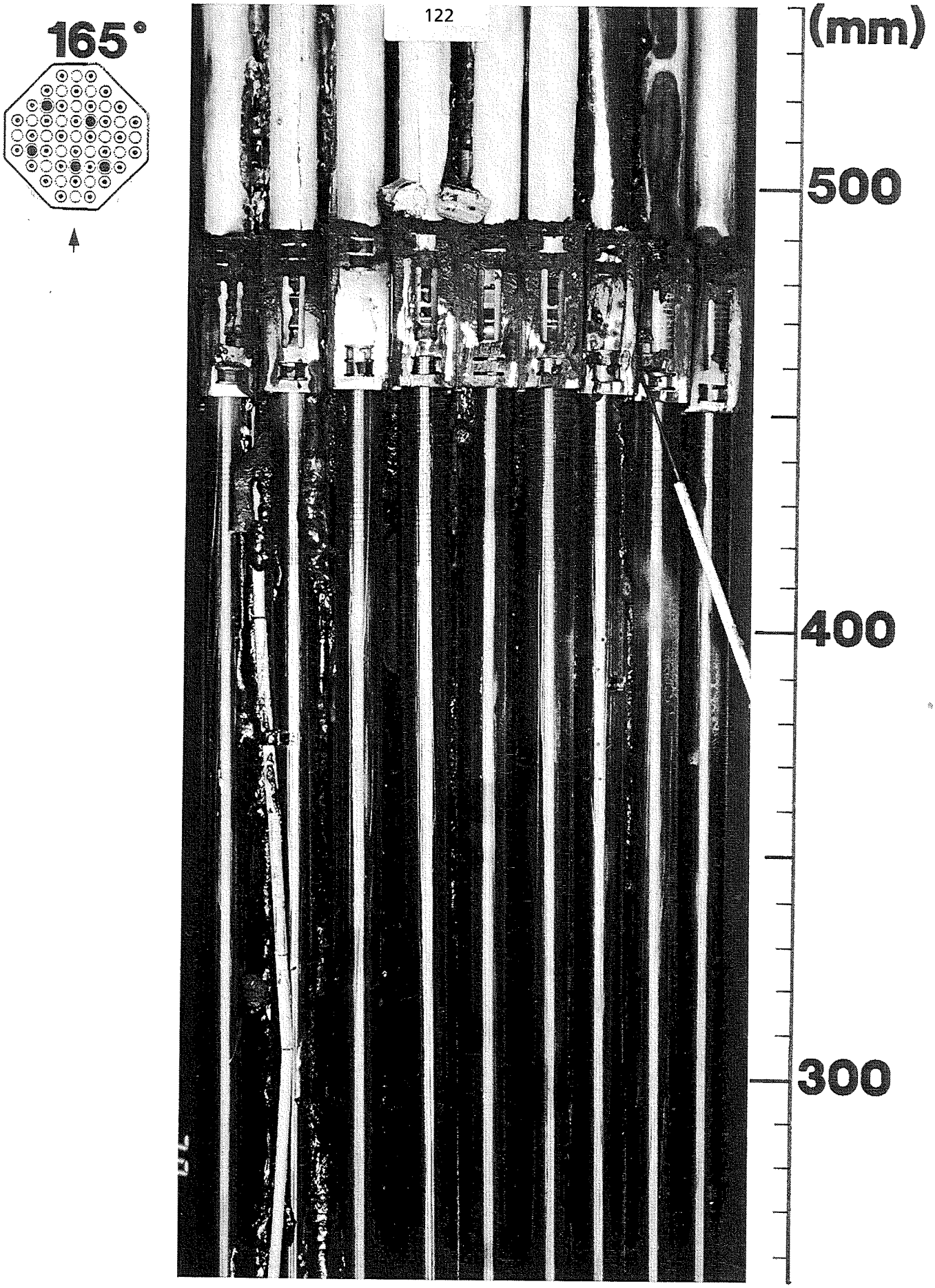

Fig. 96: Post test view of bundle, 165° partial view, 250-500 mm

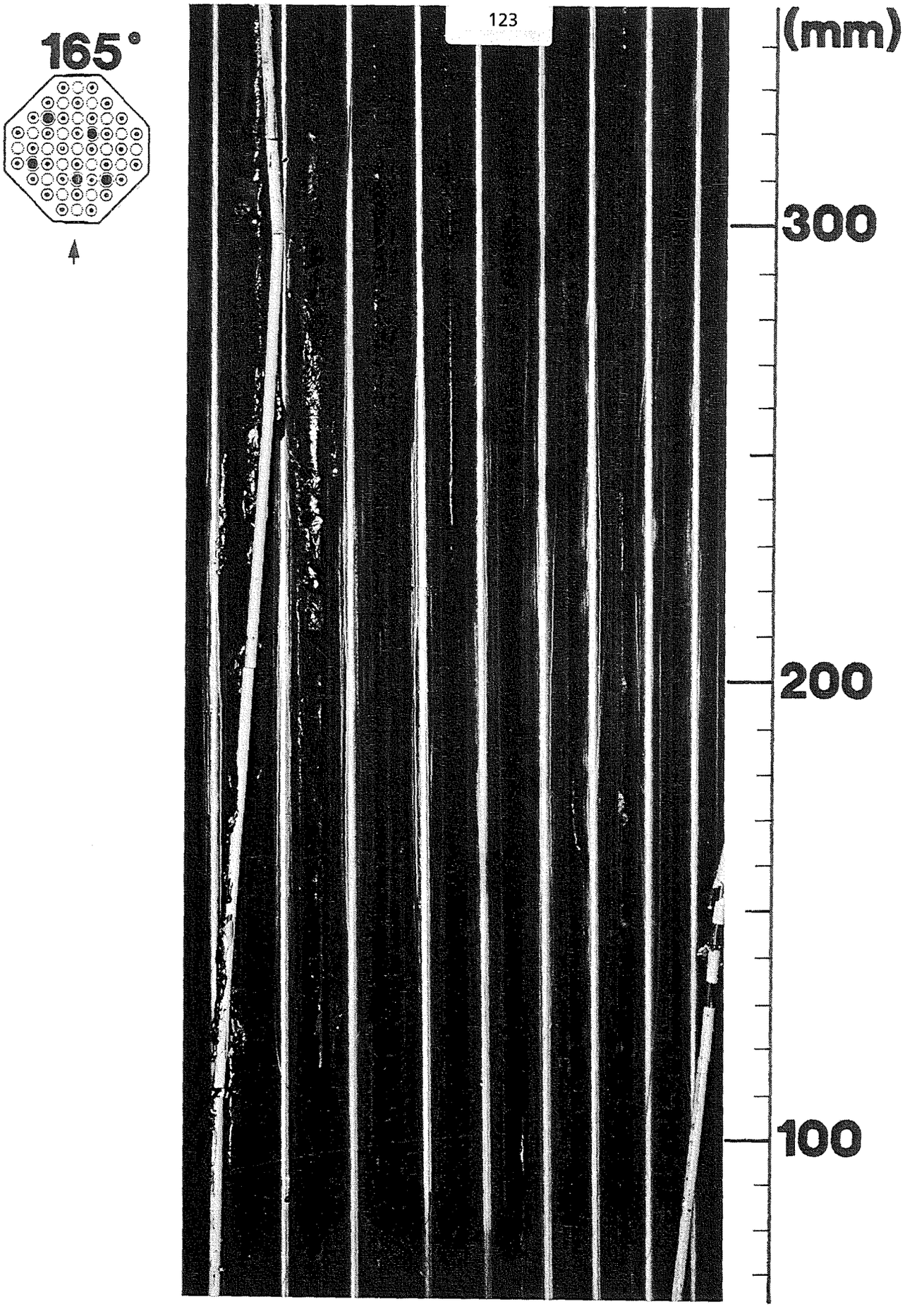

Fig. 97: Post test view of bundle, 165° partial view, 100-350 mm

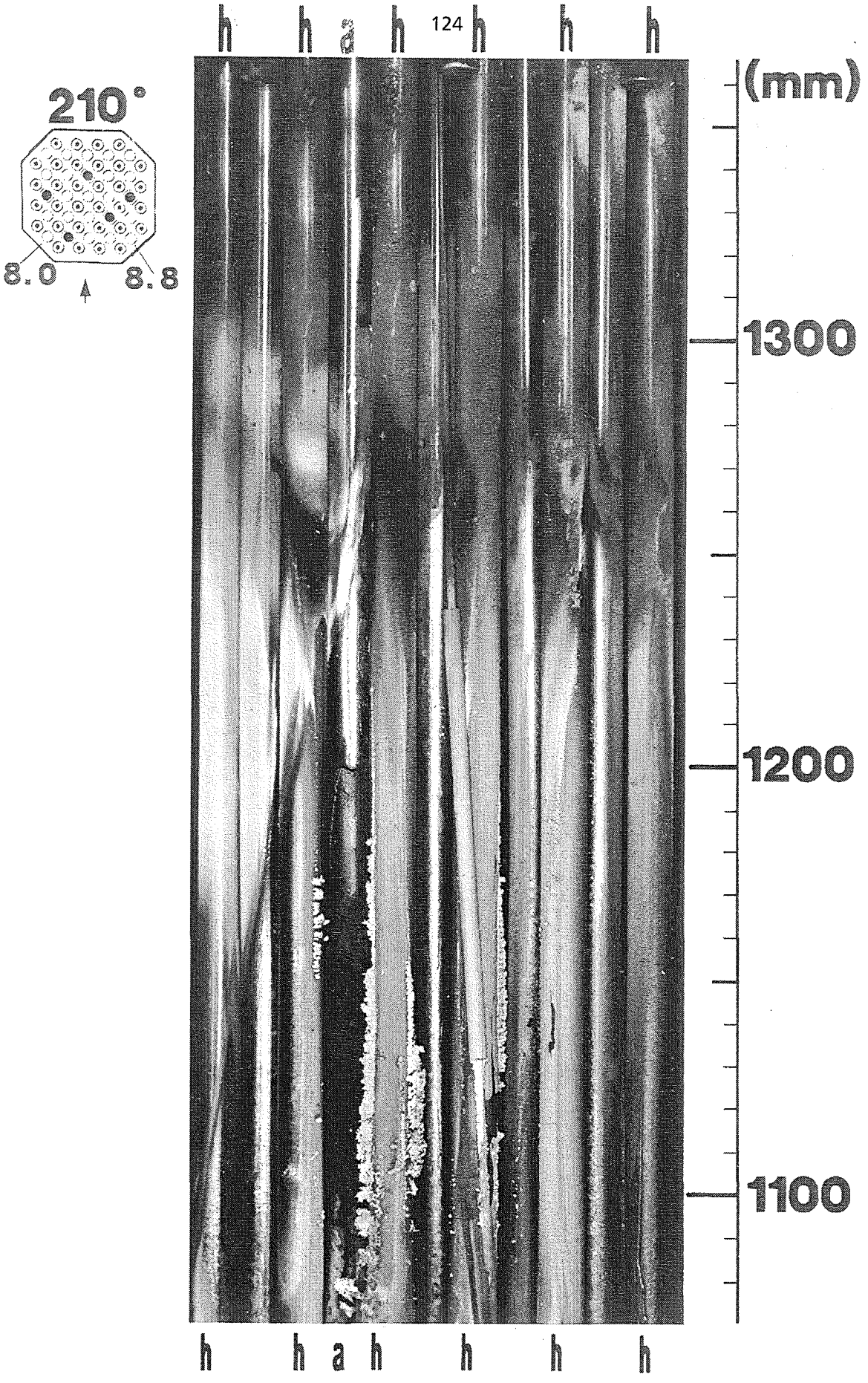

Fig. 98: Post test view of bundle, 210° partial view, 1050-1350 mm

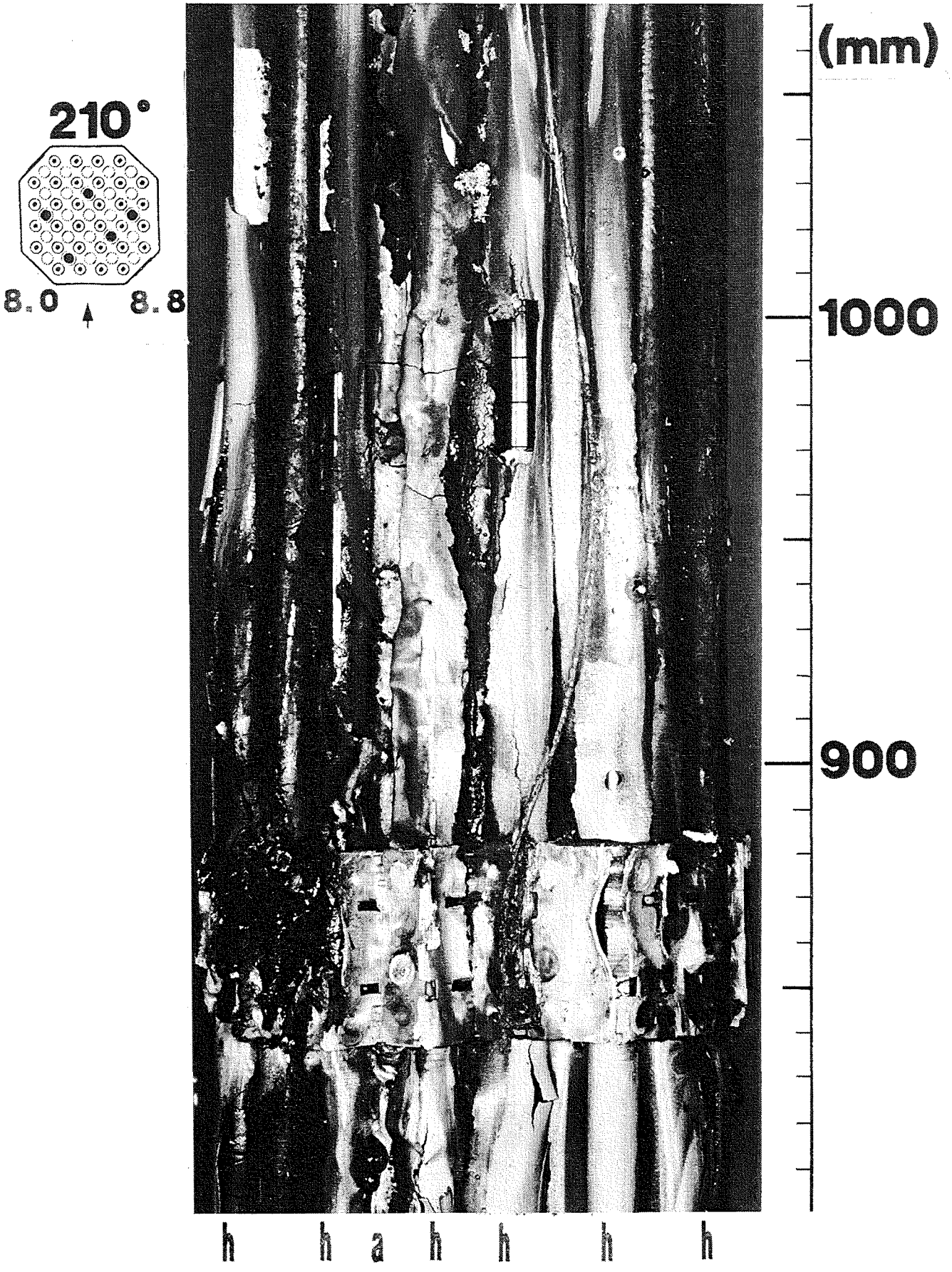

Fig. 99: Post test view of bundle, 210° partial view, 800-1050 mm

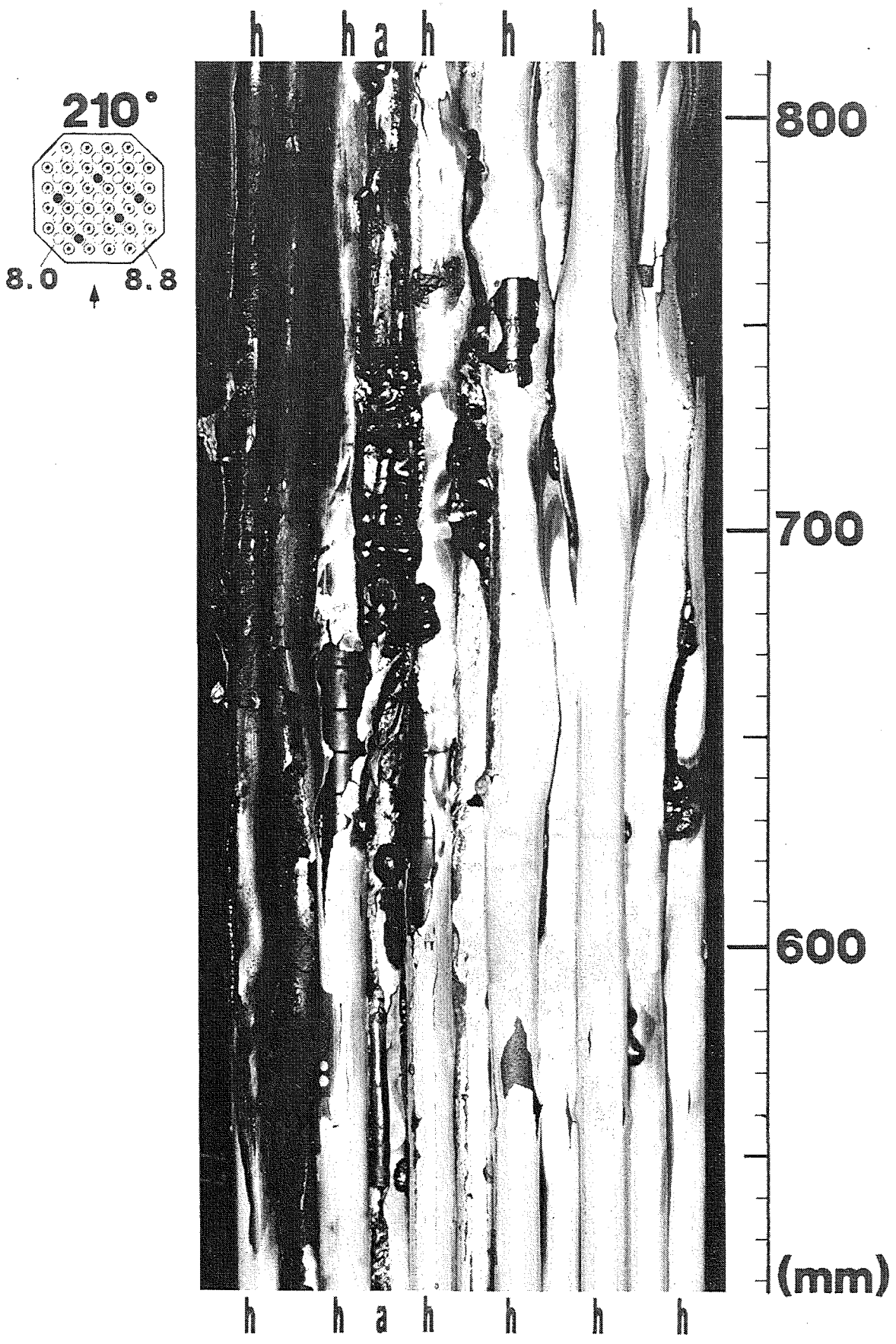

Fig. 100: Post test view of bundle, 210° partial view, 500-800 mm

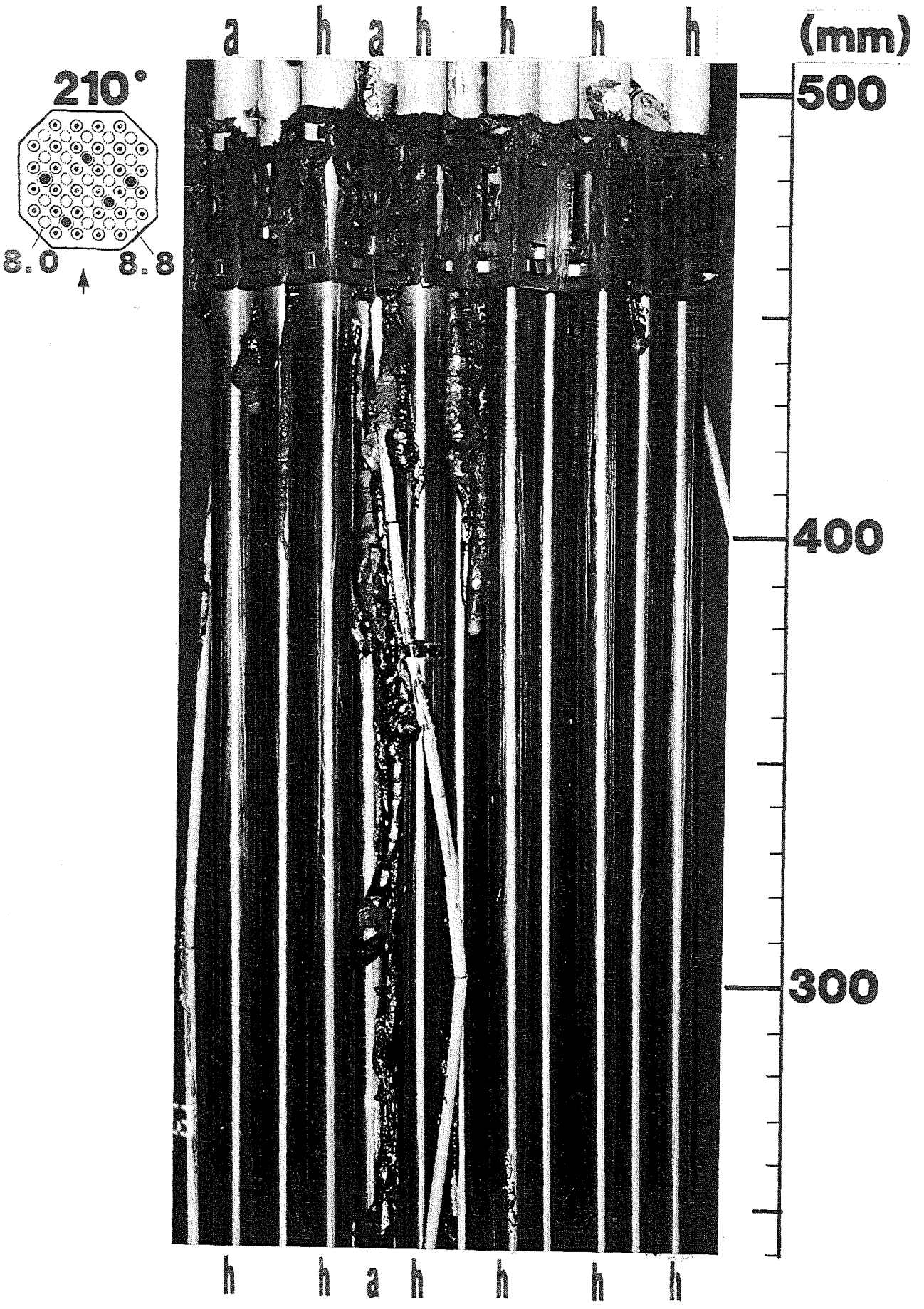

Fig. 101: Post test view of bundle, 210° partial view, 250-500 mm

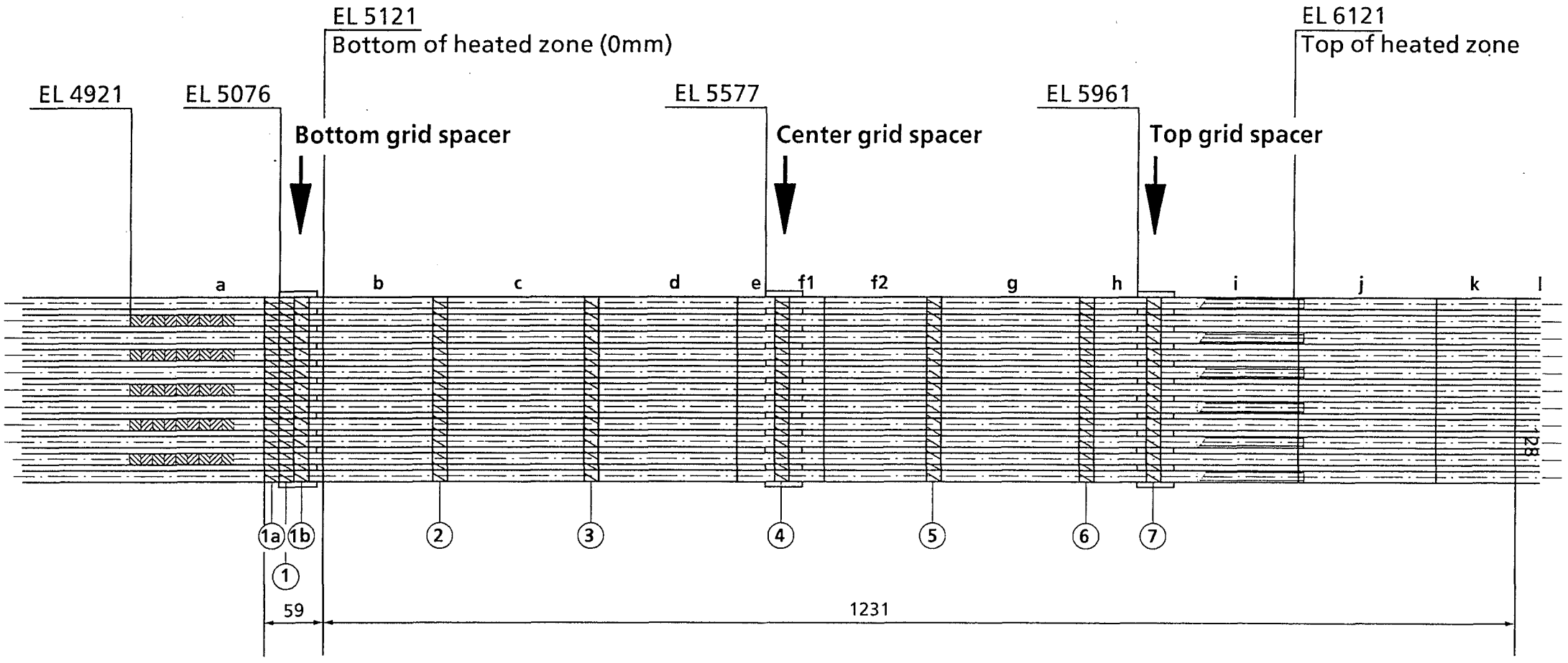

Vertical sections of remnants d, e, f

Height of horizontal sample : 13mm (marking distance = 15mm)

Bundle viewed from 30°, 120°, 210°, and 300°, respectively

Fig. 103: Bundle sectioning

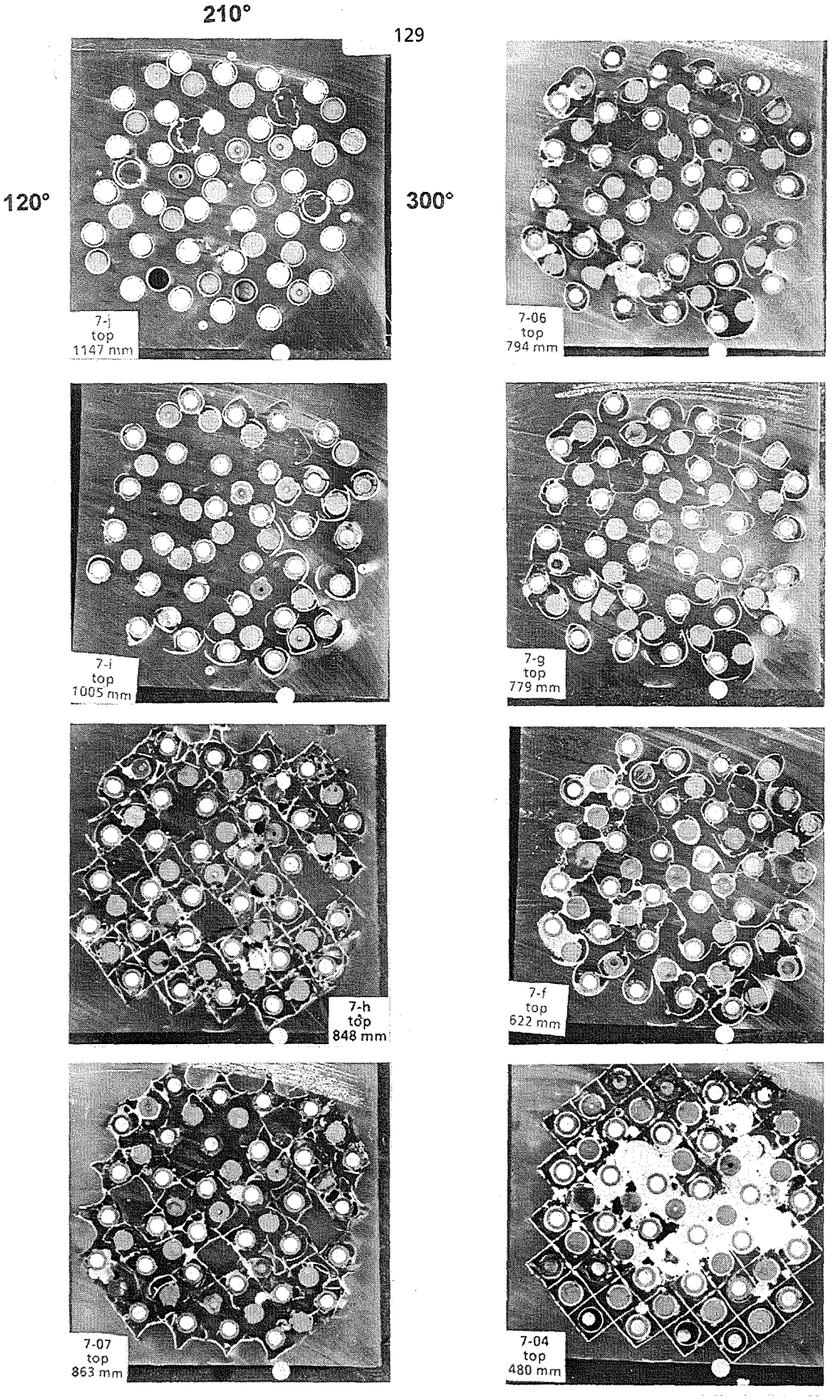

Fig. 104: Horizontal cross sections of bundle CORA-7, top view, 1147 to 480 mm elevation

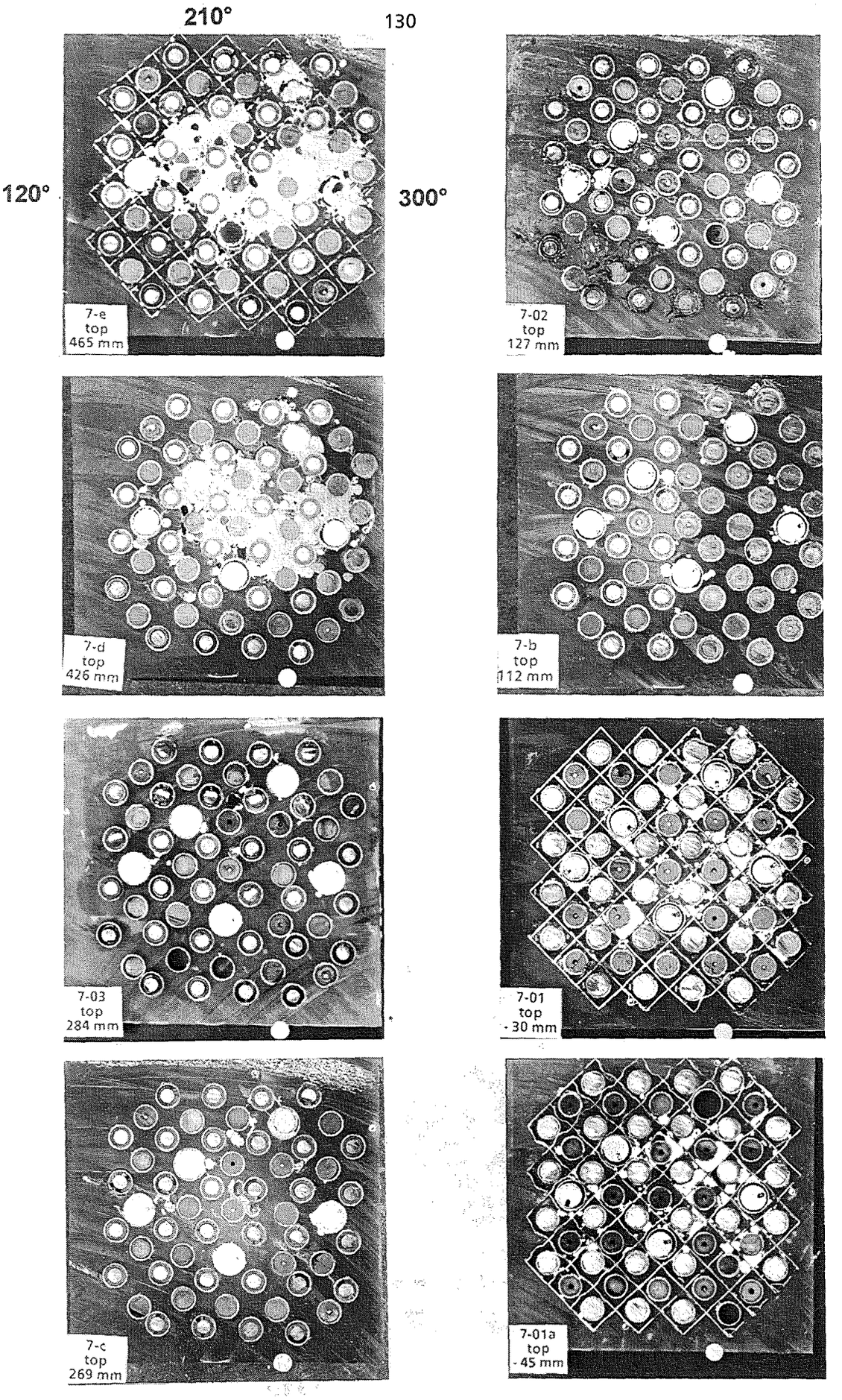

Fig. 105: Horizontal cross sections of bundle CORA-7, top view, 465 to -45 mm elevation

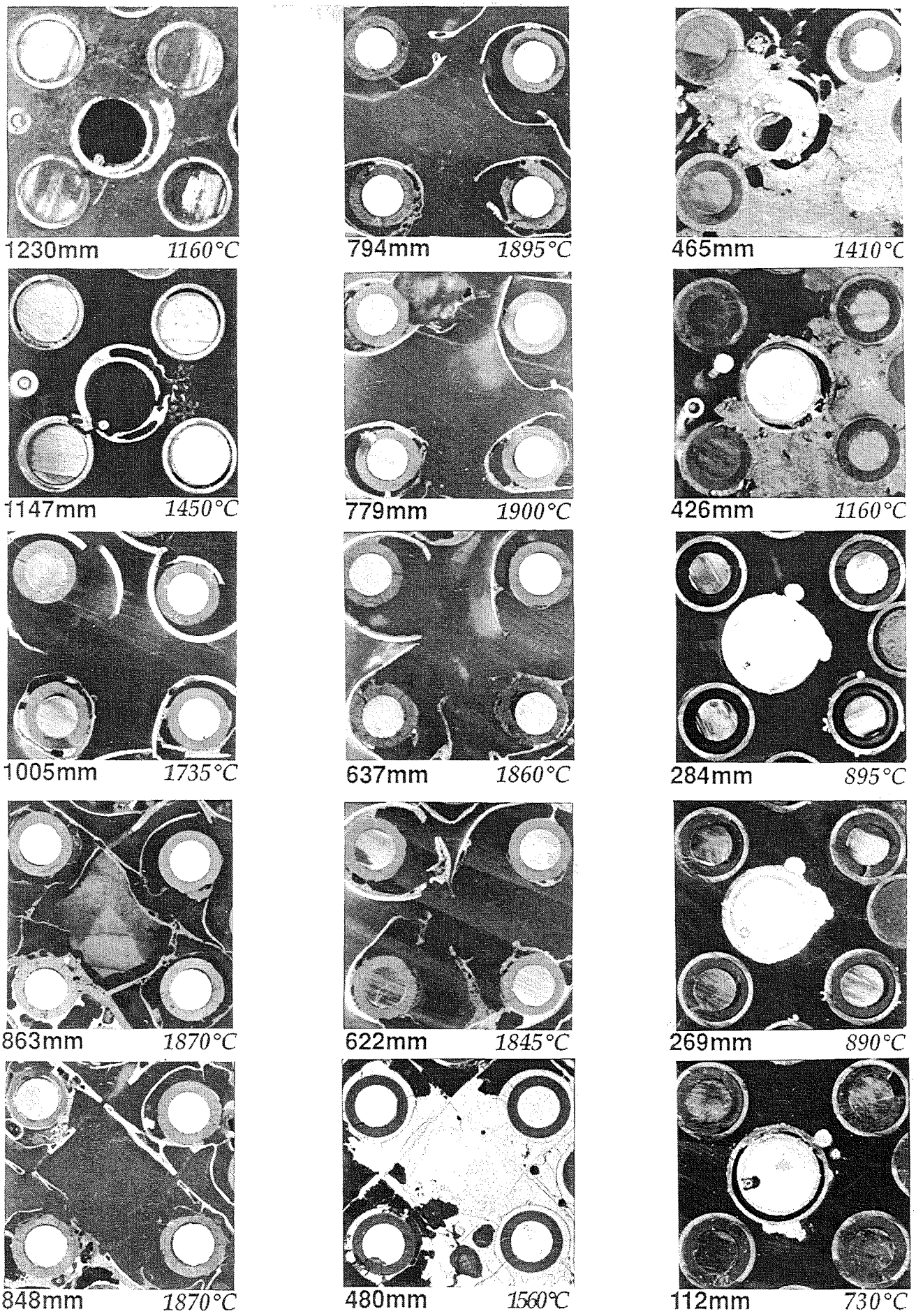

Fig. 106: CORA-7; region of absorber rod 4.0

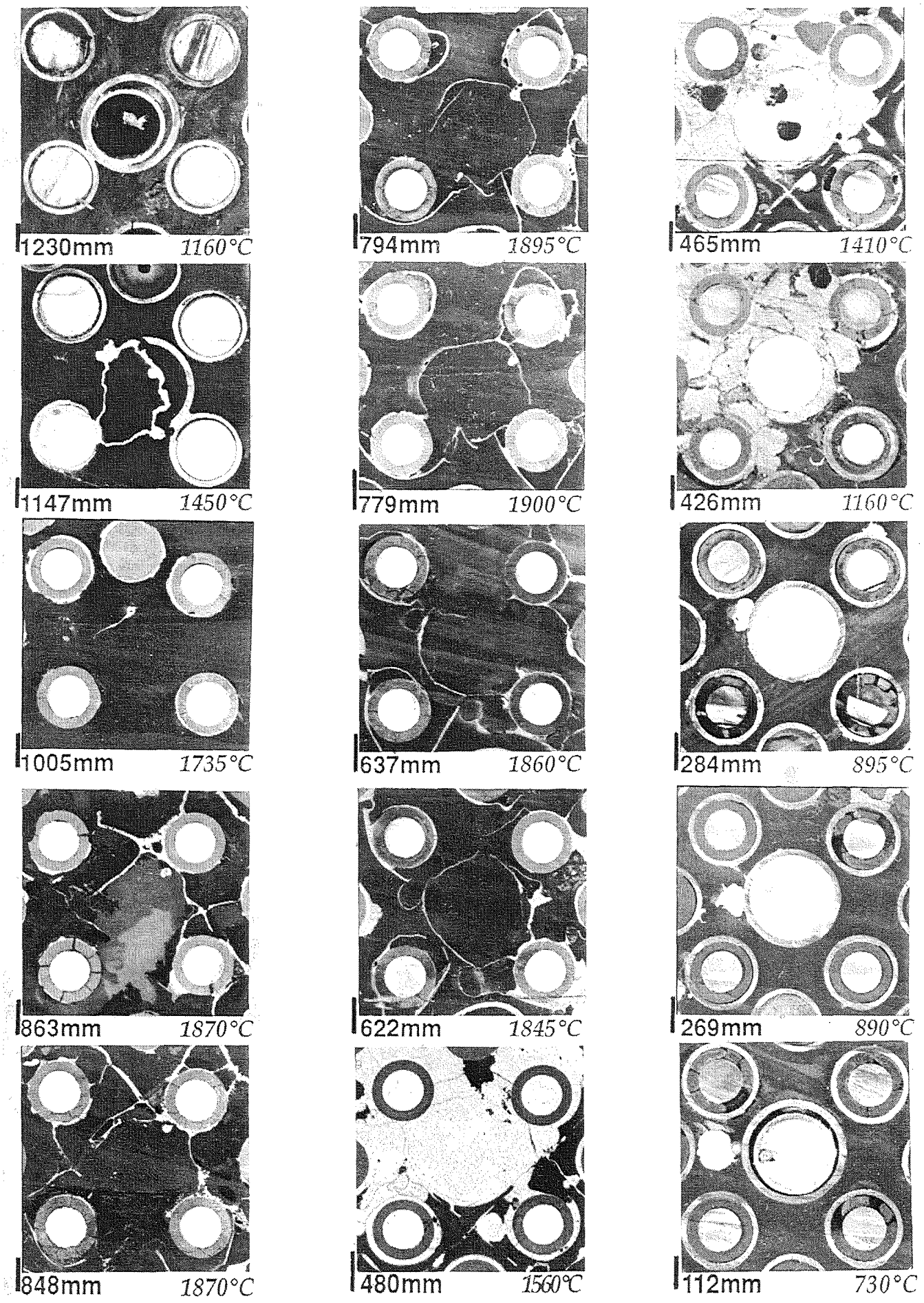

Fig. 107: CORA-7; region of absorber rod 6.6

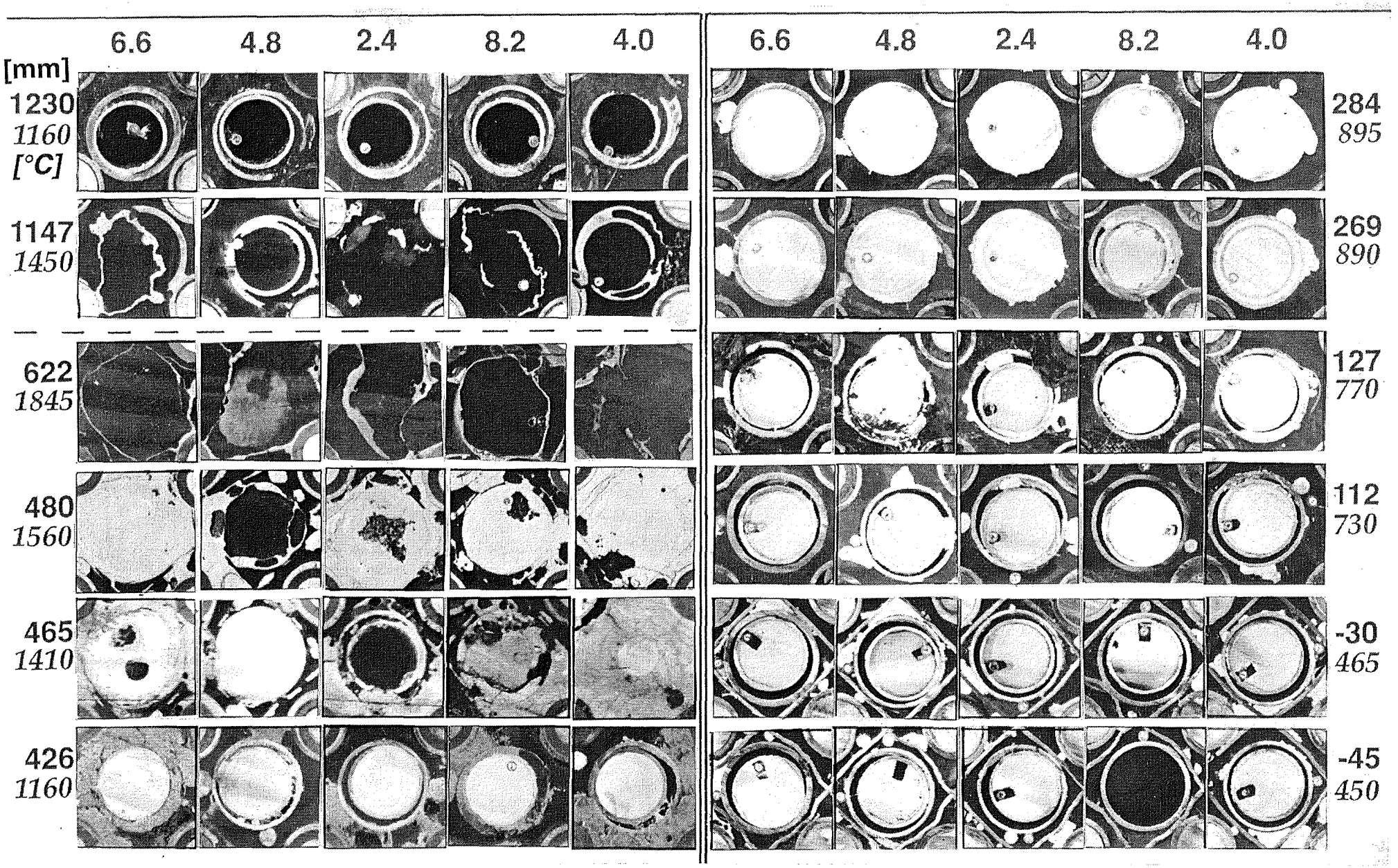

Fig. 108: CORA-7; Failure of the 5 absorber rods

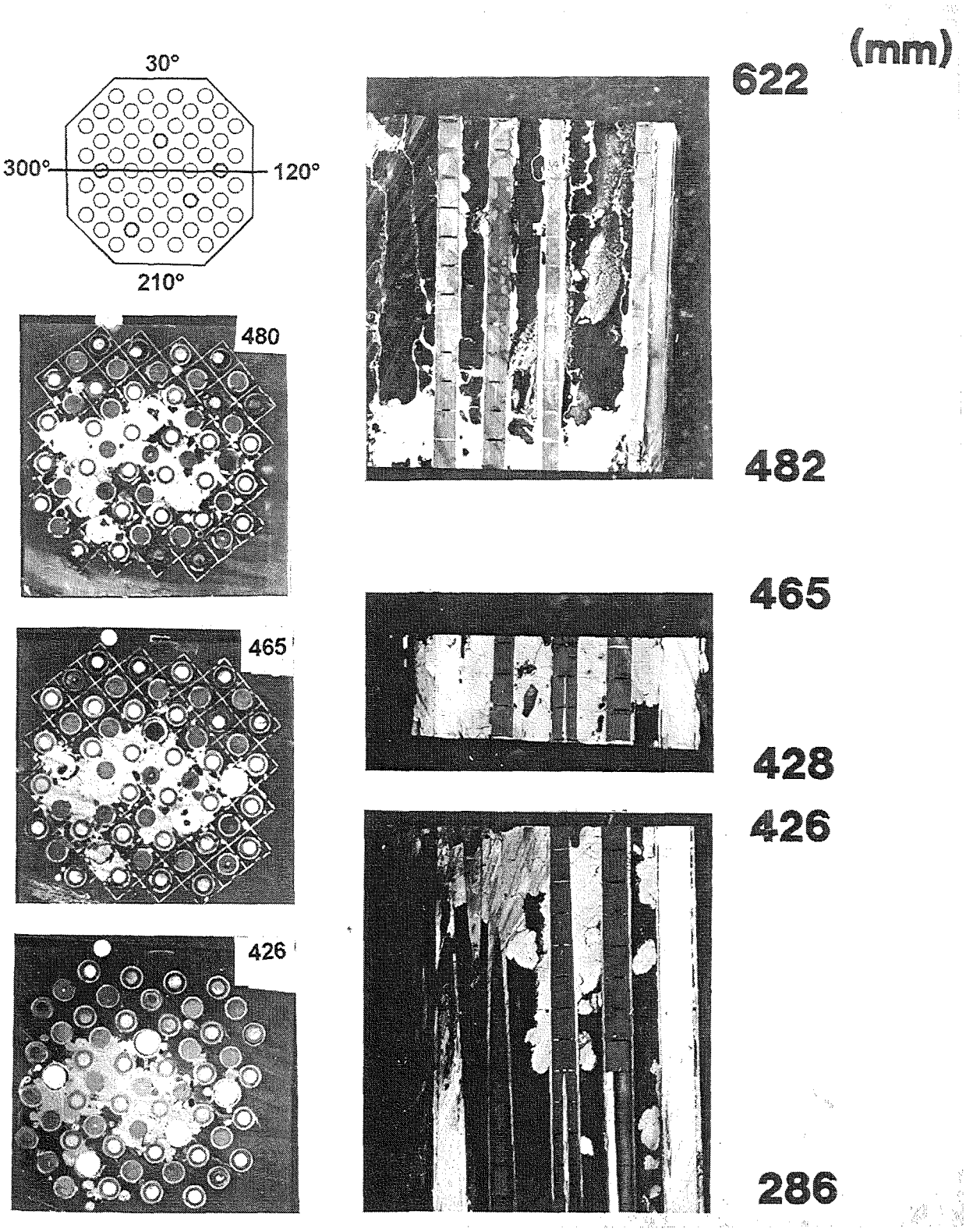

Fig. 109: CORA-7; Comparison of horizontal cross sections and vertical cross sections through absorber rods 4.0 and 4.8 (268 - 622 mm)

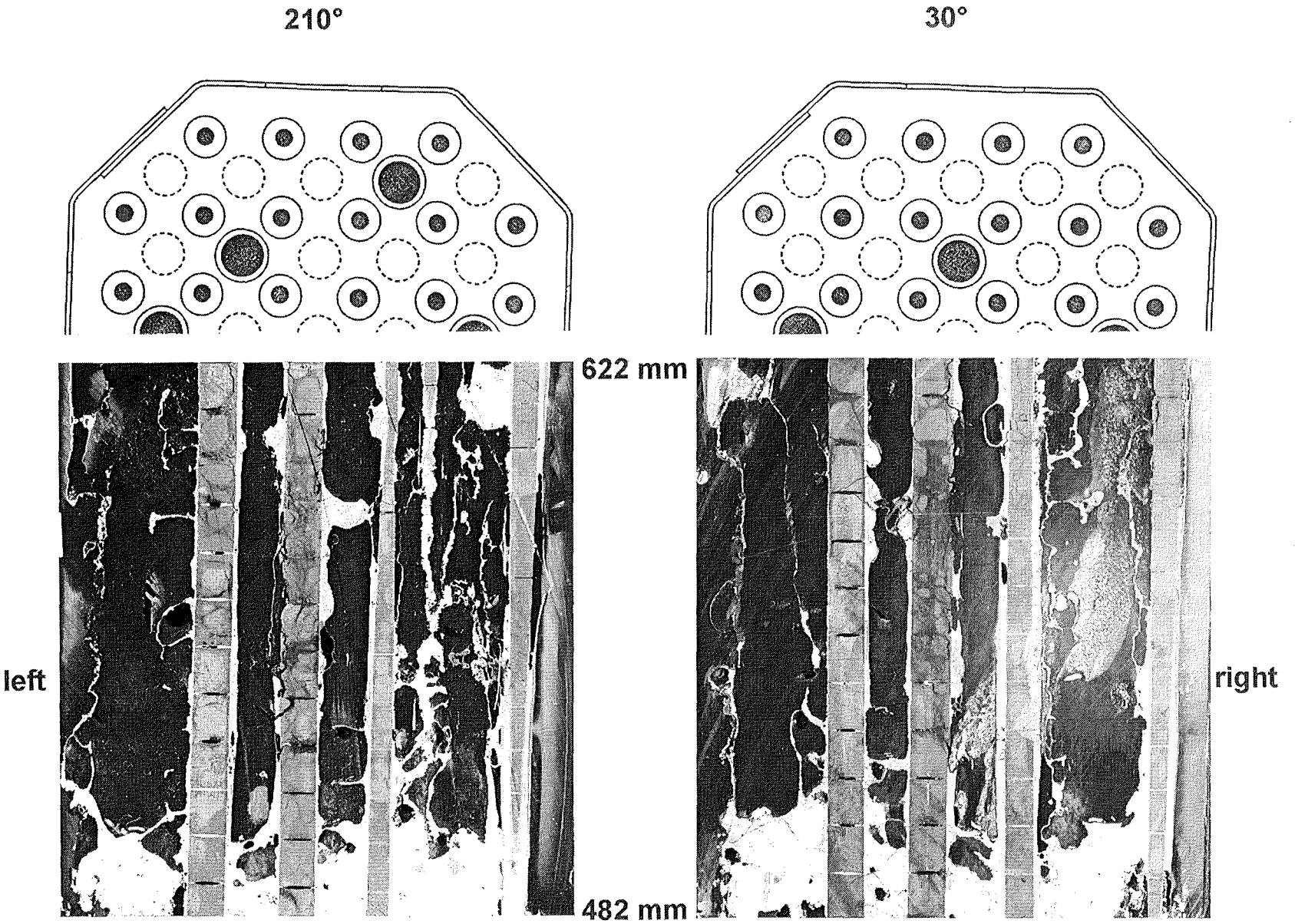

Fig. 110: CORA-7; Comparison of left and right sights of vertical cut through absorber rods 4.0 and 4.8

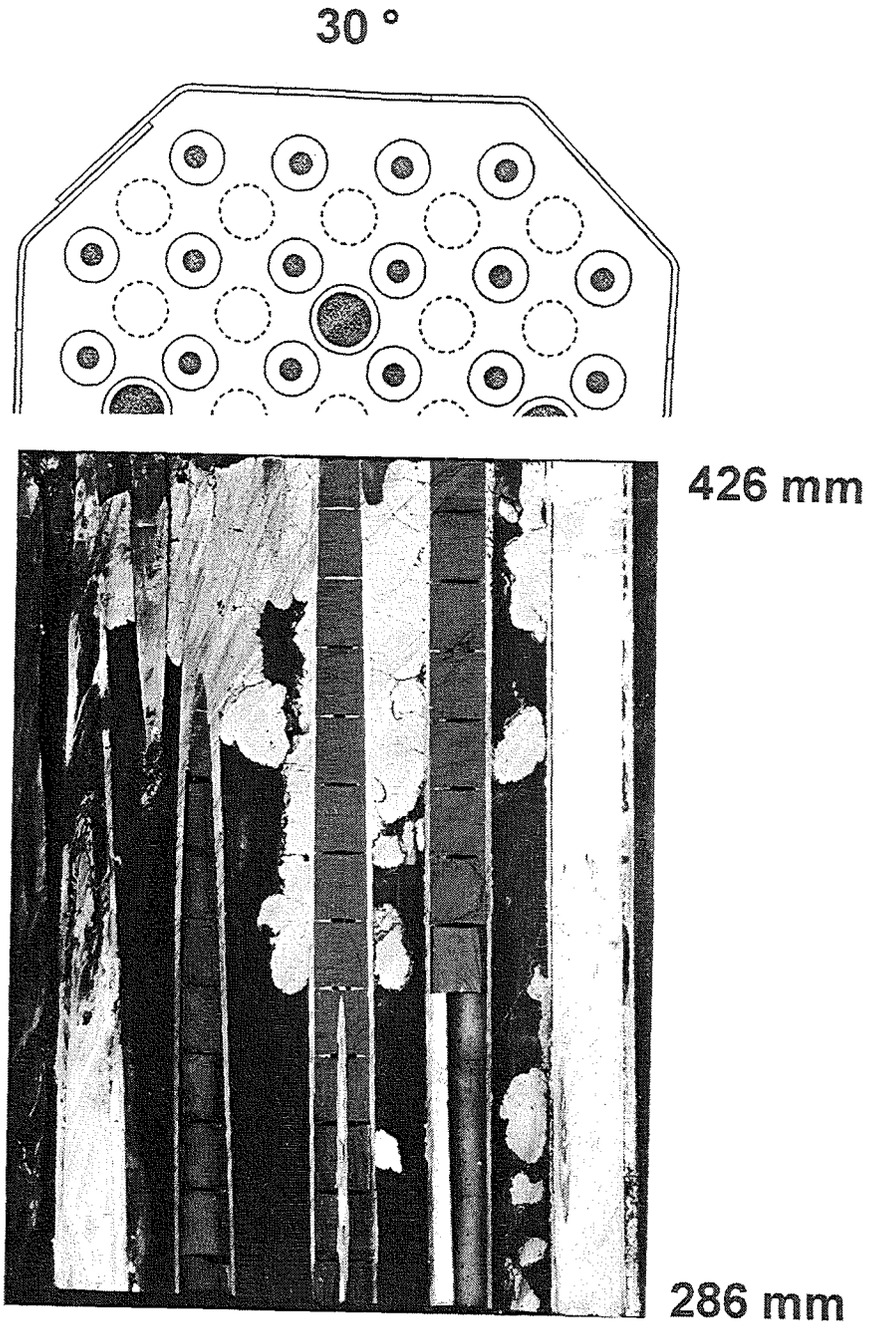

Fig. 111: CORA-7; Vertical cross section through absorber rods 4.0 and 4.8 (286-426 mm)

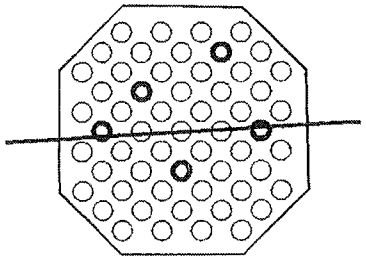

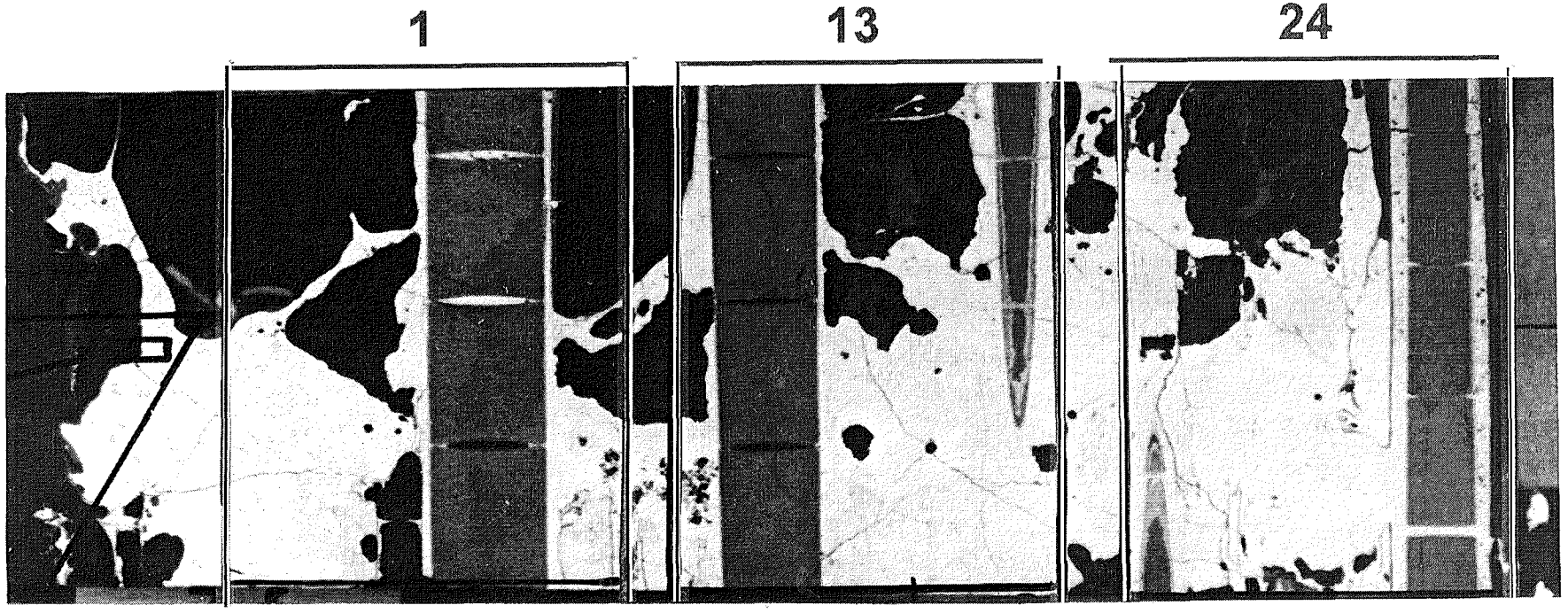

Fig. 113: CORA-7; Vertical cross section (482 - 516 mm) used for further examinations. Compare Fig. 109.

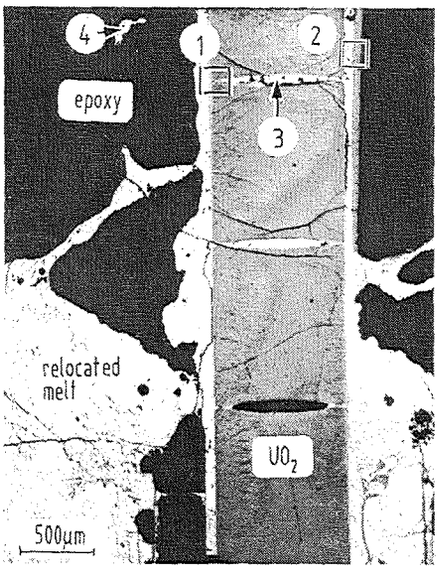

detail of longitudinal section CORA 7-f

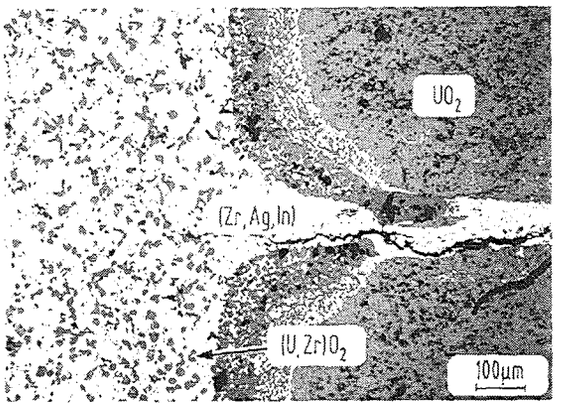

UO_2 dissolution by molten Zircaloy

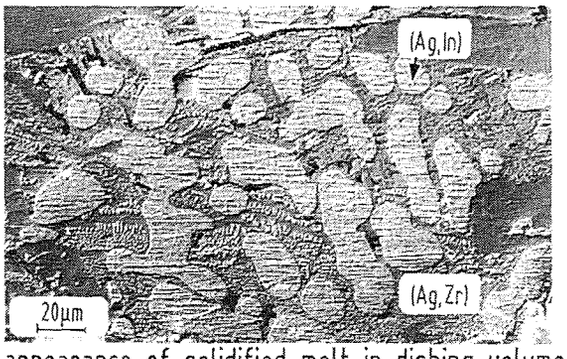

appearance of solidified melt in dishing volume (interference contrast)

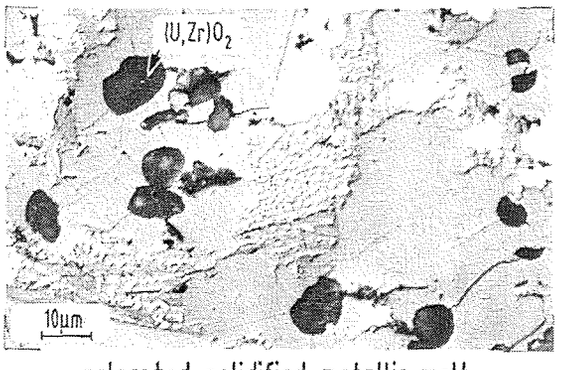

relocated solidified metallic melt (interference contrast)

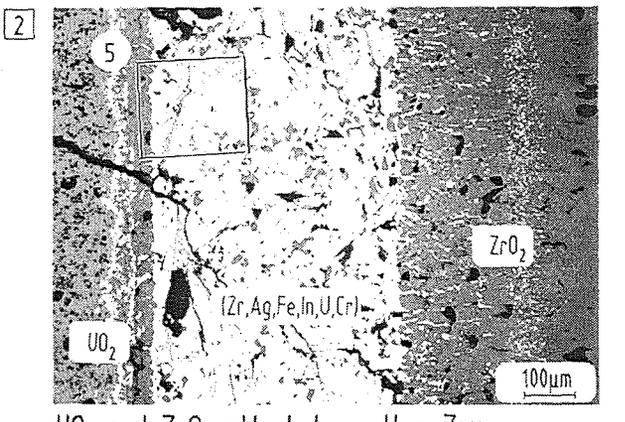

UO_2 and ZrO_2 attack by molten Zry

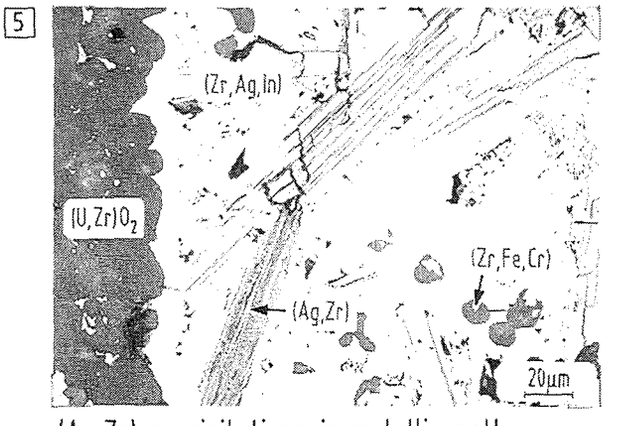

(Ag,Zr) precipitations in metallic melt

Fig. 115a: Overview: Microstructures of area 1 of the vertical cross section 482 - 516 mm; CORA7-f (see Fig. 113)

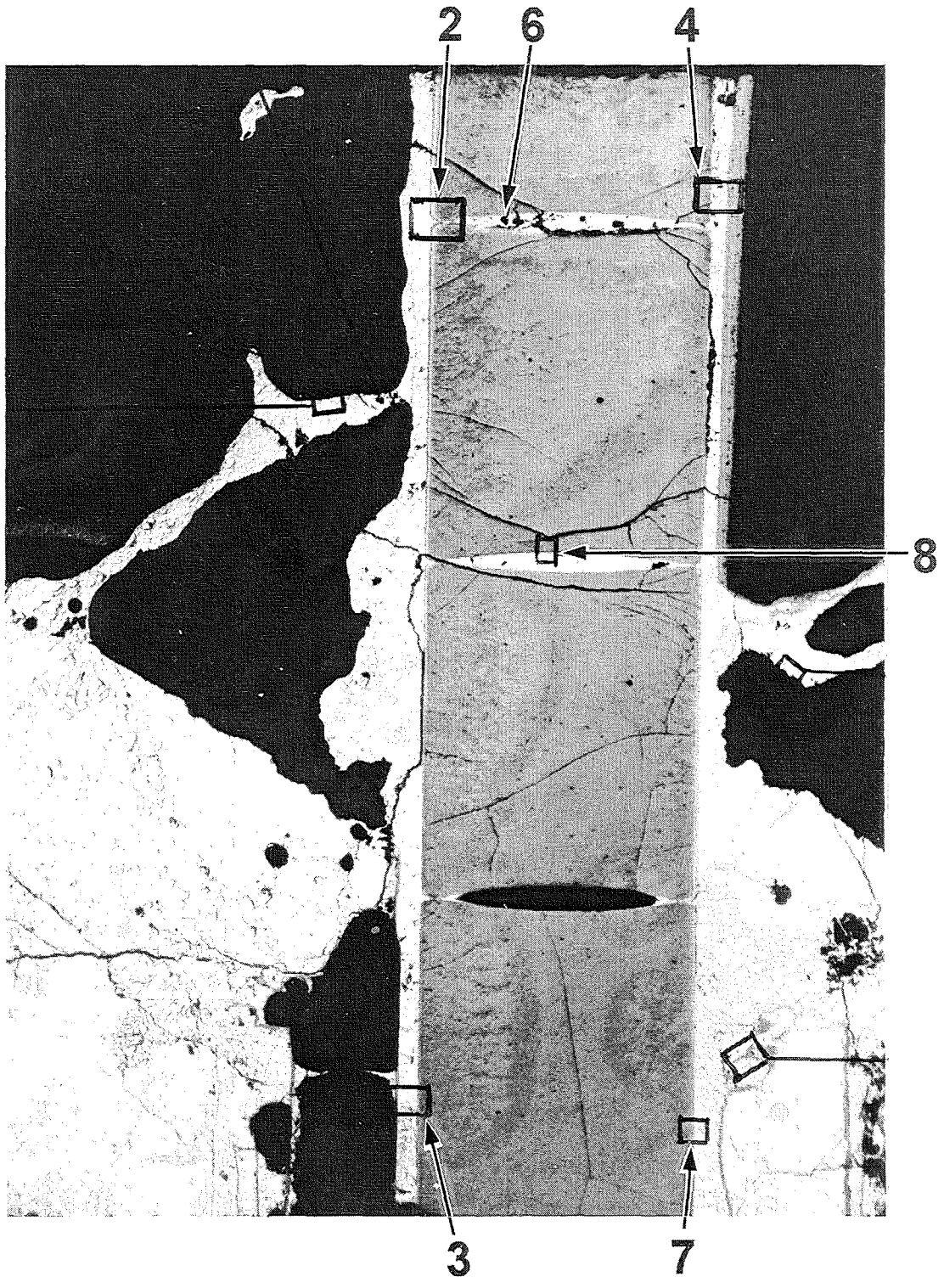

Fig. 115: CORA-7; Positions of examination of region 1

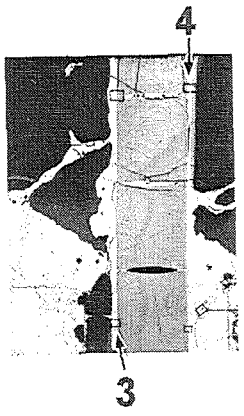

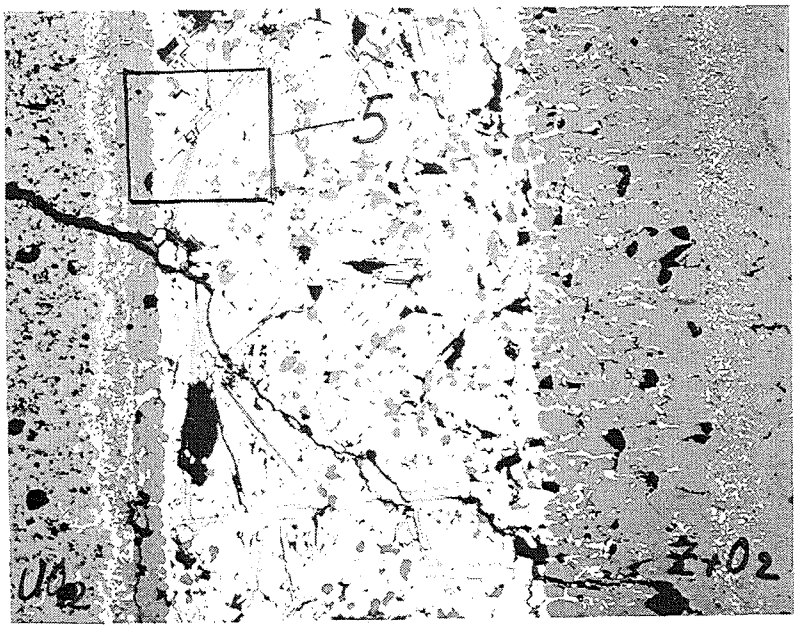

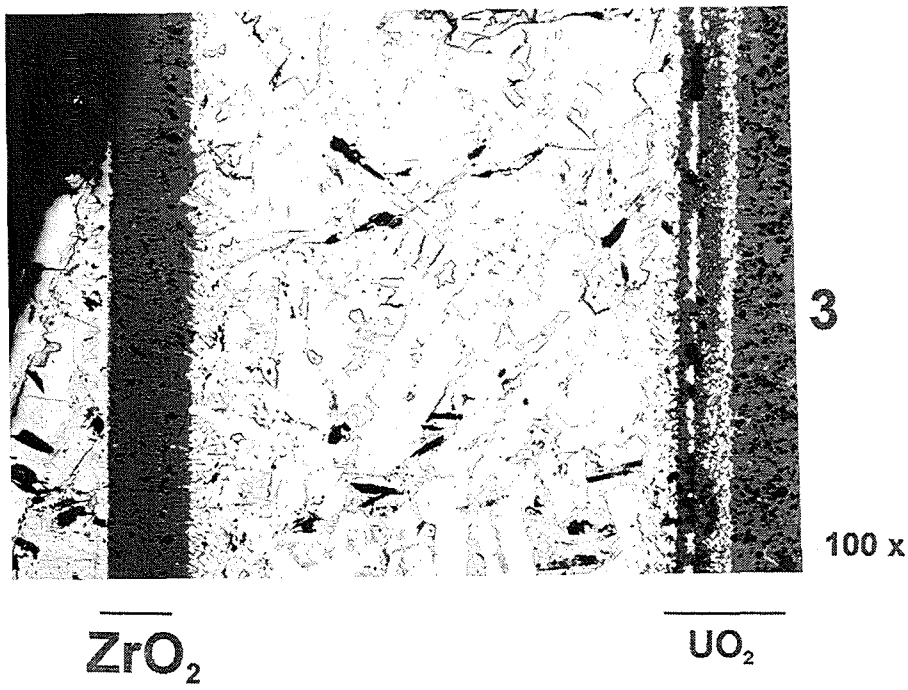

Fig. 116: CORA-7; Oxidation at positions 4 and 3 (picture 1)

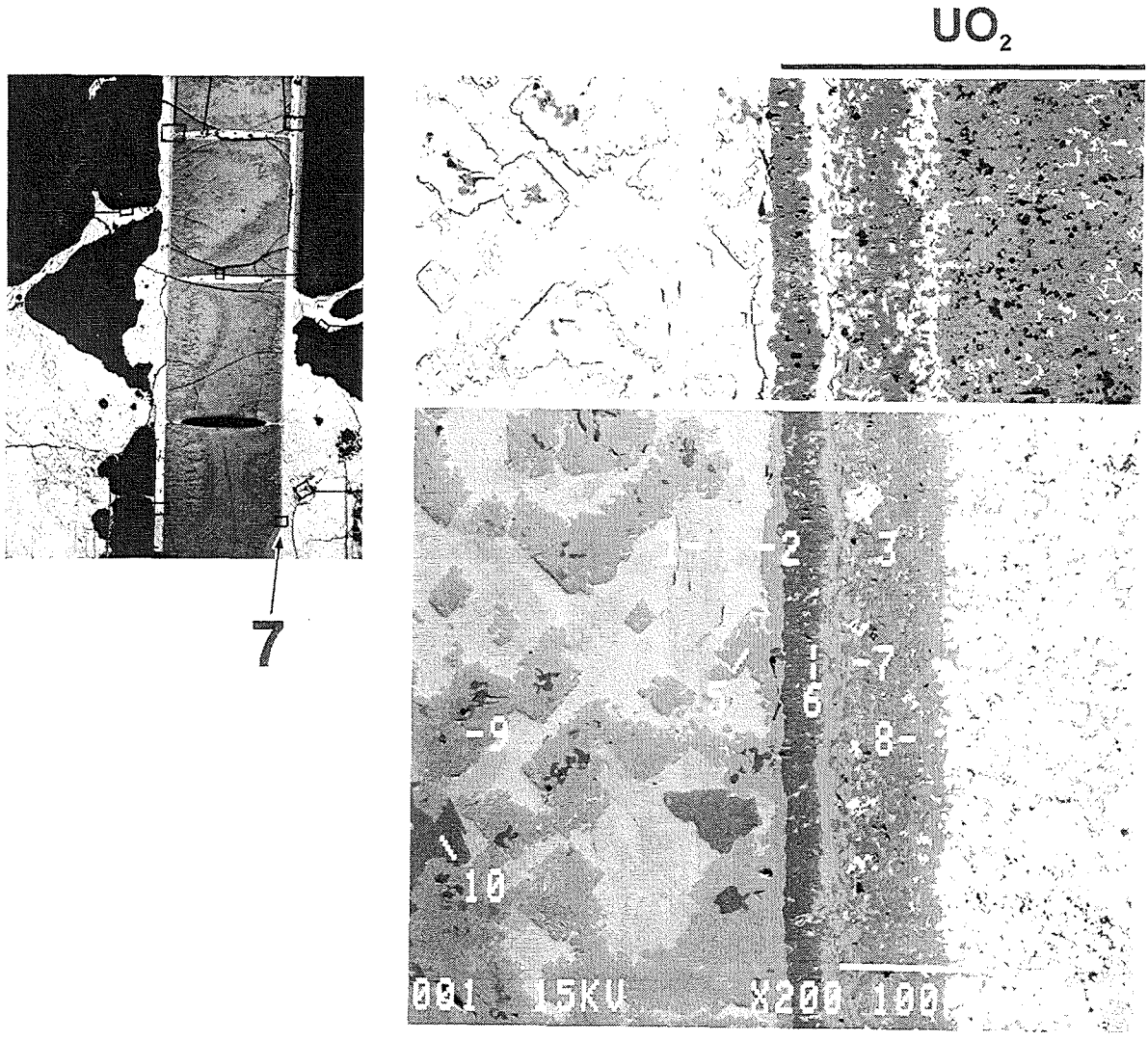

Pos.	Zr	U	Fe/Cr/Ni	Ag/In/Cd	
1	*43*		*5/-/3*	*17/30/1*	*met.*
2				*84/10/6*	*met.*
3	*10*	*90*			*oxi.*
4		*100*			*oxi.*
5	*68*	*7*	*16/3/3*	*4/-/-*	*met.*
6	*91*	*9*			*oxi.*
7	*66*	*10*	*13/3/2*	*2/-/.1*	*met.*
8	*72*	*28*			*oxi.*
9	*67*	*6*	*18/5/2*	*3/-/-*	*met.*
10	*45*	*2*	*40/12/2*		*met.*
Int.	*45*	*3*	*11/3/2*	*28/6/1*	*met.*

Fig. 117: CORA-7; pellet / melt interaction (region 1, position 7)

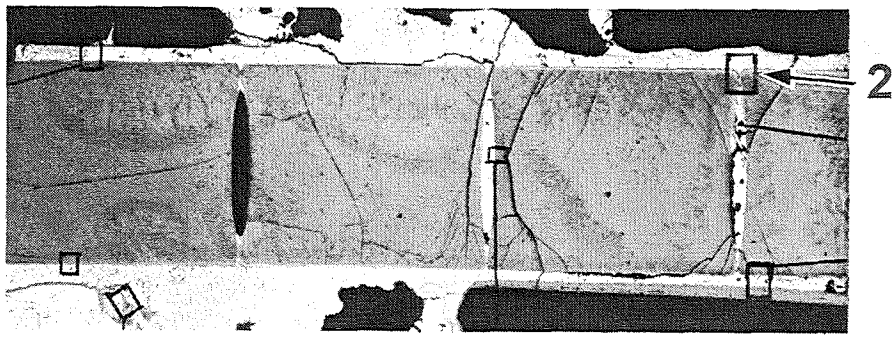

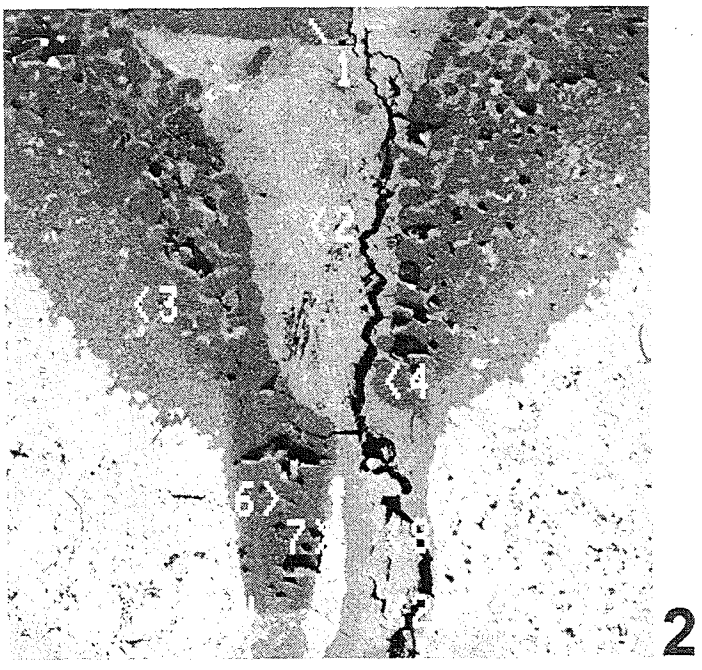

Pos.	Zr	U	Fe/Cr/Ni	Ag/In/Cd	
1	*88 wt%*	*11*	*1/-/-*		*oxi.*
2	*23*	*3*	*3/-/2*	*55/14/-*	*met.*
3	*63*	*37*			*oxi.*
4	*86*	*14*			*oxi.*
5		*100*			*oxi.*
6	*88*	*12*			*oxi.*
7		*100*			*oxi.*
8	*50*		*1/-/2*	*6/10/1*	*met.*

Fig. 118: CORA-7; pellet / melt interaction (region 1, position 2)

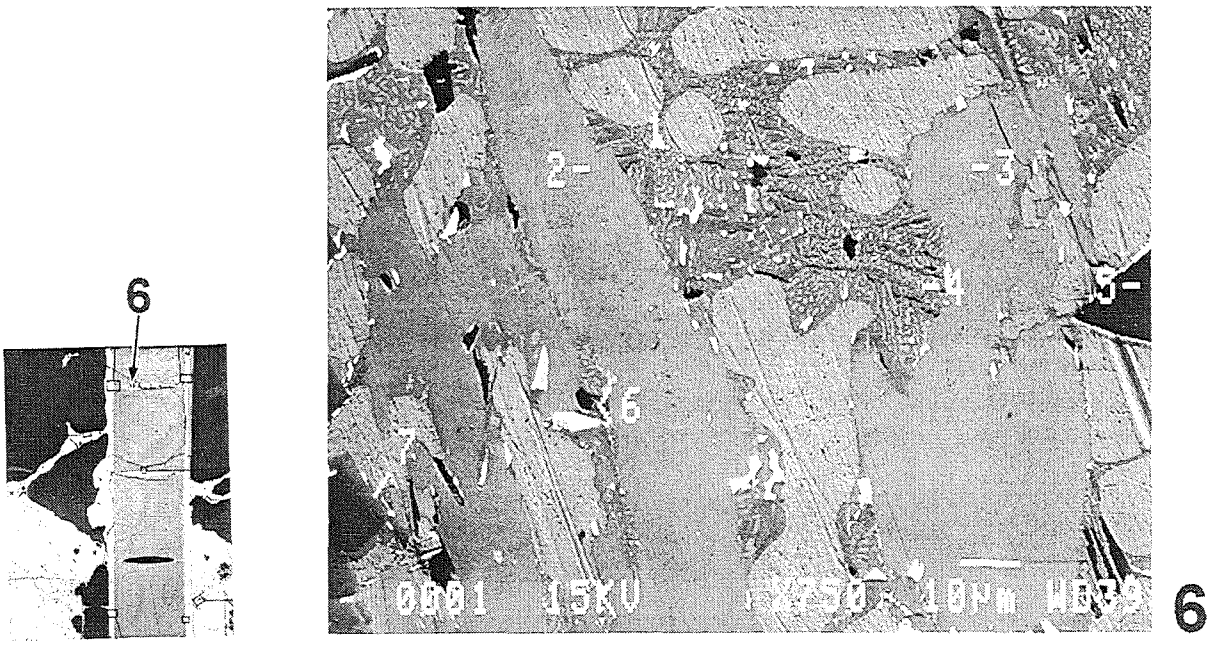

Pos.	Zr	U	Fe/Cr/Ni	Ag/In/Cd	
1				*94/5/1*	*met.*
2	*52*wt%		*-/-/1*	*6/7/.2*	*met.*
3	*49*		*-/-/1*	*9/13/1*	*met.*
4	*30*	*.3*	*1/-/-*	*62/6/1*	*met.*
5	*43*	*6*	*39/10/2*		*met.*
6		*96*	*4/-/-*		*met.*
Int.	*32*	*6*	*5/.4/2*	*43/7/-*	*met.*

Fig. 119: CORA-7; Phase composition in gap between pellets (region 1, position 6)

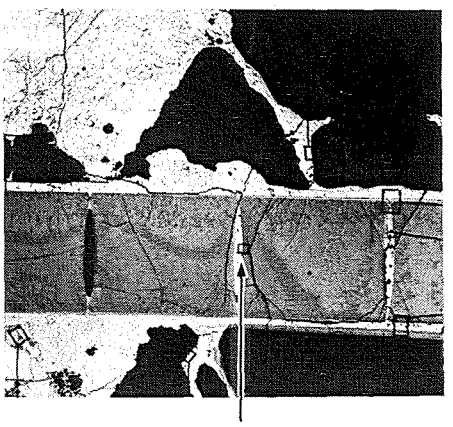

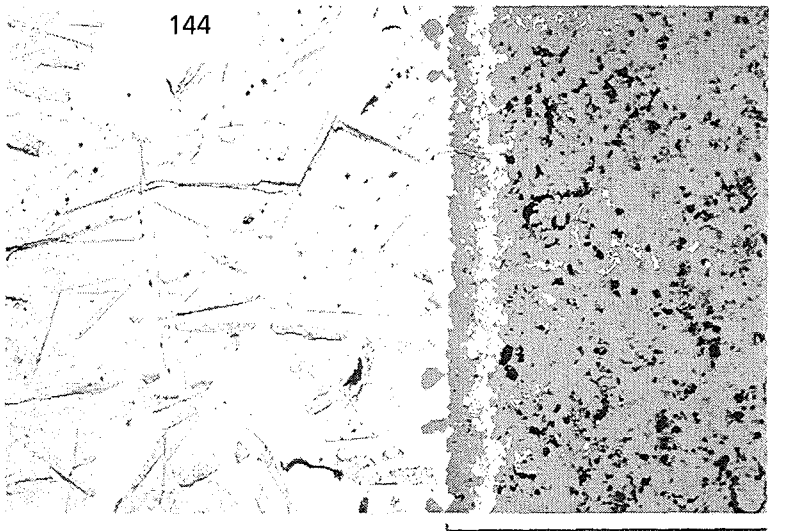

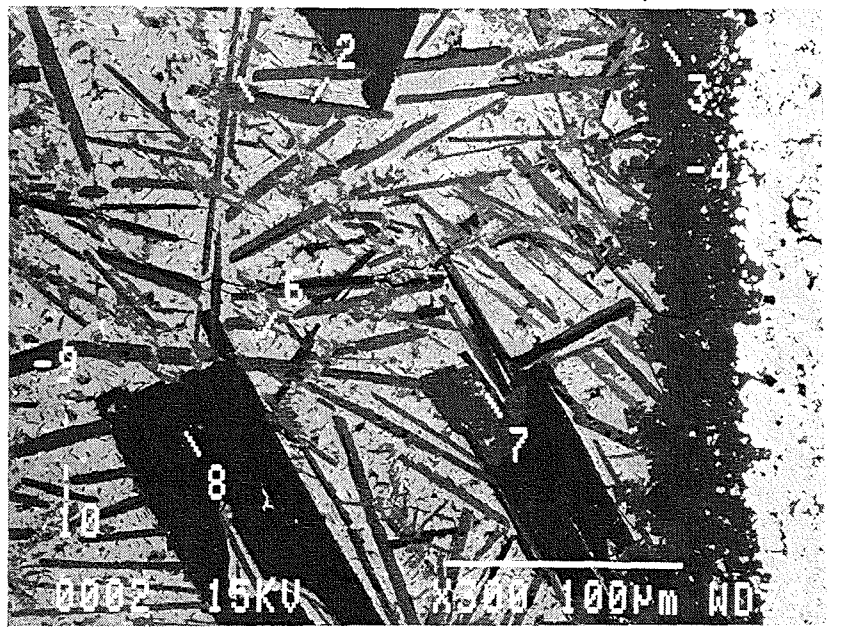

Pos.	Zr	U	Fe/Cr/Ni	Ag/In/Cd	
1	*51wt%*			*10/12/1*	*met.*
2	*65*		*5/-/2*	*2/-/26*	*met.*
3	*62*	*16*	*16/4/2*		*met.*
4	*62*	*9*	*20/8/1*		*met.*
5		*100*			*oxi.*
6	*35*	*49*	*12/-/4*		*met.*
7	*63*	*14*	*17/4/2*		*met.*
8	*44*	*6*	*34/16/-*		*met.*
9	*46*			*54/-/-*	*met.*
10	*32*	*51*	*13/-/4*		*met.*
Int.	*41*	*23*	*15/4/2*	*11/-/2*	*met.*

Fig. 120: CORA-7; pellet / melt interaction (region 1, position 8)

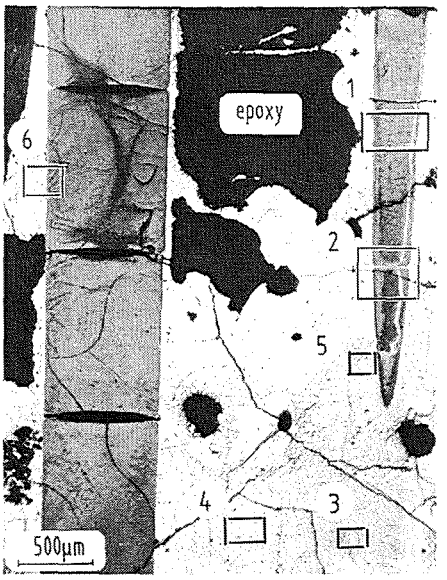

detail of longitudinal section CORA 7-f

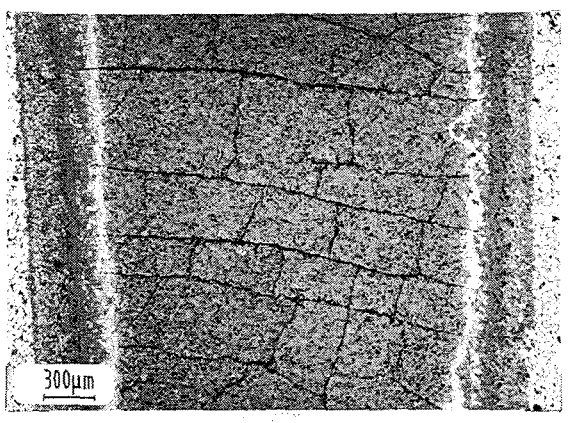

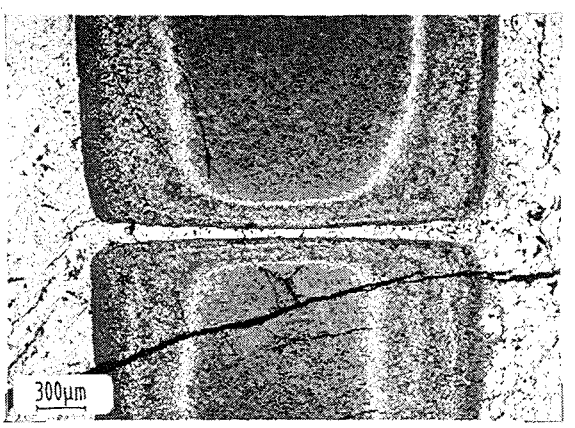

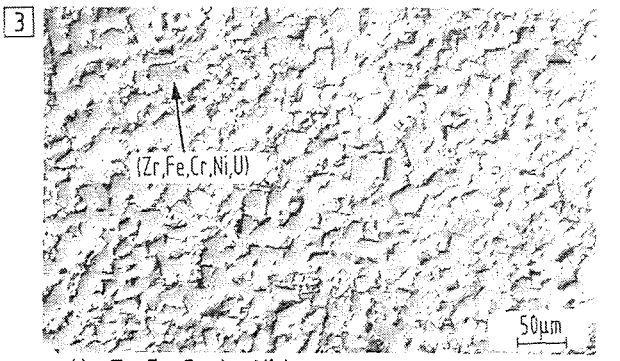

melt: Zr,Fe,Cr,Ag,Ni,In

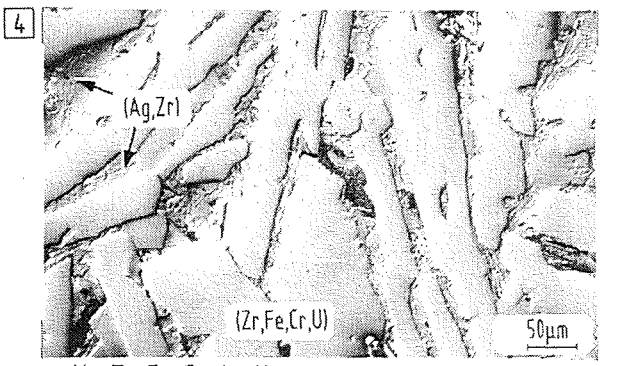

melt: Zr,Fe,Cr,Ag,U

melt: Zr,Ag,Fe,Cr,In,U

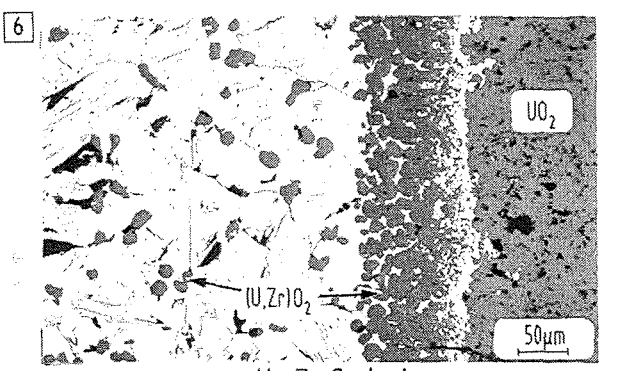

melt: Zr,Sn,In,Ag

Fig. 121a: Overview: Microstructures of area 13 of the vertical cross section 482 - 516 mm; CORA7-f (see Fig. 113)

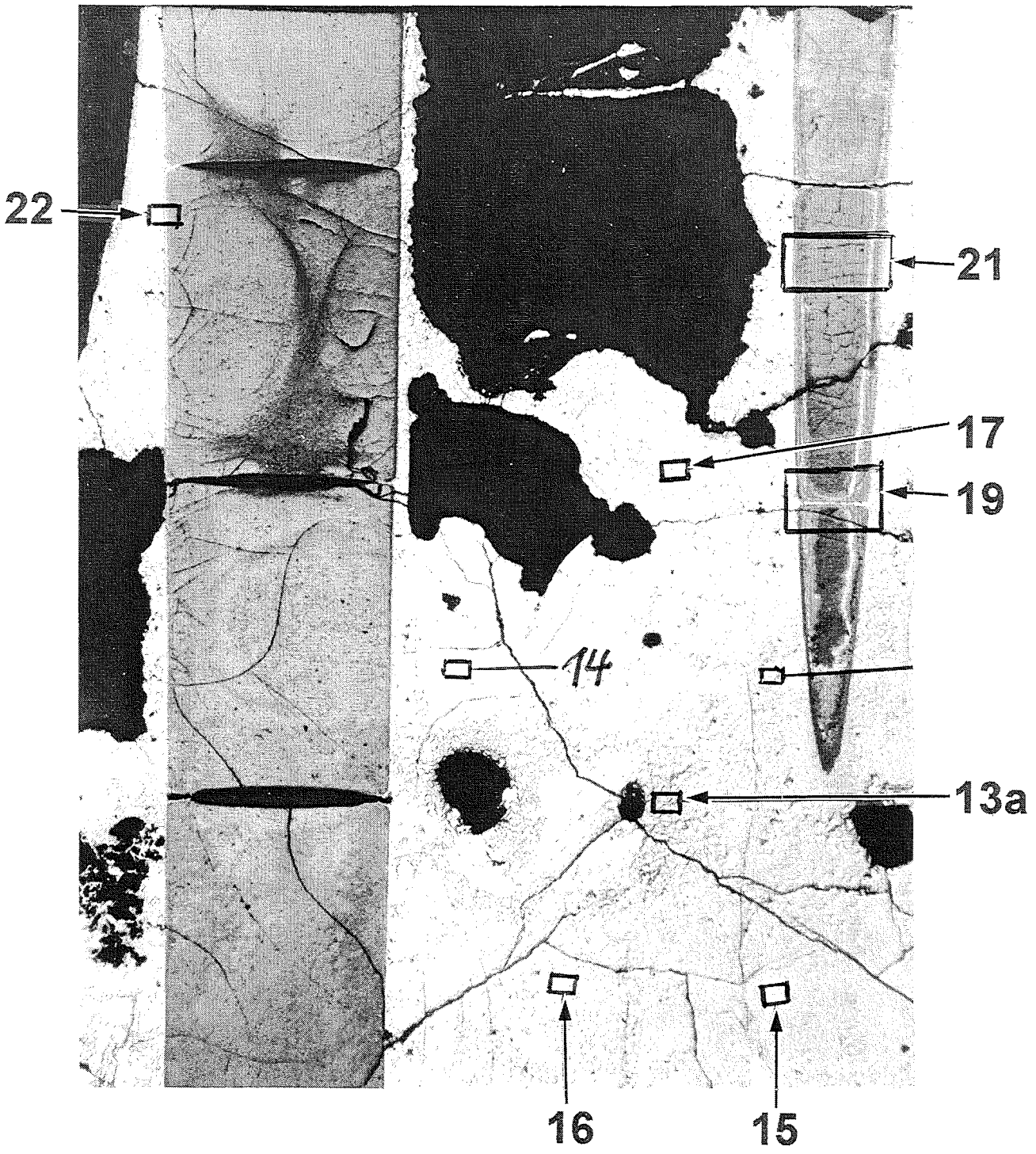

Fig. 121: CORA-7; Positions of examination of region 13

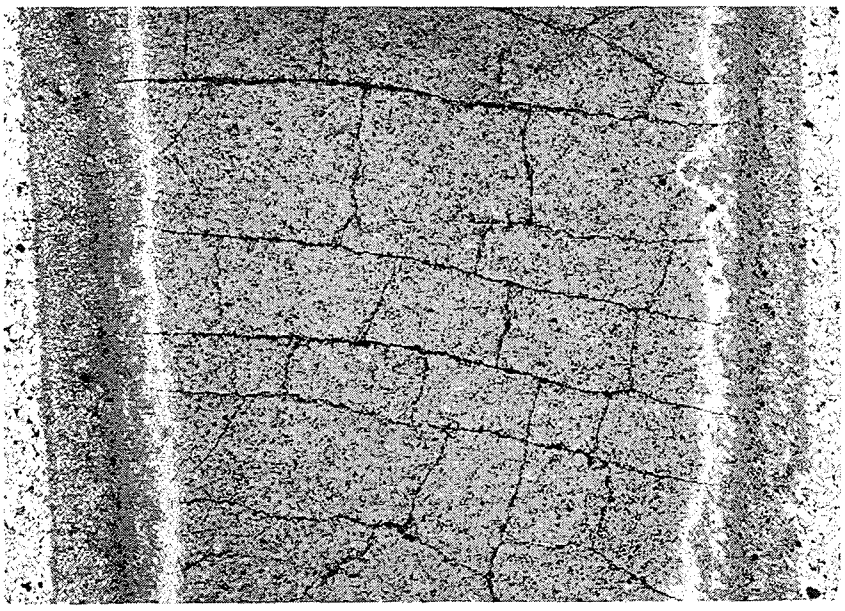

21

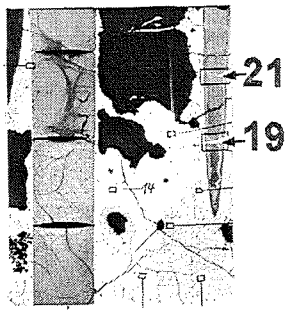

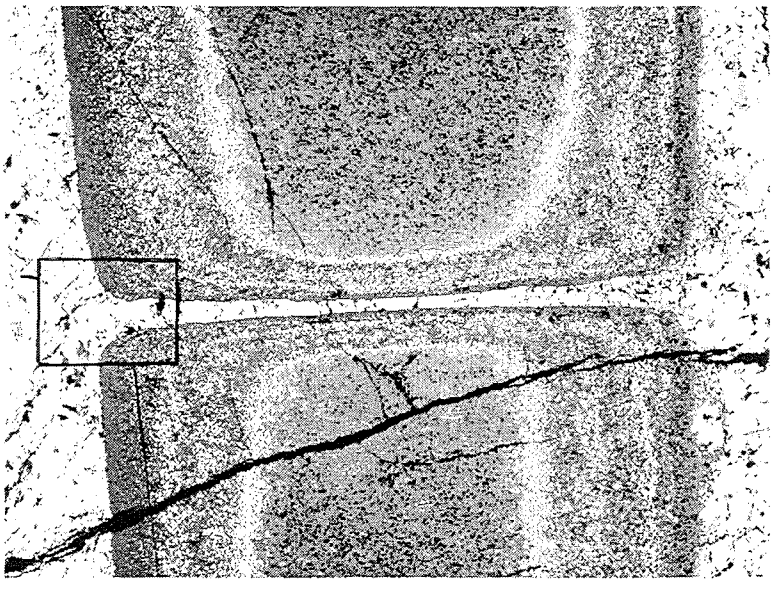

19

Fig. 122: CORA-7; Interaction Zry / UO_2

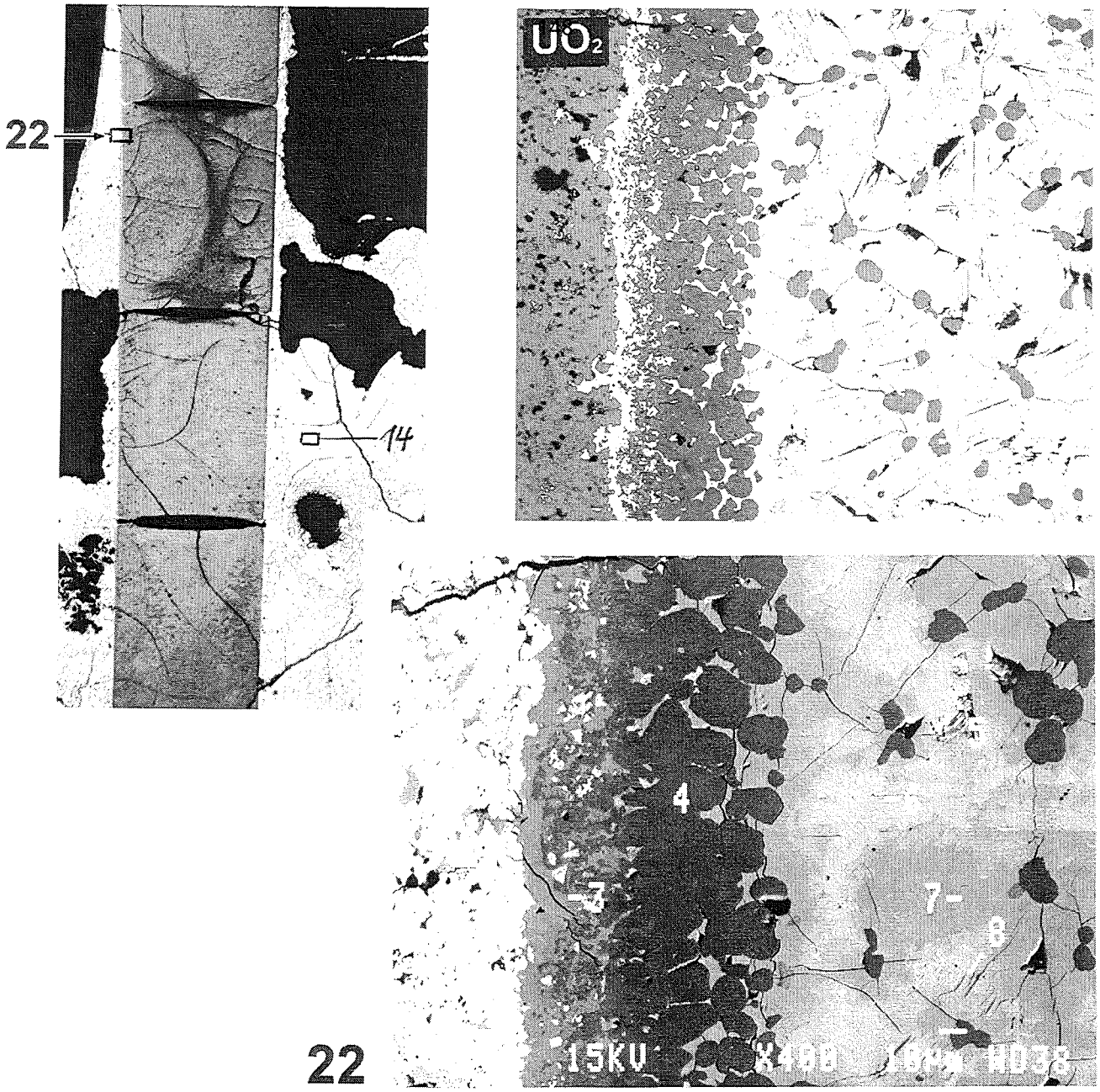

Pos.	Zr	U	Fe/Cr/Ni	Ag/In/Cd	
1		*100*			*keram.*
2	*49wt%*	*.1*		*12/13/-*	*met.*
3	*60*	*12*	*9/1/1*	*12/4/-*	*met.*
4	*89*	*11*			*keram.*
5	*49*	*1*		*11/16/-*	*met.*
6	*50*			*11/20/.4*	*met.*
7	*65*	*9*	*14/4/2*	*5/1/-*	*met.*
8	*44*			*54/2/1*	*met.*
Int.	*54*	*8*	*8/2/1*	*21/4/-*	*met./ker.*

Fig. 124: CORA-7; Composition of phases at melt / pellet contact (region 13, position 22)

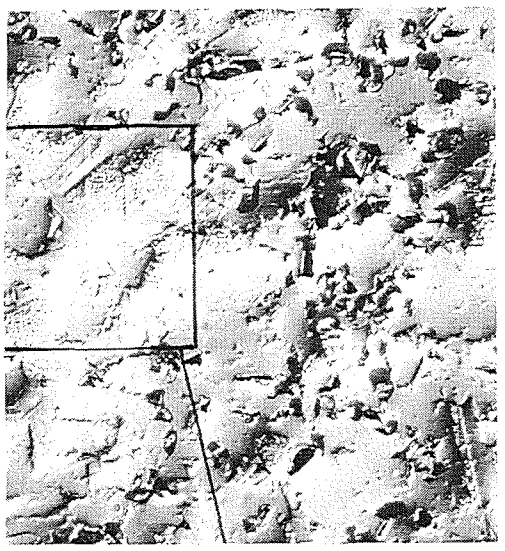

17

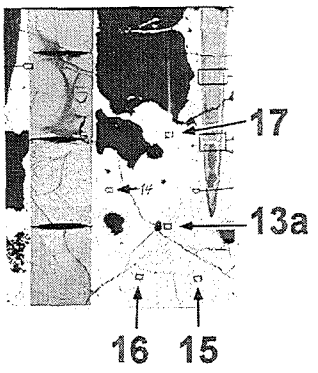

200 x

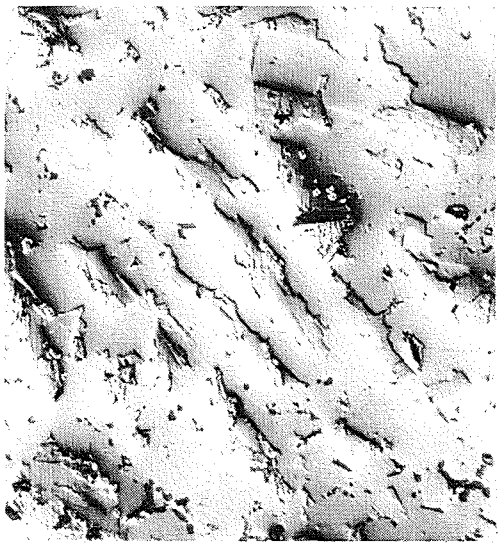

14

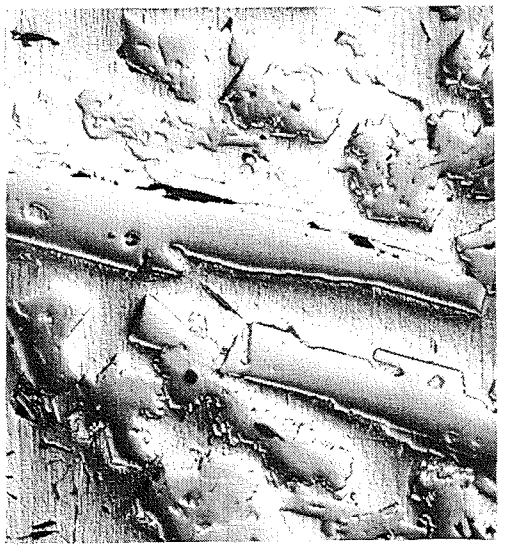

13a

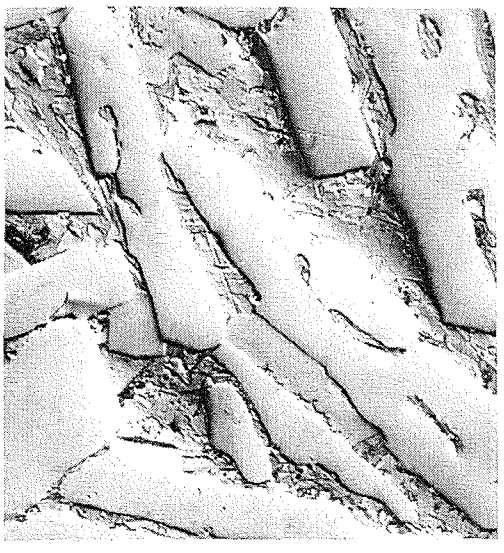

16

15

Fig. 125: CORA-7; Structure of refrozen melt

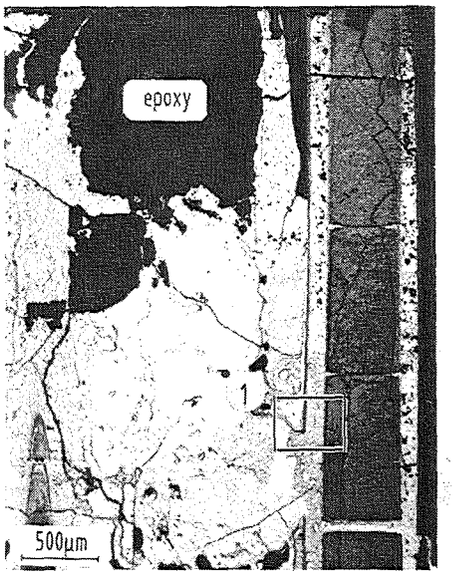

detail of longitudinal section CORA 7-f

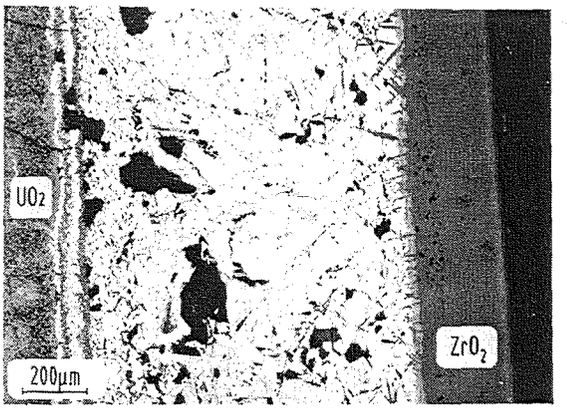

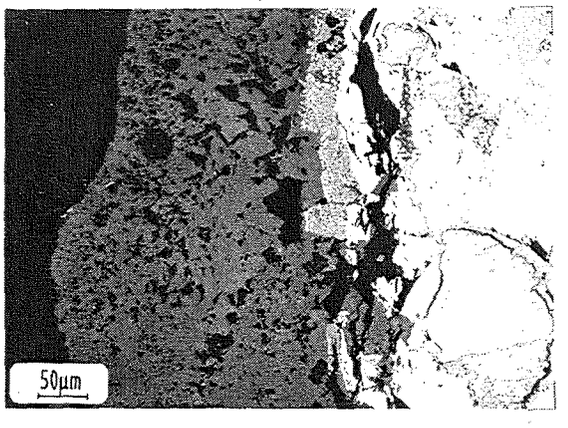

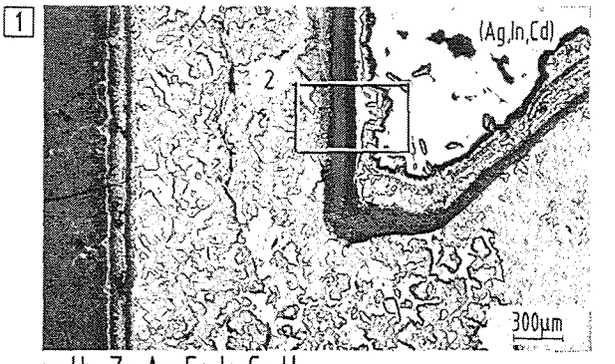

melt: Zr,Ag,Fe,In,Cr,U

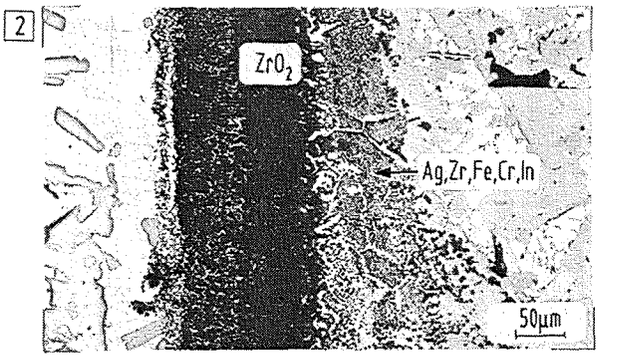

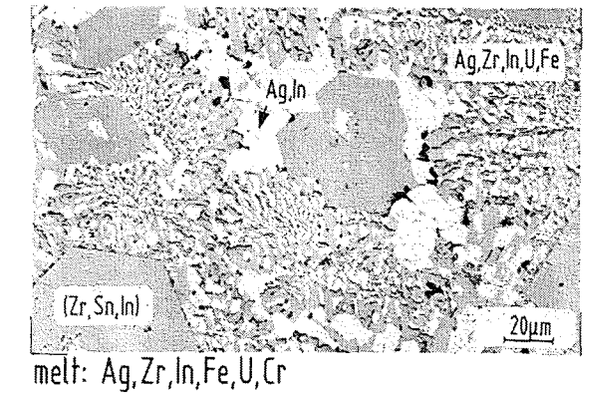

melt: Ag,Zr,In,Fe,U,Cr

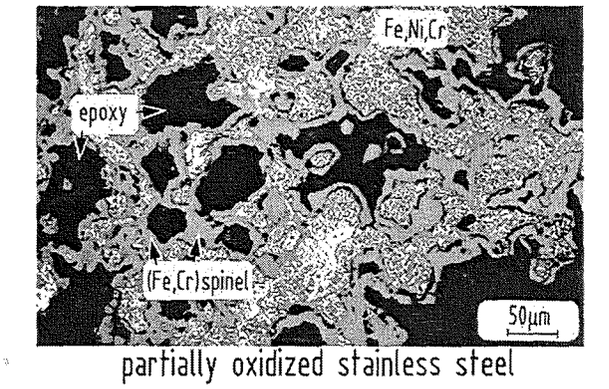

partially oxidized stainless steel

Fig. 128a: Overview: Microstructures of area 24 of the vertical cross section 482 - 516 mm; CORA7-f (see Fig. 113)

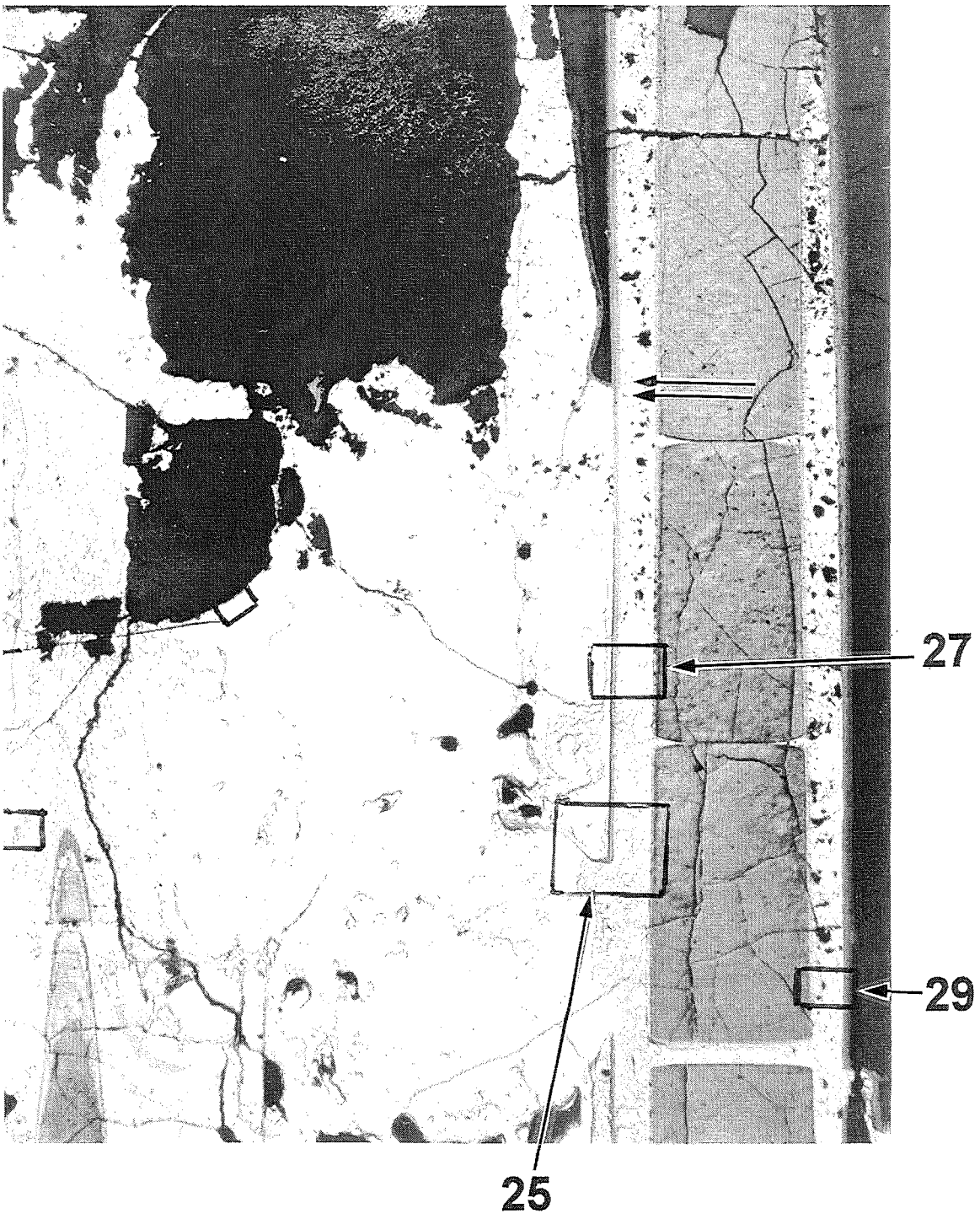

Fig. 128: CORA-7; Positions of examination of region 24

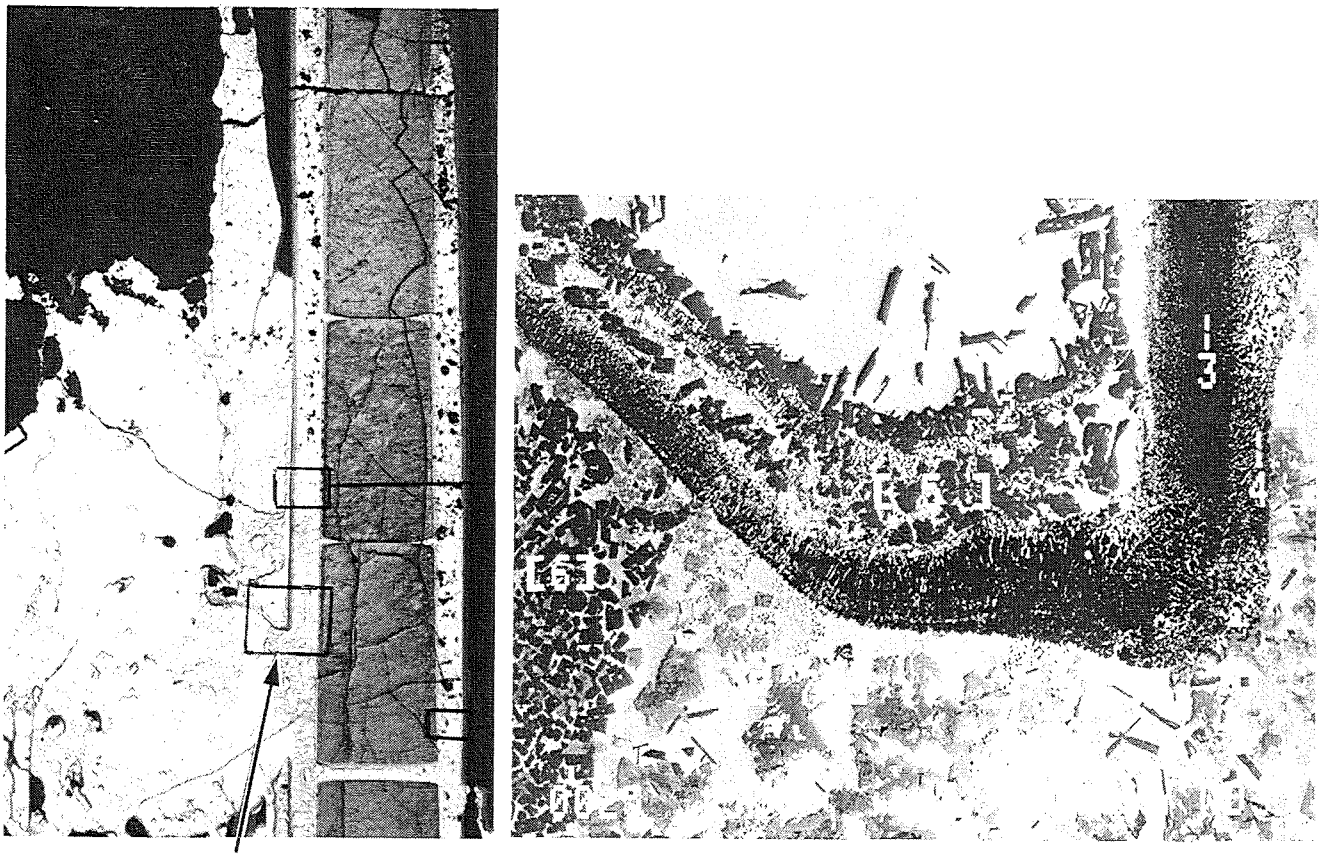

Pos.	Zr	U	Fe/Cr/Ni	Ag/In/Cd	
1				*84/14/2*	*met.*
2	*43wt%*	*2*	*38/15/2*		*met.*
3	*100*				*met.*
4	*64*	*5*		*26/4/1*	*met.*
5	*29*	*2*	*22/9/1*	*31/5/1*	*oxi.*
6	*41*	*4*	*27/8/2*	*15/3/-*	*met.*
7	*32*	*5*	*12/4/1*	*39/7/-*	*met.*

Fig. 129: CORA-7; composition around oxidised relocated melt (region 24, position25)

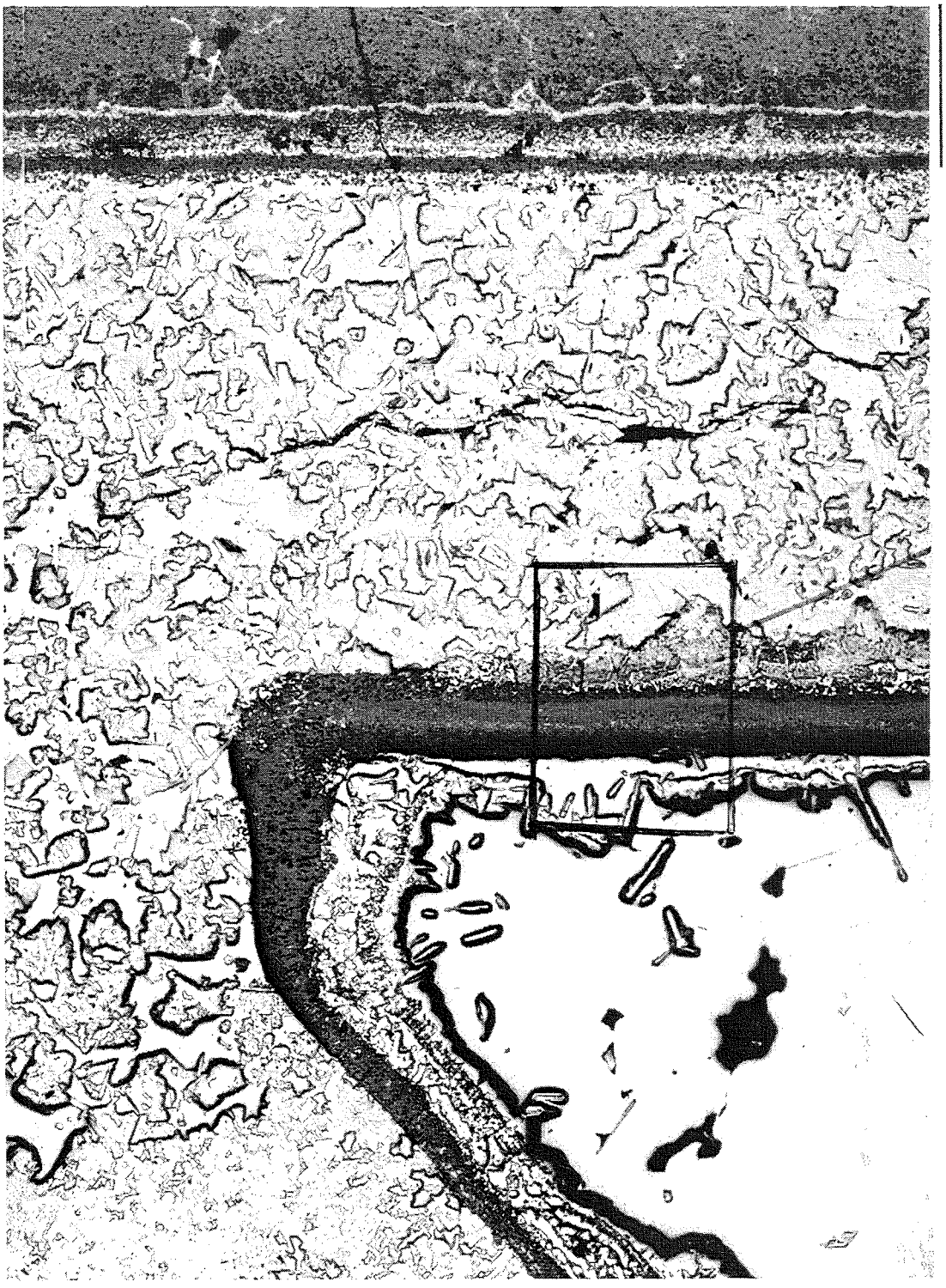

Fig. 130: CORA-7; Oxidised cladding and oxidation of relocated melt

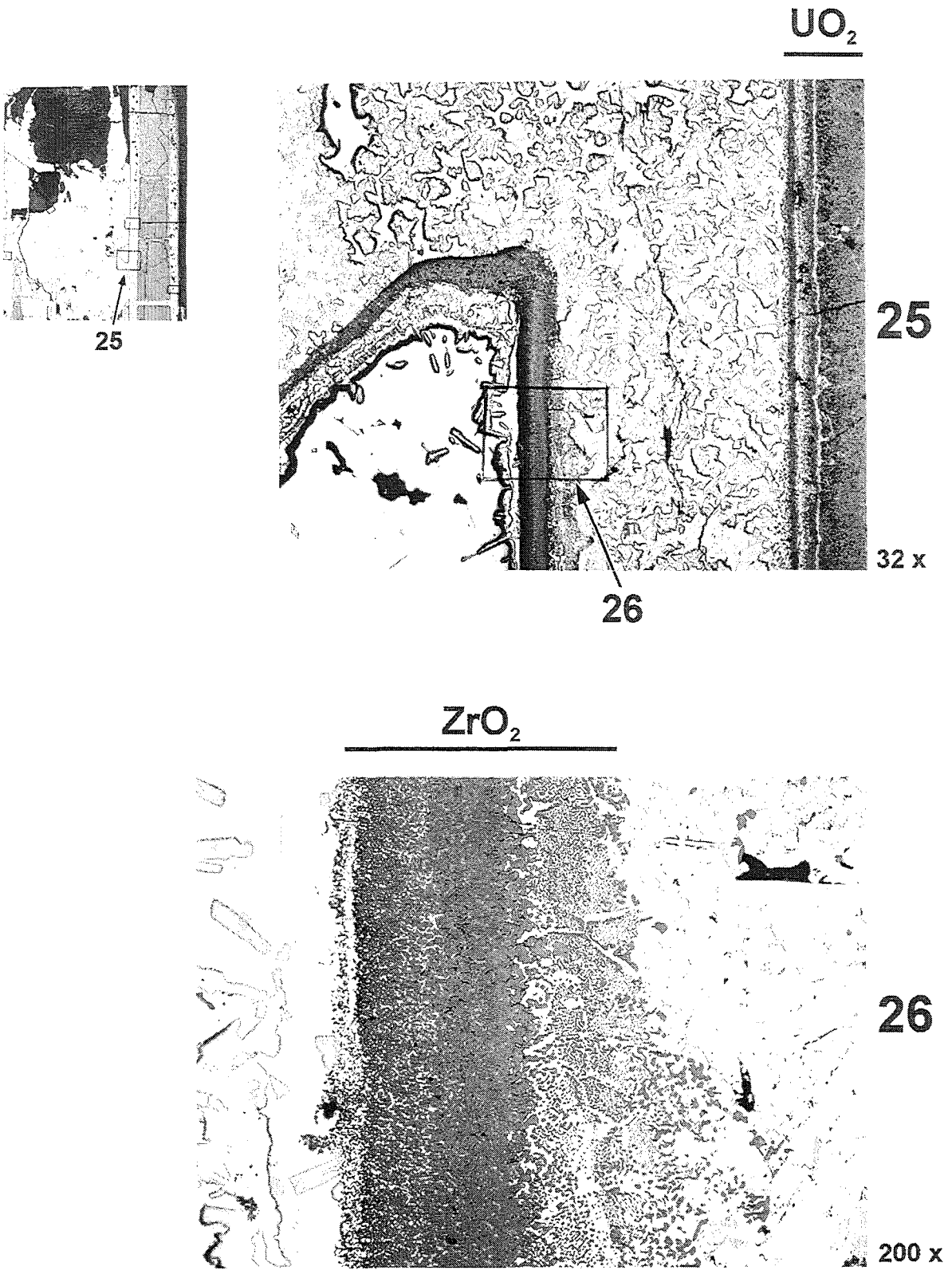

Fig. 131: CORA-7; Interaction of melt with oxidised cladding

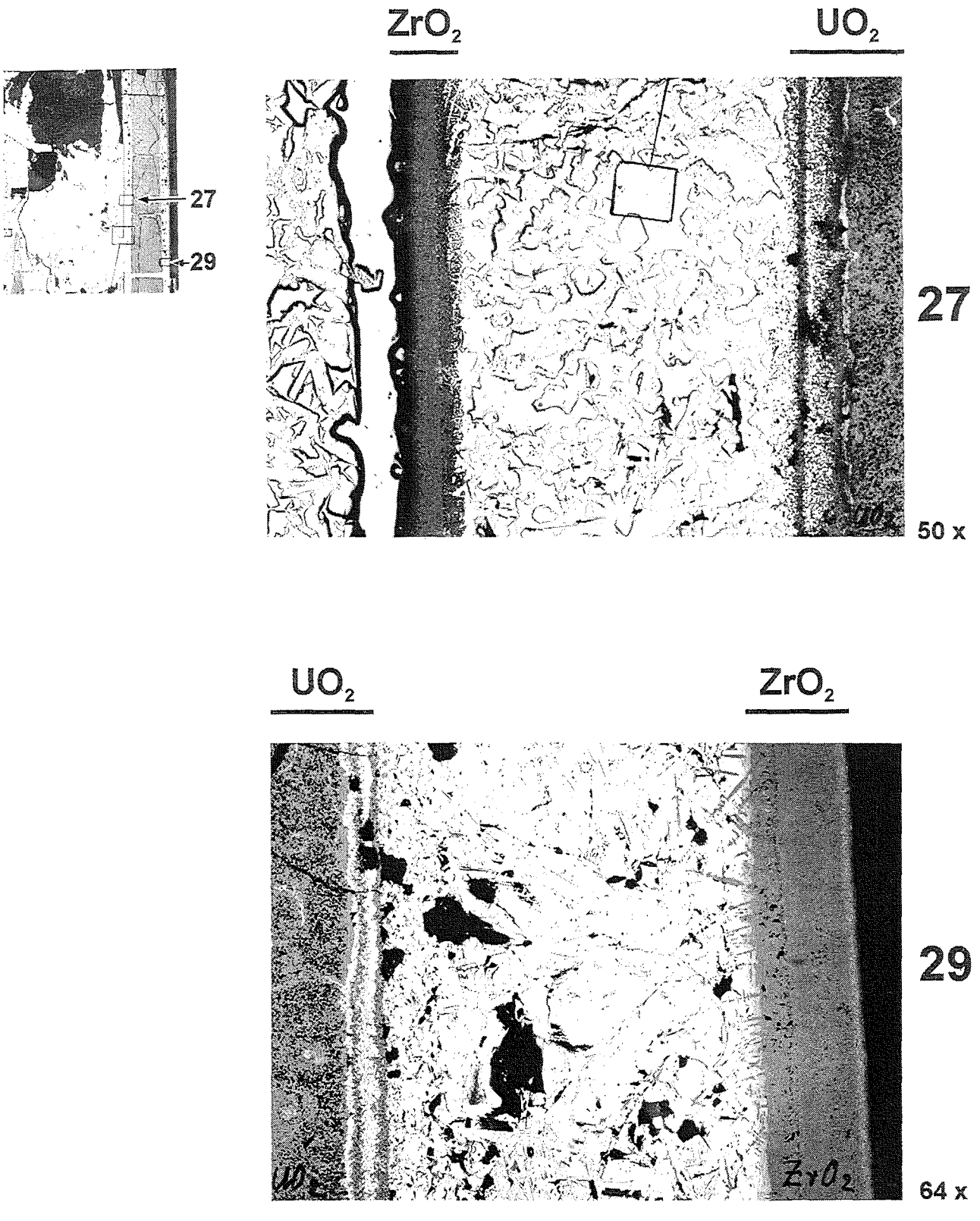

Fig. 132: CORA-7; Oxidised cladding

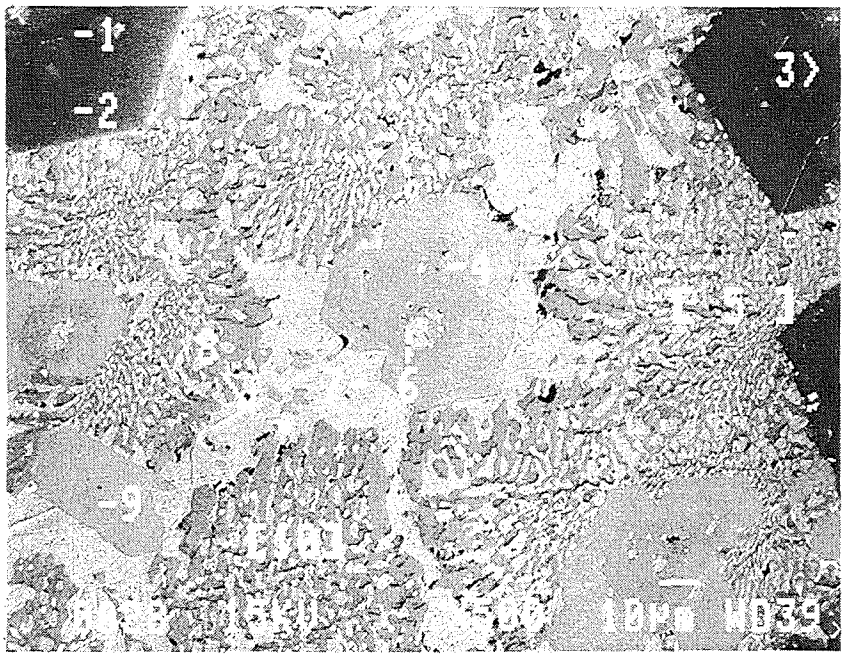

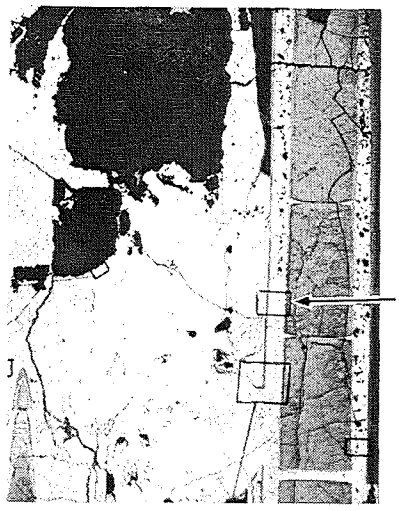

Pos.	Zr	U	Fe/Cr/Ni	Ag/In/Cd	
1	*64wt%*	*4*	*20/1*	*.4/-/-*	*oxi.*
2	*64*	*11*	*16/4/3*	*3/-/-*	*met.*
3	*85*	*15*			*oxi.*
4	*55*			*-/8/-*	*met.*
5	*23*	*4*	*2/-/1*	*58/12/.4*	*met.*
6				*95/4/2*	*met.*
7				*93/6/2*	*met.*
8		*96*	*4/1/-*		*met.*
9	*51*	*1*		*7/9/-*	*met.*
10	*21*	*2*	*2/-/1*	*62/11/-*	*met.*
Int.	*34*	*5*	*7/2/1*	*41/8/.6*	*met.*

Fig. 133: Composition of melt inside the oxidised cladding

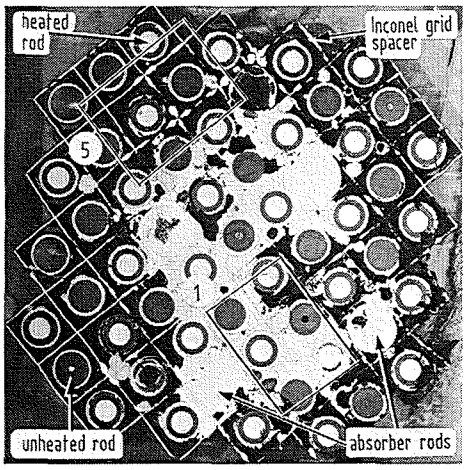

cross-section CORA 7-04 (480mm) 2mm

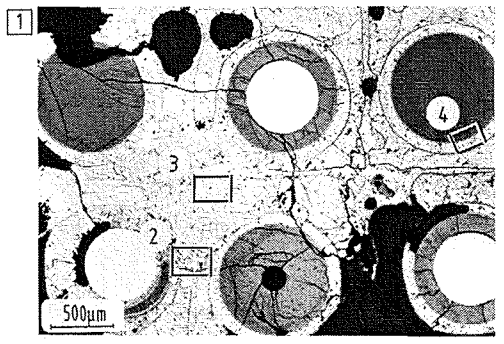

relocated solidified metallic melt

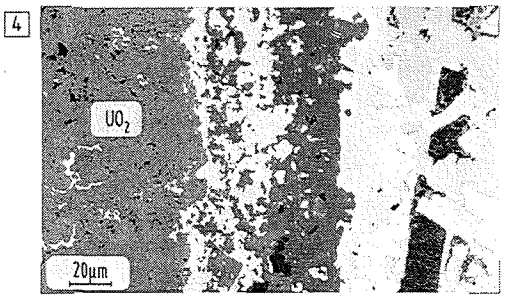

chemical attack of UO_2 pellet

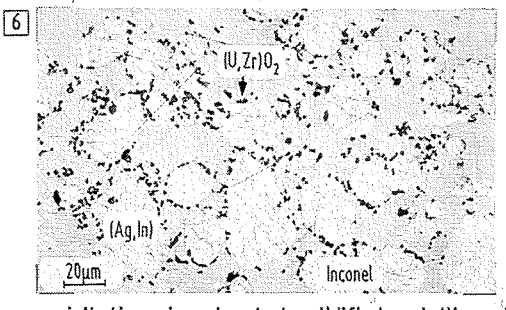

precipitations in relocated solidified metallic melt

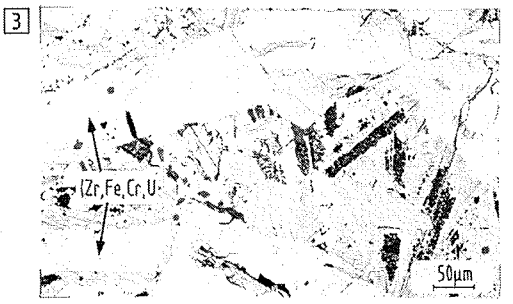

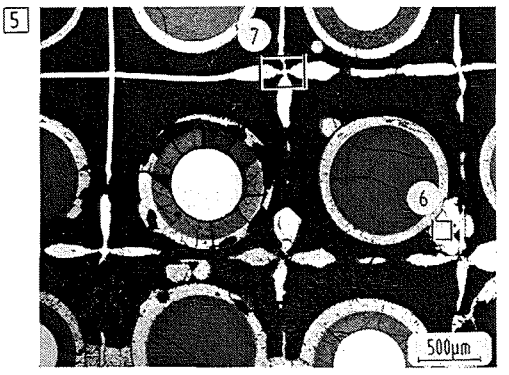

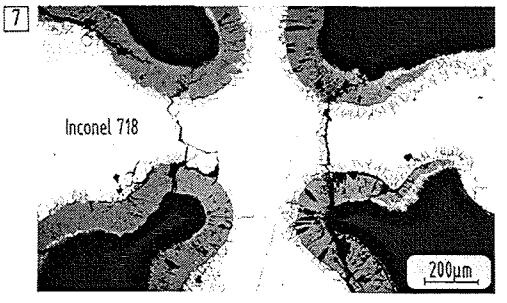

partially oxidized Inconel grid spacer

Fig. 135a: Overview: Material behavior at the inconel grid spacer cross section CORA7-04 (480 mm)

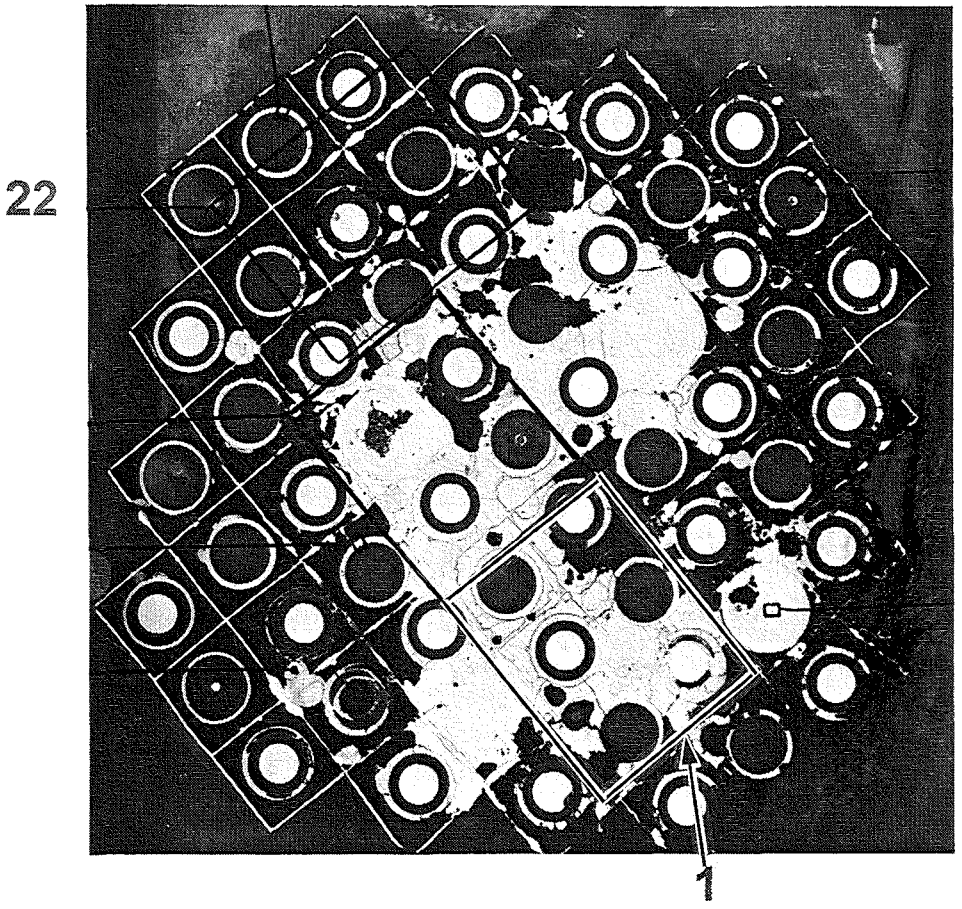

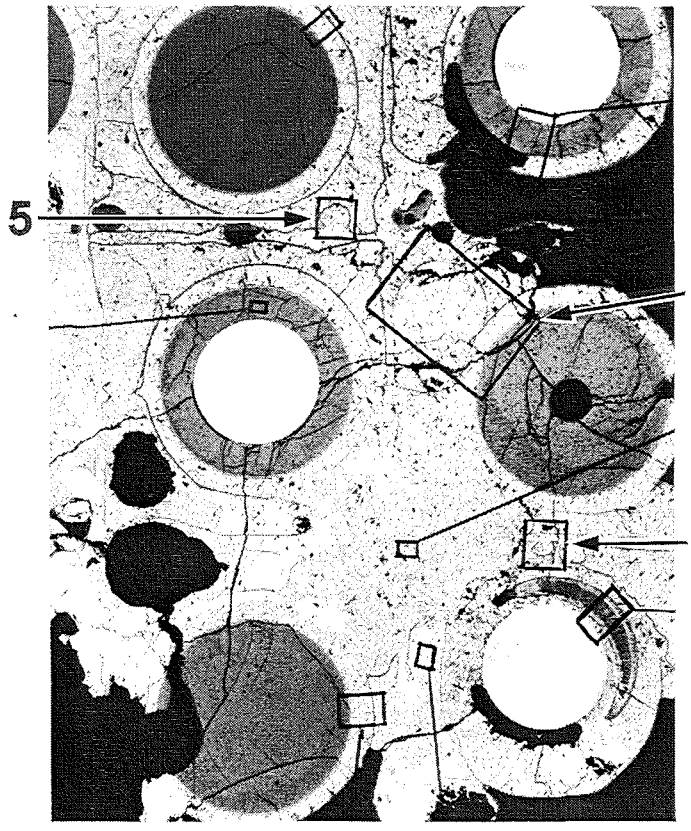

Fig. 135: CORA-7; Cross section at 480 mm used for further examinations

4 50 x

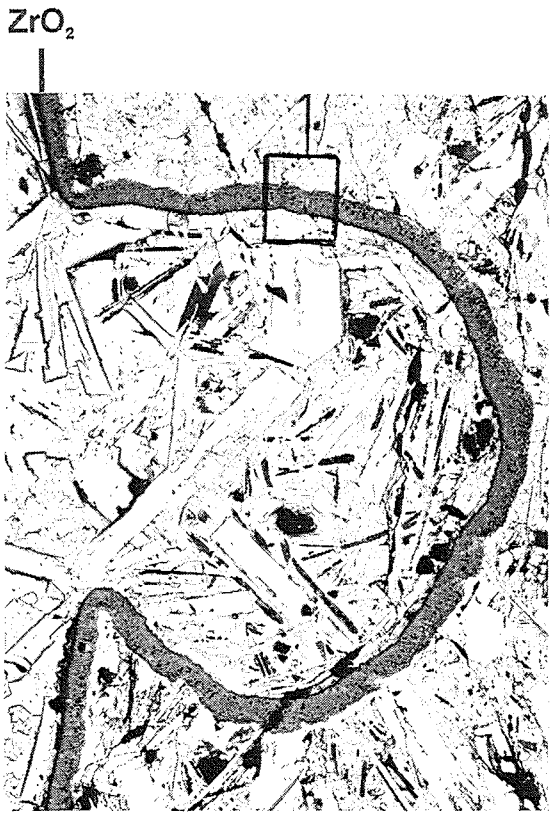

5 50 x

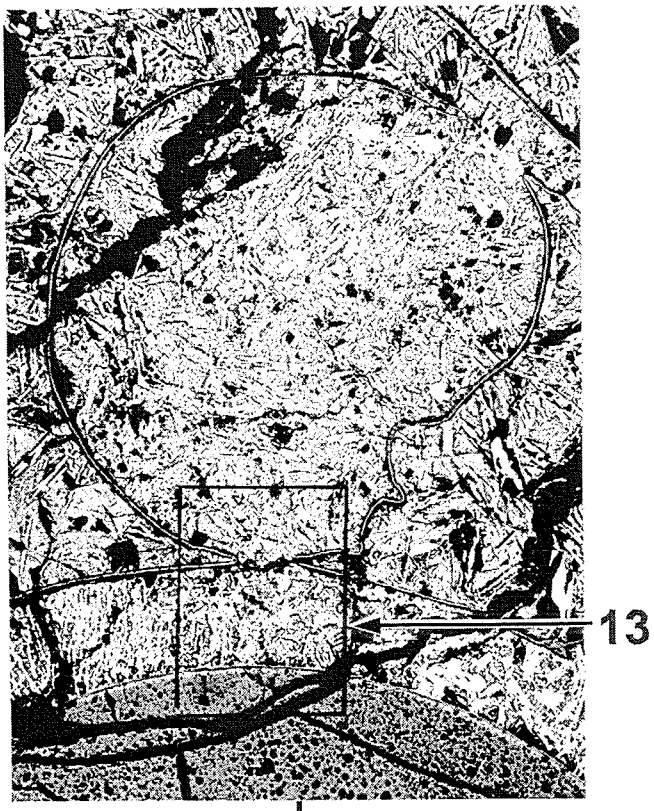

12 16 x

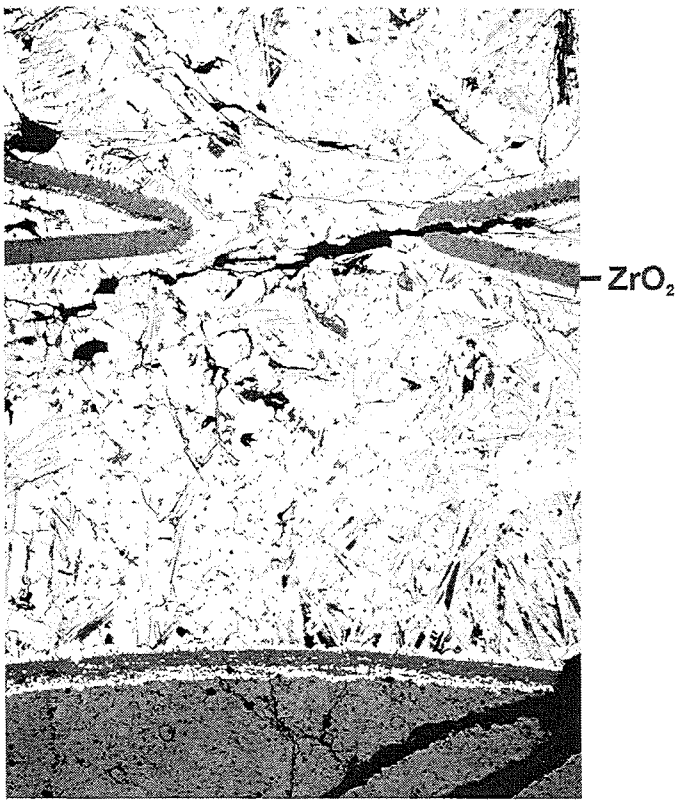

13 64 x

Fig. 136: CORA-7; Oxidation of relocated material (480 mm)

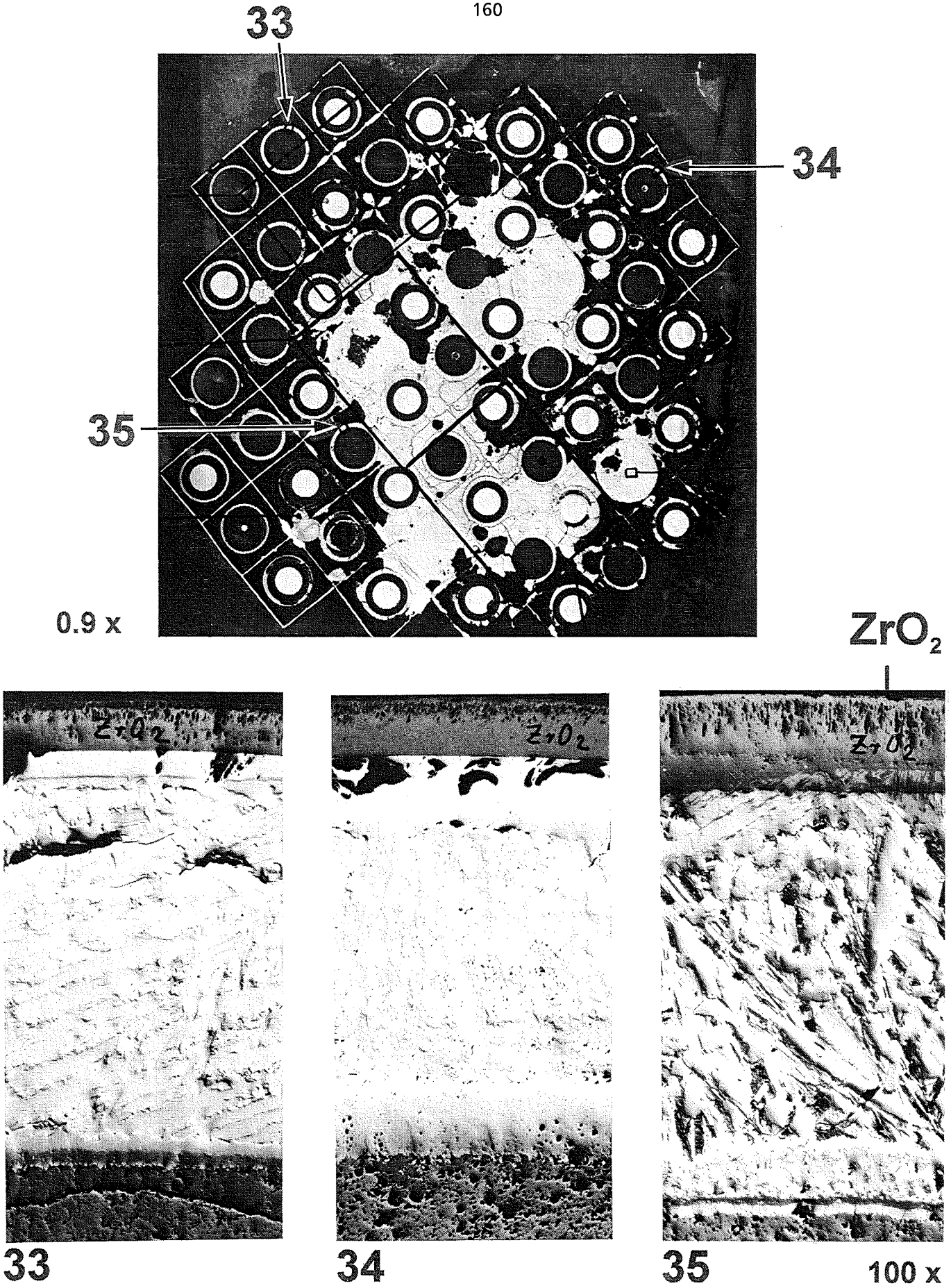

Fig. 138: CORA-7; Oxidation of the cladding at different positions within the bundle (480 mm elevation)

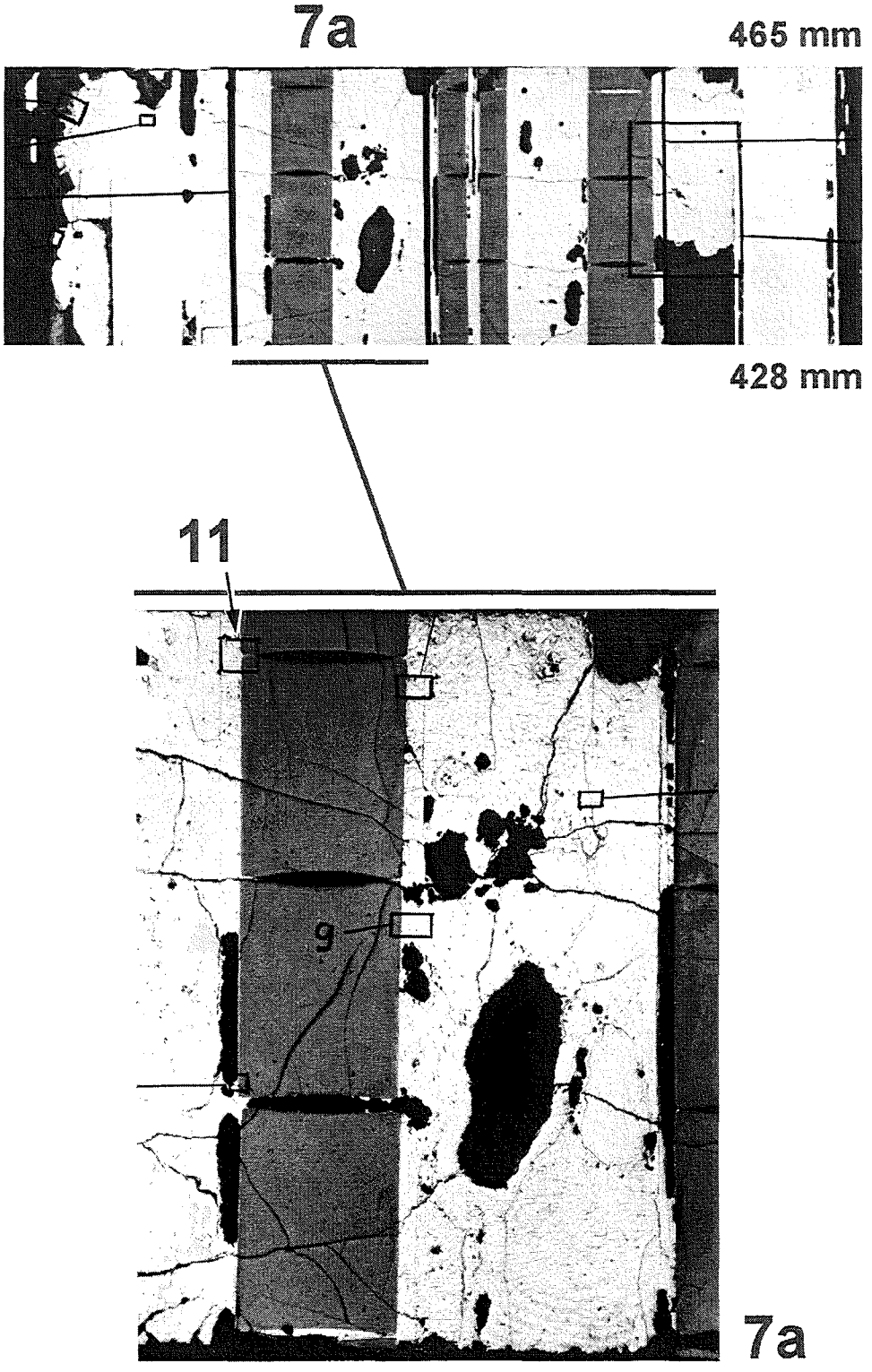

Fig. 140: CORA-7; Vertical cross section 428 - 465 mm and region 7a

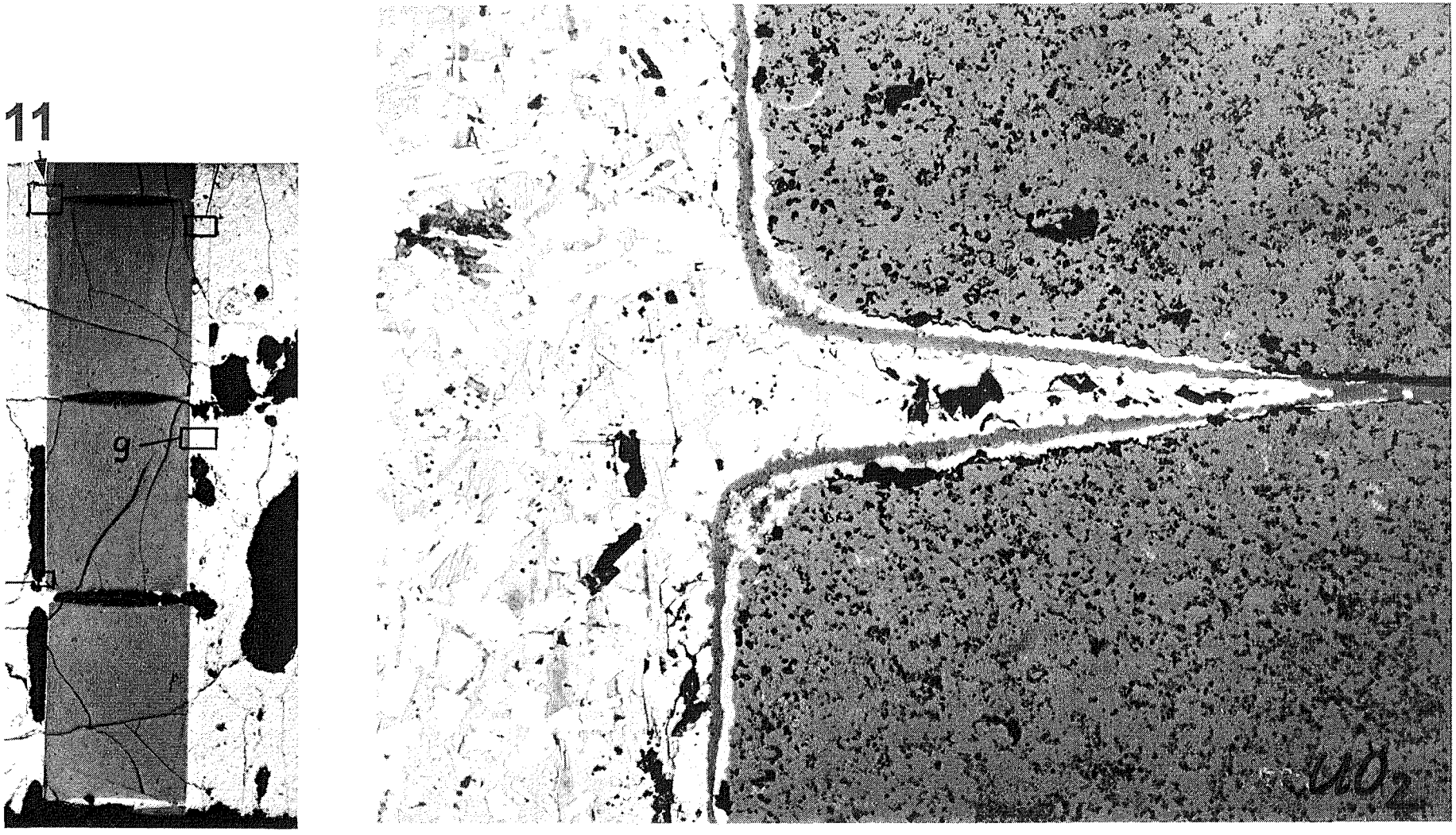

Fig. 141: CORA-7; Melt penetration into pellet gap (region 7a, position 11)

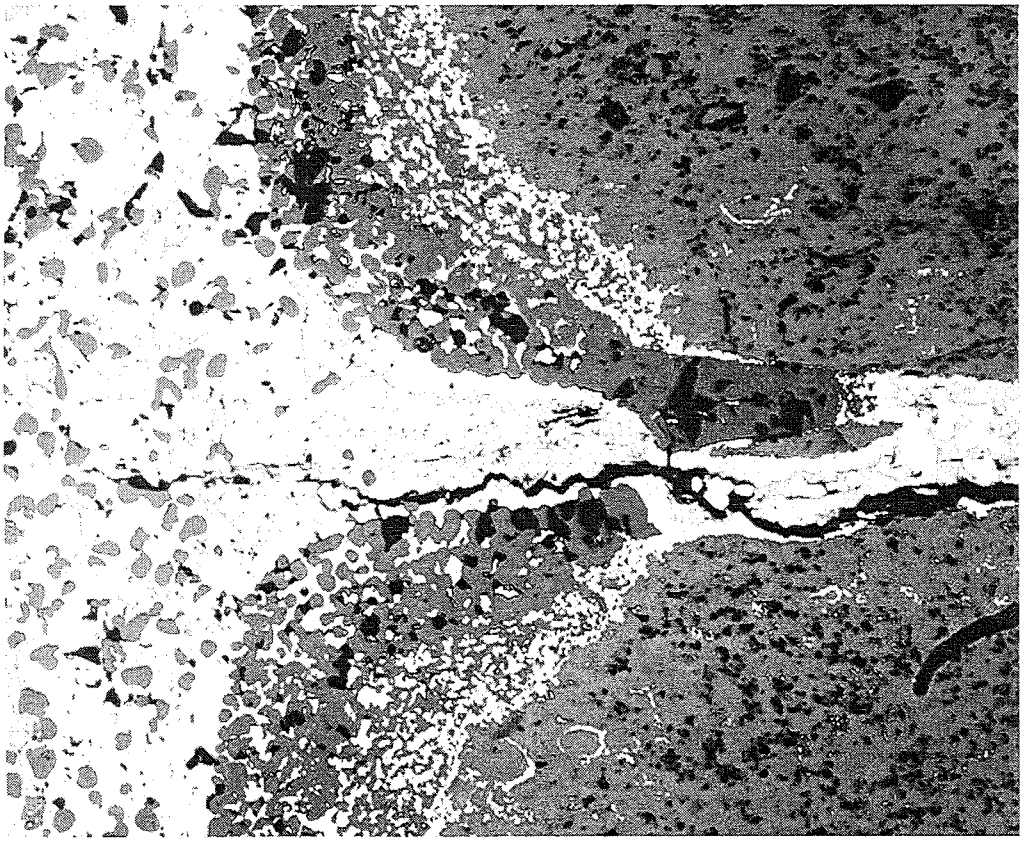

512 mm

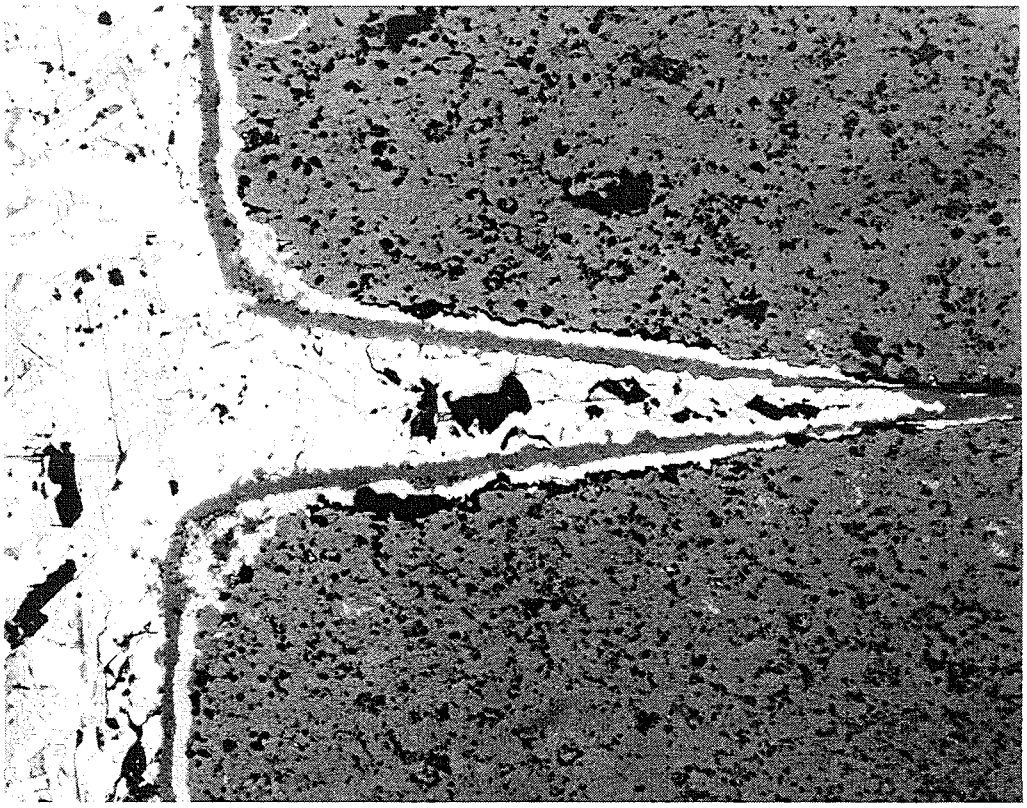

462 mm

Fig. 142: CORA-7; Comparison of melt / pellet interaction at 512 and 462 mm

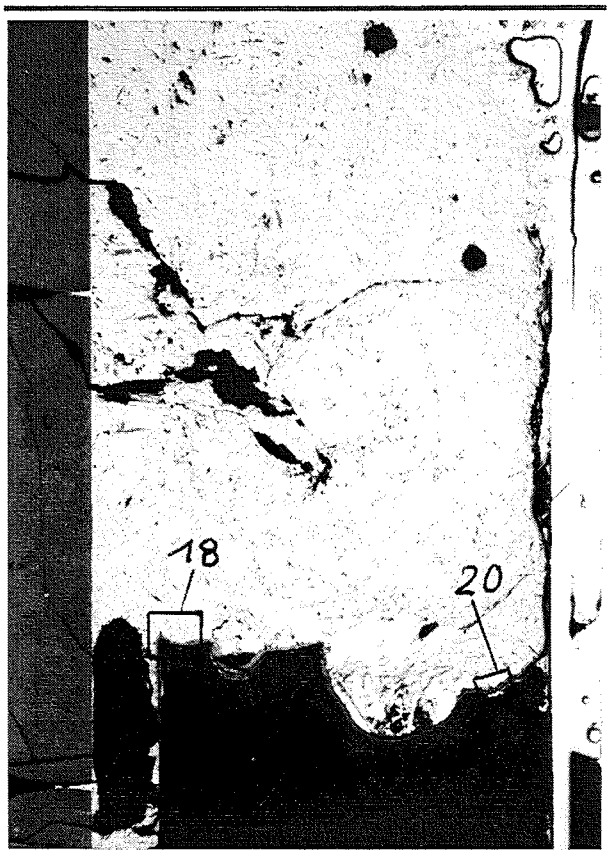

Fig. 143: CORA-7; Region 17 of vertical cross section (428 - 465 mm) used in further investigations (see Fig. 109)

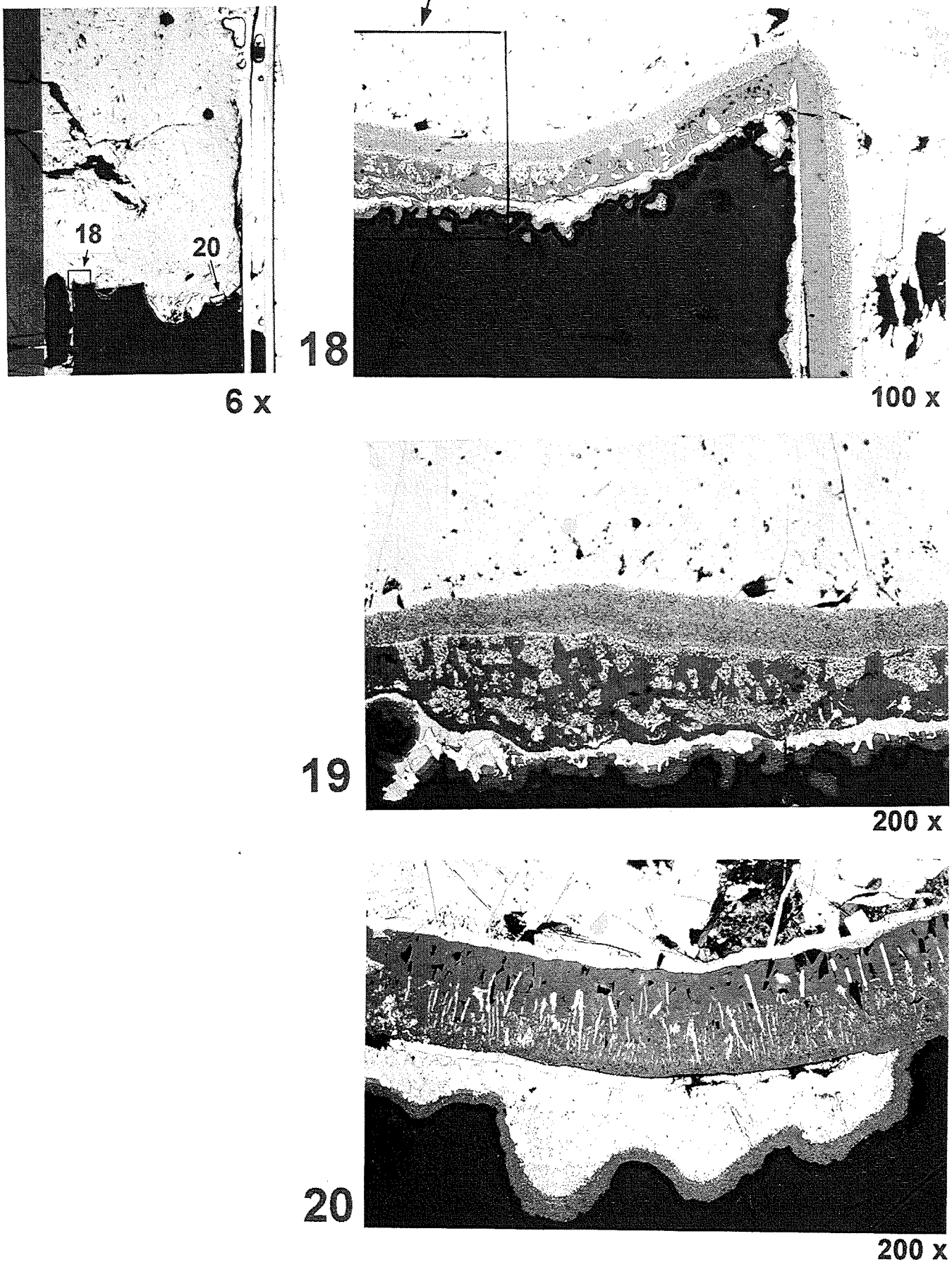

Fig. 144: CORA-7;Oxidation of relocated melt (region 17)

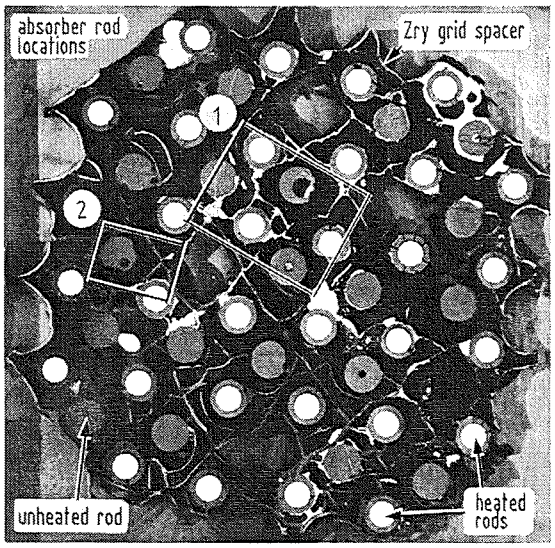

cross-section CORA 7-07 (863mm) 1mm

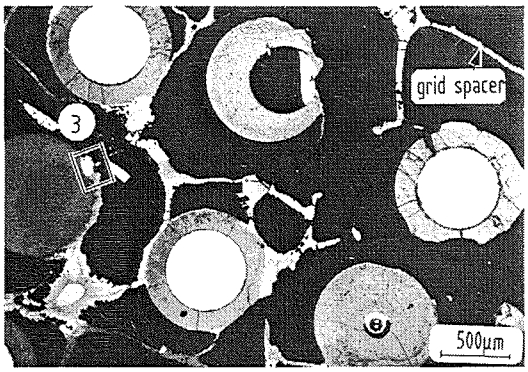

declad UO_2 fuel pellets

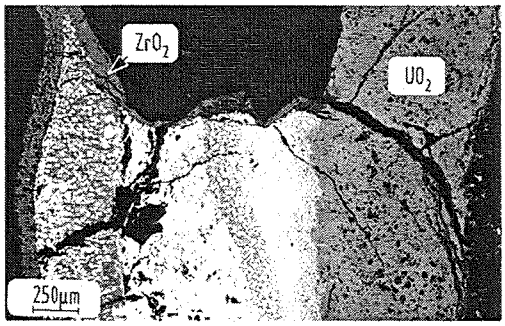

molten Zircaloy/UO_2 interaction

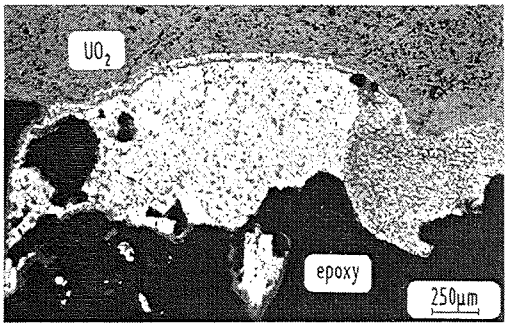

localized UO_2 attack by molten Zry

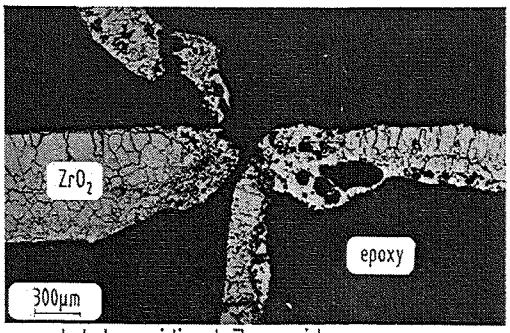

completely oxidized Zry grid spacer

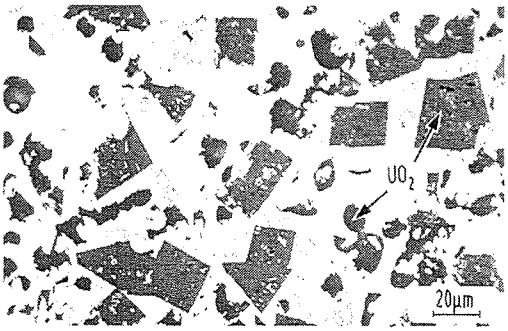

metallic melt with ceramic precipitations

accumulation of solid fragments

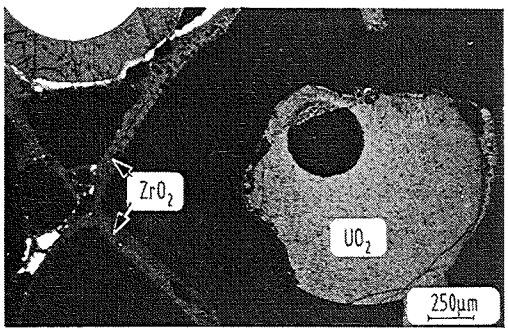

partially dissolved UO_2 pellet

Fig. 145a: Overview: Material behavior at the zircaloy grid spacer cross section CORA7-07 (863 mm)

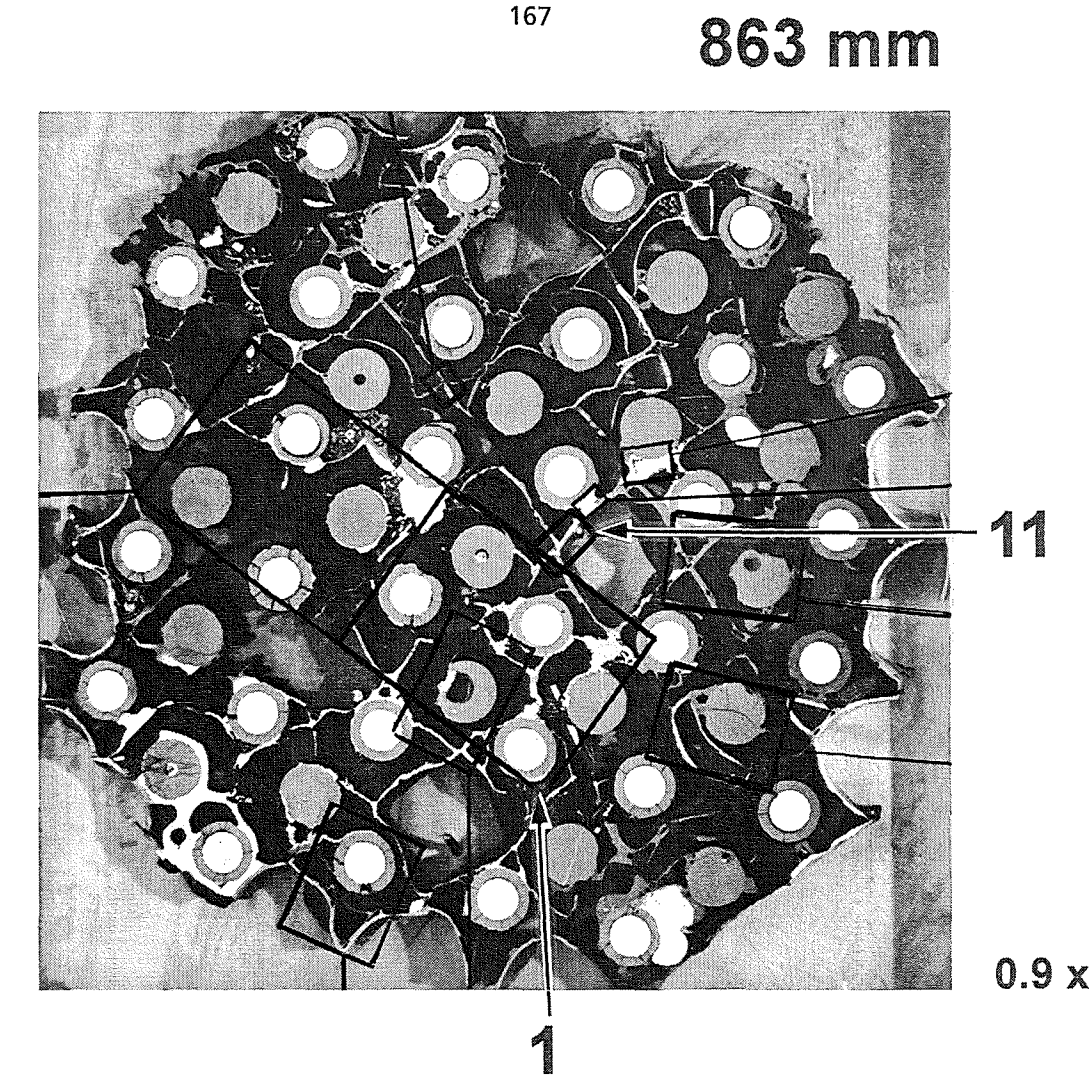

Fig. 145: CORA-7; Cross section at 863 mm and region 1 used for further examination

863 mm

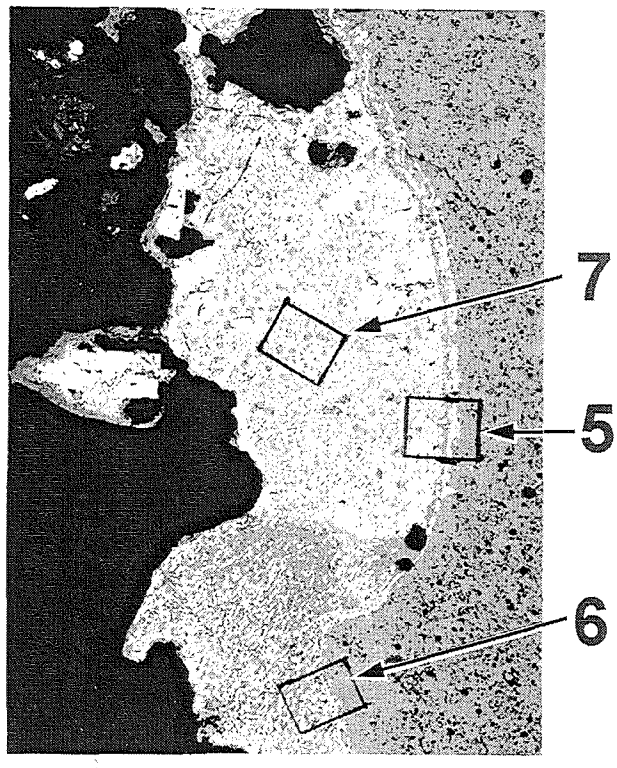

4 40 x

7 500 x

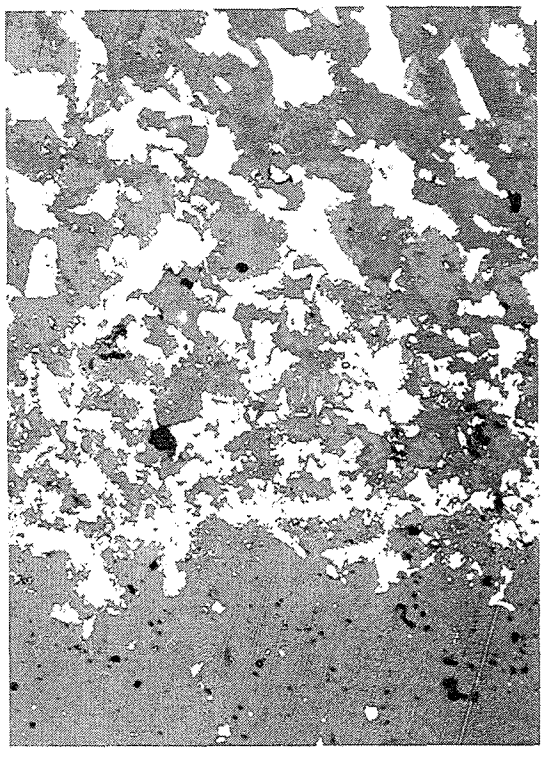

6 500 x

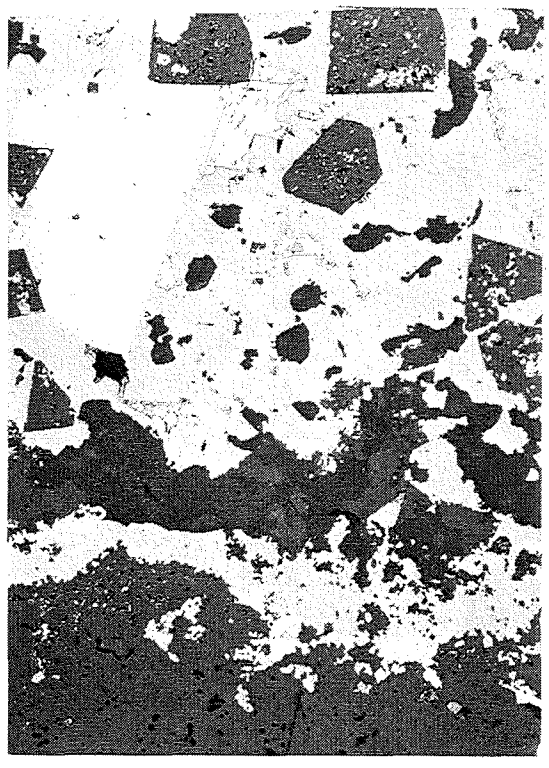

5 500 x

Fig. 146: CORA-7; UO_2 / Zry interaction (region 1, position 4)

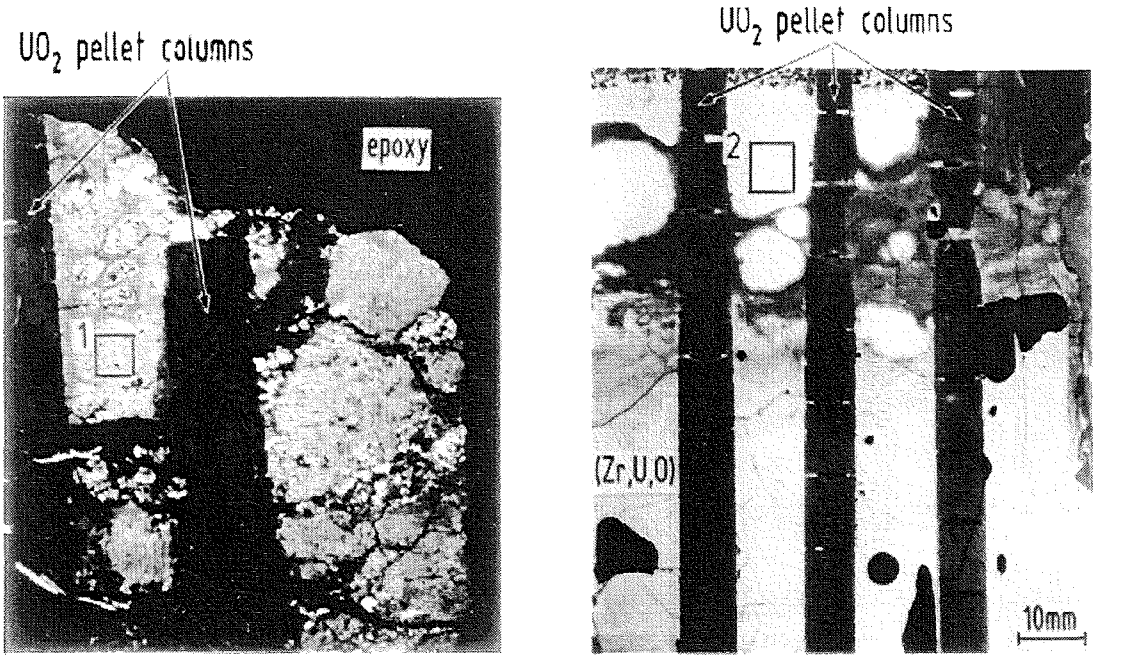

TMI-2 core bore specimen K9-P1/F

CORA bundle vertical cross-section 3-b

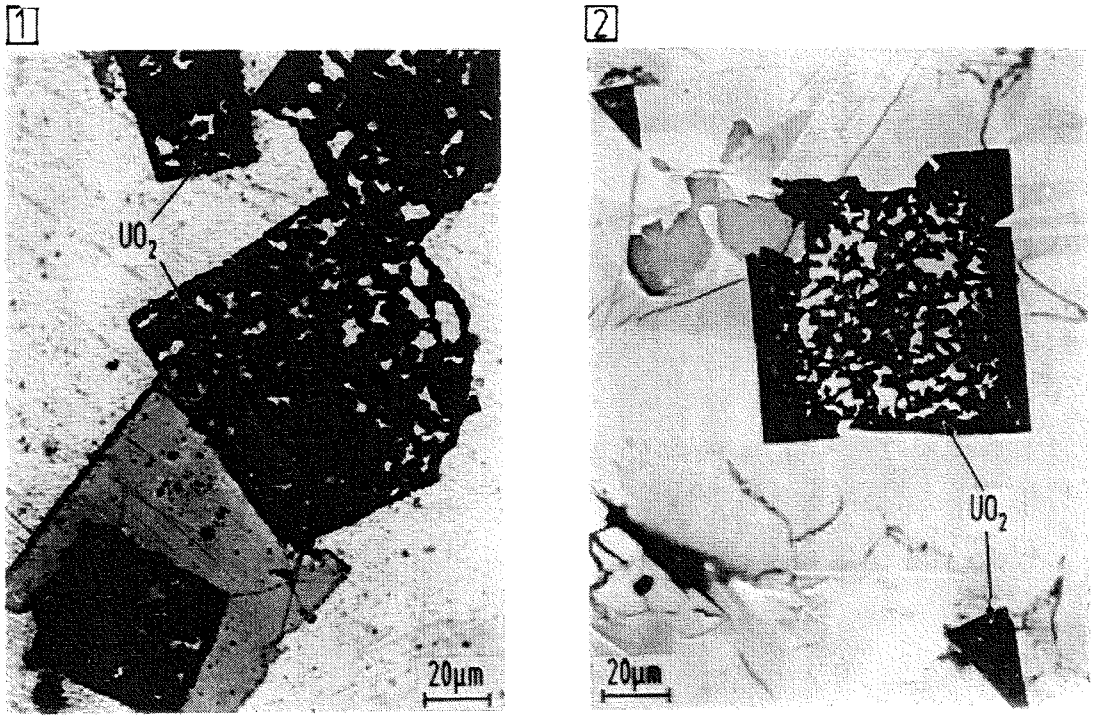

UO_2 particle dissolution by metallic melt

Fig. 146a: Comparison of microstructure of TMI-2 core bore specimen K9-P1/F and CORA-3 vertical cross section 3-b

Appendix A

Pre-heat phase CORA-7

Figures A1 - A17

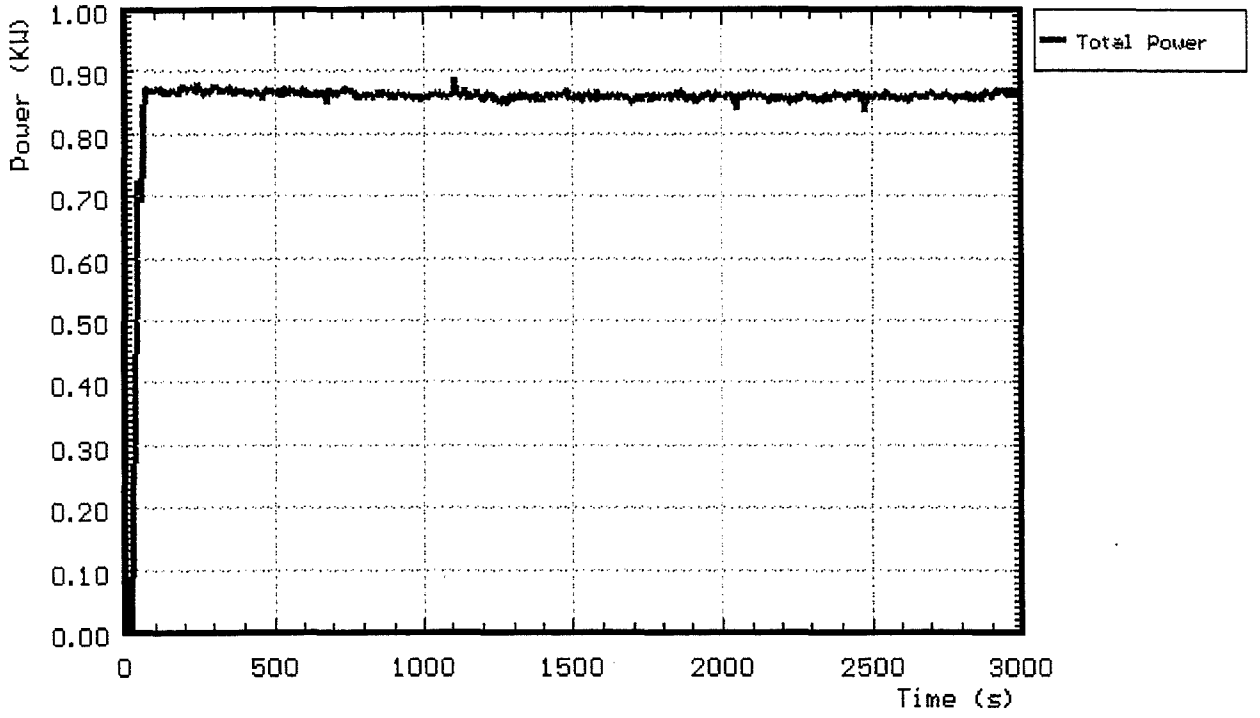

Fig.A1: CORA-7; Power input during pre-heat phase

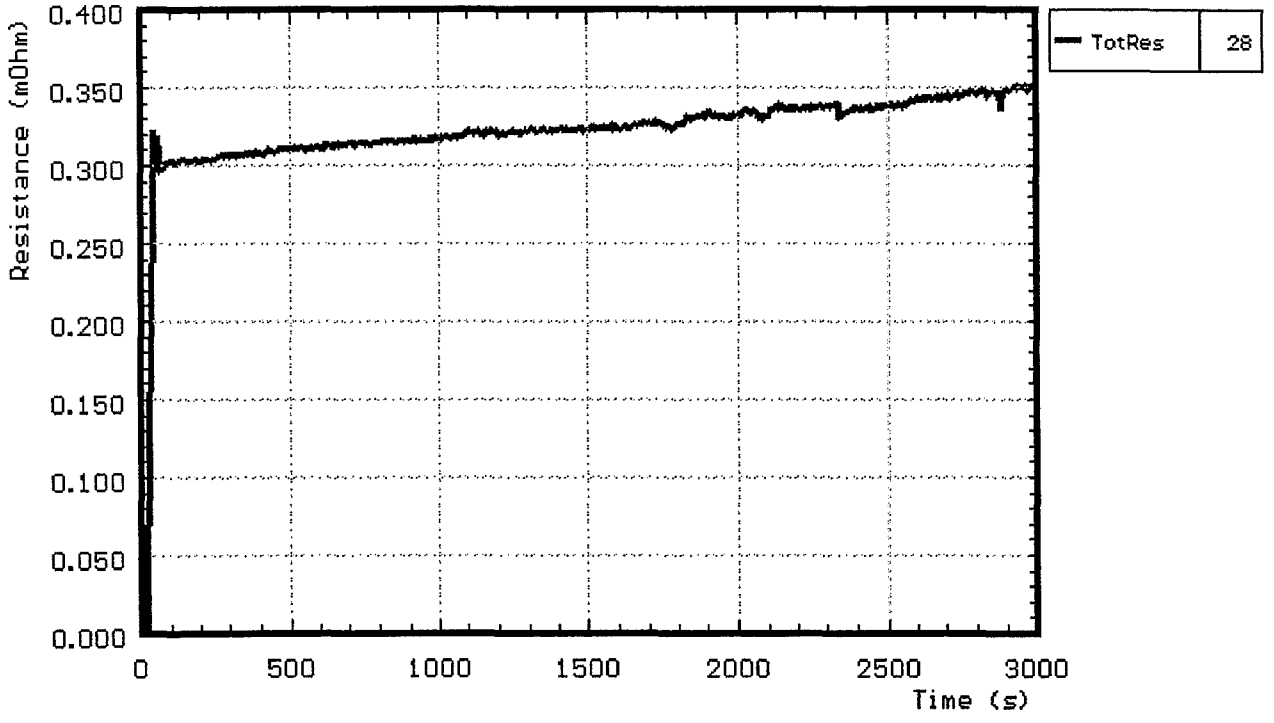

Fig. A2: CORA-7; Resistance of bundle during pre-heat phase

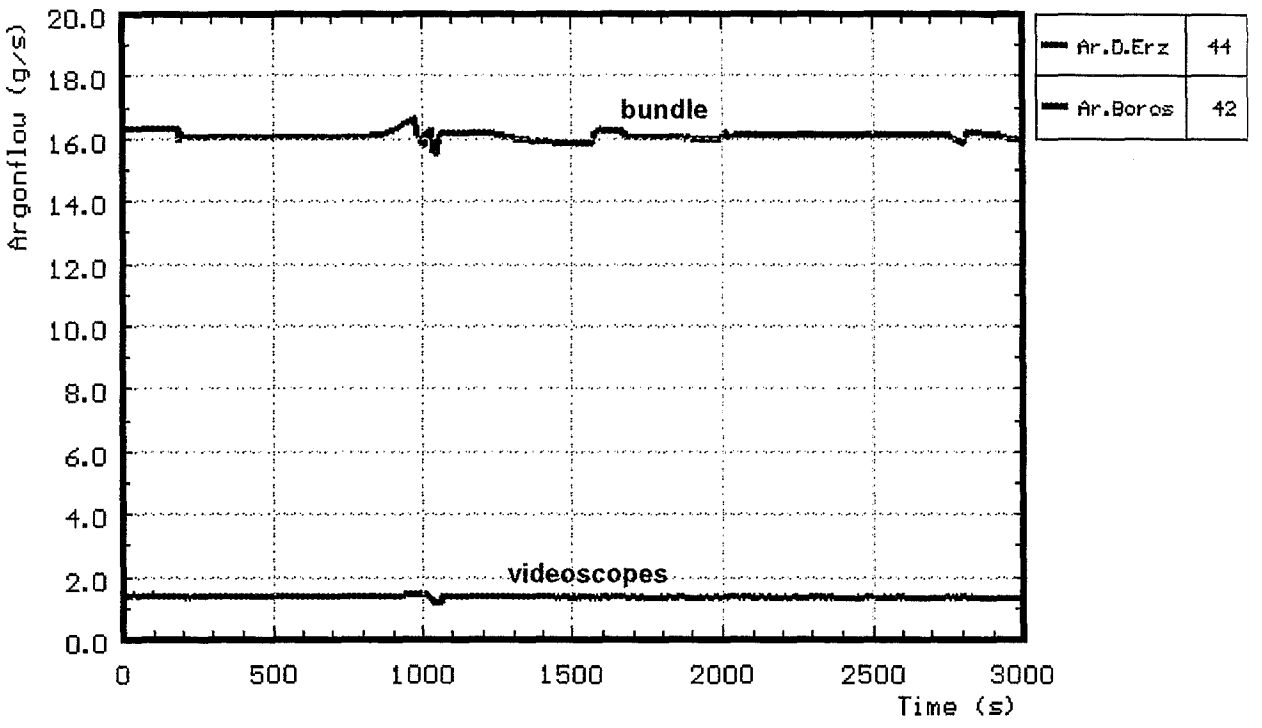

Fig.A3: CORA-7; Argon input prior to test

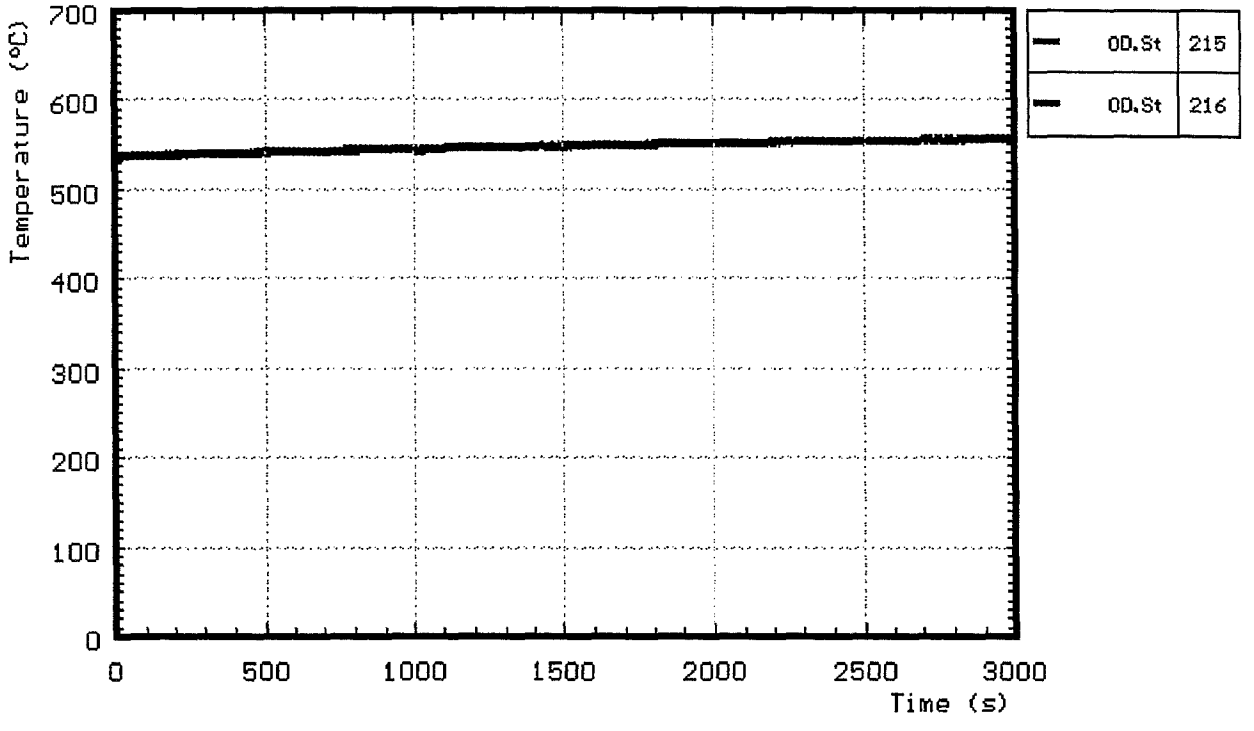

Fig. A4: CORA-7; Temperatures at steam inlet; pre-heat phase

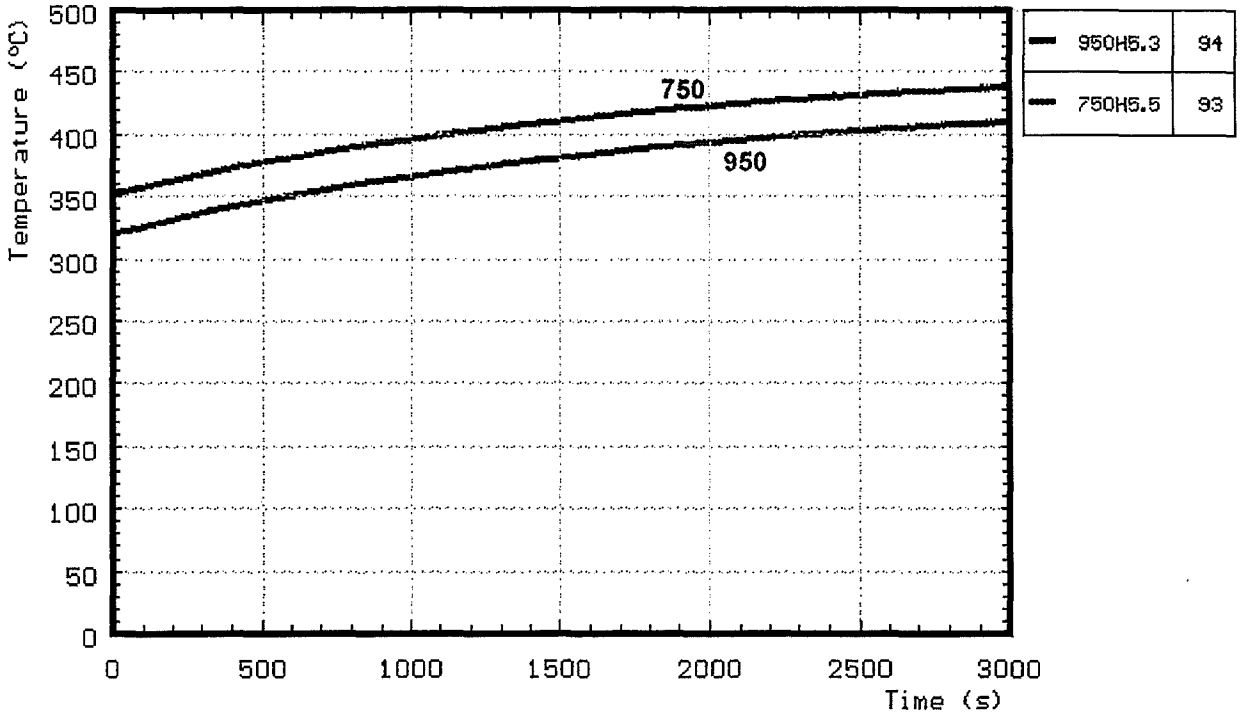

Fig. A5: CORA-7; Temperatures of heated rods; pre-heat phase

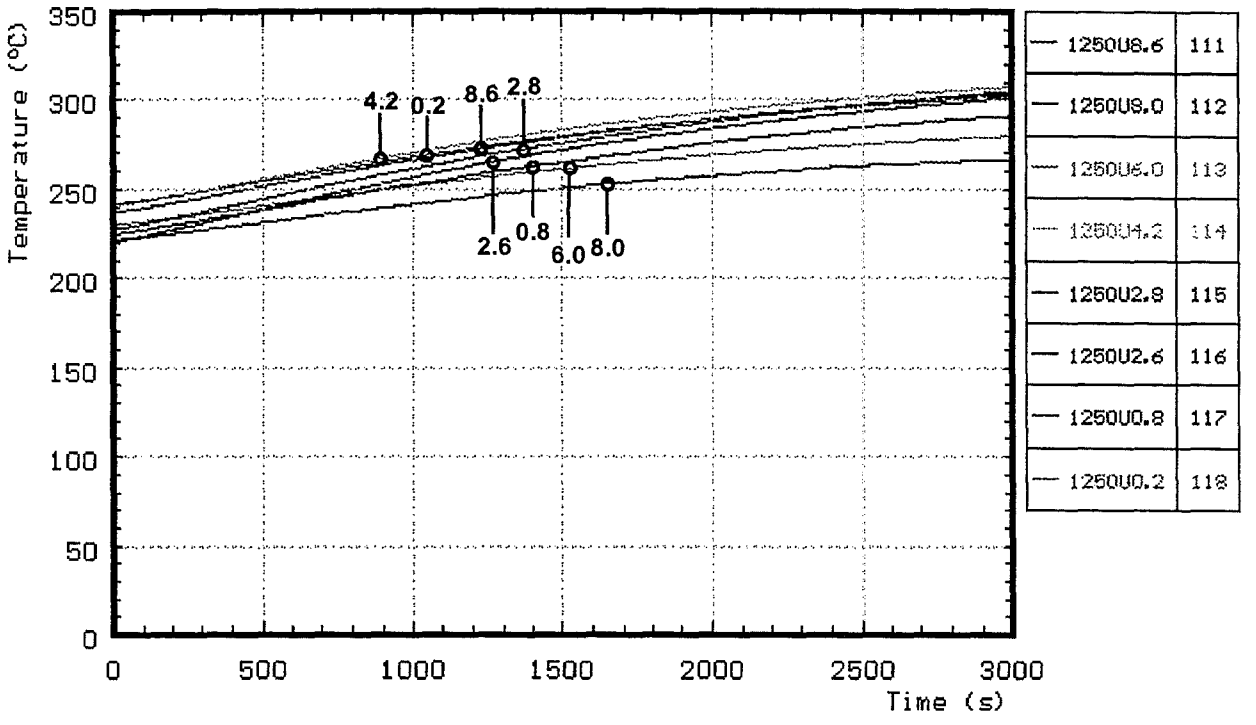

Fig. A6: CORA-7; Temperatures of unheated rods, 1250 mm elevation; pre-heat phase

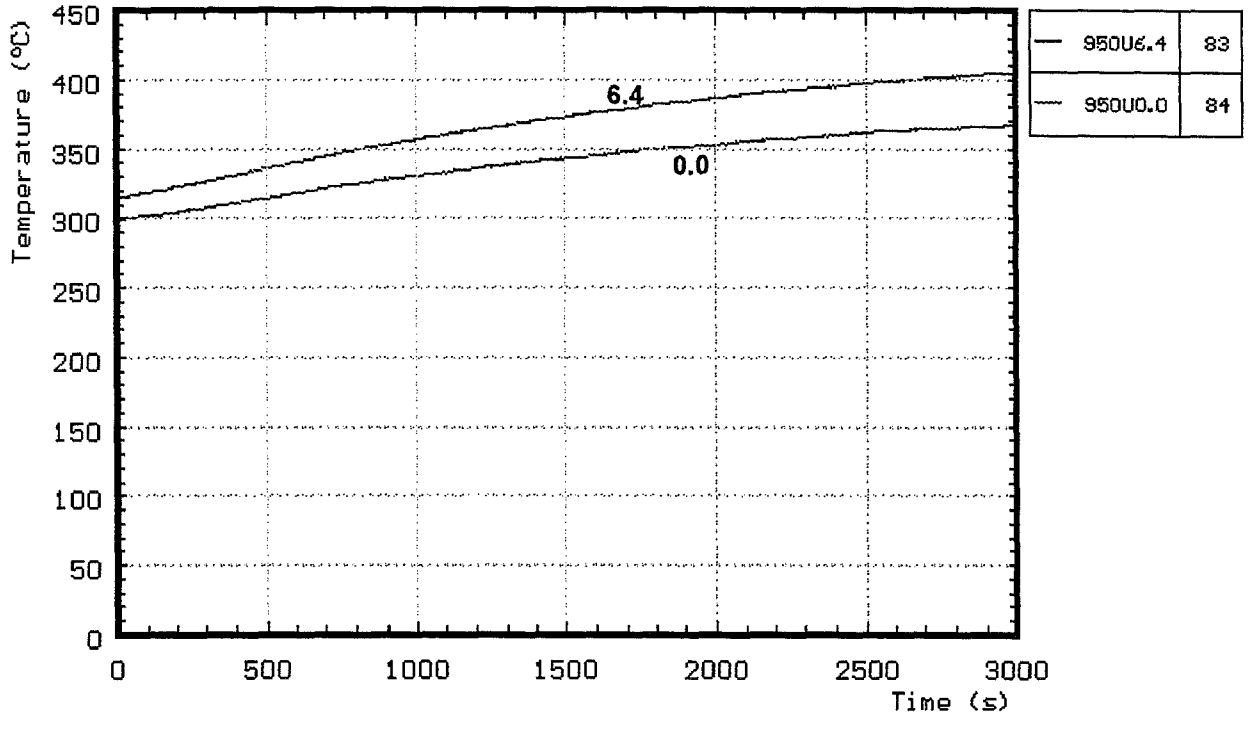

Fig. A7: CORA-7; Temperatures of unheated rods, 950 mm elevation; pre-heat phase

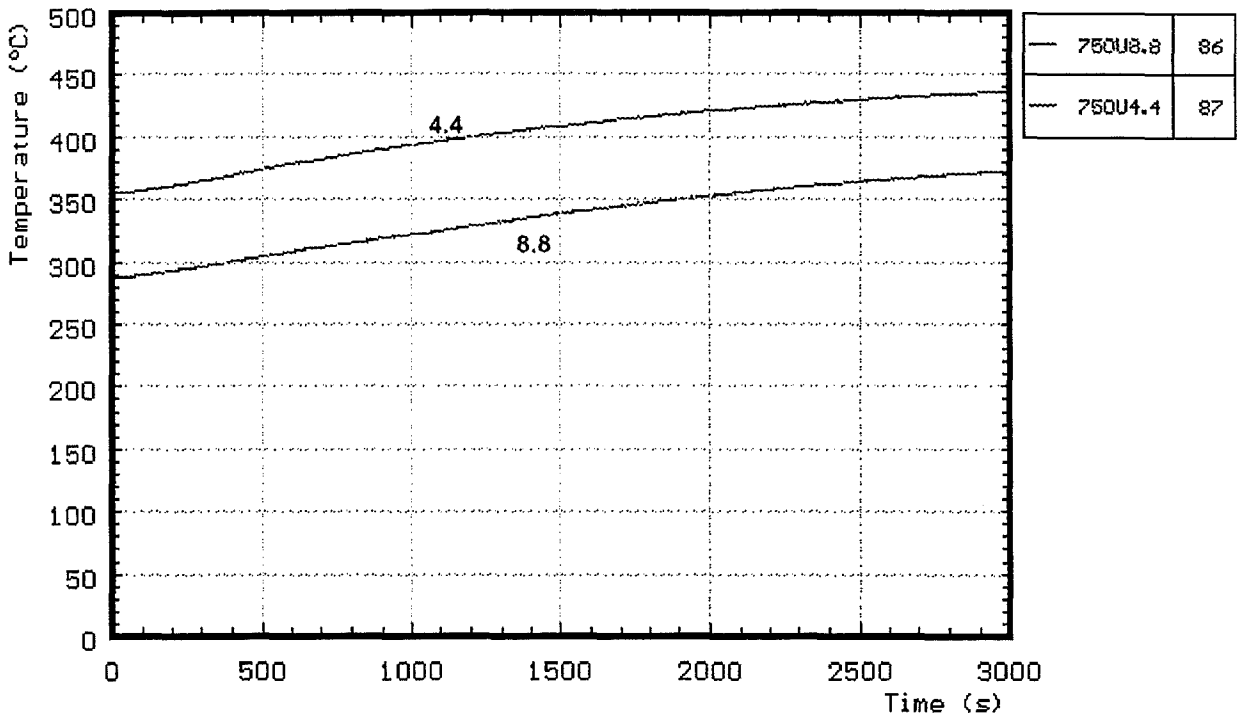

Fig. A8: CORA-7; Temperatures of unheated rods, 750 mm elevation; pre-heat phase

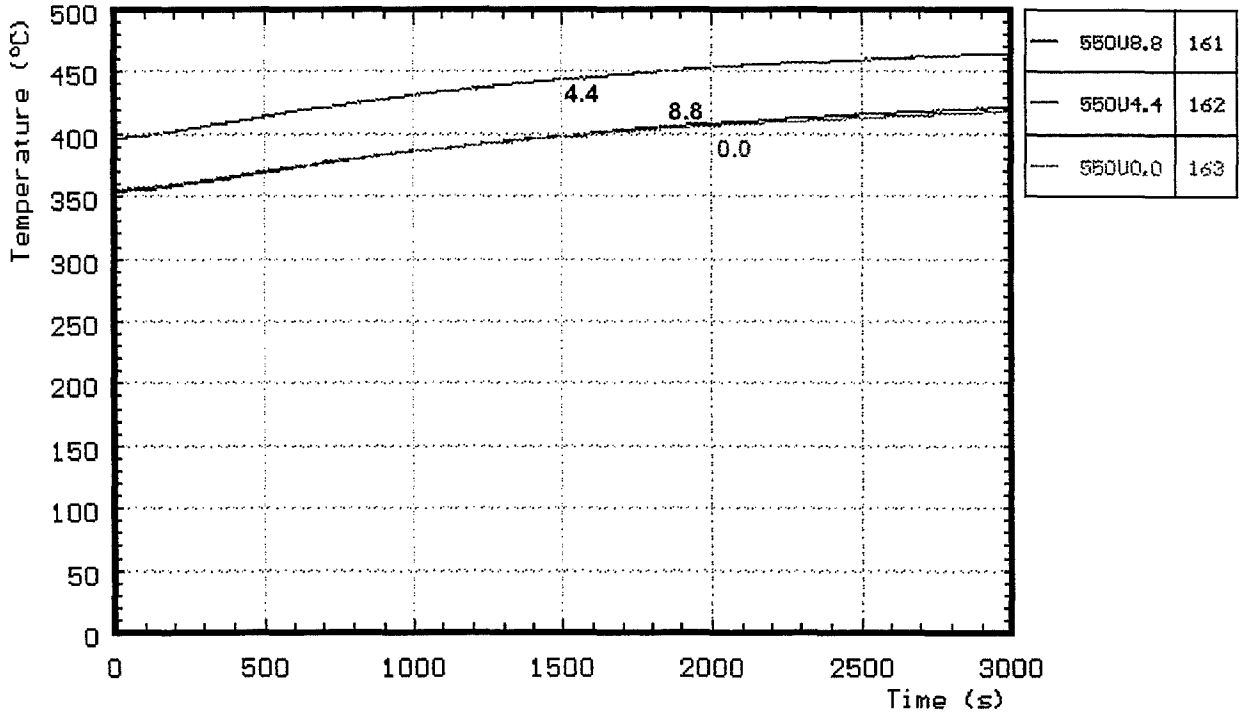

Fig. A9: CORA-7; Temperatures of unheated rods, 550 mm elevation; pre-heat phase

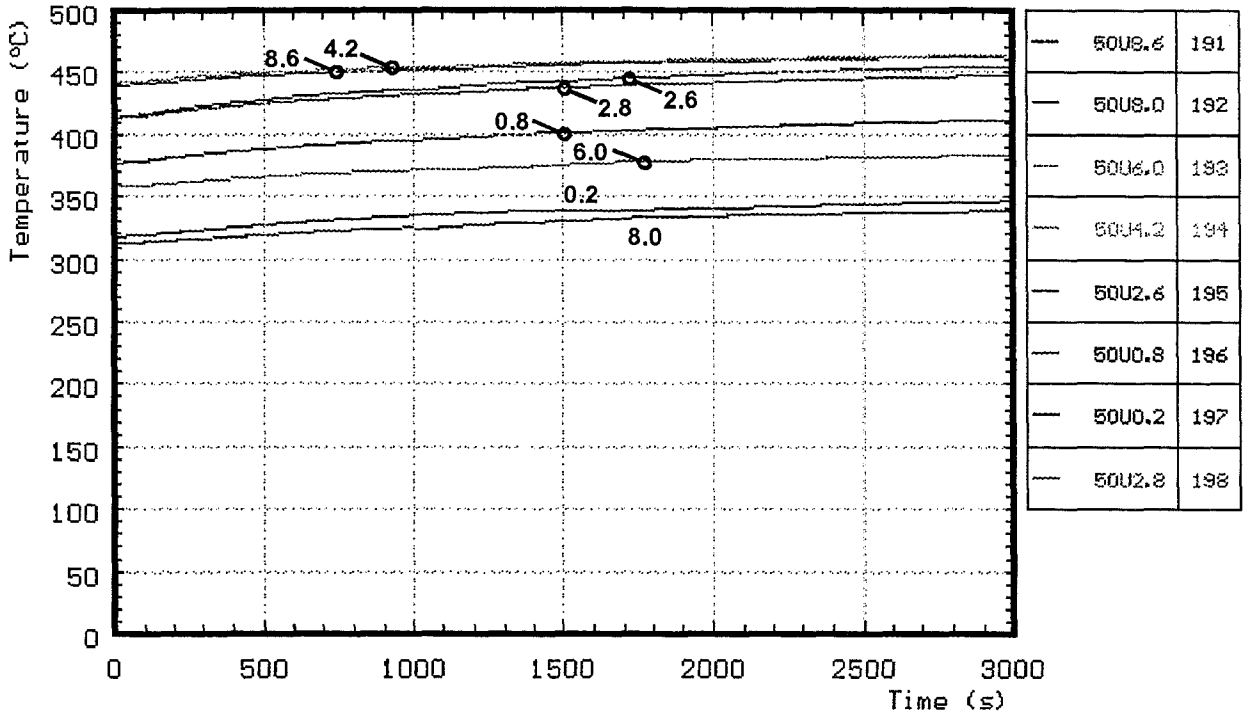

Fig. A10: CORA-7; Temperatures of unheated rods, 50 mm elevation; pre-heat phase

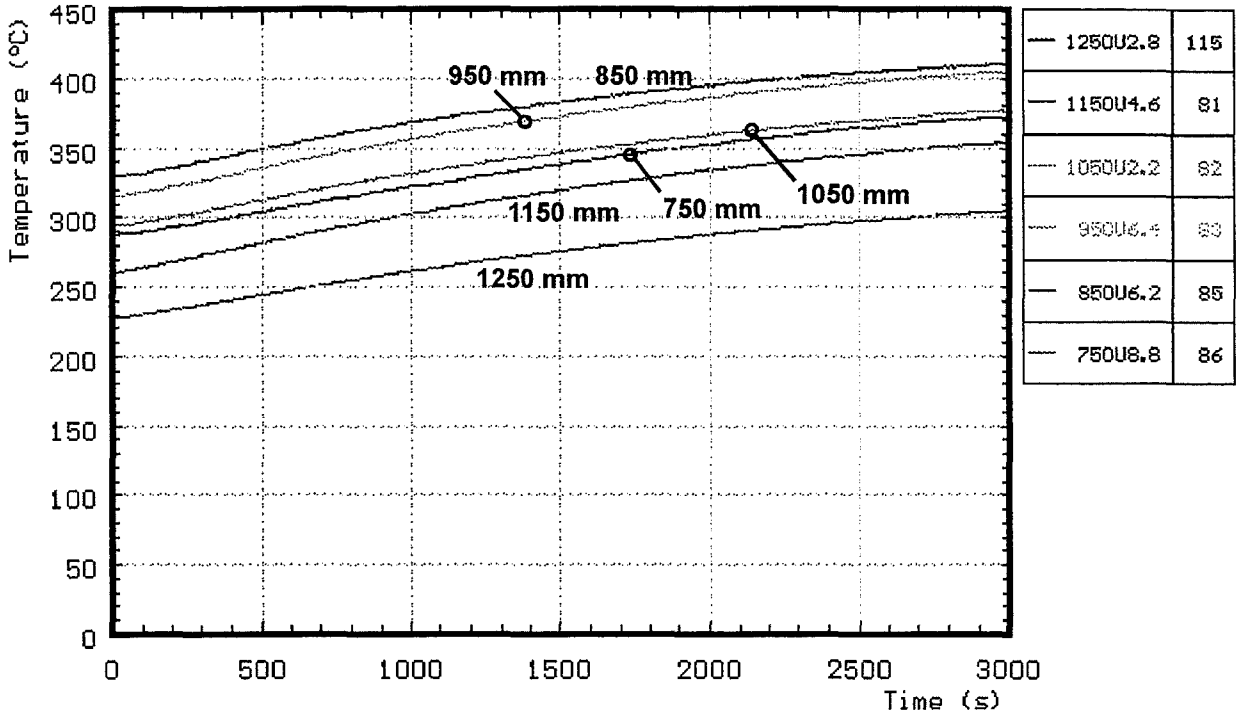

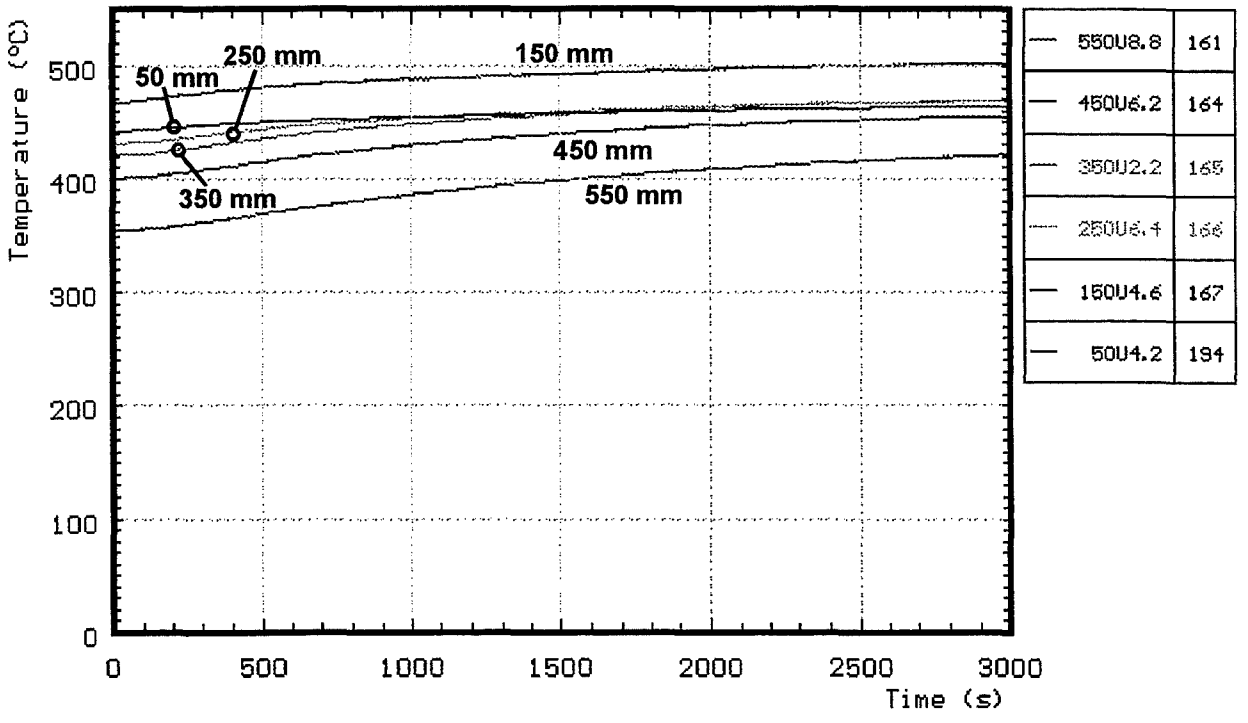

Fig. A11: CORA-7; Temperatures of unheated rods (TCs in central position); pre-heat phase

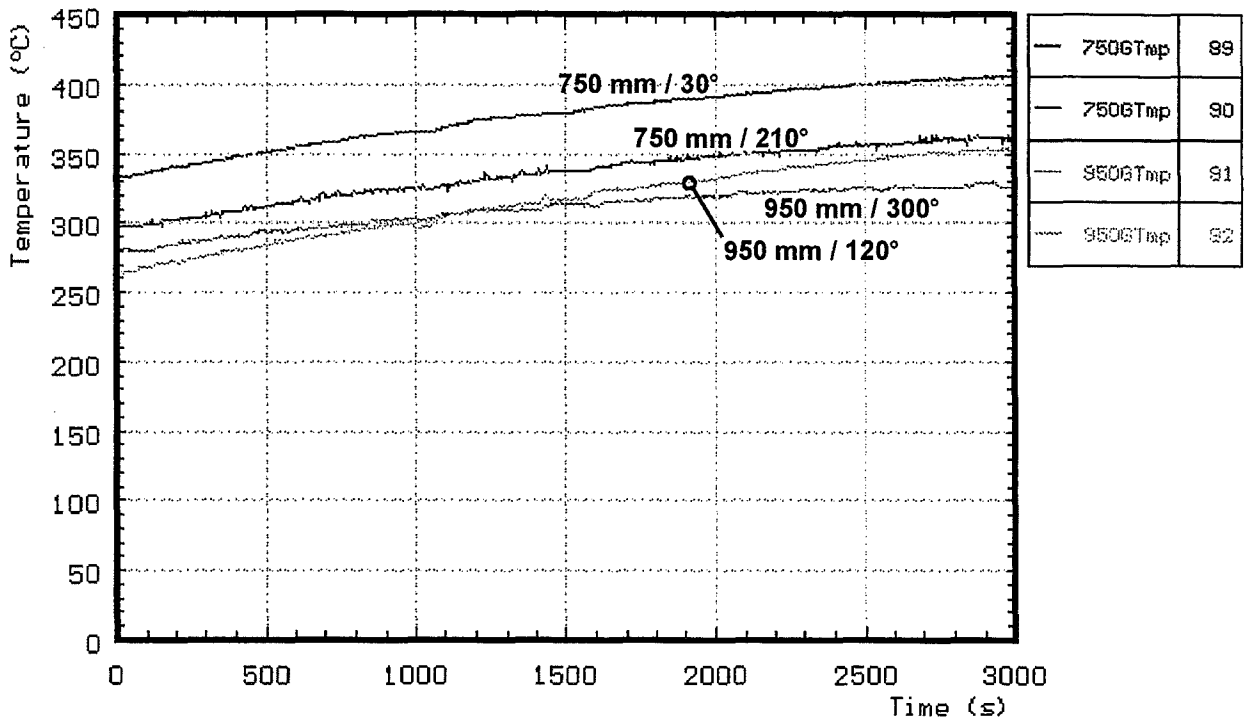

Fig.A12: CORA-7; Temperatures between bundle and shroud measured with ceramic protected TCs; pre-heat phase

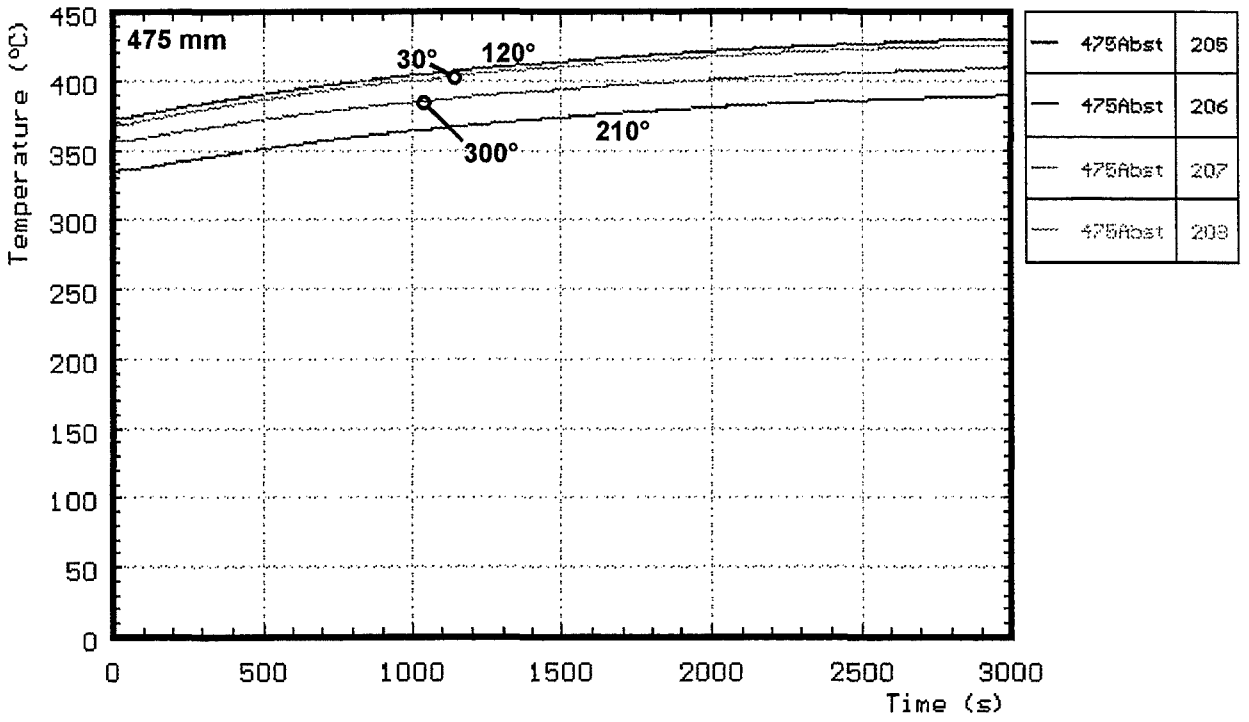

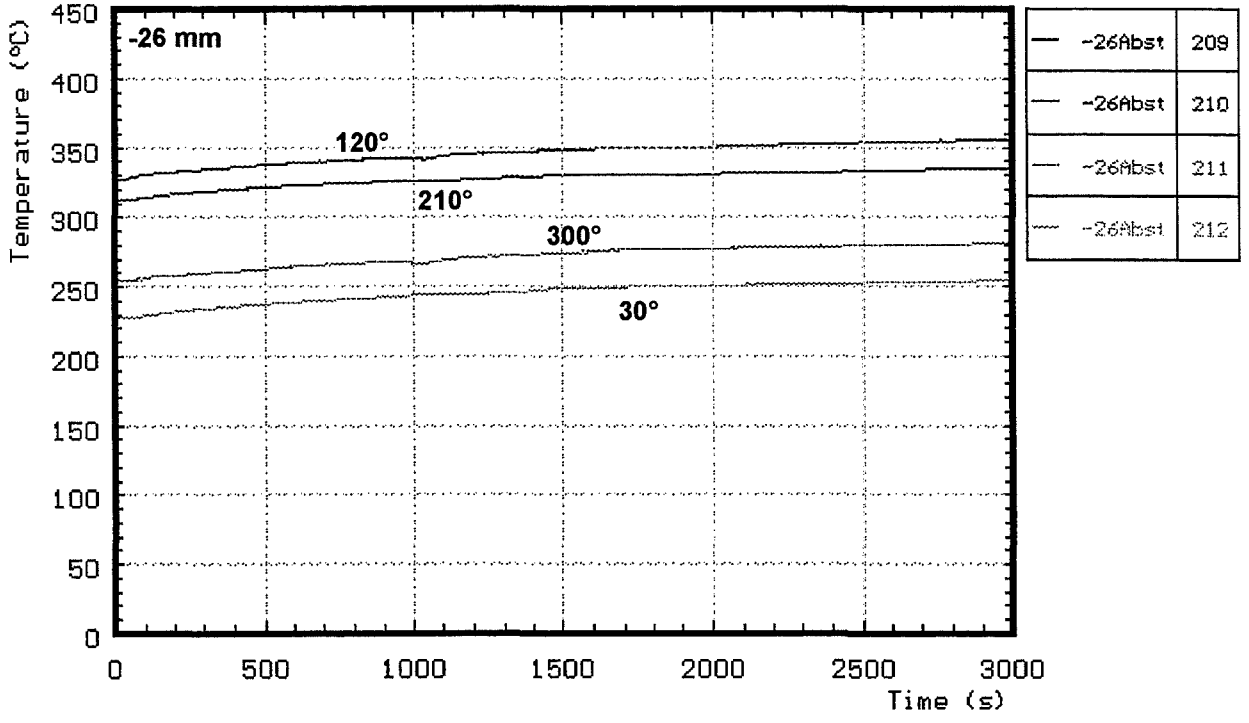

Fig. A13: CORA-7; Temperatures of the spacers; pre-heat phase

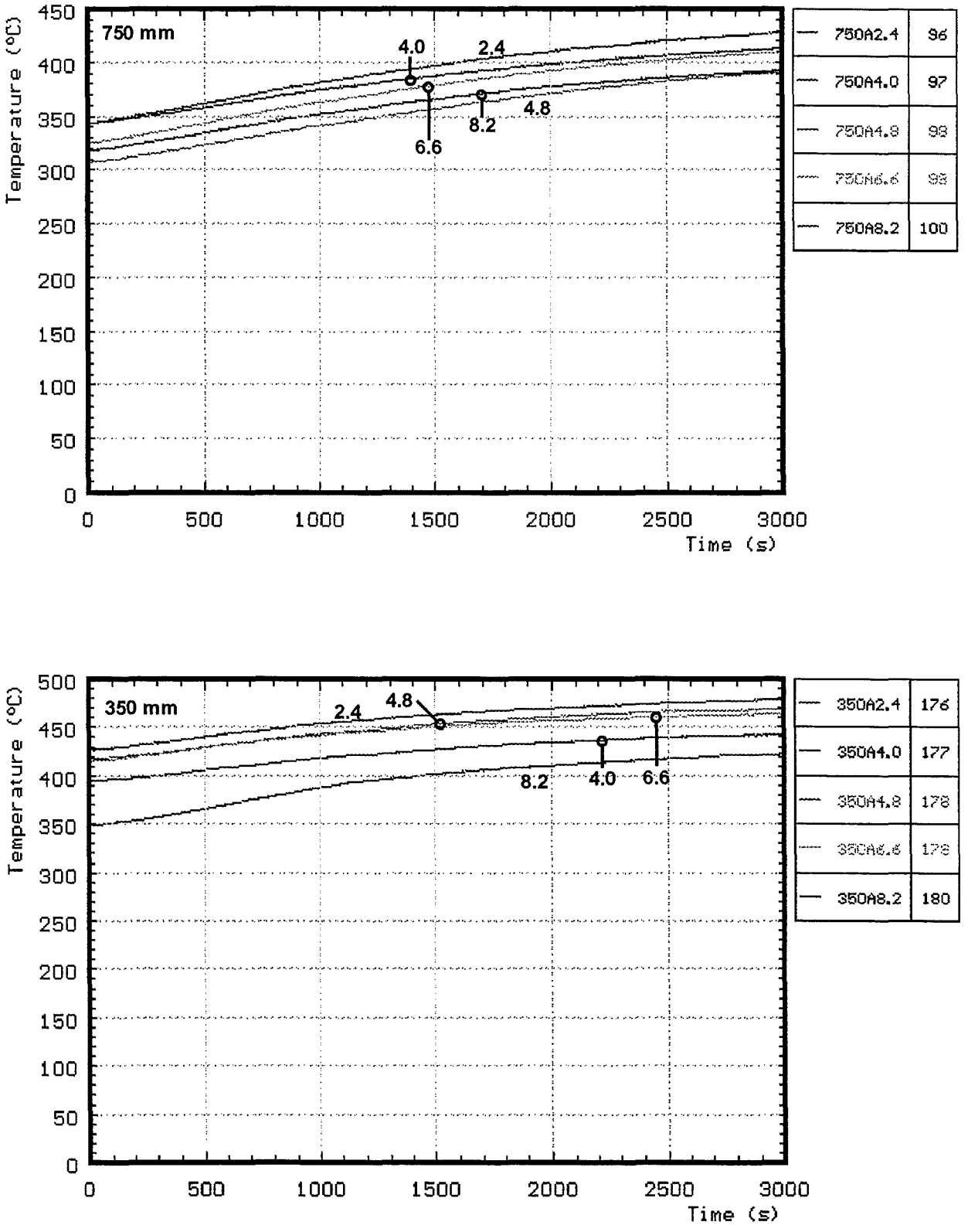

Fig. A14: CORA-7; Temperatures of the absorber rods; pre-heat phase

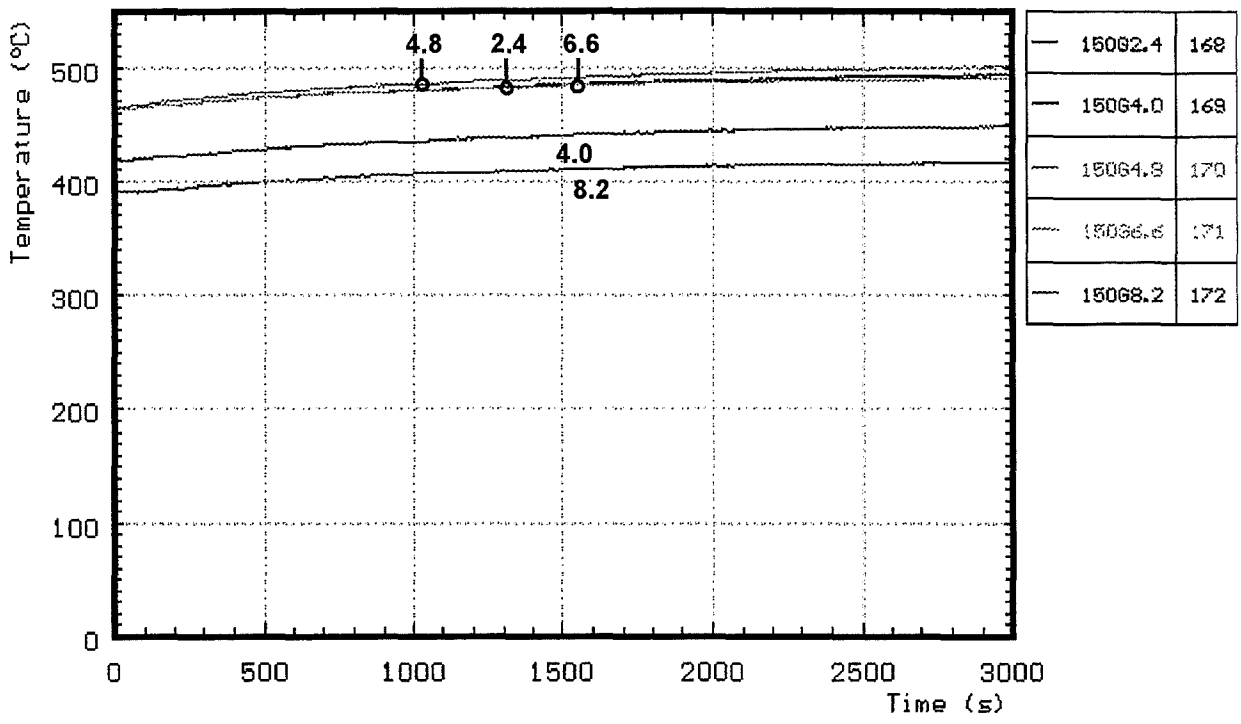

Fig.A15: CORA-7; Temperatures of the guide tubes of absorber rods; pre-heat phase

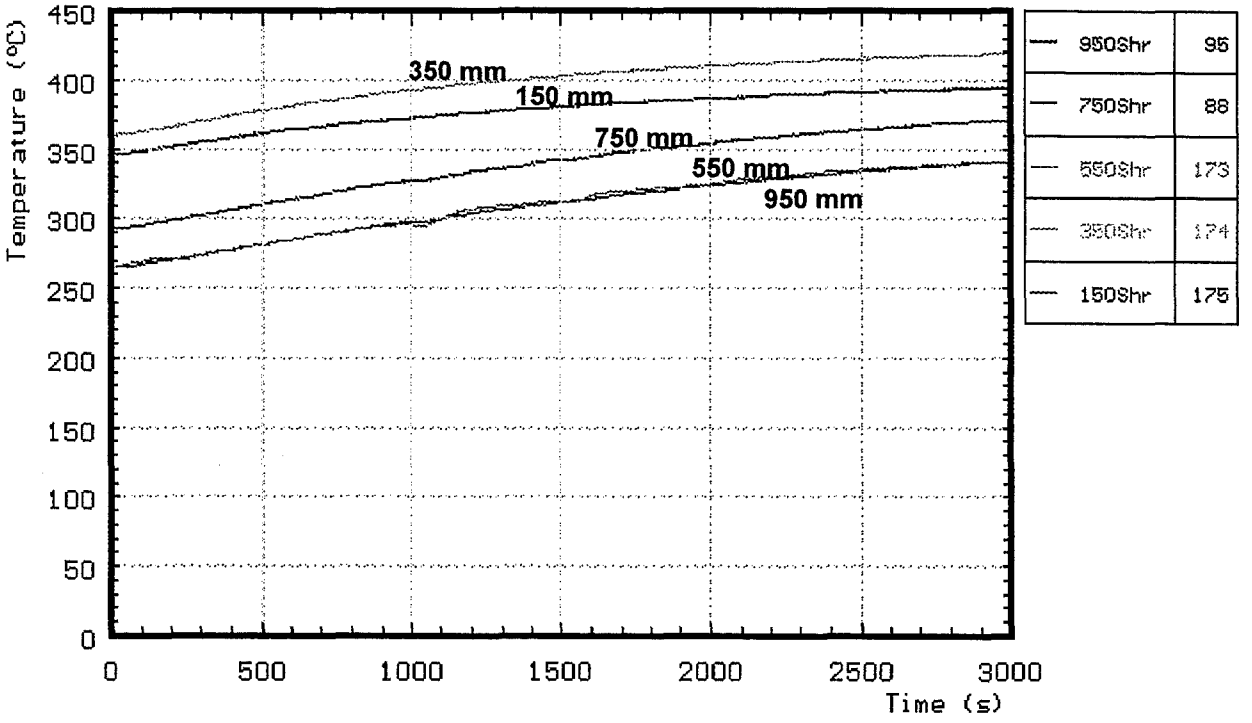

Fig.A16: CORA-7; Temperatures of outer side of shroud; pre-heat phase

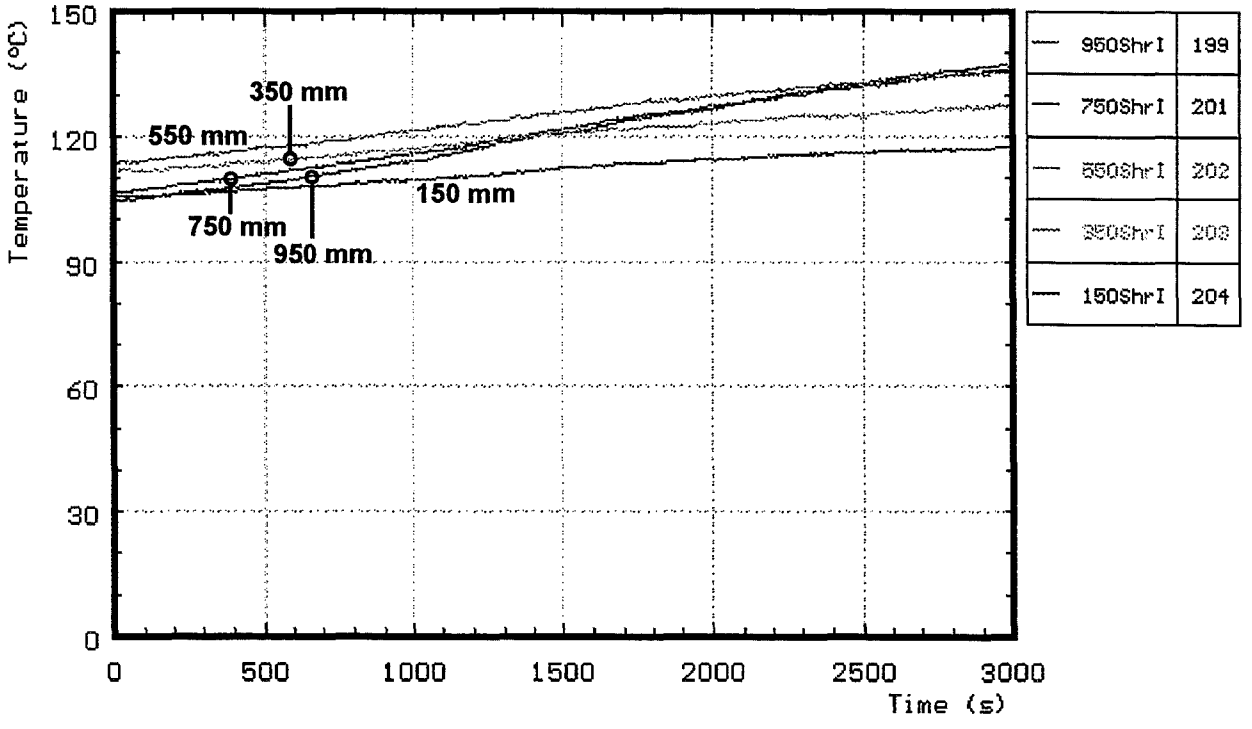

Fig.A17: CORA-7; Temperatures of the shroud insulation; pre-heat phase

Appendix B

Pretest CORA-7

Figures B1 - B7

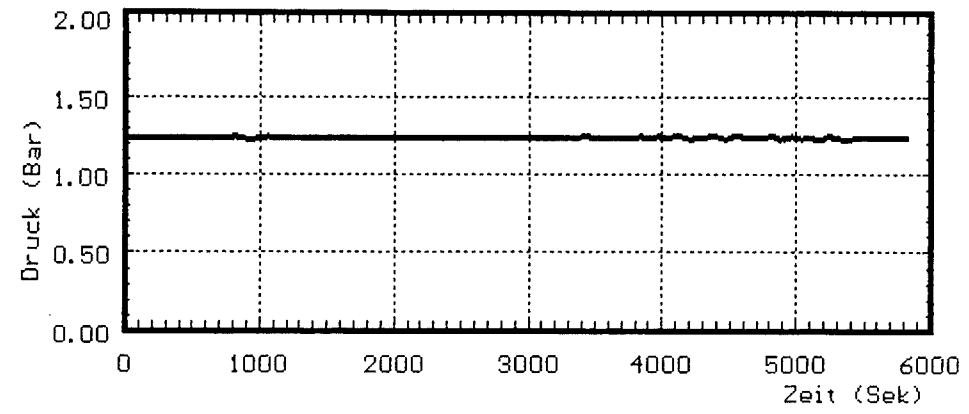

System overpressure

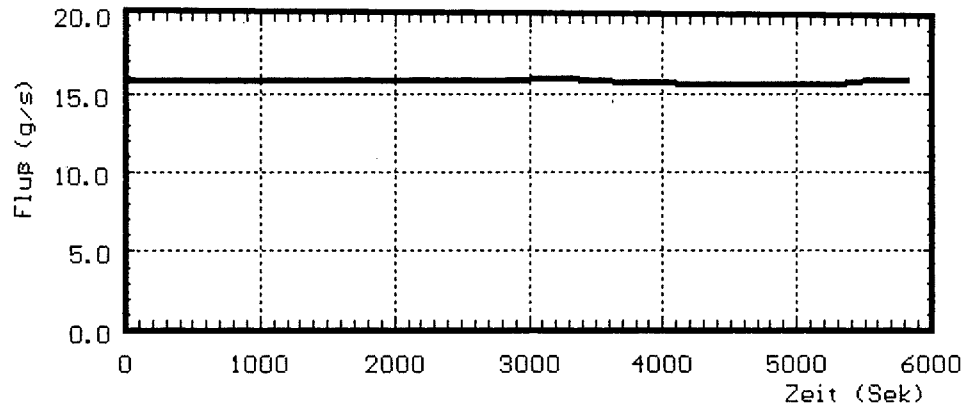

argon flow

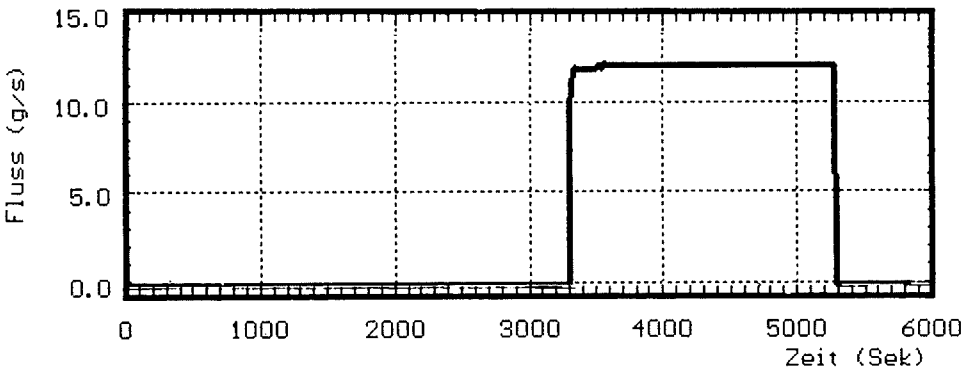

steam flow

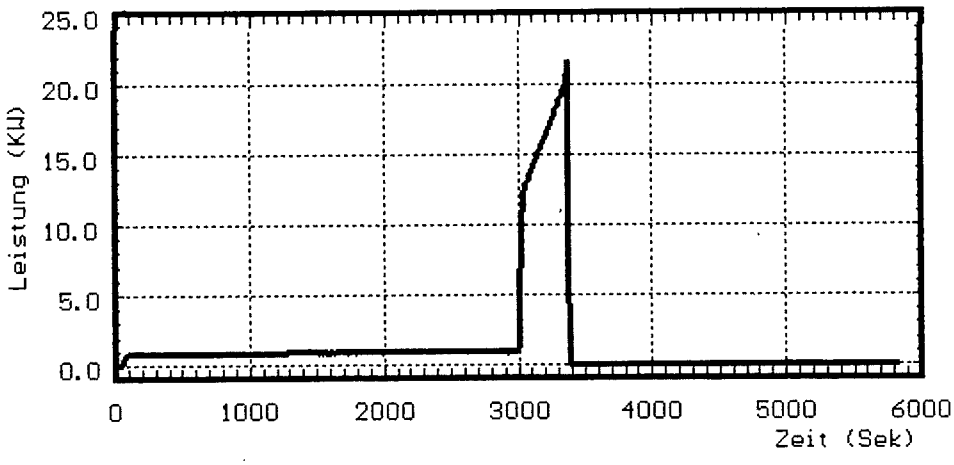

power

Fig. B1: System overpressure, argon flow, steam flow and power (Pretest CORA-7)

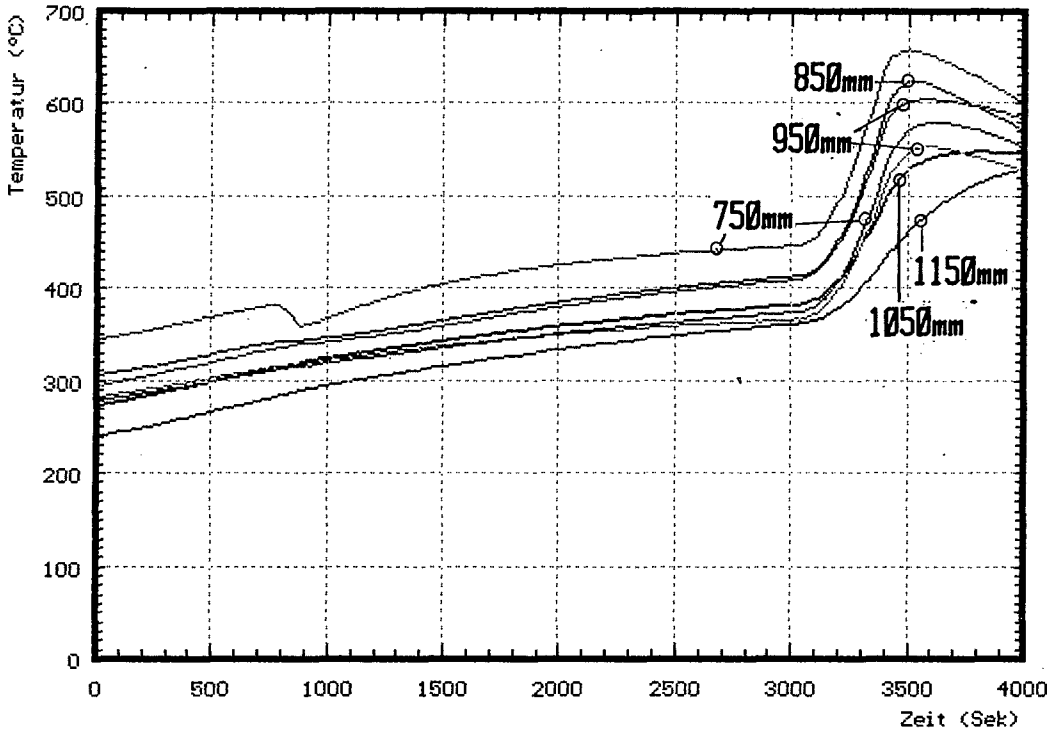

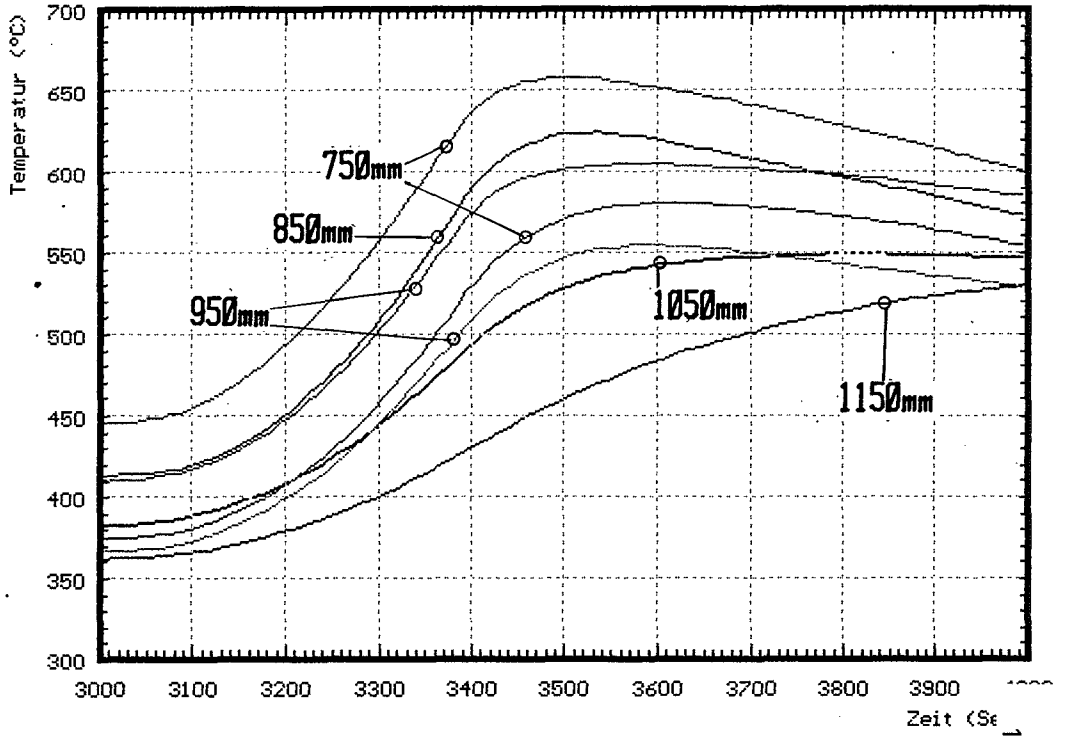

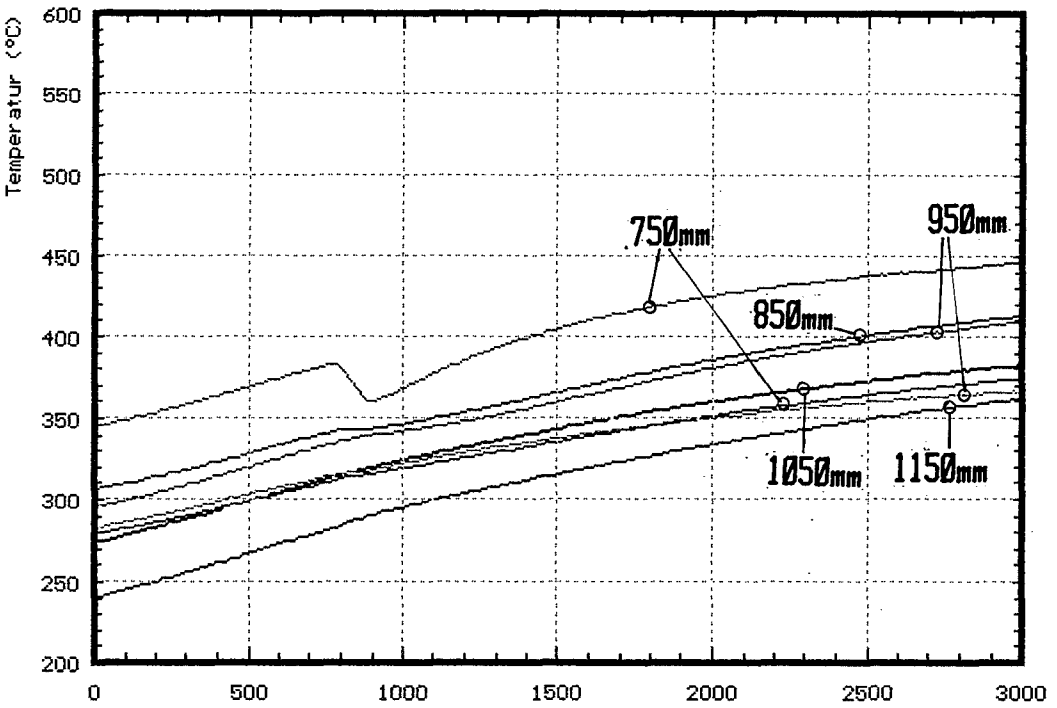

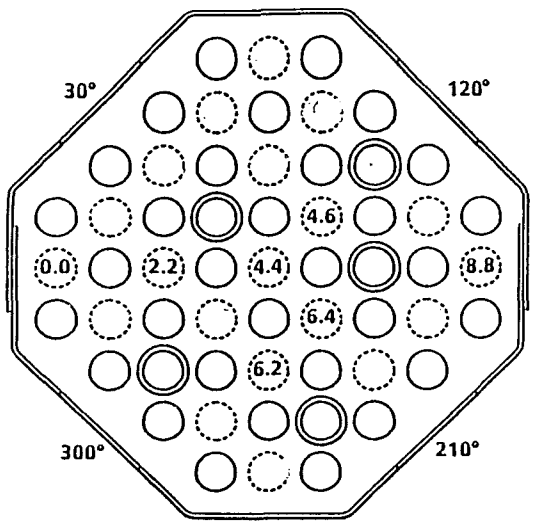

Fig. B2: Pretest temperatures in unheated rods at elevations given (Pretest CORA-7)

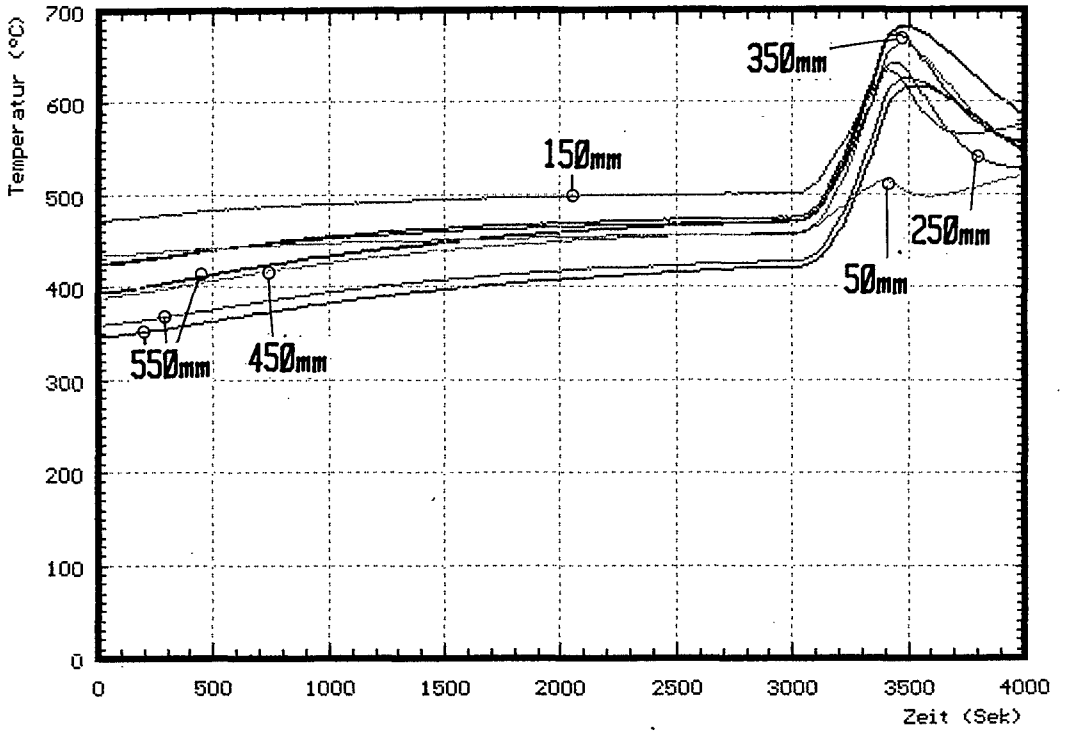

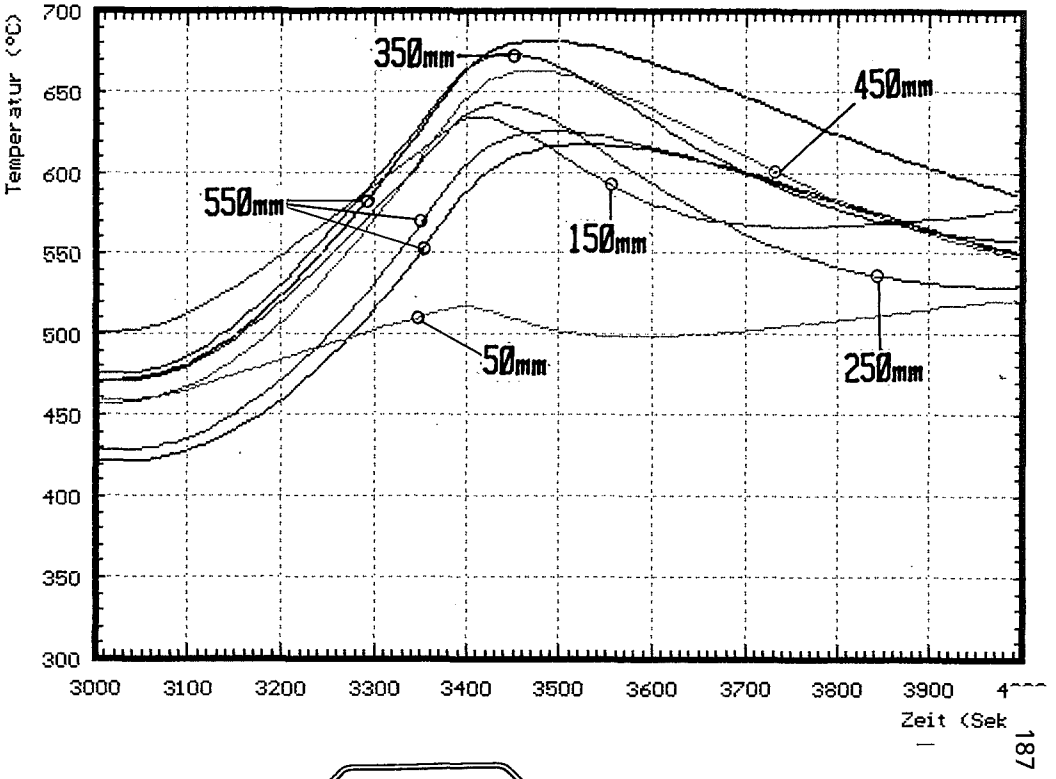

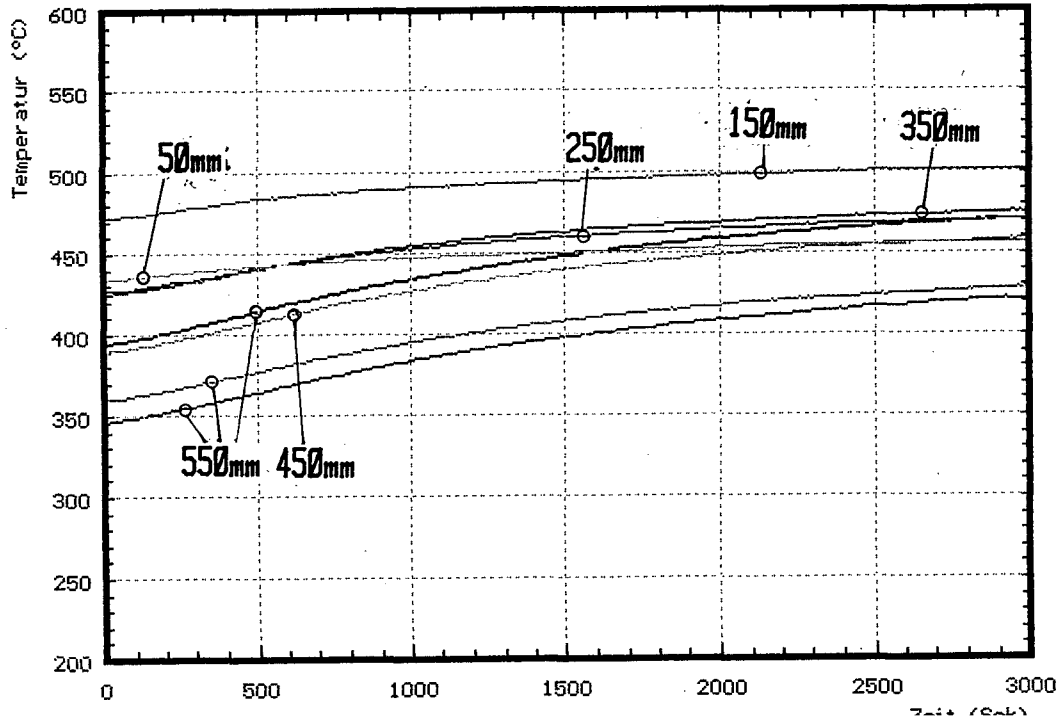

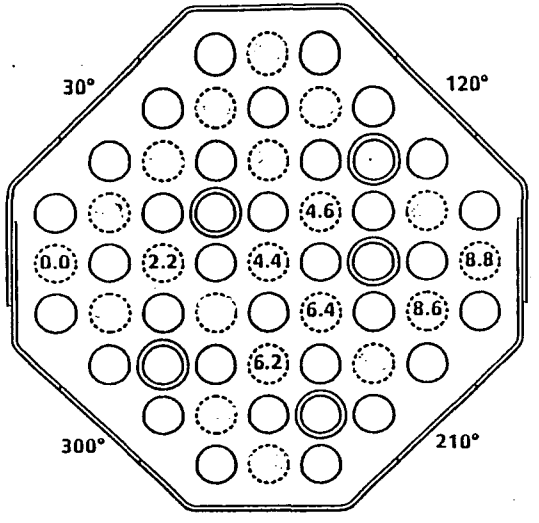

Fig. B3: Pretest temperatures in unheated rods at elevations given (Pretest CORA-7)

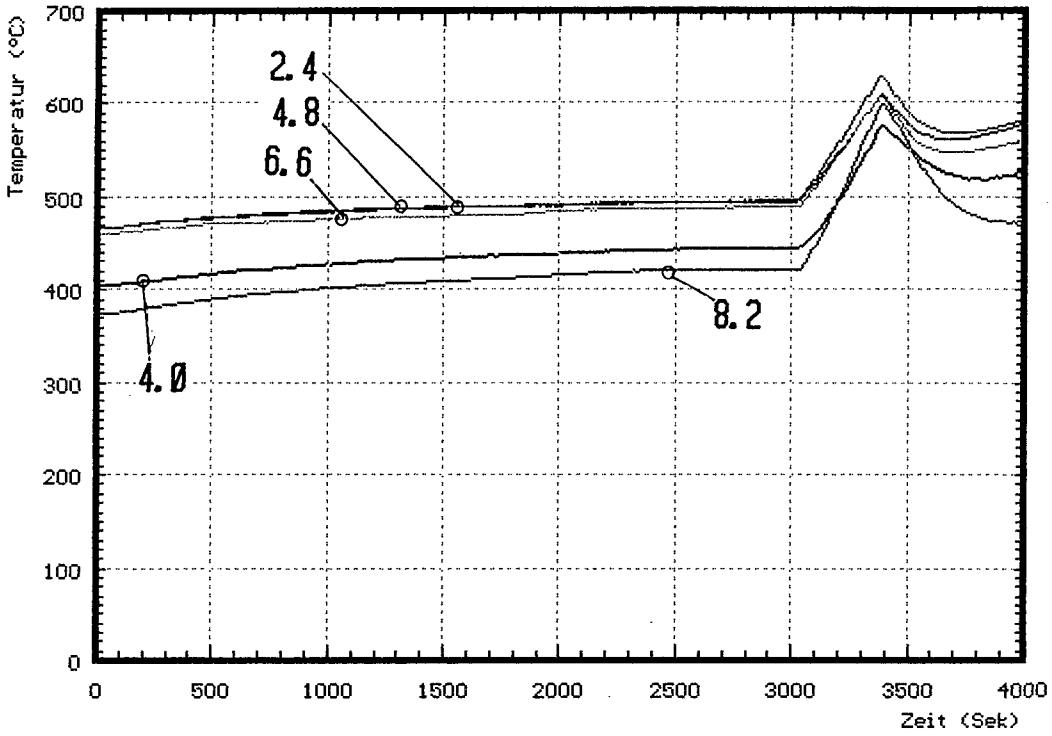

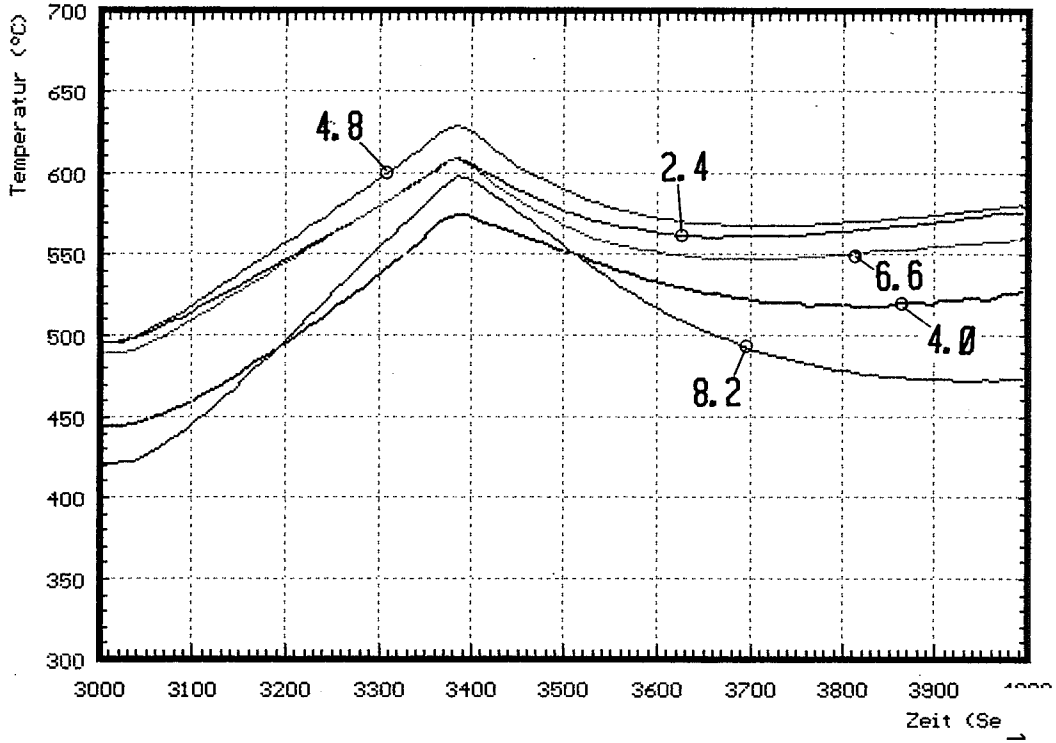

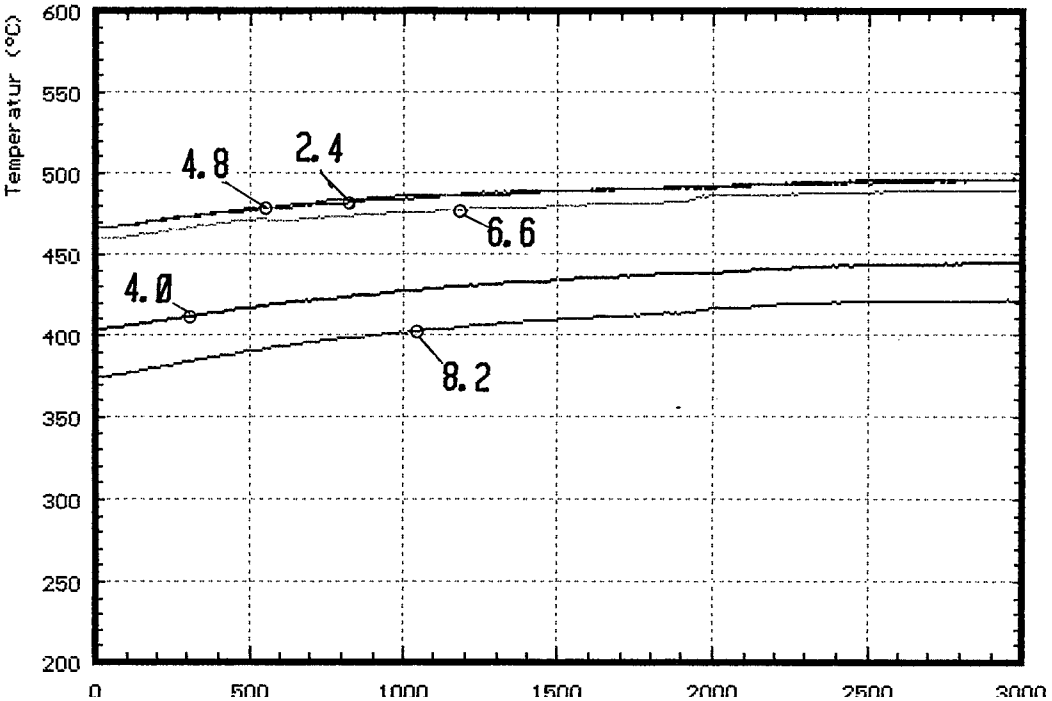

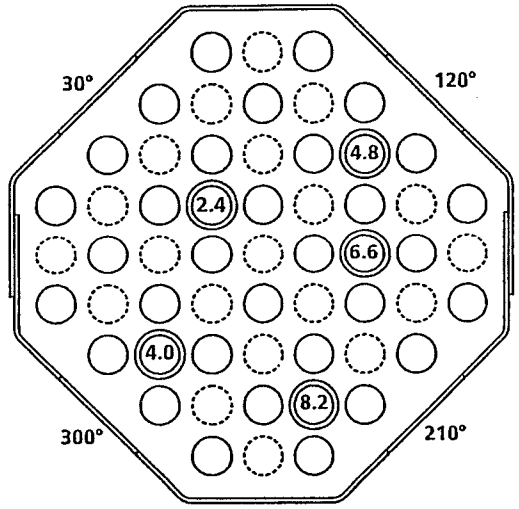

Fig. B4: Pretest temperatures on the guide tube at 150 mm elevation (Pretest CORA-7)

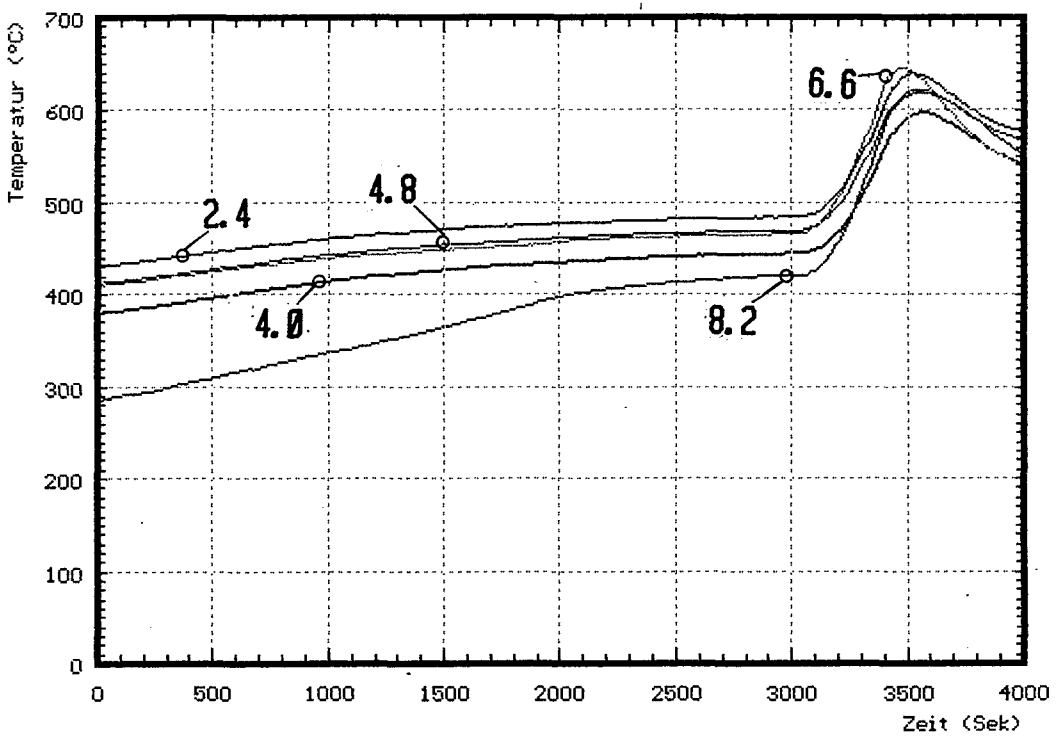

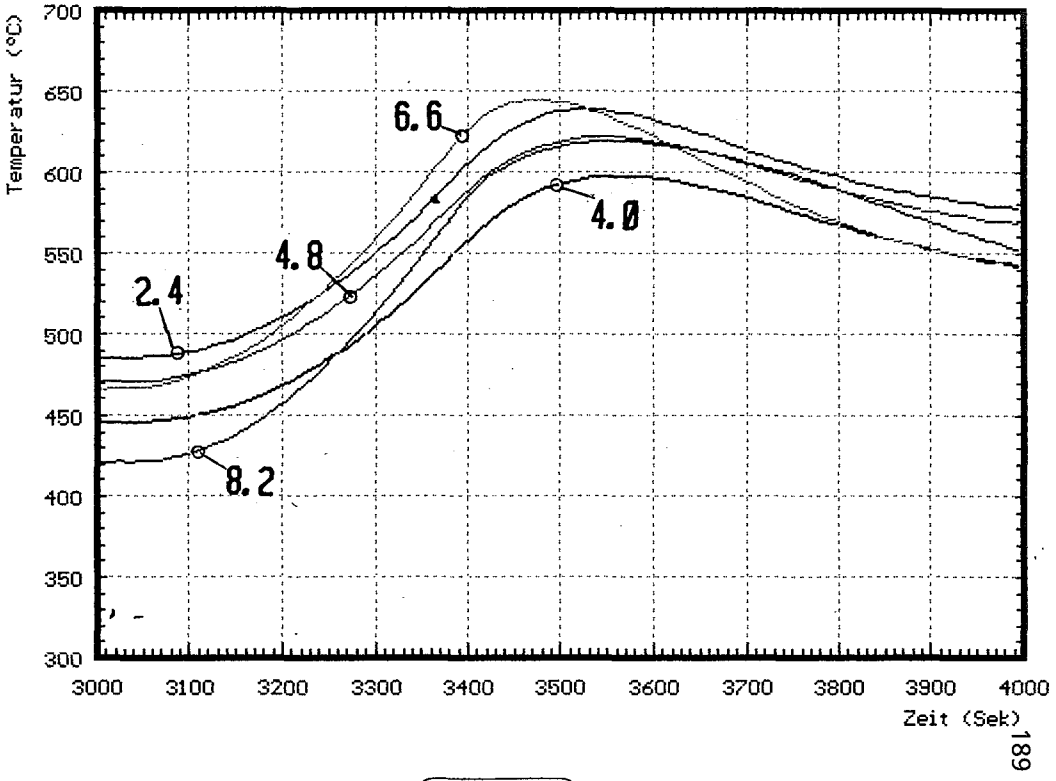

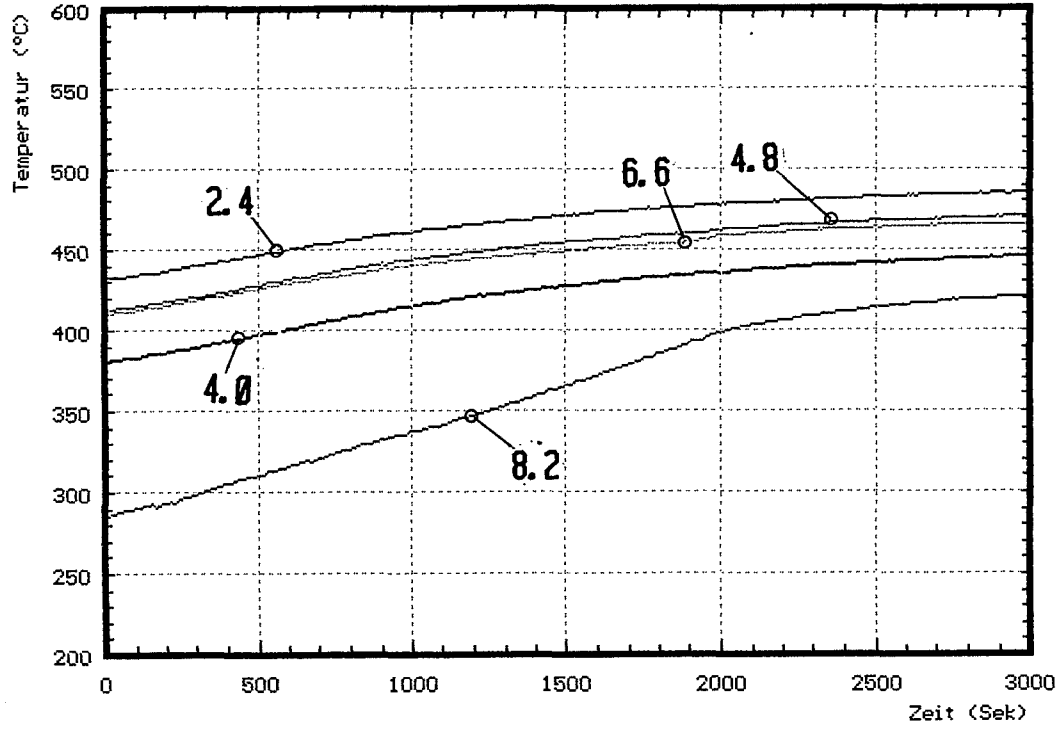

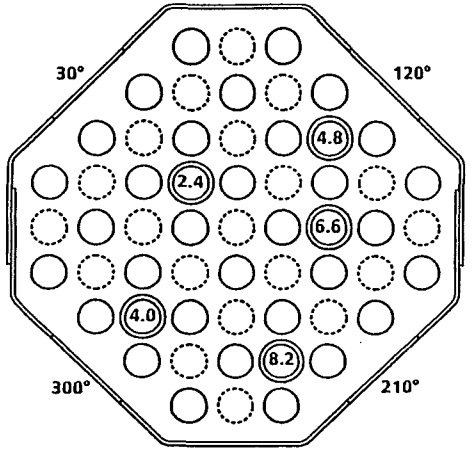

Fig. B5: Pretest temperatures in absorber rods at 350 mm elevation (Pretest CORA-7)

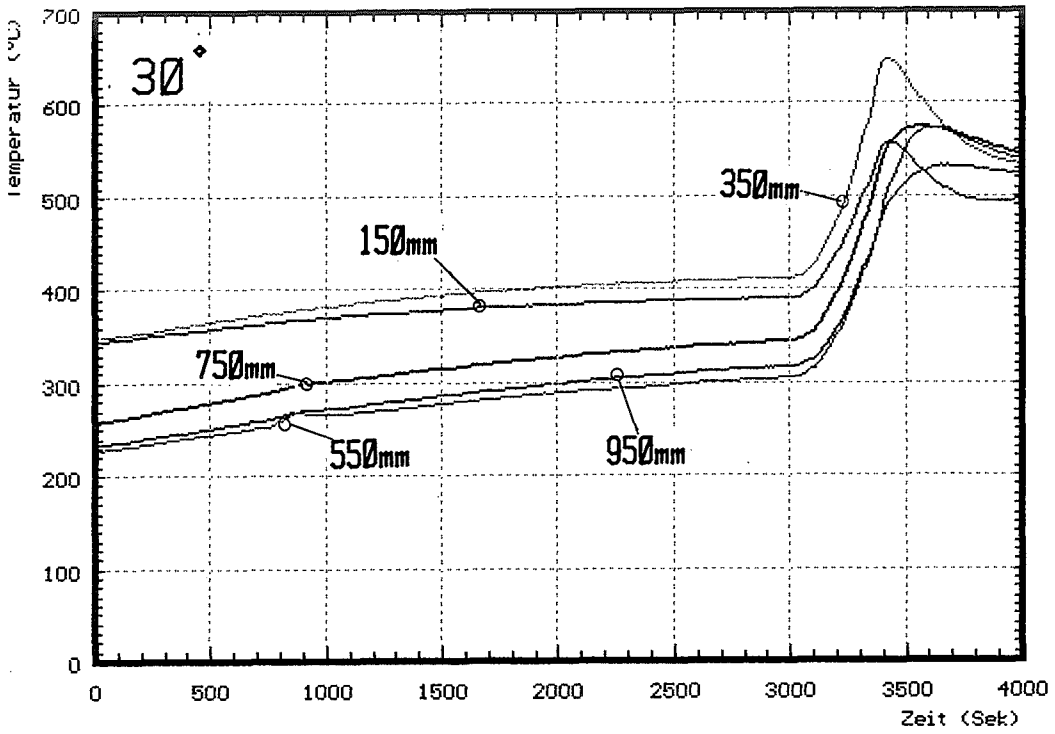

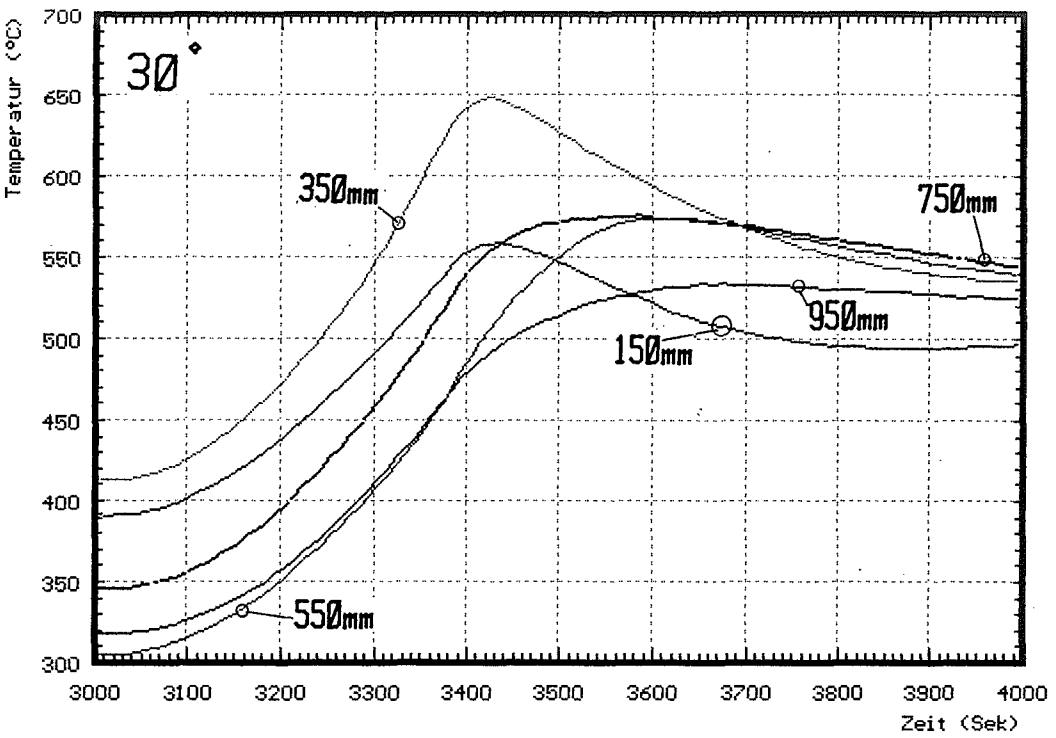

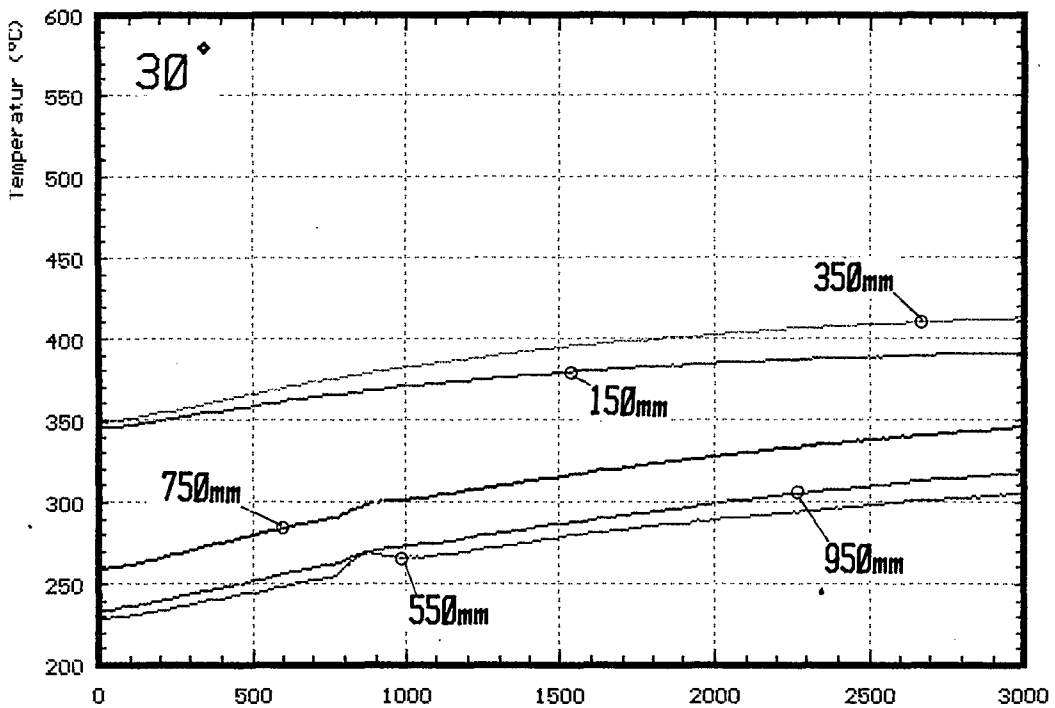

Fig. B6: Pretest temperatures on the shroud at elevations given (Pretest CORA-7)

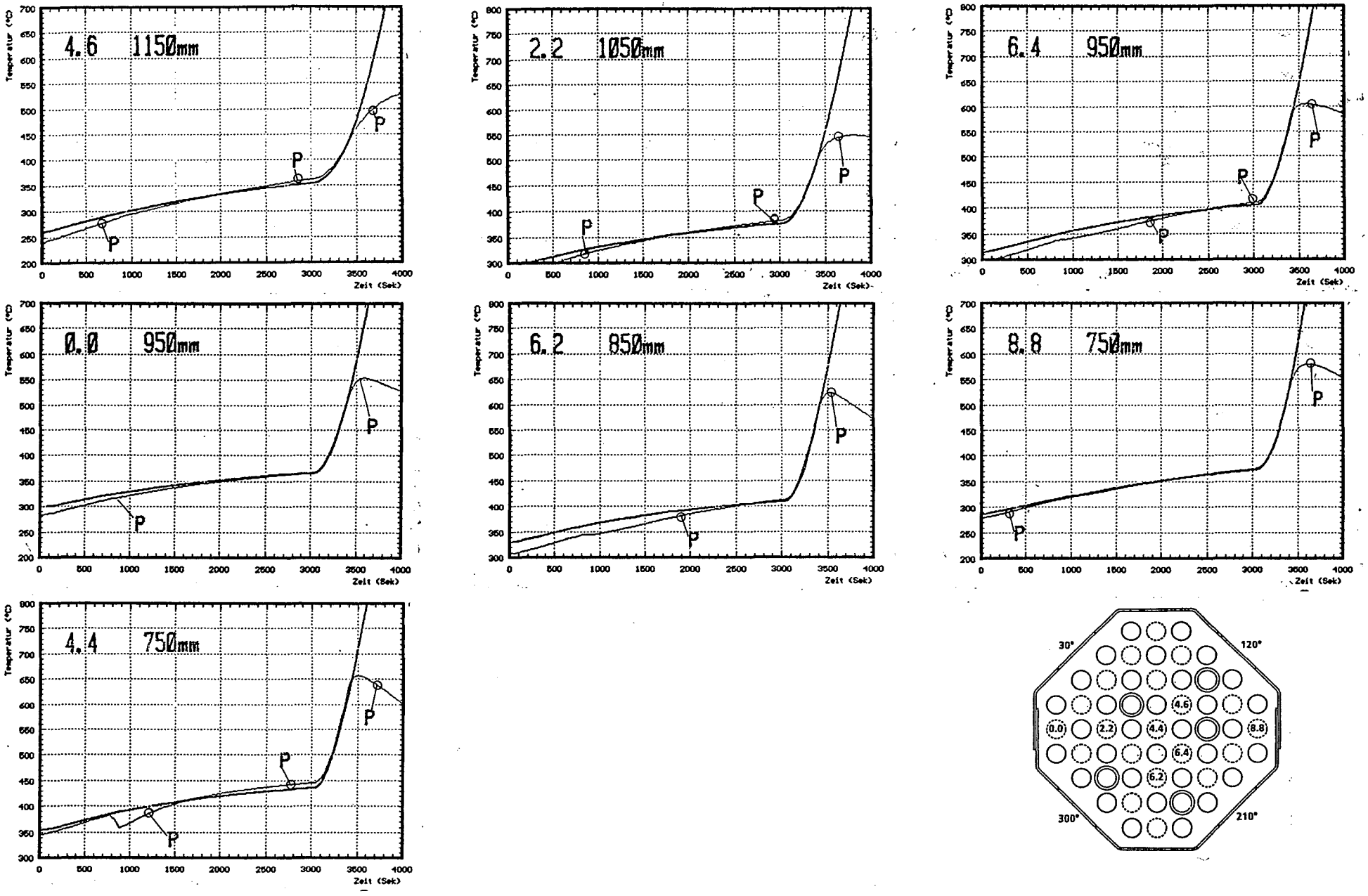

Fig. B7: Comparison of temperatures in unheated fuel rod simulators at elevations given for pretest (P) and test CORA-7

Appendix C

Complete set of horizontal cross sections

Figures C1 - C19

CORA 7 1230 mm

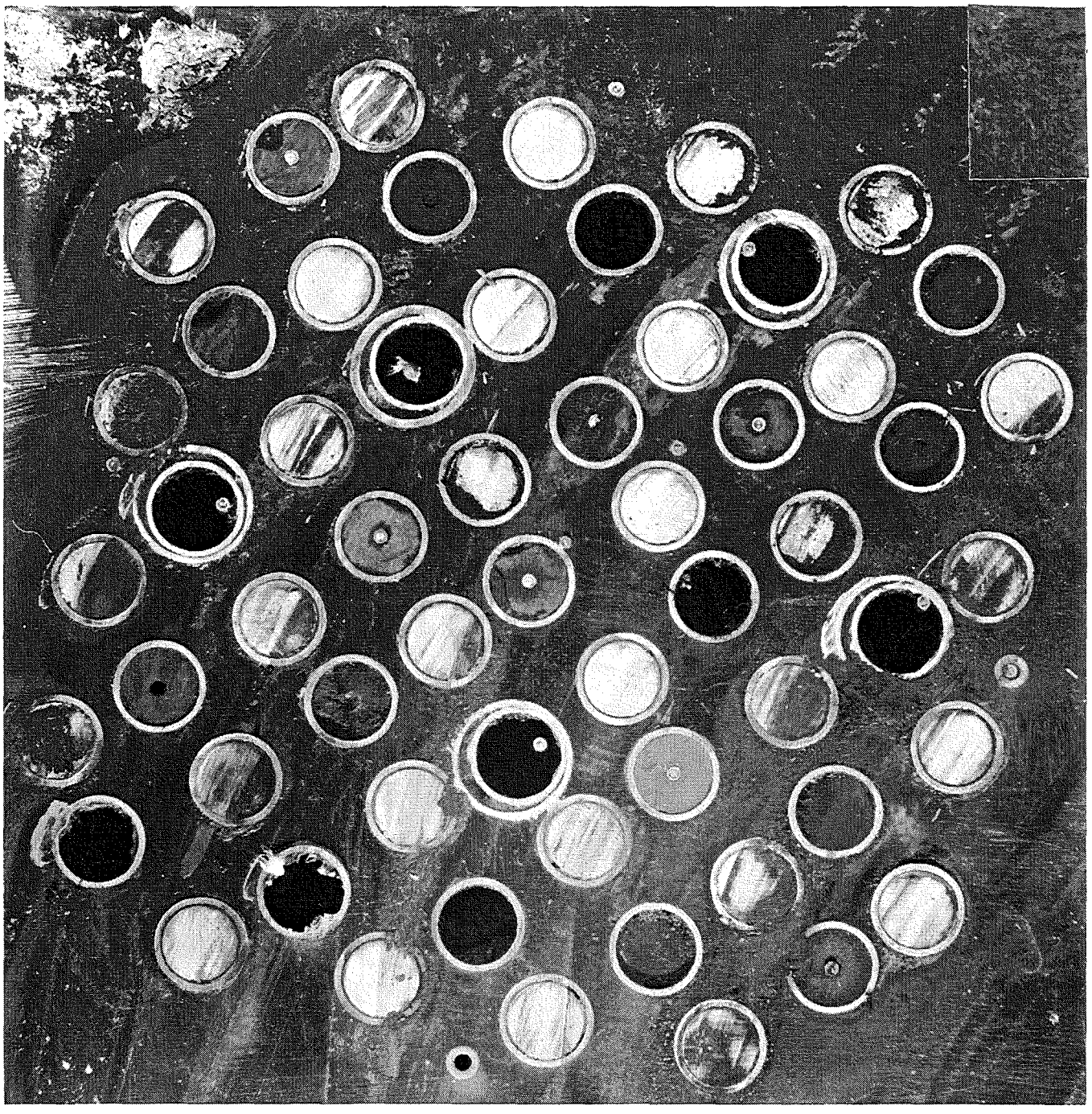

Fig. C1: Horizontal cross section; top view

CORA 7

1147 mm

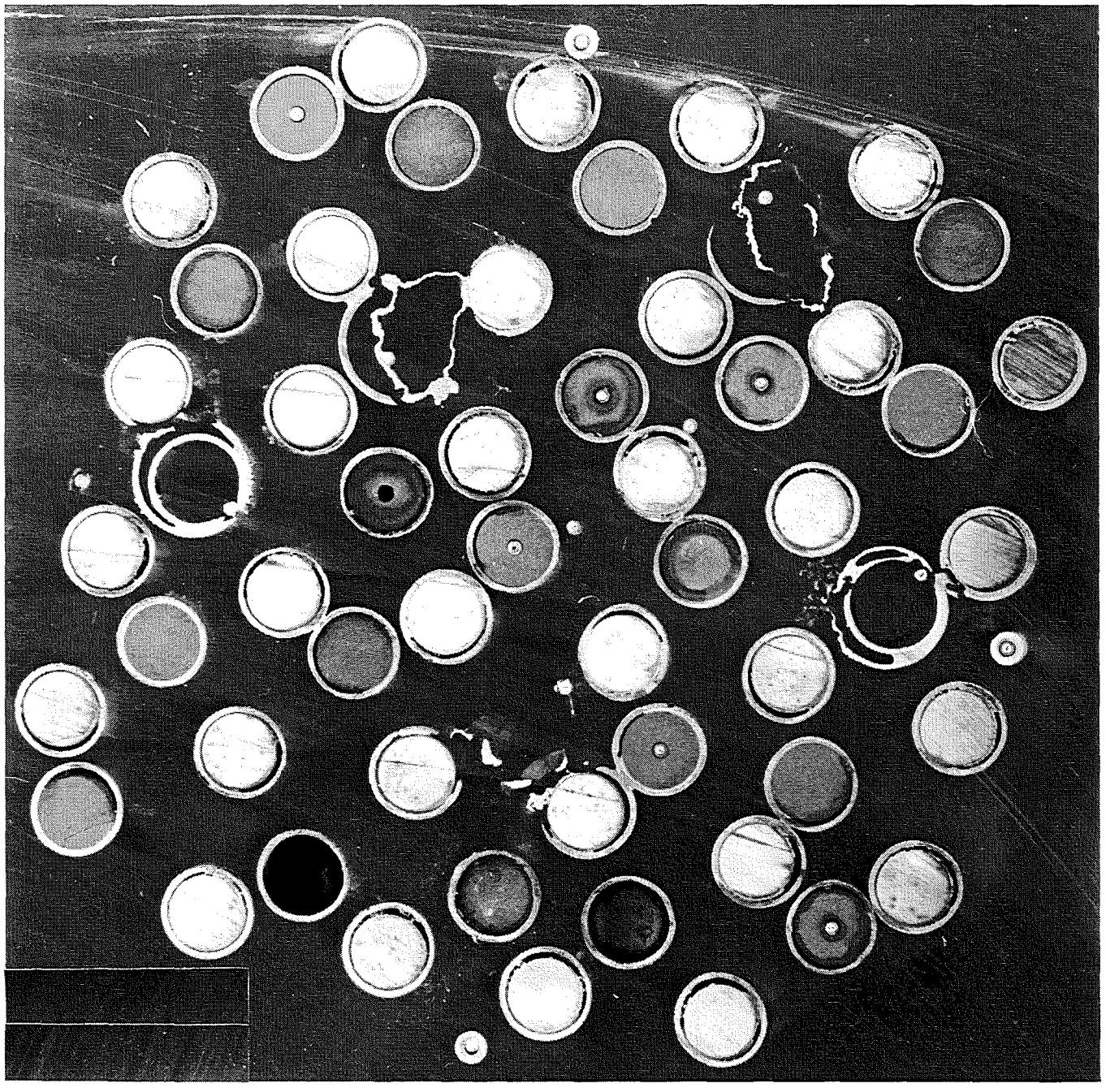

Fig. C2: Horizontal cross section; top view

CORA 7 1005 mm

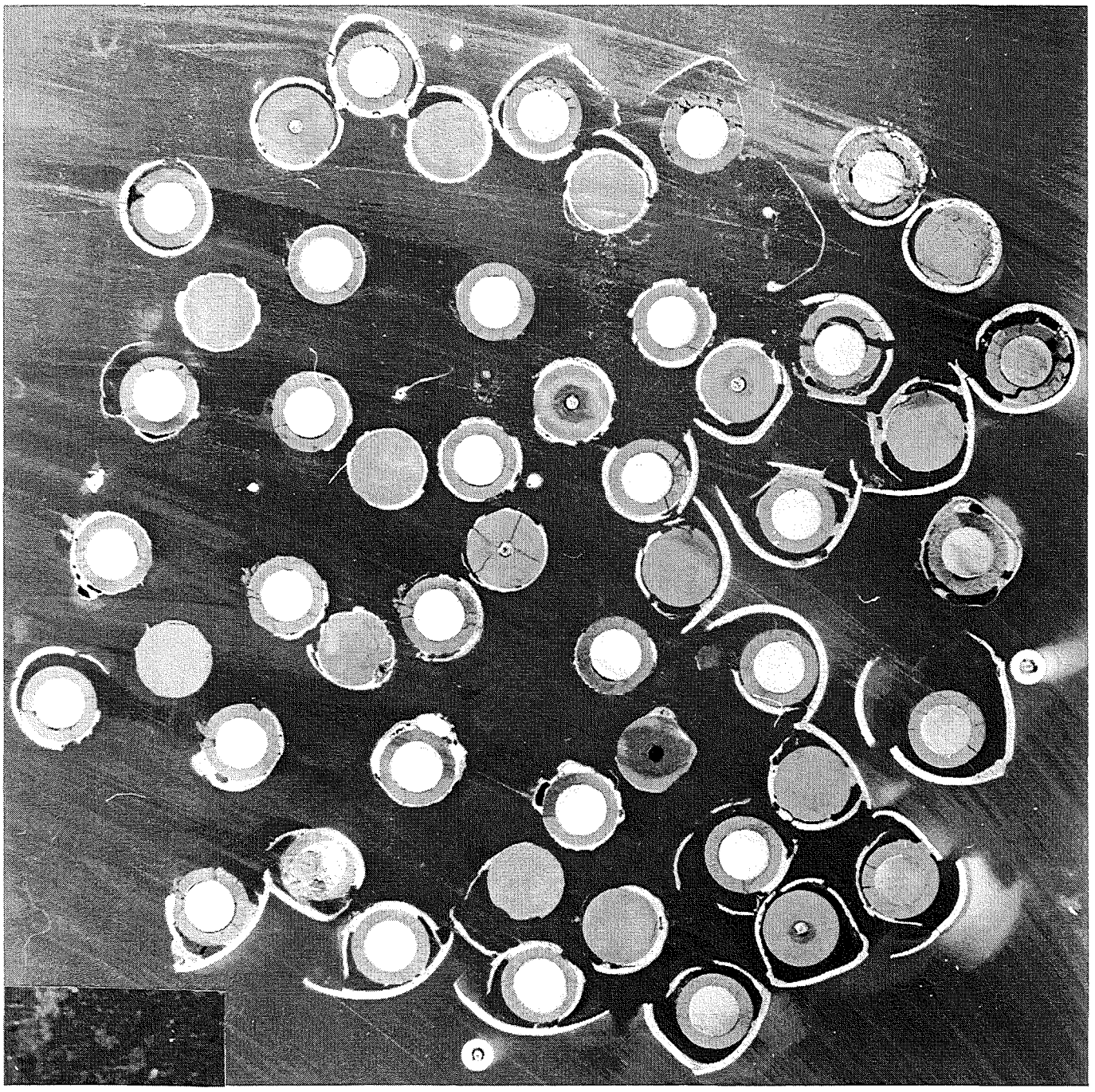

Fig. C3: Horizontal cross section; top view

CORA 7

863 mm

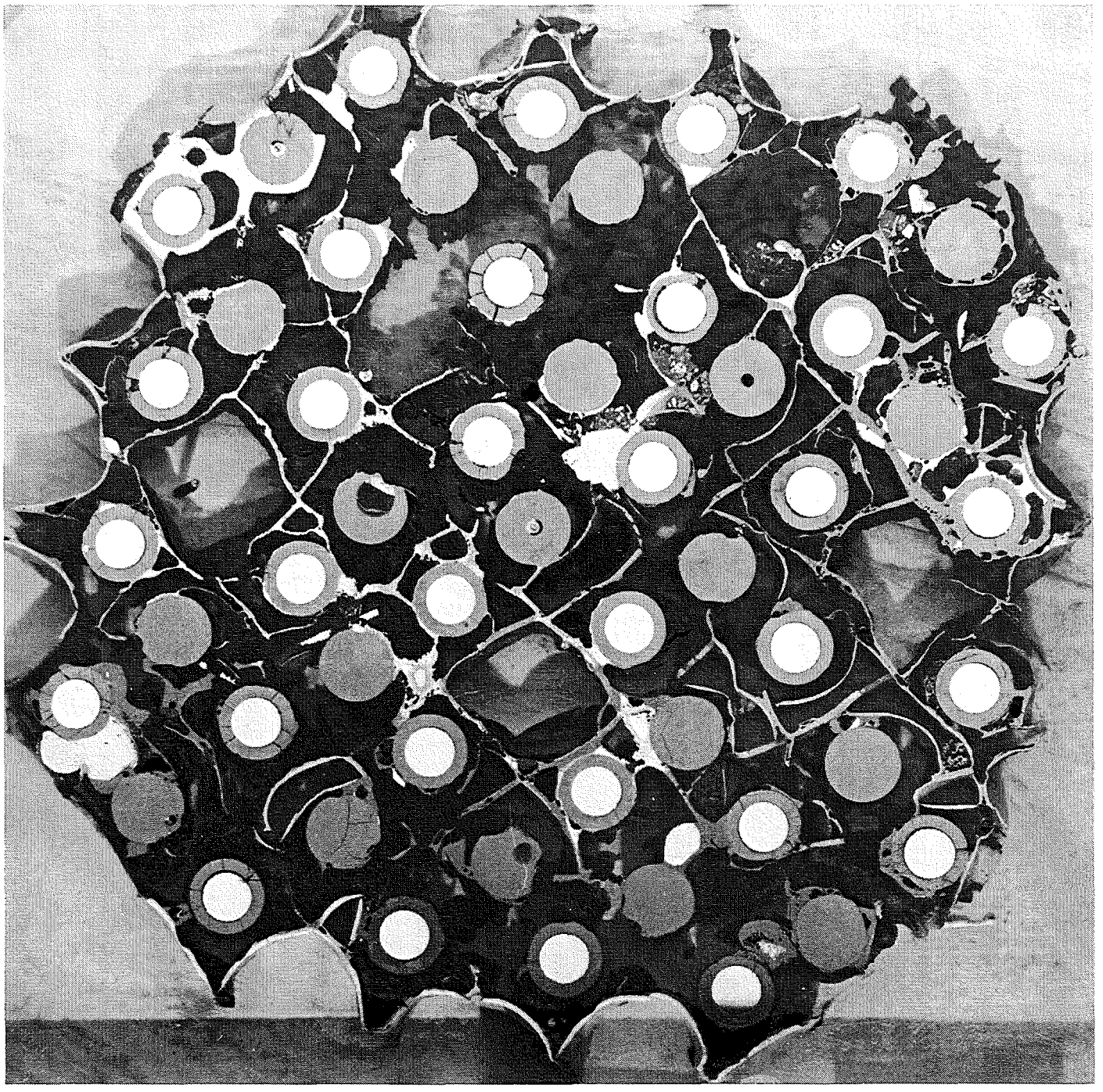

Fig. C4: Horizontal cross section; top view

CORA 7

848 mm

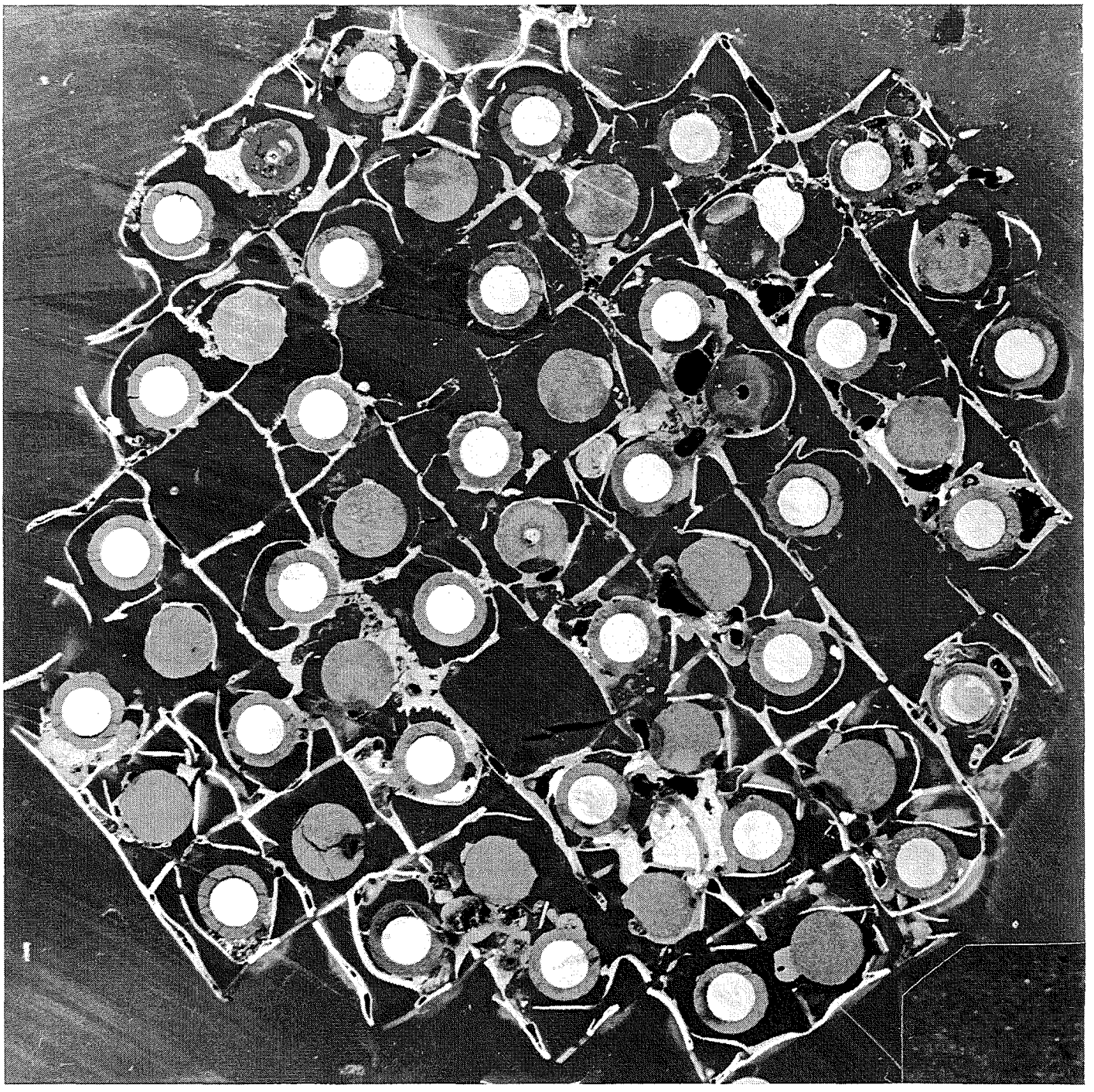

Fig. C5: Horizontal cross section; top view

CORA 7 794 mm

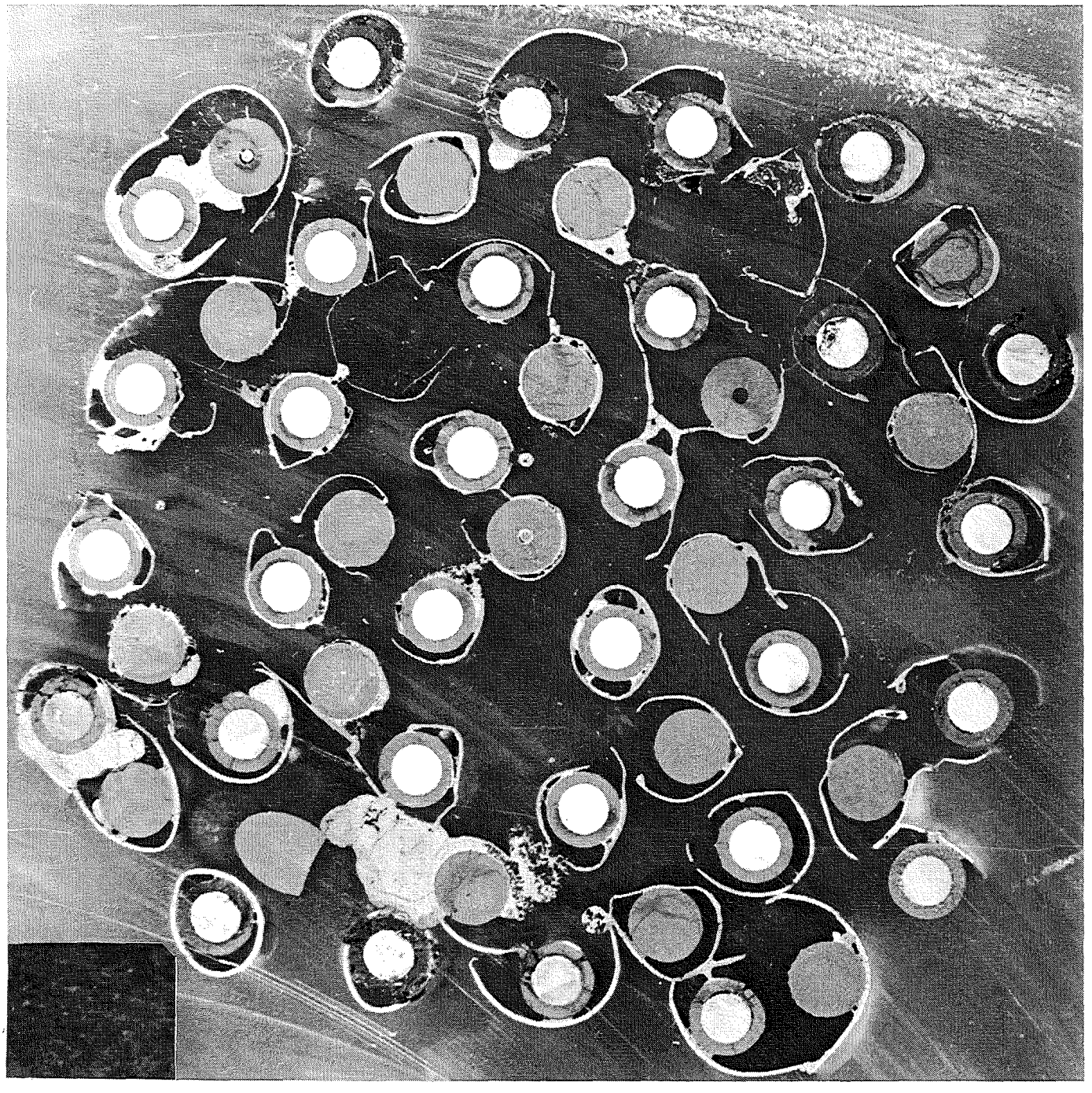

Fig. C6: Horizontal cross section; top view

CORA 7 779 mm

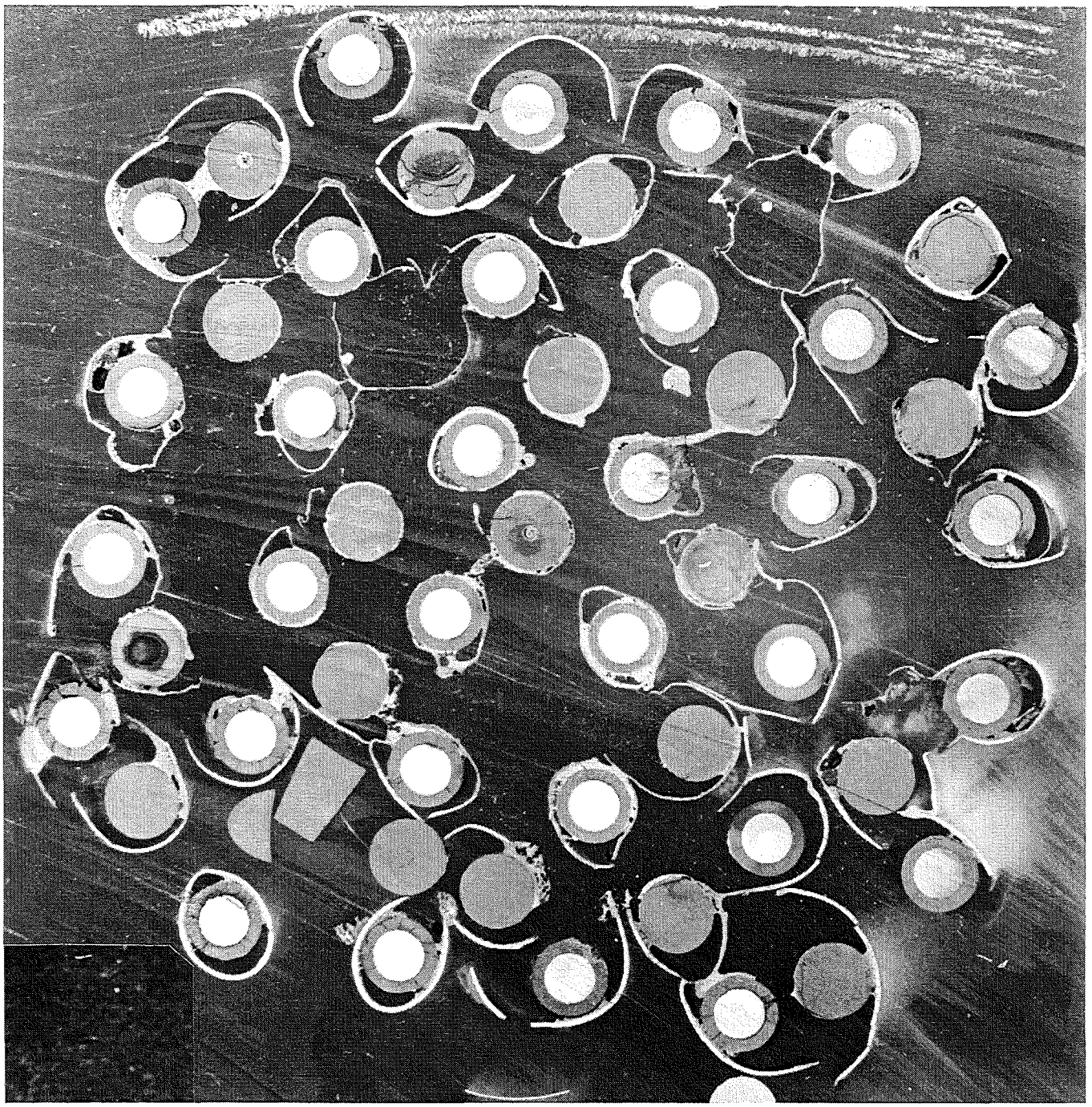

Fig. C7: Horizontal cross section; top view

CORA 7

637 mm

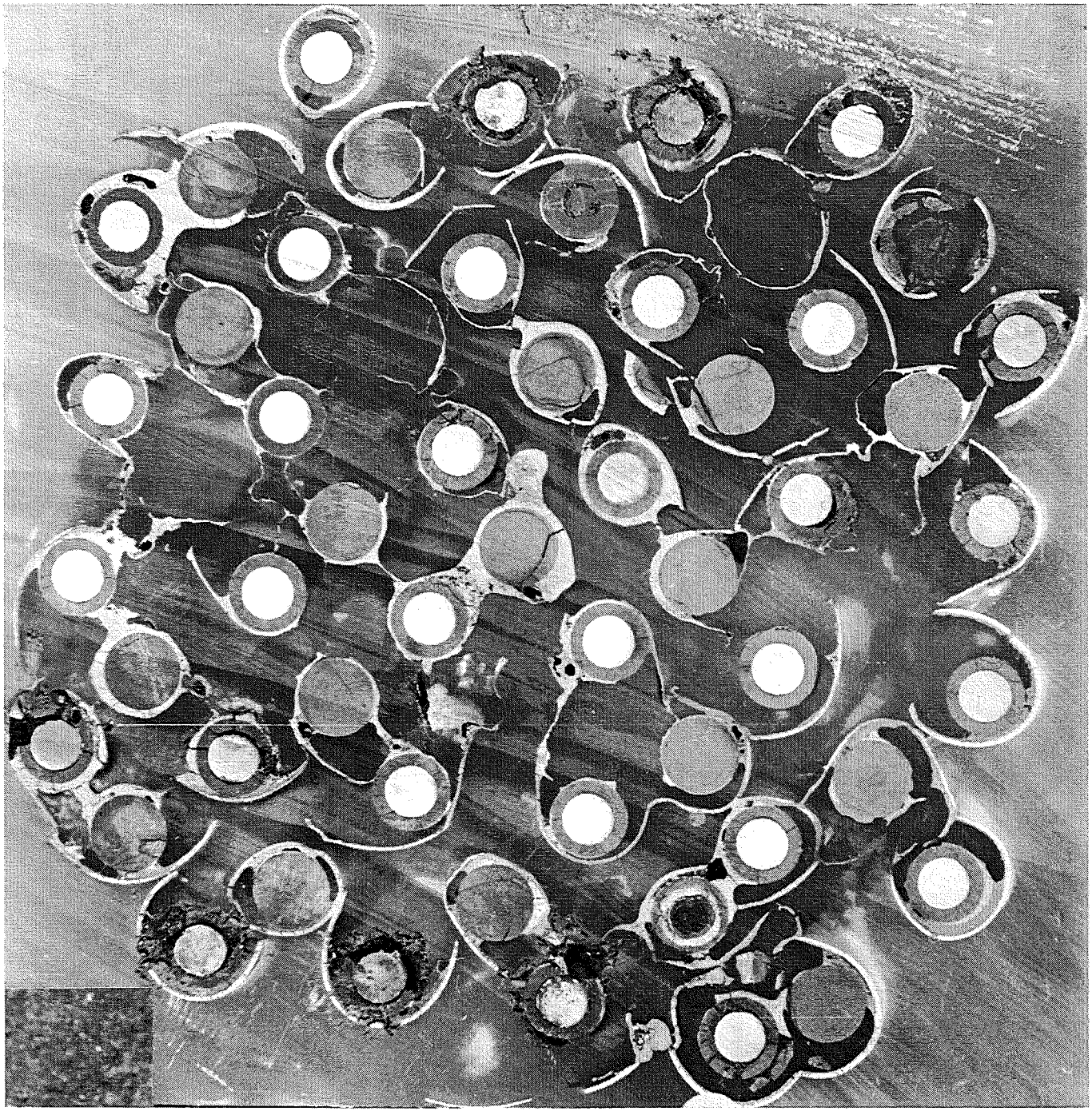

Fig. C8: Horizontal cross section; top view

CORA 7

622 mm

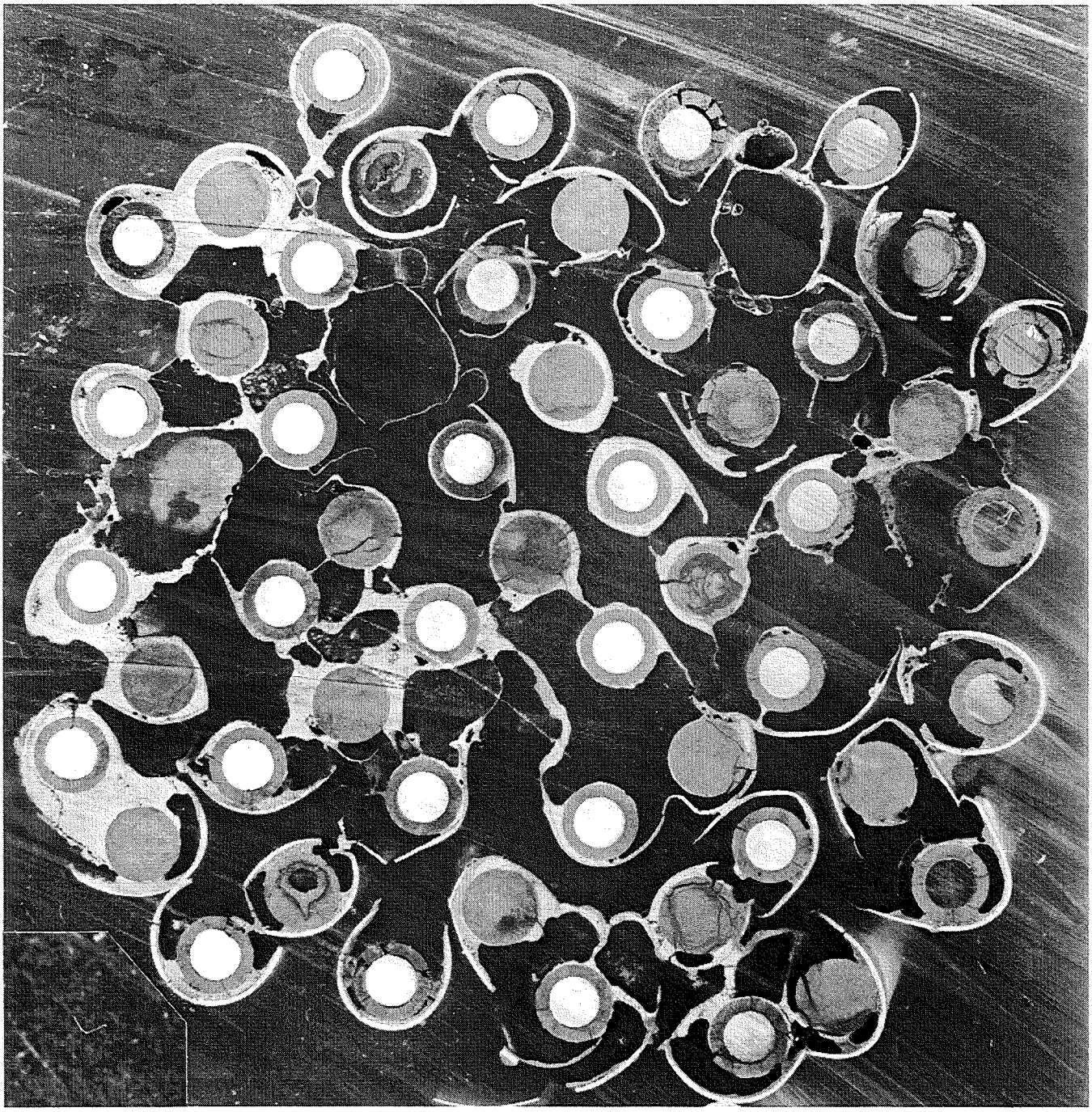

Fig. C9: Horizontal cross section; top view

CORA 7 480 mm

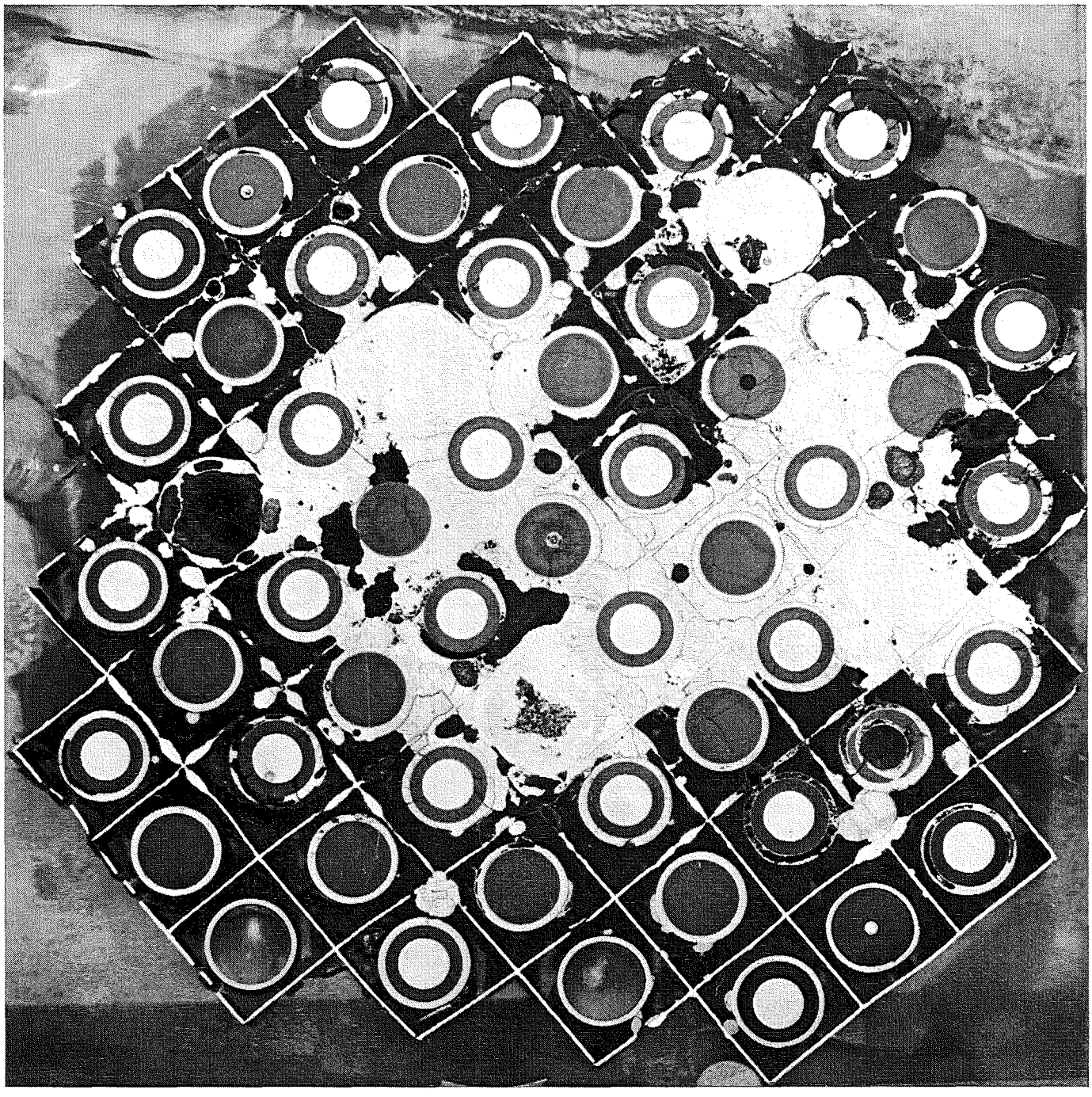

Fig. C10: Horizontal cross section; top view

CORA 7 465 mm

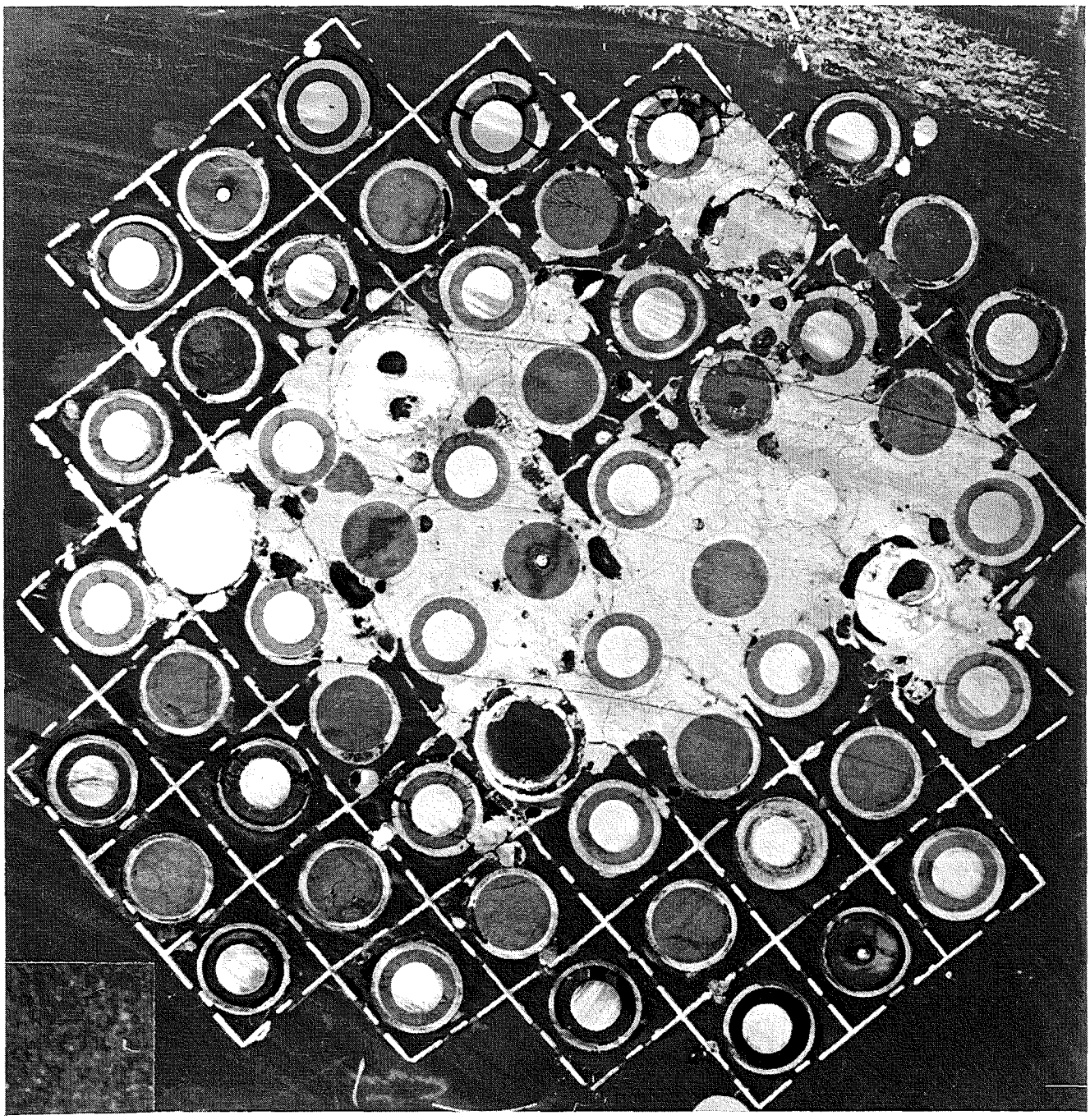

Fig. C11: Horizontal cross section; top view

CORA 7

426 mm

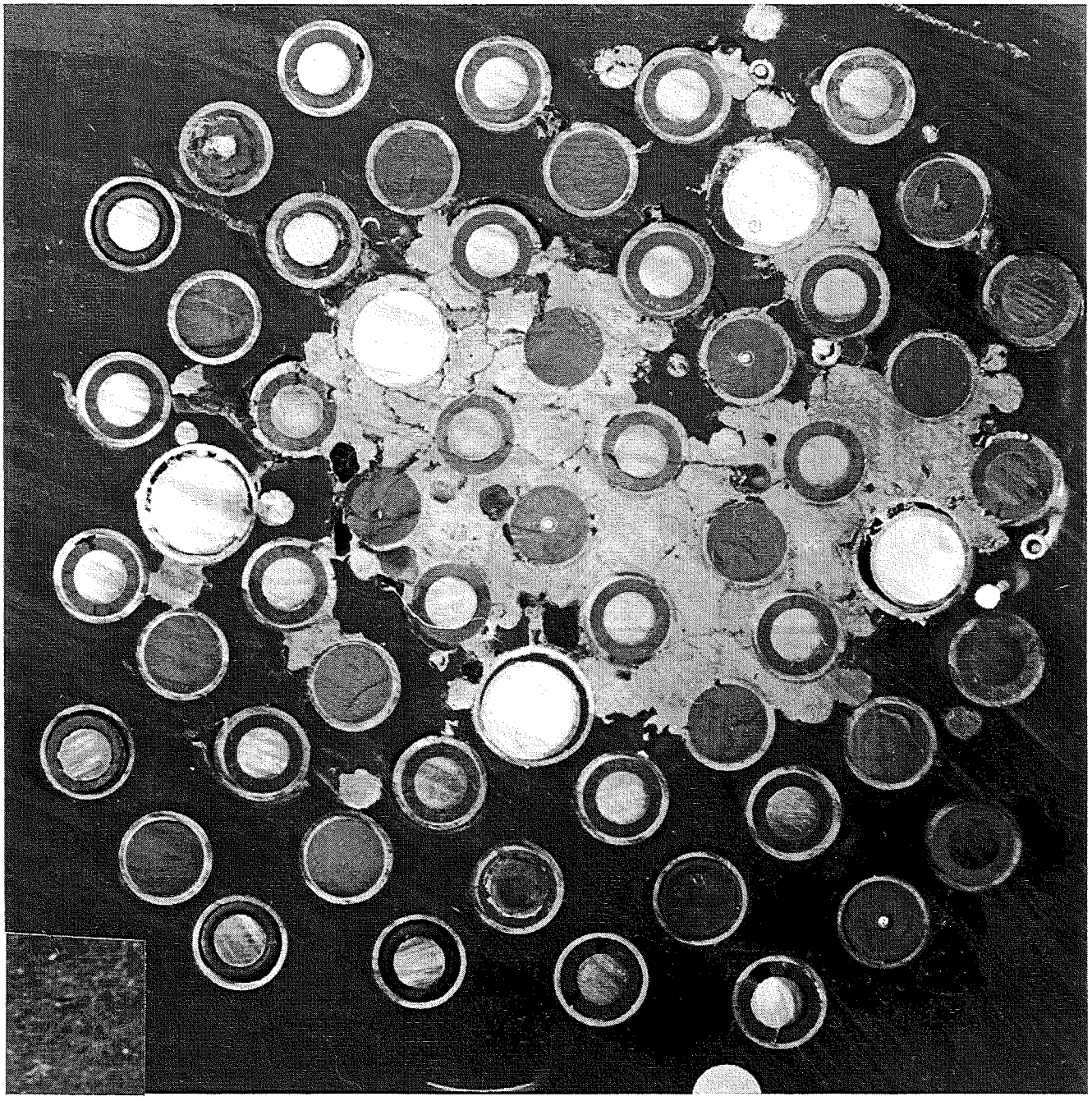

Fig. C12: Horizontal cross section; top view

CORA 7

284 mm

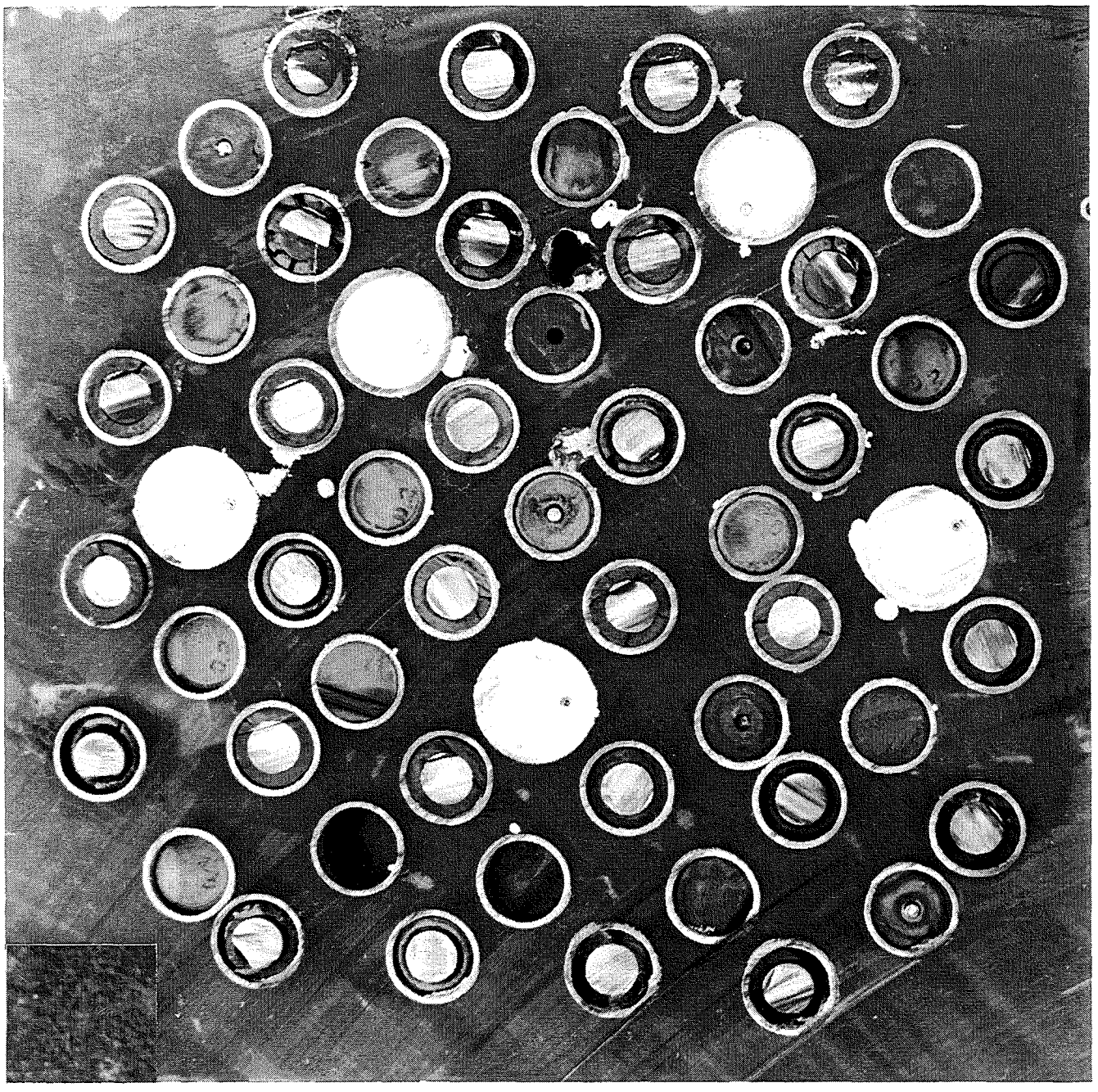

Fig. C13: Horizontal cross section; top view

CORA 7 269 mm

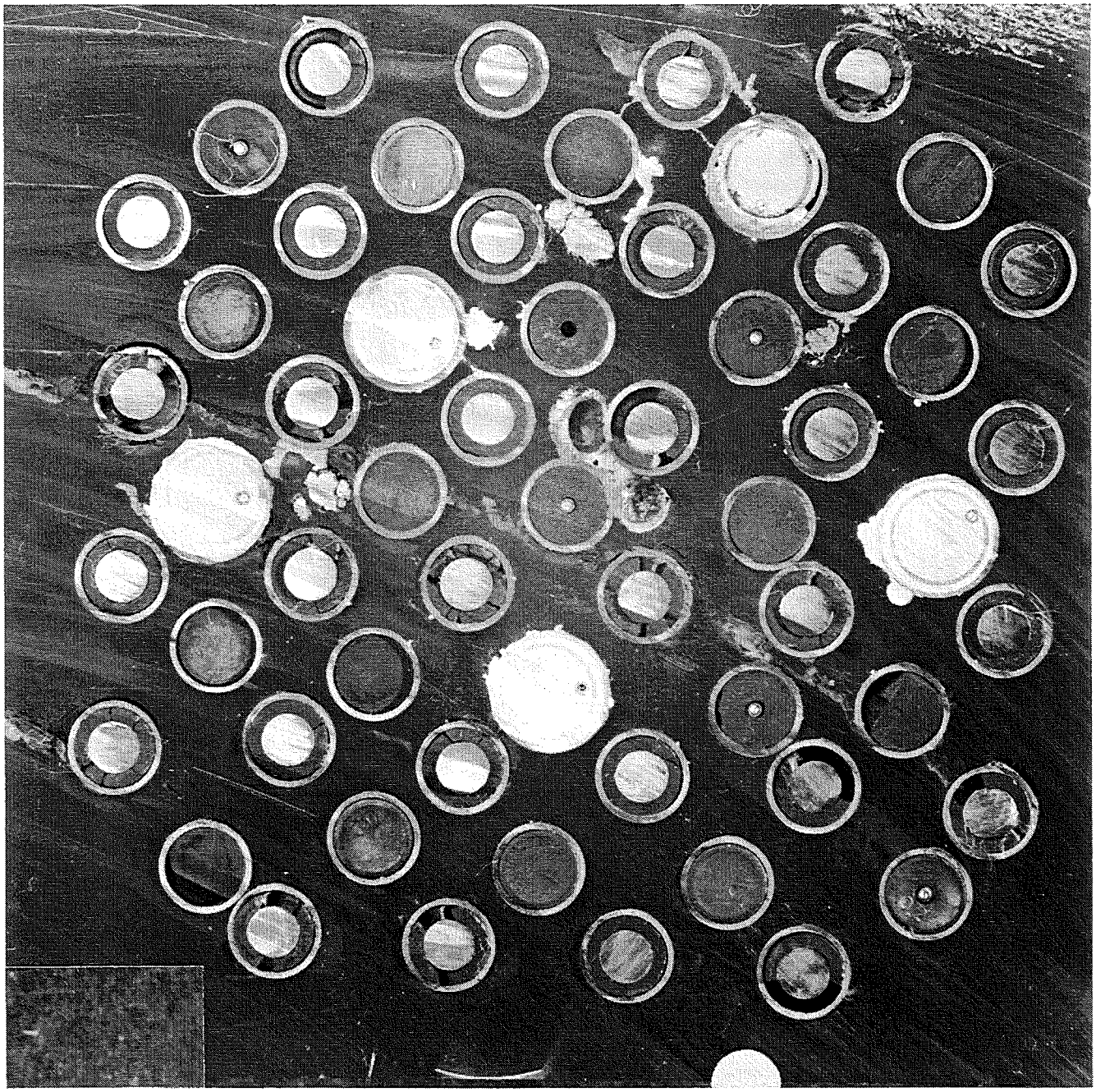

Fig. C14: Horizontal cross section; top view

CORA 7 127 mm

Fig. C15: Horizontal cross section; top view

CORA 7 112 mm

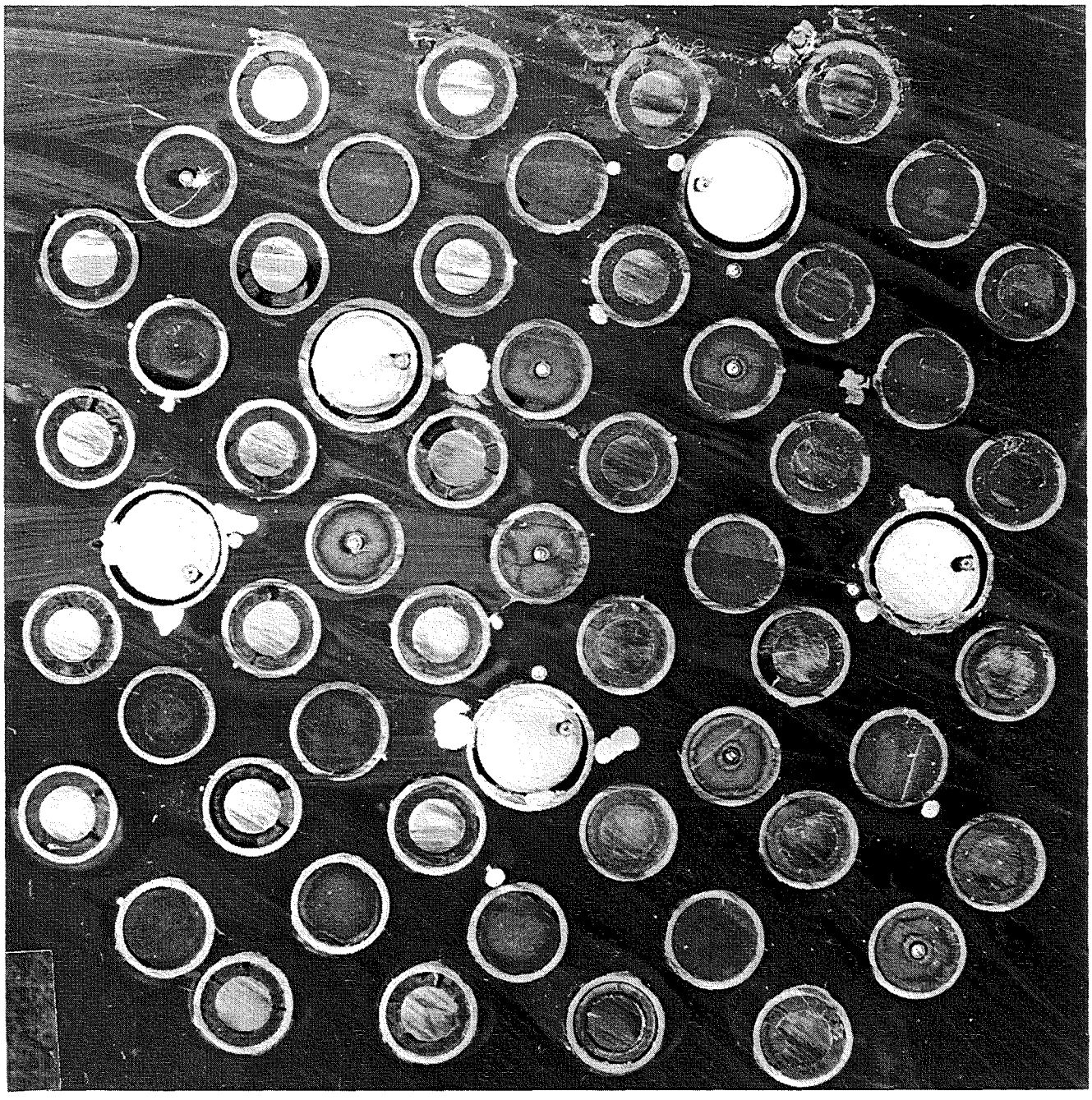

Fig. C16: Horizontal cross section; top view

CORA 7 -30 mm

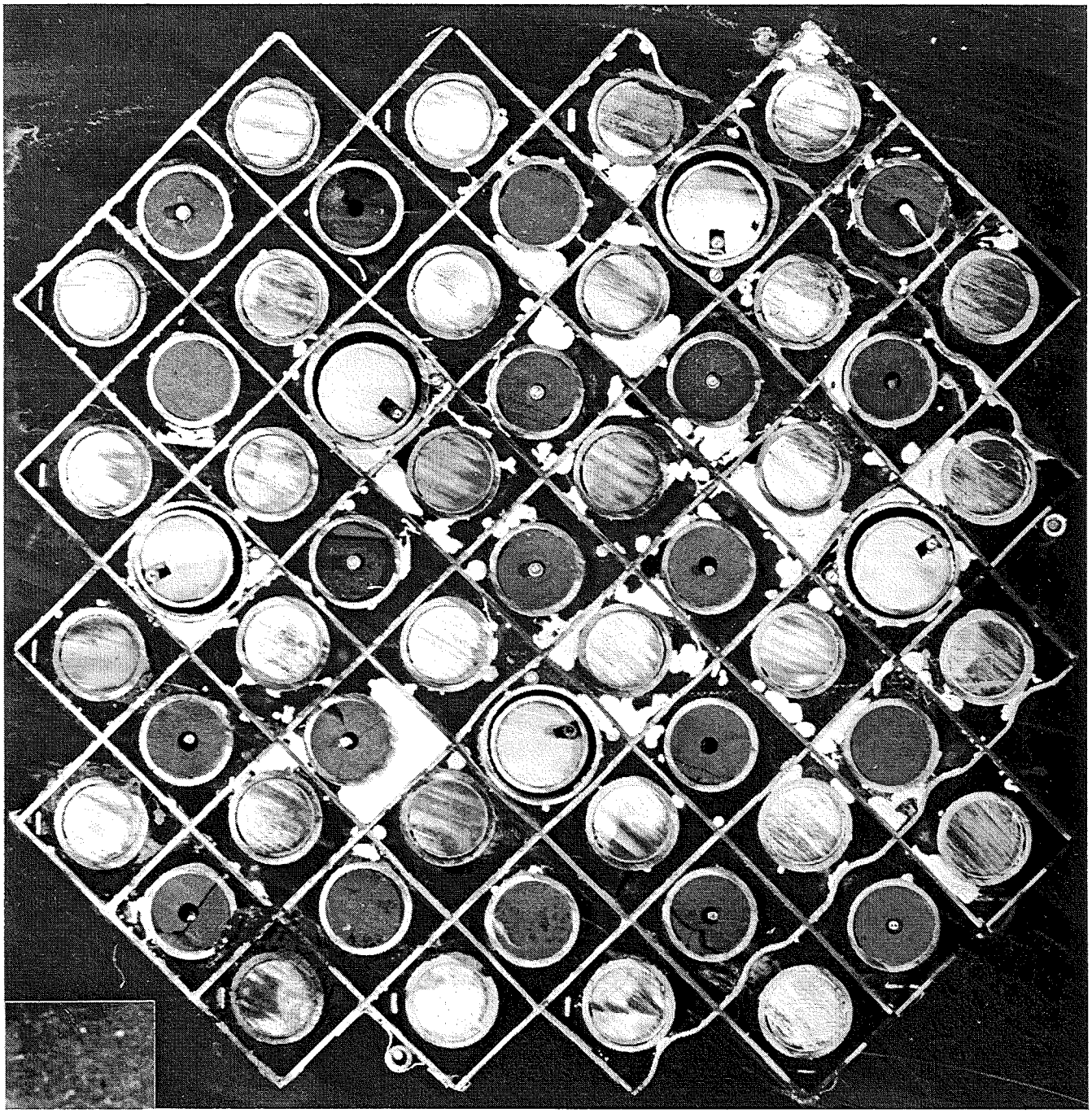

Fig. C17: Horizontal cross section; top view

CORA 7 -45 mm

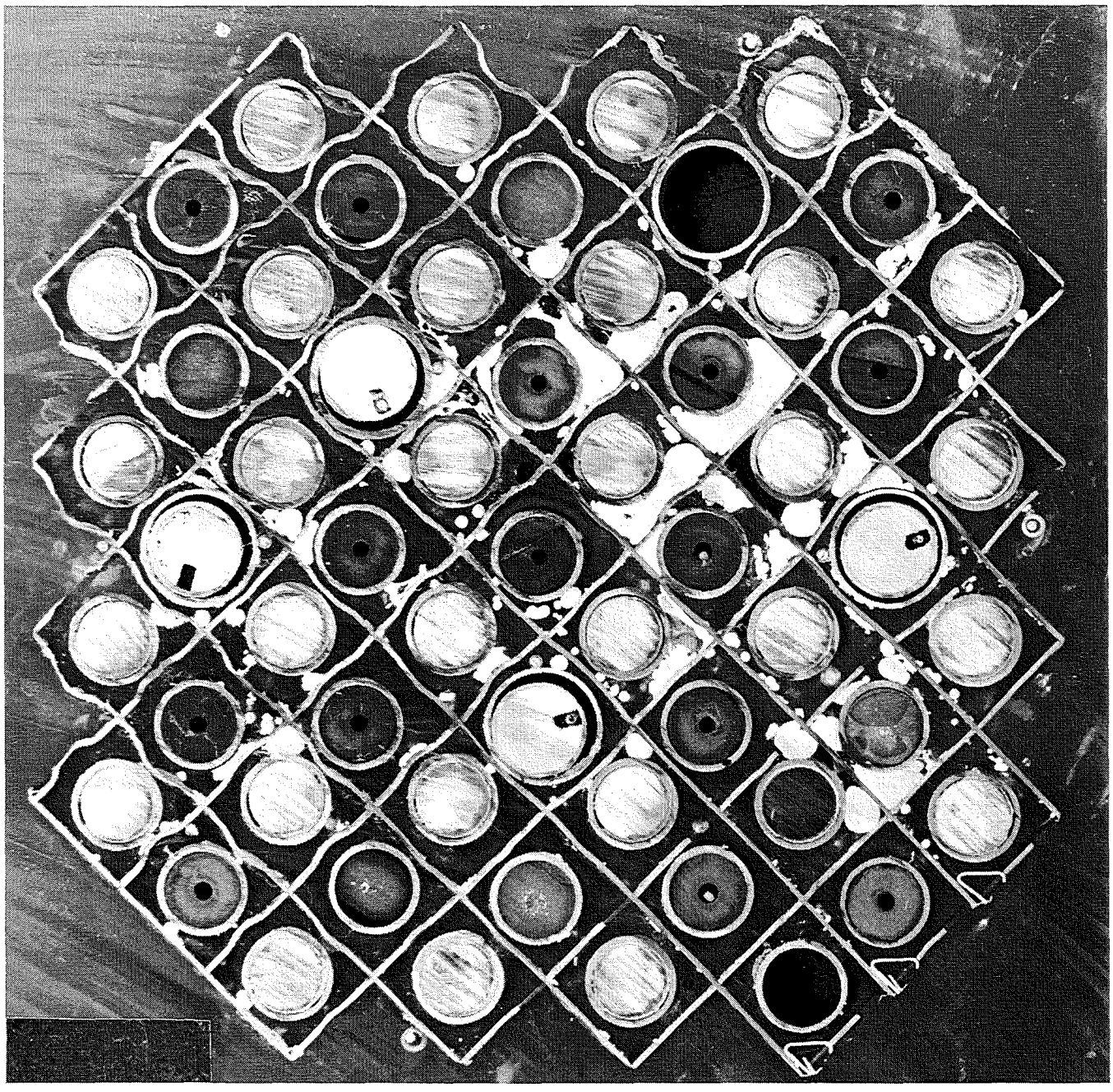

Fig. C18: Horizontal cross section; top view

CORA 7

-58 mm

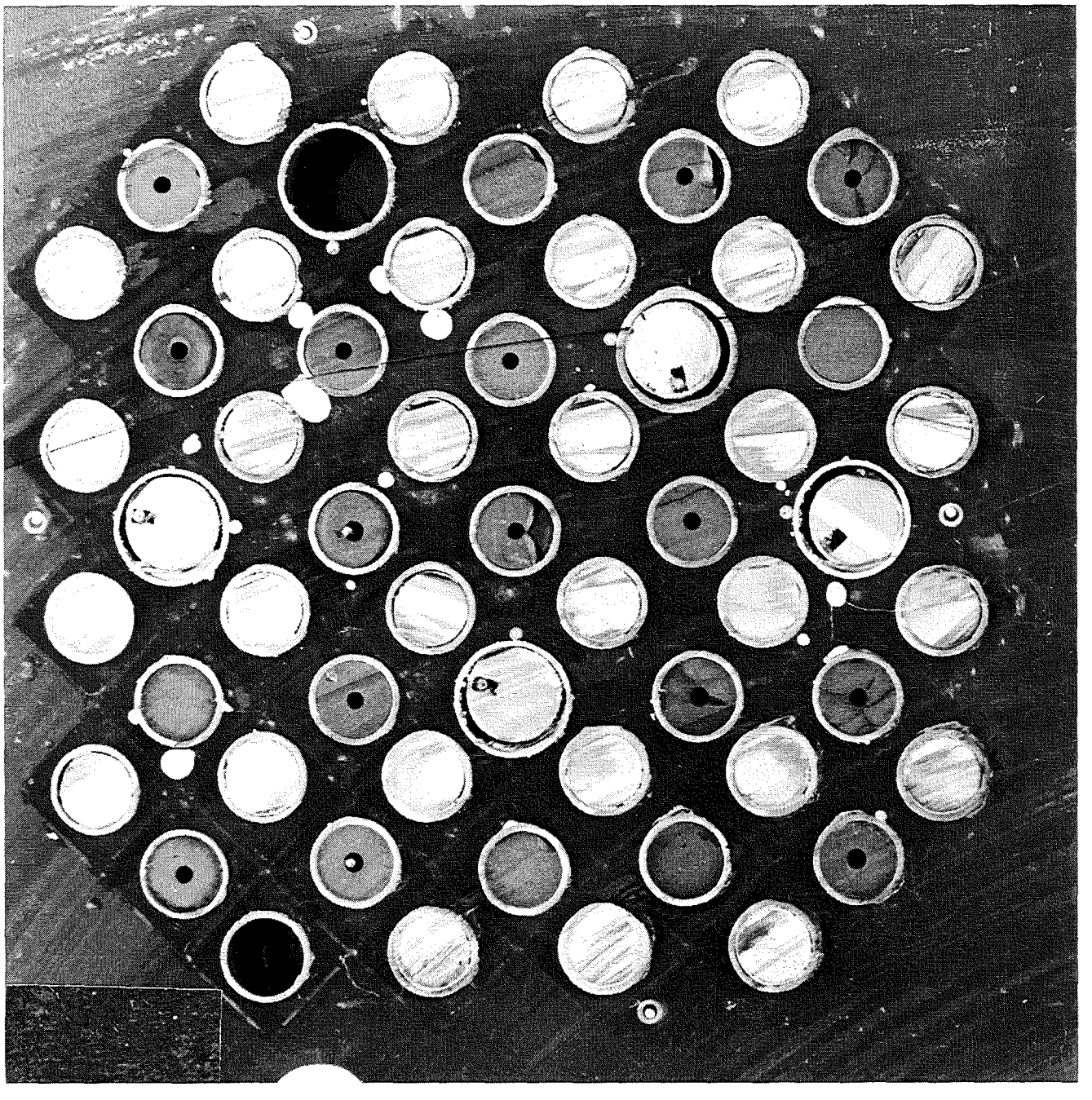

Fig. C19: Horizontal cross section; bottom view